Cardiff University

Development of a Metamaterial for use in American Football Head Protection.

A thesis submitted for the degree of Doctor of Philosophy

f

Benjamin Hanna
9-30-2020

Declaration

This thesis is the result of my own independent work, except where otherwise stated, and the views expressed are my own. Other sources are acknowledged by explicit references. The thesis has not been edited by a third party beyond what is permitted by Cardiff University's Use of Third Party Editors by Research Degree Students Procedure. This thesis contains approximately 48,054 words, including all including appendices, bibliography, footnotes, tables and equations, and has 100 figures.

Acknowledgements

I am most thankful to my supervisors Dr Peter Theobald and Dr Shwe Soe, for their time, guidance and patience that contributed to this Thesis. Significant recognition must also be given to Roy Burek and Matt Stewart of Charles Owen for the funding of my PhD and insight into helmet manufacture and testing.

Thanks must also go to my parents, who put up with years of me taking things apart, and to my wife, Louise, who without I may have never finished writing this.

Benjamin Hanna

Abstract.

American football athletes are exposed to a high number of head impacts of varying severity throughout the course of regular play. The sport has a high rate of concussions, despite mitigating strategies, including protective helmets, when compared to other contact sports.

Current helmets commonly use elastomeric foams as the principal energy absorption mechanism to protect players from injury. However, these foams have limited performance ranges due to their mechanical properties. Therefore for better player protection, a novel material was required. Novel materials and structure combinations presented the ability to leverage material properties that had the potential to expand the performance range of a helmet liner. This study investigated a metamaterial based on stacked layers of the Miura Ori folding pattern, which offered both improved performance and ample scope for optimisation.

The Taguchi method was used to design a series of samples manufactured from thermoplastic polyurethane, tested using a series of validated impacts. Data from these impacts were used to refine the geometry, using statistical processes, such that measured accelerations and injury metrics were minimised. The metamaterial's final design was then tested as part of a helmet to establish the improvement in performance offered over the original foam liner.

The selected geometry reduced the risk of a player sustaining mild brain injuries while offering comparable protection against catastrophic injuries when impacted. This risk reduction not only reduces the number of injuries that could be expected over players' careers but also has the potential to reduce the probability of players developing neurogenerative conditions later in their lives.

Table of Contents.

Table of Figures

Chapter 1: Introduction.

Contact Sports, defined as sports where players purposefully collide with other players or inanimate objects, are popular worldwide. Both non-contact and contact sports have an association with forms of head injury, though the severity of sports-related head injuries tends to be lesser than those that arise in the automotive space [1,2]. Sports-related head injuries account for an estimated 18% of all head injuries reported, with approximately 300,000 sports-related mild traumatic brain injuries (mTBI) occurring each year in the United States [2,3].

The risk of an athlete sustaining a head injury within any given sport has been assessed by a variety of metrics, including per match, per season, or the number of Athlete Exposures (AE), with one AE being equal to one athlete taking part in one play session [4]. When mTBIs are considered, contact sports (e.g. rugby) have reported rates of injuries that are closer to combat sports (e.g. karate), where victory is achieved by purposefully injuring or incapacitating the opponent, than non-contact sports such as volleyball [4,5]. For more serious traumatic brain injuries (TBI), it is harder to establish a similar relationship between these categories of sports, due to the low incidence rates [6]. Multiple cases of mTBIs have been associated with the development of neurodegenerative conditions, and these conditions have been reported at higher rates for elite athletes compared to general populations across a range of sports [7-11].

Given the relatively high rates of injury, many contact sports have historically introduced specific head protection equipment. Some sports such as rugby, have refused to introduce any head protection due to the concern of a paradoxical increase in head injury rates, which may arise due to more aggressive actions undertaken by emboldened players [12]. Since the introduction of helmets to contact sports, the number of reported incidents of TBIs has reduced; however, numbers of mTBIs have remained unchanged or increased [13]. This suggests that these measures were effective in reducing the most severe head injuries seen within sports but has potentially failed to address more mild injuries.

Sports helmets consist of two primary components in their design that aid in injury prevention: a thin outer shell made from hard plastics such as Acrylonitrile Butadiene Styrene (ABS) to resist punctures to the helmet and to spread the load, overlaying a thicker energy-absorbing liner [14]. When head impacts are expected to be singular events, such as crashes in cycling, helmets commonly employ elastic-plastic materials, such as Expanded Polystyrene foam (EPS), as the material of choice due to its high weight to performance ratio [15]. In contact sports where athletes are exposed to multiple head impacts in a single practice or competitive session, helmets must employ a recoverable elastic material that can withstand high stains without permanent deformation, whilst returning to an undeformed state in a short time frame [16,17].

Helmet liners are commonly constructed from cellular materials, due to their ability to provide consistent resistive forces, whilst being deformed during impact. The use of this class of material has been extensively studied in head protection literature [18]. Foams are a subclass of cellular materials with their performance defined by the density and material properties of the base material; however, fundamental limitations prevent optimisation over a range of impact conditions [19]. Alternative cellular structures have begun to appear in a range of helmets, seeking to reduce injury rates by providing better energy absorption over a range of velocities and providing more scope for optimisation to a given scenario [20-34]. New classes of materials have also been considered for energy-absorbing purposes including auxetics (i.e. those with a negative Poissons ratio), viscoelastic materials (i.e. whose increased strain-stiffening response may allow for favourable performance over an increased range) and origami-based structures (where geometry may allow for control over part collapse under compressive loads) [20-34].

While various casting methods can manufacture polymer foams, more complex cellular geometries are challenging to manufacture. Metallic lattices, for example, are limited in cell size by material flow restrictions [24]. Whilst some novel geometries are developable, meaning they can be constructed from flat sheets of material, this construction method poses its own challenges, as individual sheets must be bonded together in some manner for a true cellular material to be formed [31].

Additive manufacturing (AM) methods enable the fabrication of a wide range of cellular geometries from a wide range of polymer-based materials [35,36]. It has been established that cellular materials' performance is reliant on the behaviour of the walls, and as such, the homogeneity and dimensional accuracy of any novel cellular structure is vital [19]. The fused filament fabrication (FFF) process – an economical and accessible (if not 'hobbyist') form of AM, is capable of manufacturing high-quality functional components from a variety of materials, presenting advantages in terms of cost and manufacturing time for small scale experimental development versus established AM processes including selective laser sintering and stereolithography [37-39].

Recent developments in the FFF process have facilitated the use of elastomer base materials to produce functional components, most notably from thermoplastic polyurethanes (TPEs) [40-42]. TPEs are of particular interest in the application of personal protective equipment (PPE), as the copolymer possesses not only the high strain capability of other elastomers but also high abrasion resistance. TPEs are already seen as candidate materials for novel structures within helmets [41,42].

By leveraging these advances in AM technology, this study aims to reduce mTBI risk in American football, by developing a novel cellular structure for use as a liner material within helmets. This thesis systematically describes the journey to achieve this aim.

CHAPTER 2: This chapter outlines the current understanding of the major topics of this study. It includes the type, rate, and current mitigations to head injuries in American football, the impact environment of American football, the mechanics by which cellular materials absorb energy, potential material types that could provide benefit to a helmet liner and the additive manufacturing process available to manufacture a novel material. This knowledge is used to define a design specification for a candidate material and appropriate metrics for optimisation.

CHAPTER 3: This chapter covers the process to generate an appropriate TPE printing profile. The ability of this profile to manufacture components that were both dimensionally accurate and fully dense were vital to the process of optimising the selected geometry. The suitability of the process was assessed through the use of micro-computed tomography (μCT) imaging, which allowed for precise measurements of dimensional accuracy and internal pore volumes.

CHAPTER 4: This chapter presents a scoping study to validate the experimental design used to optimise the selected geometry in later chapters. The experimental factors covered in this section include parameter selection, range of parameters examined base material selection and the existence of interactions between parameters.

CHAPTER 5: This chapter covers the main effort in the optimisation of the selected geometry. A series of developed samples are exposed to both quasi-static compression and impact events that represent the impact environment of American football. The data captured in these tests allowed for the examination of the structural behaviour and deformation mechanisms of energy absorption. Standardised injury risk metrics were calculated and used in well-established statistical methods to identify combinations of geometry that enabled favourable performance over the range of impact conditions.

CHAPTER 6: The performance of the optimal geometries developed in **Chapter 5** was noted to be different from the expected response of an auxetic material. This chapter investigates whether downscaling cell volume to increase complete cells per sample could restore the auxetic response of the selected geometry and thus improve impact performance.

CHAPTER 7: This chapter selects from the developed geometries to identify the sample with the most preferential performance for injury prevention from those developed in **Chapter 6.** The selected geometry was used to generate a replacement liner pad for the front of a commercially available helmet recommended by the governing body for professional-level American football. The helmet was then tested under standardised conditions so that appropriate comparisons to contemporary protection systems could be made.

Chapter 2: Literature Review.

2.1. American Football as a Case Study of Head Injury in Sport.

American Football, henceforth referred to as football, makes for an ideal case study for the development of a novel impact protection material for use within head protection. The sport has a large and diverse player base ranging wildly in skill level, experience and fitness, which can be split into four cohorts:

1. Youth or "Sandlot": The youngest and least skilled cohort, with ages ranging from 5 – 13, and a team size on average of 20 to 25 players. Participation is estimated to be between 2.8 and 3 million athletes [43,44].
2. High School: Players age ranging from 14 – 18 with a more formalised training regime and a longer playing season. Teams have an average of 77 players, with an estimated 1.1 million athletes in active participation [43,45].
3. College: Players age range between 18 – 23, having been selected from among the high school cohort's best. Training intensity and regularity increase again, with an average of 110 players per team in 2016, and a reported 73,660 athletes in active participation [43,46].
4. Professional: All players playing for a commercial team governed by the National Football League (NFL). There are 32 NFL teams are formed of 53 players each, with 46 being available for each game, and approximately 26,000 former players [47]

For each team within these four categories, three further subdivisions have been made based on playstyle, and on-field objective.

1. Offensive Team: The line-up of players used by teams for any on-pitch plays for which they start in possession of the ball.
2. Defensive Team: The line-up of players used by teams for any on-pitch plays for which they start not in possession of the ball.
3. Special Team: The line-up of players used by teams for kick-offs, kick-off returns, punts, punt returns, field goals and extra-point attempts [48].

Each of these subdivisions can also be split between skill and line positions with skill positions tending to be involved in higher velocity collisions on the pitch [49,50]. Line and skill positions also vary in height weight and body fat percentage [51-53]. Due to rules limiting the number of skill-based actions they can partake in, athletes in line positions have become physically larger over time as their role has been reduced to blocking and tackling actions [52,53]. Almost all player positions have seen increases of up to 15% in average player weight when current athletes are compared to their historical counterparts, with a concurrent increase in player strength and speed, due to better nutrition and training [52]. Finally, body composition changes by country with Japanese players tending to be smaller and less physically capable than their American counterparts [51].

When compared to other sports, football has a staggeringly high rate of head injuries. Estimates suggest that head injuries of all types account for 19 to 21% of all non-fatal injuries within football, compared to 4.5% for all sports and rugby where the rate is 16% [2,54]. High school football accounts for 47% of all Sports-Related Concussions (SRC) reported in this age group, and collegiate men's football accounts for more concussions than the next three highest college sports, in terms of absolute numbers of SRCs, combined [55,56]. Additionally, the sport has a long history of enforced helmet use at all levels, and for a significant period, the design of the helmets in use have remained fundamentally unchanged [17,57]. There is a large body of data, across a wide range of time, assessing the performance of these helmets, through a range of metrics. Data for both the number of head injuries of all types and the severity of causal impacts, assessed by speed and weight and translational and rotational accelerations, are available across all levels of play and on pitch position.

2.2. Causes of Brain Injuries in Sports.

Understanding the impact environment to which football athletes expose themselves is vital to providing context for the reported head and brain injuries they sustain. The following subsections define this impact environment in terms of the number of impacts, the distribution in impact magnitude, impact location and the effects of player position. These values are vital to the development of a novel helmet material.

Since 2007, there have been numerous studies quantifying the number of head impacts sustained across football. However, there is no published work quantifying the number of impacts sustained by professional level players, because the NFL determined that the most commonly used in-helmet measurement system, the Head Impact Telemetry (HIT) system was unsuitable [58].

Figure 2-1: HIT player unit, consisting of 6 accelerometers in spring-loaded holders, frequency modulation antenna, and rechargeable battery pack.[59]

The HIT system is an array of 6 linear accelerometers in a spring-mounted casing. When a single accelerometer crosses a threshold value, usually 10 – 15g, 40ms of data are recorded, with between 8 and 12ms of pre-trigger data [59,60]. The system has been validated against the Hybrid III headform with linear accelerations over-estimated by between 0.9 and 4% (r^2 = 0.903) and rotational accelerations under-estimated by between 4 and 6.1% (r^2 = 0.528), with the lower reported accuracy for rotational accelerations attributed to the system's inability to precisely capture impacts centred on the face shield of a helmet [59,61]. The systems' ability to identify the impact site was found to be within 2.41° of the impact site [59]. This accuracy level meant that the identified location of impact was within the diameter of the impactor [61]. The system has an estimated false positive rate of 2%, where the system records an impact where no on-pitch collision has occurred, and concerns have been raised over the system's accuracy when separation between the helmet and players head occurs during impact [61,63].

Compared to video replays of instrumented sessions the HIT system was found to have correctly categorized 70% of recorded impacts, with 23% of impacts seen in video replay not being recorded by the system [375]. This would suggest that it is likely that the number of impacts received by players in American football reported elsewhere in the literature serve as a potential underestimate of actual on-field impact numbers.

Other systems reported in the literature such as xPatch (X2 Biosystems, Seattle, WA) and the Vector MouthGaurd (Athlete Intelligence, Kirkland WA) are less well-validated by comparison, with xPatch in particular severely overestimating peak accelerations by 64±41% and angular acceleration by 370±456%, with a false positive rate of approximately 14% [62,63]. While this would invalidate any analysis of impact magnitudes using data recorded by this system, the number of impacts recorded may still have been accurately captured and therefore remain useful. In comparison the mouthguard based systems reported between errors consistent with the HIT system for both linear and rotational accelerations, although the system has been noted to be more sensitive to potential error sin the recording or rotational values as the mouthguard may rotate separately from the head [376]. While no single sensor system can accurately record all events on the pitch, the gold standard for which should be video recordings from multiple angles, these systems' uses allow for the capture of data outside of recorded games. When the data is viewed as a whole population rather than single events, useful patterns will emerge and overcome these systems' limitations.

The total number of impacts sustained by a single athlete in a single season, and how this varies by cohort, position and play type is an essential metric for understanding the highly cyclical environment head protection in football undergoes. The reported average impacts per season for both the high school and youth cohorts, approximately 200 and 500, remain stable across the available literature [49,60,64-74]. When concussed high school players were studied in isolation, they reported a significantly higher number of head impacts than average [71].

Compared to these two cohorts, the per-season average number of impacts for college players is less well defined, ranging from 281 - 1354 [48,69,70,75-78]. The lower value estimates come from studies where not all sessions within a season were recorded, or from studies based in Japan, where a mix of body composition and play culture may have lowered the total number of impacts [79,80]. Accounting for these factors, a value of approximately 750 impacts per season seams realistic.

Both high school and college football players sustain substantially more impacts during games than practice sessions, with relative rates ranging from 1.27 to 5.39 [73,74,76,79,81]. This difference is most likely driven by the highly competitive nature of games where players take more substantial risks in both offensive and defensive actions as they have a perceived in-game benefit. Another factor to consider is the relative intensity of practice sessions, where low-intensity sessions result in little head impact risk. Low-intensity practices make up around 62% of all sessions in a given season for College teams, and as such, the inclusion of these sessions may decrease the average number of impacts [82].

However, it should be noted that non-helmeted practices are naturally excluded from data capture and so would limit the influence of the low-intensity sessions. Youth players sustain a similar proportion of head impacts during both games and practice sessions, though this is likely due to the tendency of practice sessions for this cohort to be of a similar intensity to games [64,65,67]

The large number of impacts that football players sustain needs to be understood in two ways. Firstly, through the velocities and masses involved in these impacts, any method used to develop protective equipment must be based on these statistics to provide a suitable protective system. Secondly, the magnitude of accelerations induced in the head by these impacts should be quantified so that novel materials' performance can be placed into context.

Little research has been carried out concerning the dynamics of head impacts within American football, with the vast majority of papers concerned with the resultant accelerations from on-pitch events rather than the players' pre-impact momentums. Pioneering work into the prevalence of concussions within the NFL in 2003 identified an average impact velocity of 9.3 ± 1.9 ms^{-1} for injured players, with uninjured players sustaining impacts at 7.0 ± 2.6 ms^{-1} [83].

As the initiating players had much higher effective striking mass, due to their ability to align their head and torso, the 2003 study estimated that the change of head velocity of the struck players was 7.2 ± 1.8 ms^{-1} for injured players, with uninjured players reporting a lower change in velocity of 5.0 ± 1.1ms^{-1} [83]. A study based on testing of modern helmets reported that the change in velocity for headforms fitted with current helmets was 60% of the inbound velocity, or 5.58ms^{-1} [84].

The latest estimate of the change in head velocity resulting from an injury-causing impact puts the value at 4.29 ± 1.71ms^{-1} significantly lower than previous estimates [85]. This

study was based on data from the HIT systems, rather than reconstruction from game footage, which may explain the variation. Change in head velocity has also been reported to be influenced by the contact location on the head [86]. When a players position has been considered, offensive skill positions, such as quarterback and wide receiver, had a much more significant change in head velocity, around 11ms^{-1}, compared to the team average and positions such as lineman 3.28ms^{-1} [49,50]. Effective impact mass also varies wildly with linemen typically able to recruit more body mass, 28kg, into their low-speed contacts than skill positions can, 13.1kg, into their high-speed contacts [50].

The vast majority of the large numbers of head impacts sustained by players result in relatively low resultant accelerations with average values ranging from 17 – 27.3g and 671 – 1430 rads^{-2} depending on the level of play [60,66,75]. Impact magnitude is reported to vary with both player position and on helmet location, with impacts to the top of the head reporting higher linear accelerations but lower rotational accelerations than other areas of the head [49,69,76]. The reported distribution of both linear and rotational accelerations are heavily skewed towards lower magnitudes, with 86– 97% of reported accelerations as being below 40g and 3000 rads^{-2}, depending on a players age group, Figure 2-2. As such, few recorded impacts exceed the previously proposed thresholds for mTBIs, which is expected given the relatively low number of SRCs compared to the number of sustained impacts.

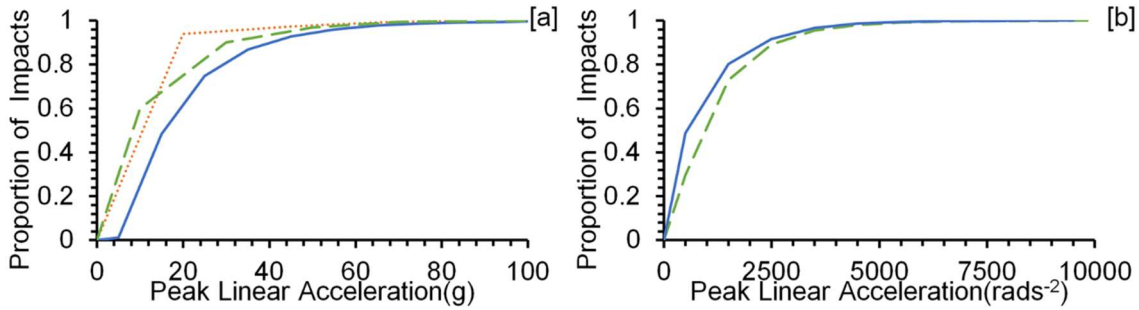

Figure 2-2: Cumulative distribution of linear [a] and rotational [b] accelerations sustained by youth (orange dot), high school (blue line) and college (green dash) players as reported in the literature [60,66,75].

High school players seemingly report a higher average peak acceleration than their college counterparts, which would reinforce the idea that high school players hit harder than college players. However, the similarity in body mass and height in these two groups would suggest similar biomechanical forces result from impacts, and therefore the difference may be driven by high schools players having less refined technique [60,64,65,74,77,78]. However, it must be acknowledged that these studies focused on

single teams over limited periods and may not be representative of the whole football population.

The reported evidence on the number and nature of impacts paints a clear picture of a demanding impact environment in which American football helmets must operate. A large number of impacts each season naturally specifies a rigid material, while the multiple impacts in games and practice sessions happening at a variety of velocities require a material with both quicky recovery from being loaded and a wide range of performance. Although current helmet designs can perform under these conditions, they offer the same protection to all onfield positions despite the identified differences between player positions, both number of impacts and impact energies. Therefore a novel solution may have the capability to offer bespoke position-specific protection.

2.3. Head and Brain Anatomy and Physiology.

No discussion of head injuries seen within American football can be conducted without understanding the head and brain's anatomical structures. Although the brain comprises part of the central nervous system, the other structures of this system, such as the spinal cord are not discussed here. The head comprises five primary structures: face, scalp, skull, meninges and the brain.

The scalp is the head's outer covering and is itself a complex structure of several layers, including connective tissues skin and the periosteum [87]. Due to the thinness of the scalp, 5-7mm, and a large amount of connective tissue, damage to the scalp often leads to profuse bleeding [87,88]. Eight bones of the skull form a vault-like structure for the brain, varying in thickness from 4-7mm. The rest of the skull comprises 14 bones that define the facial structure, all of which bar the mandible are fused with the rest of the skull.

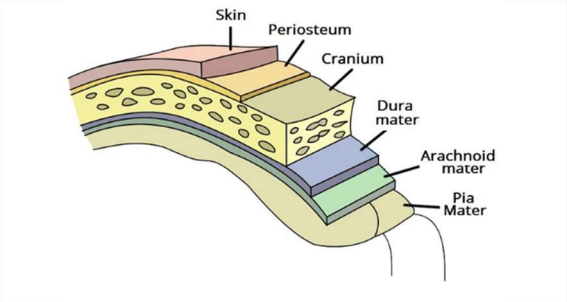

Figure 2-3: Overview of the meninges, and their relationship to the skull and brain. [89]

Beneath the skull lies the meninges, three distinct membranes that cover the brain. The outermost of these layers is the dura mater, which is tough and inflexible. The dura matter also provides vascular function for the cranium allowing blood to drain from the brain to the heart. The next layer is the arachnoid matter covering the entire brain and spinal cord trapping cerebrospinal fluid, which provides protection, buoyancy and chemical stability to the brain. The final meninges are the pia mater, which is the only membrane that follows all the brain's contours and is responsible for supplying the neural tissue with blood [89].

The brain consists of a network of neurons and supporting tissue, divided into grey and white matter [87]. The grey matter forms the brain's outer surfaces and is responsible for cognition and processing, while the white matter forms the deeper parts of the brain and connects the various areas of the grey matter. The brain itself is separated into four lobes; within each lobe are select groups of neurons dedicated to individual tasks.

2.4. Traumatic Brain Injury

For any novel impact protection material to be developed such that it is fit for purpose, the reported pathology of head impact-related injuries, both historic and contemporary, needs to be evaluated. Although it is used synonymously with TBI, head injury is a broad category, including injuries such as scalp lacerations that have no impact on the brain. TBIs focus on recoverable and non-recoverable damage to the brain structures and are differentiated by severity, mechanism and focal area [90]. TBIs are distinguished from other brain injuries by the presence of an external mechanical force.

Within the literature, three distinct classes of brain injury are reported for both current and former athletes of all levels:

1. Catastrophic Head Injuries (CHI): This category covers the most severe forms of head injuries and TBIs, defined by three distinct clinical outcomes; fatal, non-fatal with permanent disability and serious with no permanent disability [2,3].

2. mTBI and SRC: The most common form of head injury experienced by football players, SRCs and mTBIs often presents short recoverable neurological deficits, but a minority of patients suffer long term effects [91-96].

3. Neurodegenerative Diseases (ND): A wide range of NDs, including but not limited to Alzheimer's Disease, Amyotrophic Lateral Sclerosis (ALS), and Chronic Traumatic Encephalopathy (CTE) have been diagnosed in former football players [7]. Links between these injuries and sustained TBIs have been made, but have yet to be fully established [97,98].

For most of the papers presented in the following sub-sections, some caveats must be acknowledged; firstly, the small study effect, where low study populations may produce higher effect estimates and may be less reproducible. Secondly, any comparison between football players and the general population inherently disregards differences in physical fitness, and therefore, may overestimate the impact football has [47]. Finally, it must be noted that in 2010, the faculty at Johns Hopkins found that almost all research concerning SRCs in football failed to meet Class 1 evidence-based criteria. As such, any data reported before this date should be considered carefully, and the reported rates may be non-representative [99].

2.4.1. Catastrophic Head Injuries.

Catastrophic injuries have been tracked by the National Center for Catastrophic Sports Injury Research at the University of North Carolina-Chapel Hill since 1982. Catastrophic injuries are an injury that results in either brain or spinal cord injury or skull or spine fracture [100]. The National Centre for Catastrophic Sports Injury Research relies upon reporting of catastrophic injuries by multiple sources, including athletic trainers, state sports governing bodies and online new sources. To validate these reports, contact is made with the injured players, trainer or coach, such that specific detail around the type and causes of injury can be accurately captured and logged [100]. While best efforts are made to capture all known catastrophic injuries, difficulties arise when capturing data for CHIs with complete recovery, where the rate may be up to double that reported, and non-affiliated clubs and educational institutions, whose data may not be collected at the state level [377].

When CHIs are viewed in isolation, the majority, 75 of the 95 football-related CHIs between 1989 and 2002, present as Subdural Hematoma (SDH) [101]. SDHs are caused by bleeding and blood collection, between the dura and arachnoid mater surrounding the brain [102]. This bleeding leads to compression of the delicate brain tissue, which can lead to death if damaged brain matter remains untreated.

Since records began, Subdural and Epidural Heamotomas account for 65% of all CHIs with incomplete recovery across all play levels [100]. None of the CHIs documented between 1977 and 2018 presented with a skull fracture. This suggests that the biomechanical forces present during CHI impacts had sufficient magnitude to cause these injuries, or that helmets utilised within football were capable of diffusing the impact energy over a sufficient area, such that the focal loading required for skull fracture was not present [101,103].

Between 1931 and 2018, 1875 fatalities from participation in organised football have been recorded [104]. Of these 1057 direct deaths arose from participation in American football's fundamental skills, with the remaining 818 deaths being attributed to causes that were not unique to the sport, such as heatstroke. CHIs accounted for 69%, of fatalities reported between 1945 and 1999, rising to 82% by 2018 [104,105], as the number of spinal injuries reduced [104].

2.4.2. Concussion and Mild Traumatic Brain Injury.

Sports-related concussion (SRC) is the most common head injury sustained by football players in both practice sessions and competitive play. Interchangeably termed as mild traumatic brain injury (mTBI) in the literature [92,93], it has been suggested in recent years that the two terms should describe different forms of mild head injury, with the latter associated with permanent or persistent symptoms; however, for this review, the two terms are considered to be synonymous.

SRC present initially on impact as a mild form of diffuse axonal injury, where axons within the brain are traumatically sheared [93,106]. This mechanical damage leads to the disruption of cell membranes within the brain, allowing for the depolarization of neurons. The cellular process that responds to this ionic imbalance requires increased cell metabolism, and thus lactic acid is produced [93,107]. This process ends with the slowing of glycolysis within the brain, leading to the symptoms experienced by those with an SRC [108].

SRCs are associated with four domains of symptoms: somatic, cognitive, mood, and sleep, with these symptoms typically resolving within 7 to 10 days [92-94,109,110]; however, 12.2 – 15% SRCs take longer to resolve and are associated with more severe symptoms [93,111-113]. No consistent effects of concussion have been seen in Magnetic Resonance Imaging (MRI) datasets of those diagnosed with acute SRCs [114]; therefore, the neuronal dysfunction that leads to the full range of symptoms for SRCs is unlikely to be linked to any structural damage [110].

Historically SRCs have been defined by many grading systems, with the severity of each system's highest grade ranging from simple loss of consciousness to death [115]. Prof Cantu proposed an evidence-based system in 2001, Table 2-1, and a formalised system for grading the severity of SRCs has been developed and updated by the concussion in sports group [115,116]. The majority of SRC reported in the literature are grade 2 on the Cantu system [112]. Only 6 - 8% of SRCs result in loss of consciousness, which may explain why SRC data that does not use the Cantu system report the majority of cases of as the least severe form, while some older studies base injury severity on time loss with the mild category being defined as anything less than seven days lost [112,117-119].

Table 2-1: Grades of SCRs as Proposed by Cantu, R. (2001)[115]

Grade	Definition
1	No loss of consciousness; posttraumatic amnesia* or post-concussion signs or symptoms are lasting less than 30 minutes.
2	Loss of consciousness lasting less than 1 minute; posttraumatic amnesia* or post-concussion signs or symptoms lasting longer than 30 minutes but less than 24 hours
3	Loss of consciousness lasting more than 1 minute or posttraumatic amnesia* lasting longer than 24 hours; post-concussion signs or symptoms lasting longer than 7 days

SRC rates vary between 0.31 and 6.61 per 1000 athlete exposures (AEs), depending on level and type of play [55,120]. It has been estimated that between 38 and 61% of football players sustain at least one SRC during their career, with 6 to 24% of athletes sustaining three or more [97,121,122]. Each season 5% of players sustain a concussion, almost double the rate reported for other sports [123].

Early studies suggest that in the 1970s 15 – 20% of high school players per seasons sustained an SRC [124,125]. By the 1980s, this had fallen to 10% and then 4% - 6% by 2000 [126,128]. Systematic reporting of SRCs across all levels of play began in 1995 [129]. At the professional level, the concussion rate has remained at around 0.4 concussions per game between 1996 and 2007 [129]. Some play levels have seen increases in recent years, with the rate of concussion doubling in high school players between 2005 and 2011 and college players between 1995 and 2010 [128,130,131]. This trend continues for the professional level of play, with more concussions in the seven years between 2012 and 2019 than the twelve years between 1997 and 2007 [129,132,133]. While this increase may be due to dangerous in-play practices or an increase in players' physical capability, there are alternative causes.

Historically there has been a systematic under-reporting of SRCs by players, with an estimated 53% not reporting in 2004 [134]. This under-reporting has many causes, from players being unaware of their injures' seriousness to players not wanting to miss the next match, with some players seeing the symptoms of an SRC as an expected result of their position [120,134-136]. This under-reporting rate has reduced dramatically in recent years to around 12% for various reasons [135,136]. Governing bodies and states have tightened legislation about how concussions are reported and managed, whilst there has been an increase in qualified athletic trainers available at most levels of play [131,135,137]

Additionally, there is a higher level of SRC awareness and their risks amongst coaches and players and parents, which has led to an increase in reporting of injuries that would have been previously ignored [130]. In the case of former players, no matter the highest form of play achieved, it has been found that players identified significantly more SRCs sustained than recorded when given the latest medical definition [138].

Repeated SRCs have not been shown to have an increased risk of more severe symptoms, and it has been suggested that those suffering a second SRC were less likely to report these symptoms [122,128]. However, repeated SRCs have been linked to permanent physiological change within the white matter in the brain and inefficient neural recruitment associated with neurological degeneration and cognitive and behavioural impairment [112,140,141]. Repeat SRCs have also been linked to both increased recovery times for each subsequent concussion and an increased likelihood of further SRCs, with ratios of reported rates between 4.17 and 3.4 times more likely for those who have sustained three SRCs to suffer another, compared to those who have sustained no or one SRC [112,141].

2.4.3. Neurodegenerative Disease and Long Term Effects of Head Injury.

The final classifications of head injuries reported for former AF players are commonly seen in later life, long after playing careers. Due to this latency, NDs and chronic conditions such as chronic post-concussion syndrome (CPCS) cannot be linked to single impact events, unlike CHIs and SRCs.

The age that an athlete first starts participating in full contact or tackle football has been linked to worse cognitive outcomes [142-144]. Those who start before the age of 12 are twice as likely to have impairment in behavioural regulation and three times as likely to have elevated clinical depression scores, even when career length is considered [142,144]. Significant neurophysical development occurs between the ages of 9 and 12, therefore, damage to the brain during this period, even recoverable damage, may lead to lasting deficits due to a loss in developmental time [142-144]. It has also been suggested that repeated head impacts, estimated to be between 240 and 252 on average per season, can alter the development of the hippocampus and bring about memory problems in later life [142,144]

CPCS is defined as a syndrome where the symptoms associated with SRCs, persist past the usual healing period, remaining one year after initial injury diagnosis [94]. Whilst no study investigates football players in isolation, 5 - 15% of non-athletes remain suffering from a concussion a year after the initial injury [95,96].

Up to 39% of players have had worse mental health compared to the general population. Also, those reporting three or more SRCs during their college career are 2.5 times more likely to have reduced mental health than those with no SRCs [97,145,146].

Between 19.1% and 40% of retired players are either diagnosed with some form of depression or voluntarily report symptoms associated with the condition, which puts them above the 15% US national average for similarly aged males [145,147]. There have been tentative links between the number of sustained impacts and an increase in the risk of neurodegenerative and cognitive conditions [148]. By estimating the cumulative number of head impacts a player receives over their lifetime from playing football, based on participation and player position threshold values were established for the number of head impacts that lead to a statistically significant rise in the risk of worse cognitive and behavioural outcomes. However, this link has been questioned with more recent studies finding no link between the number of concussions sustained and cognitive outcomes in later life and arguing that cognitive outcomes are better linked to factors such as life stress, genetics, and chronic pain [149-151].

The delay in diagnosis for NDs has meant that cohorts of American football players are commonly compared to the rate of those conditions in the general population. Despite having a lower mortality rate in general, retired AF players are much more susceptible to NDs [7]. For some NDs such as Alzheimer's and ALS, the mortality rate can become as high as four times that of the general population [7]. NDs, in general, are challenging to study due to the low prevalence rates, 1.3% in former AF pros, as well as the delay between play and diagnosis, meaning that any on-pitch changes made to reduce the likelihood of these diseases developing cannot be accurately assessed until long after the changes have been made.

Alzheimer's disease has been identified as a prominent condition amongst retired AF players, with former NFL pros being both more likely to develop the disease than similar-aged counterparts, but also more likely to develop the disease earlier in life [97]. However, no similar relationship has been demonstrated for former high school players, and no link has been established between the number of SRCs sustained and the presence of Alzheimer's or ALS [97,98]. Large numbers of subconcussive blows have been linked to blood-brain barrier disruptions, neurocognitive deficits and damage to the white matter, linked to neurological degeneration and cognitive and behavioural impairment, as exhibited on MRI scans [139,148,152,153]. Sub-concussive blows are characterised by very low peak accelerations, typically at or below 14g [148].

Given the low presentation rate, concussive or sub-concussive blows are probably not solely responsible for NDs' manifestation. It is more likely that these repetitive impacts combined with other risk factors for NDs, such as genetic predisposition, increase football players susceptibility to long term neurodegeneration [99,142,154].

The relatively recent discovery of chronic traumatic encephalopathy (CTE) has also complicated the relationship between football and long term head health. The first reported CTE instance in an AF player, whose career lasted for three years at the collegiate level and 17 NFL seasons - a period featuring 177 consecutive games, was reported in 2005 [155]. A second diagnosis followed quickly in 2006, for a player with a college career lasting four years and in the NFL for eight consecutive years. In both cases, the former players committed suicide 12 years after their professional career ended [156].

The symptoms of CTE, such as behavioural changes, overlap with those of AD and ALS. This diagnostic complication, combined with CTE not being listed in the World Health Organisations International Classification of Diseases, may have led to reporting inaccuracies [7]. The neuropathological definition of CTE is an aggregation of hyperphosphorylation tau protein in neurofibrillary tangles (NFTs). These NFTs lead to destabilisation of microtubules in neurones, which as the disease progresses through its four identified stages leads to a reduction in brain weight, atrophy of several regions of the brain and neuronal loss, Figure 2-4 [157].

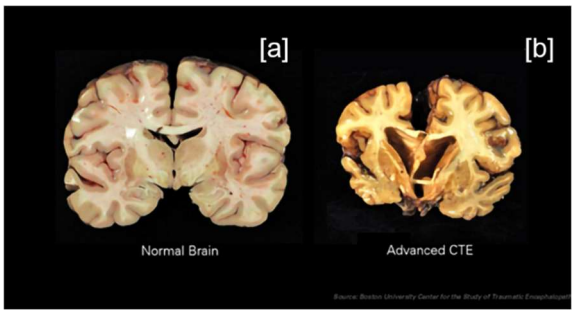

Figure 2-4: Cross-section of a healthy brain [a] and a brain with advanced CTE [b] [158]

A review of a neurodegenerative brain bank found that 1.2% of brains could be diagnosed with some form of CTE, with the percentage rising to 32% when reviewed those who played contact sports [159]. Historical estimates for CTE prevalence range from 4% to 10% when considering American football [99].

The most recent study conducted on donated brains found that 177 of 202 former AF players were diagnosed with CTE [160]. As the level of play increased so did the percentage of positive CTE cases, and the percentage of cases that presented with more severe stages of the diseases, suggesting a link between career duration and the development of CTE. In a study of 45 former players with an average of 6.8 years professional play, 87% had MRI findings showing no signs of chronic brain injury [161]; however, the MRI scans were not sensitive to the injuries.

A more recent study of 35 former professional players, with an average NFL career of 8.57 years, suggested no linear relationship between player career length, number of concussions and number of concussions with loss of consciousness and cognitive outcomes in later life [149]. However, this study excluded former professionals who had been diagnosed with significant neurological or medical conditions, including but not limited to ALS, which is a possible misdiagnosis of CTE [7].

There is difficulty in establishing true epidemiology of CTE in the American football population due to the condition's diagnosis only being possible post-mortem [143]. Therefore the disease is commonly only seen in brains donated to research institutions by concerned relatives, thus providing a significant bias to the available samples for study [378]. Without a comprehensive cohort study tracking a population of players throughout their careers and post-playing life, the use of studies into these conditions in the development of injury mitigation is limited.

2.4.4. Associated Causes of Head Injuries Within American Football.

2.4.4.1. CHI

CHIs tend to be associated with aggressive on-field actions, with 50% resulting from tackling or blocking actions. 43% of these collisions were helmet to helmet, with a further 38% of impacts being helmet to the body [101]. In general terms, defensive players tend to be more prone to CHIs with incomplete recovery than offensive players, accounting for 35% and 24% of all injuries of this type since 1984 respectively [100]. Wen individual positions are considered linebackers are the most likely to suffer from this class of injury, followed by defensive and running backs [100]. These players' role on the field requires more movement in defensive and offensive actions than linemen, and thus these players will expose themselves to impacts with more considerable impact energies. The vast majority of CHIs occur during competitive play, 77%, where athletes may justify greater risks due to perceived rewards.

In general, high school players are the most prone to CHI with the bulk of all fatalities, 66%, and injuries with incomplete recovery, 91%, being reported for this cohort [100,104]. The high prevalence in the high school cohort is probably due to the greater player numbers than the college and professional cohorts, and their physical and technical development means that some players can produce the required biomechanical forces, whilst others may lack the skill and technique to prevent injury.

The low number of catastrophic injuries, both fatal and non-fatal, presented in the literature makes it difficult to draw conclusive patterns from the presented data. While general trends may emerge over long periods, comparative year to year analysis could be misleading as a few additional cases to the previous year would significantly increase the injury rate [100, 104]. Therefore the use of catastrophic injury data to inform decisions around how injury rate may be mitigated must be carefully considered.

2.4.4.2. SRC and mTBI.

Causal on-pitch incidents that have been linked to SRCs are similar to those that have been attributed to CHI events, with 51% - 68% of impacts linked to a reported SRC happening to tackled or tackling players and a further 43% - 29% happening to players blocking or being blocked [113,162,163]. Helmet contact with an opposition player is estimated to be responsible for 82% of SRC, with helmet to helmet contact accounting for 36% [163]. Between 21 - 50% of reported SRCs result from passing plays, with 28 - 38% accrued during running plays. Both of these plays are offensive attempts to advance the ball down the pitch [163].

Given that this usually involves throwing a ball to a fast-moving player, it is unsurprising that the player to player impacts linked to these plays have a high rate of associated SRCs due to the collision energies involved. It should be noted that in comparison to the number of impacts sustained by players very few, 0.02%, result in an SRC [164].

The SRC rate also varies by player position with receivers having rates of 0.54 per 1000 AE, whilst linebackers have a rate of 0.99 per 1000 AE at the college level [112]. A more recent analysis of the professional-level play of defensive backs reported rates as high as 11.76 per 1000 AE, with defensive line players being nearly four times less likely with a rate of 3.13 per 1000 AE [165]. Running backs have been reported to sustain the most SRCs for offensive team members, yet it has been suggested that no real difference exists between all offensive positions [162]. There is, however, an inherent limitation to looking at position incident rates through the lens of AE, as this metric assumes that all positions see the same exposure to injury in terms of on-pitch time, when in fact some positions spend more time on the pitch than others and thus have a higher chance of sustaining an injury. When player positions are grouped into offensive, defensive and specialised roles, the offensive role cohort tend to be more prone to SRCs than defensive positions [122].

Despite the large number of studies that have focused upon this category of head injury in the sport, several challenges prevent these numbers' direct application to any development in player safety. In addition to the under-reporting of SRC by player bot the major internet-based reporting systems utilised, the NCAA's Injury Surveillance Program, and High School Reporting Information Online systems are both acquire data from a limited number of representative institutions rather than the maximum number available [56,91]. Additionally, the complex task of accurately identifying an SRC, due to the non-specific nature of the symptoms and, lack of and objective diagnostic test, is often left to Athletic trainers, rather than full-time medical staff, especially for the high school cohorts [5,91,123]. This increases the risk of misdiagnosis, which would naturally increase the perceived rate of injury prevalent in football nationwide. However, this factor would be present in all sports measured in such a manner, and therefore any relative rates to other sport would be expected to insensitive to this form of error.

The use of AE's as the standard metric for reporting incident rates of this type of injury may also effect perceived annual risk of injury, especially where different playing positions are concerned [123]. Thie assumption made in the calculation of AE where all activities are normalised in terms of exposure, for instance, an offensive lineman, who could be expected to participate in at least half the plays in a game would be considered

to have the same exposure as a special team member who may only participate in one or two plays in a match. This hidden disparity may cloud the genuine risk of certain positions onfield, and thus the opportunities offered for the development of position-specific head protection. However, the consistency on reported relative rates of injury between offensive and defensive positions, and between practise and game sessions, reported in the literature would suggest that the general patterns seen in the data provide a good base for the generation of novel approaches to player protection.

2.4.4.3. Neurodegenerative Disease and Long Term Effects of Head Injury.

CTE development is associated with a history of sustained concussive and sub-concussive head impacts, with only 16% of CTE cases having no SRC reported by next of kin [165,166]. However, the time delay between playing career and diagnosis of neurodegenerative conditions establishes a causal relationship between a specific impact history and the presence of the disease. Without this exact link between the two, no novel protection can be developed to protect current athletes from this head injury class.

It has been suggested that the causal impacts and accompanying neurological damage leading to CTE can be viewed in three domains: mechanical overloads from high energy impacts; mechanical fatigue from repetitive low energy impacts; and, mechanical creep due to time-dependent brain degeneration [167]. This approach explains why CTE has been found in skill players, who tend to suffer a small number of high energy impacts and linemen who typically sustain a higher number of lower energy impacts.

2.5. Brain Injury Thresholds

Each category of brain injury can be described by two categories fo thresholds; the biomechanical forces and accelerations required to cause damage to the physical structures of the brain, and defined injury metrics, which place these forces and acceleration in the context of impact time and displacement.

2.5.1. Biomechanical forces

While actual damage to the cells and structures within the head only occur when these structures are deformed beyond acceptable limits, these deformations are often associated with their causal accelerations, which are comparatively easy to measure.

2.5.1.1. CHI

Skull fractures have been associated with linear accelerations with a peak above 250g, whereas the rupture of the bridging veins that cause SDH require an acceleration above 3900g [168,169]. Thus, SDH cannot be caused by pure linear acceleration and must result from the brain's rotational movement relevant to the head. Cadaveric studies have shown that the critical SDH threshold depends on impact duration, and when the average duration of common impacts in football play has been considered an approximate threshold value of 5000 $rads^{-2}$ has been proposed [170,171].

2.5.1.2. SRC

SRCs have been linked to a wide range of impact accelerations, with peak linear accelerations ranging from 29 to 205g and rotational accelerations ranging from 102 to 9981 $rads^{-2}$ [65,86]. Various efforts have been made to link impact magnitudes with the risk of a player sustaining an SRC. The earliest effort attributed any impact with a 98g or higher linear component, carrying an 80% risk of the impact resulting in an SRC [83]. A year later, a new proposal added rotational accelerations as a factor in defining the risk of an athlete sustaining an SRC, Table 2-2. However, it has been argued that these values are inherently flawed due to the bias to injurious impact data used for the statistical analysis [172].

Table 2-2: Impact magnitudes associated with the risk of SRC development [172,173]

Study year	Injury risk (%)	Linear acceleration (g)	Rotational acceleration ($rads^{-2}$)
2004	25	66	4600
	50	82	5900
	80	106	7900
2007	1	109	6714
	5	145	8432
	10	165	9386

Compared to a player's impact history, 90% of SCR linked impacts were within the top 5 impacts experienced by the injured player [174]; therefore, the threshold for an individual sustaining SRC may depend on their biology.

The wide range of impact magnitudes linked to the development of SRCs can be explained by concussions being immediately diagnosed from a small number of high-intensity impacts; however, delayed SRC diagnosis can also arise from multiple low-intensity impacts [175,176]. It may also be challenging to assign a single acceleration threshold to the occurrence of SRC as the majority of reported SRCs result from multiple rapid impacts [163]. All attempts to establish risk curves are inherently limited due to the size of the data sets used to generate them [172].

2.5.2. Injury Metrics.

Although links have been drawn between peak linear and rotational accelerations and types of injuries, neither of these metrics account for impact duration. The first effort to describe injuries in this manner was the work carried out by Gurdjian et al. in the 1960s, which lead to the development of the Wayne State Tolerance Curve (WSTC) [177,178]. The curve was developed from cadaveric and animal data and developed a relationship between acceleration magnitude and duration, showing that lower accelerations over a longer time frame could be as injurious as shorter, sharper shocks.

Refinements on the curve came in the form of the Gadd Severity Index (GSI) in 1968 and the Head Injury Criterion (HIC) in 1971 [180,181]. These metrics used integrals to better define the relationship between magnitude and duration of acceleration pulses in terms of injury, equations 2-1 and 2-2.

$$GSI = \int a(t)^{2.5} dt \qquad 2\text{-}1$$

$$HIC = \max \left[[t_2 - t_1] \cdot \left[\frac{1}{t_2 - t_1} \int_{t_1}^{t_2} a(t) dt \right]^{2.5} \right] \qquad 2\text{-}2$$

Where $a(t)$ is a time-based acceleration pulse and t_1 and t_2 are defined time points within that dataset that maximise HIC. Both of these metrics are still currently used across a range of performance standards to assess the suitability of helmets and crash protection in vehicles, with HIC being refined through the introduction of standardised time periods for ease of comparison [182-185].

In 2008 a new metric, HITsp, was developed, which combined peak linear and rotational accelerations, values for Head Injury Criterion and Gadd Severity Index and the helmet location of impact [70]. This measure has been proven to be a better prediction of injury than previous measures, though its authors suggest that it would be improved by considering player impact history. Further research in this area has shown that statistical methods such as classification and regression trees provided a 6-fold increase in the sensitivity of a threshold to predict injury [72].

However, these metrics are inherently limited in their application to more minor injuries, as they are based on the WSTC. This curve was built on data for CHIs and TBIs, and the initial aim of these metics was to enable standards to be developed to reduce these injuries [179,186]. Other limitations include the lack of rotational accelerations and impact masses. In recent years, efforts have been undertaken to develop tolerance curves for rotational accelerations and mTBIs [179,187]. However, these curves have their limitations, such as being focused on one sport or being based on data representative of only a small set of the human population; thus, neither curve has yet to see the wide success of the WSTC.

Many different metrics for rotational acceleration have been developed in recent years, such as rotational injury criterion (RIC) and brain injury criterion (BrIC) [188-191]. These metrics either adapt a linear acceleration based metric (e.g. RIC) or are based on finite element analysis brain models (e.g. BrIC). Some novel metrics recognise that many head injuries result from linear and rotational accelerations, using a weighted combination of linear and rotational metrics [70,72,192,193]. Although many of these metrics were developed with mTBI in mind, their ability to predict injury correctly ranges from 6% to 21.3%[72].

None of these metrics has, however, been adopted by the relevant helmet standards. For instance, the NOCSAE standard has only recently adopted a simple rotational test, conducted at a velocity of 6 ms^{-1} with a pass-fail threshold of 6000 $rads^{-2}$ [190,191]. Most recently, an attempt to bridge the gap between brain injury metrics developed utilising finite element analysis, and kinematic data has led to the development of DAMAGE [194]. This metric's development allowed for estimation into the maximum principal strains within the brain that result from angular accelerations, without the need for complex and time-consuming brain simulations.

2.6. Current head injury mitigation technologies.

With both the typical head injuries and impact environment of American football being well defined by the literature, the sport's governing bodies' efforts to mitigate these injury risks can be appropriately placed into context. Injury mitigation has been performed in two ways: reactively through introducing new rules, and proactively through the introduction and refinement of personal protective equipment (PPE).

2.6.1. Rules changes.

A sharp increase in the number of deaths between 1965 and 1976 resulted in two substantial changes to American football, Figure 2-5.

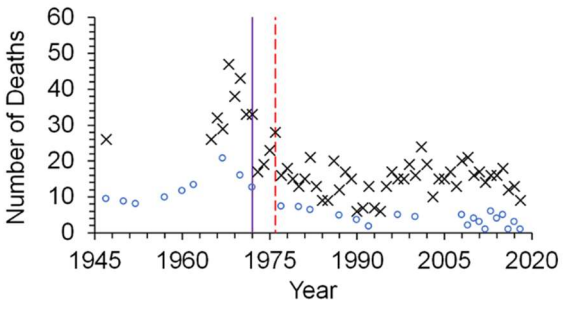

Figure 2-5: Number of reported deaths from direct causes (black cross) and brain-related deaths (blue circle) with the 1976 rule change (red dashed) and 1973 introduction of standardised helmet testing (solid purple) for reference [104].

The National Operating Committee on Standards for Athletic Equipment (NOCSAE) was founded and produced the first standard for football helmet performance in 1973 [105]. This standard was adopted by the National Collegiate Athletic Association (NCAA) and the National Federation of State High School Association in 1978. Safer helmets, however, emboldened players in taking more on-field risks, evidenced by the increase in direct deaths, between 1973 and 1976, Figure 2-5. A significant rules change was implemented in 1976 to combat this rise, which outlawed a range of overly aggressive tackling and blocking manoeuvres conducted by players [196]. The introduction of these measures balanced a reduction in deaths whilst retaining the sport's physicality, an essential element for football players and supporters.

The game rules' evolution continues to this day, with more recent changes penalising players for unnecessary roughness and hitting defenceless players [47,129,197,198]. However, these rules' effectiveness is debatable with some changes having no notable effect on injury rates [92,199-201]. Rules are also reactive measures as associated punishments can only be handed out once an infraction has been committed; thus, player safety relies on goodwill.

2.6.2. Helmet Design and Use.

The earliest recorded use of helmets within American football dates back to 1893, but they were not a mandatory requirement at any level until 1939 when their use was enforced by the NCAA, with the NFL following suit in 1940 [18]. Until the introduction of the aforementioned NOCSAE standard in 1973, helmet performance was rigorously assessed, with 84% of available helmets failing to meet the requirements of the standard [57]. Post its introduction, it was estimated that the standard helped reduce the risk of head injury from 55 to 12% [202].

The earliest helmets used within the sport were of leather construction with padding becoming prevalent by the 1920s. The first "modern" helmet, made of a hard outer shell with an energy-absorbing liner, was manufactured in 1939 [203]. Three broad groups of shell-liner helmets became common: suspension, padded and suspension-padded. Suspension systems have become less favourable, as they were less able to prevent injury [57].

Current helmets comprise five primary components, a hard outer shell, a flexible energy absorbing liner, a rigid facemask, a retention system and a comfort layer. Of these only three, the shell, liner and facemask, are designed with player safety in mind with the retention system and comfort liner primarily focused on player comfort. Although it has been reported that an incorrect fit can lead to worse outcomes in instances of SRC, this is due to the of incorrect use of retention systems rather than an inherent limitation in their design [201].

The liner and shell perform the vast majority of impact energy absorption, the latter of which is estimated to absorb between 18 and 34% of the impact energy [15,16,204]. Due to the football impact environment's repetitive nature, helmets typically employ either vynile nitrile or other cross-linked foams, rather than the expanded polystyrene found in other sports helmets [16]. Helmet performance has increased significantly, with current helmets being considerably more able to reduce injury risk [17]. Whilst some of this performance comes from increased liner thickness, other structures and materials have been introduced in recent years [17,21,22]. These novel structures allow for leveraging of novel materials, such as the Schutt ion 4D system, which comprises an array of elastomeric cones, or manufacturing methodologies, for instance, the Riddel Diamond system, which leverages additive manufacturing processes to design novel. Alternative approaches to load management, such as the Awareflow shock absorber, utilise pressure release airbags to limit the maximum force transmitted to the head.

Beyond the realm of American football, further developments have been made in helmet safety by employing additional structures, such as Wavecell and the Multi-directional Impact Protection System (MIPS) [379,380]. Both systems act an addition to a helmets protective liner, enabling reductions in rotational acceleration via either the introduction of a slip plane, in the case of MIPS or through a collapsable structure designed to reduce the shear strength of the helmet overall [379,380]. These systems, however, offer no additional protection from linear impacts and must relly upon existing liner components to offer all-round protection. Additionally, neither system has been employed outside of the context of single-use helmets, and there may be additional challenges in the implementation to football helmets given the multi-impact environment of the sport described previously.

This improved performance has come at a cost; however, both helmet size and weight have increased substantially [17]. Despite nominal increases in helmet performance, many of the metrics they are assessed against are based on CHI thresholds, and so their ability to reduce risk of mild injury is limited [11,201,205]. Youth helmets are also tested to the same conditions as other helmets, despite the clear difference in the players' physicality and thus differing biomechanical forces [206].

2.6.3. Assessment Methods for Contemporary Helmets.

Traditionally football helmets were tested using guided drop rigs, where the helmet was attached to a standardised headform and dropped from a series of heights onto a standardised anvil [184,207]. The helmets are required to provide equivalent performance all around the helmet and at a range of temperatures.

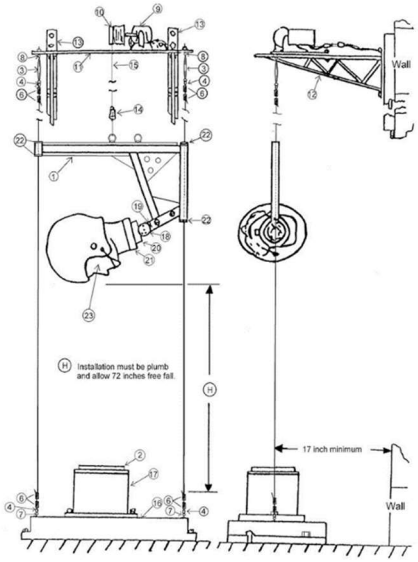

Figure 2-6: Wire guided drop rig used in the NOCSAE helmet test.[361]

There has, however, been concern over the ability of these methods to represent on-pitch conditions adequately. Most notably, the current standards utilise test velocities that are significantly lower than the observed impact conditions associated with injuries [17,84,184], and until recently the NOCSAE standard did not assess the rotational performance of helmets. This requirement is present in the latest revision of the standard where a pneumatic ram assembly is utilised,

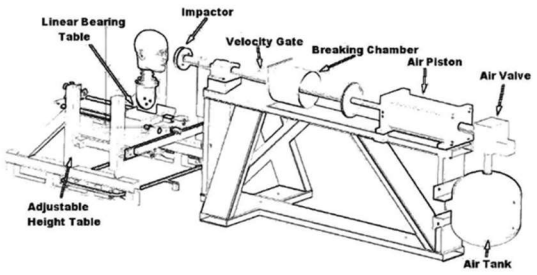

Figure 2-7: Pneumatic ram utilised for assessment of the rotational performance of American football helmets, The headform is attached to a sledge which is restrained to linear motion, and is struck by a pneumatic ram that is in line with the centre of mass of the headform [371].

Several attempts have been made to refine the testing of helmets by introducing new impact rigs capable of utilising biofidelic head and neck assemblies, whilst also reaching higher impact velocities by adopting greater impact masses [17,195,207,210].

Testing methods commonly utilise multiple impacts in rapid succession across multiple helmet locations, best represent the football collision conditions and ensure that the helmet has been designed to offer all-around protection [184,195,209].

Although helmets must meet the performance requirements of the relevant standards for use in organised play, these standards act as a binary metric of performance, with no distinction between helmets' performance that passes the required tests. This limitation prompted the development of the Virginia star tech test method, which combined the results of a range of impact tests into a single score, with individual impacts being weighted by both injury risk and on-field exposure [209].

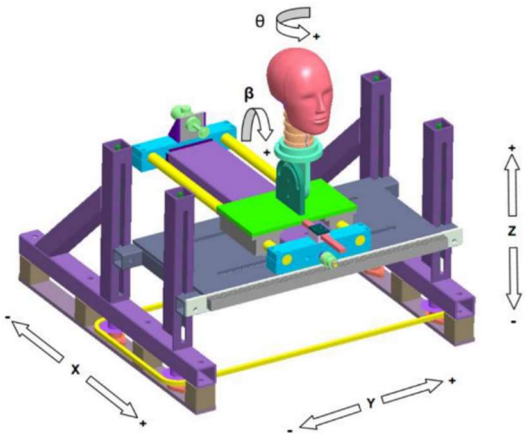

Figure 2-8: Impact Sled utilised by the Biocore impact testing methodology. The Combined Sled, Neck and Head assembly allows for size degrees of freedom in the movement of the headform.

In their efforts to better represent "real world" conditions, new methods tend to have more compliant elements in the testing setup than the simpler linear drop rigs, which reduces the impact energy that the helmets are required to absorb. For example, the latest testing methodology released by Biocore utilises a head and neck assembly on a moveable sledge, as well as a foam capped impactor, whereas the NOCSAE standard calls only for the use of a rubber anvil surface [184,195]. These testing methodology differences result in a change in head velocity of 60% of the impact velocity, with the remaining impact energy absorbed by the system. [84]. Although these testing methods utilise different headforms, the different responses are minimal and consistent across various impact conditions [211].

Most interestingly the Biocore system is the first assessment method for American football helmets that utilises the average impact velocities for SRC identified by Viano et al. [84,195]. Although the Virginia Tech Star methodology uses concussion risk as a weighting mechanic for the calculation of its final score, the impact velocities used differ from the study by Viano et al. [84,209]. Therefore it can be argued that the Bicore methodology is the first built from the ground up to reduce the risk of players sustaining an SRC.

The Biocore assessment method also used a weighted score to determine overall helmet performance[195]. Like the Virginia Tech Star methodology, concussion injury data was used to weigh each impacted location's importance based upon its prevalence in recorded concussive injuries. Impact results were also weighted by test velocity to prioritise the average closing velocity of injury. At each test velocity, both HIC and

DAMAGE, discussed in section 2.5.2, are calculated, before combined into a single HARM metric using equation 2-3 [195]. It is these HARM values that are then weighted to provide the overall helmet performance score (HPS), equation 2-5, with a unique weighting factor for each helmet location and impact velocity, Table 2-3.

$$HARM = C_1 \cdot HIC + C_2 \cdot DAMAGE \quad 2\text{-}3$$

$$HPS = \sum_{i=1}^{18} M_i \cdot HARM_i \quad 2\text{-}4$$

Table 2-3: Weighting Factors used in the calculation of the Helmet Performance Score. [195]

Impact Location	5.5ms^{-1}	7.4ms^{-1}	9.3ms^{-1}
Side Upper	2.93e-2	1.82e-2	2.33e-2
Oblique Front	9.49e-3	6.01e-3	7.82e-3
Oblique Rear	5.83e-3	3.71e-3	4.72e-3
Side	9.96e-3	6.24e-3	8.13e-3
Facemask Side	3.92e-3	2.58e-3	3.58e-3
Facemask Central Oblique	6.87e-3	4.93e-3	6.87e-3

In addition to these new testing methodologies, the NFL and NFLPA have introduced a ranking of helmets based upon performance, to serve as a recommended list for players [360]. While the exact methodology used to generate the ranking is not stated, it does provide insight into the comparative performance offered by contemporary American football helmets.

2.7. Specification of an idealised material for head impact protection.

Both the identified biomechanical thresholds for head injury risks and the defined impact environment prescribed the requirements of a novel impact protection material:

1. **Repeatable**. The high number of impacts per game each helmet is exposed to requires that any novel material can sustain multiple impacts in rapid succession, with minimal loss in performance due to incomplete strain recovery.

2. **Recoverable**. The chosen material needs to be able to recover from impact-induced deformation within a small time frame. This requirement naturally excludes a range of materials, such as metals and elastic-plastic polymers.

3. **Resilient**. The novel material must be resistant to a range of factors. Depending on player age and playing position, the material will have to be capable of sustaining an average of 200 - 1500 impacts per year before significant degradation [48,49,60,64-78]. Secondly, football is played in a wide range of climatic conditions so the material must be insensitive to temperature changes [33].

4. **Optimisable**. Head impact forces range widely depending on football player age, position and location [49,50,77]. An idealised material should have a large number of parameters that influence its geometry and performance so that multiple variants can be developed for this range of impact conditions.

5. **Multi-velocity performance**. Impacts in American football cover a wide range of velocities, with those linked to injury averaging 9.3ms^{-1} compared to impacts associated with regular play in the range of 5.5ms^{-1} [84]. A novel material should have the ability to achieve accelerations below identified brain injury risk thresholds, such as those covered in Table 2-2, for this range of impact velocities.

Several classes of material reported in the literature show promise in meeting a number of these requirements. Auxetic materials, those with a negative Poisson's ratio, have been shown to provide a better response over a range of impact energies compared to non-auxetic foams [212]. Thermoplastic Elastomers (TPEs), copolymers combining the benefits of thermoplastic and elastomeric properties, are a class of materials suited to the demands of the football environment as they are highly flexible materials with short relaxation times [41,42,213].

2.8. Emerging Helmet Liner Technologies: Structures

The majority of current football helmets utilise elastic cellular material as the principal source of energy absorption; hence, the mechanics of how these materials respond to such loading conditions need to be understood. An ideal material would be capable of dissipating or converting the impact energy while keeping the resulting impact forces below an identified injury threshold [19,214]. While the biomechanical forces linked to mTBI and SRCs have been estimated from recreations of on-pitch impacts, the active area of liner material compressed during impact has not [215-217]; hence, exact stress limits of materials can be challenging to establish.

2.8.1. Cellular Materials.

The majority of current helmets approved for use in football utilise some form of cellular material as part of their energy absorption system. Cellular materials can be broken into four broad categories; lattice-based, surface-based, foams and honeycombs [19,218,219]. Helmets most commonly employ foams, though a brief description of all types is presented here. Throughout this section material properties referring to the cellular solid are marked with a superscript c while those referring to the base material of the cellular solid are identified with a superscript b

2.8.1.1. Mechanics of cellular materials.

Although the exact mechanics of how the various cellular structure types vary, these mechanics are extensively covered in the literature and rely on cell geometry and loading direction [19]. Classic mechanics informs us that for materials to absorb energy, they must provide both a sufficient resistive force and space for deformation. The amount of energy that a material can absorb under impact can be visualised as the area under a force-deflection or stress-strain curve, in which case the area is representative of volumetric energy. The response of a generic cellular material is shown in Figure 2-9.

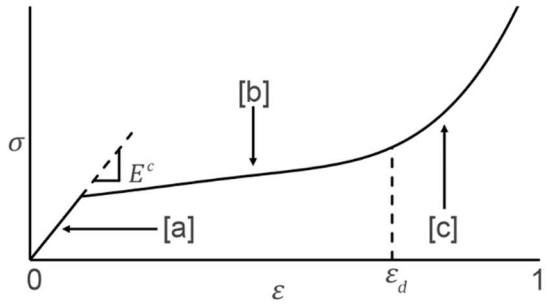

Figure 2-9: Stress-strain curve of a generic elastomeric, identifying the three phases of response; [a] Linear elasticity, [b] plateau region and [c] densification. The linear elastic

region defines the youngs modulus of the cellular material (E^c), while the plateau and densification regions are separated by the Identified densification strain (ε_d)

When subjected to compressive loading, elastomeric cellular materials typically follow a three-phase response to loading. Initially the Youngs modulus of the cellular material ($\mathrm{E^c}$) defines a linear elastic response, Figure 2-9. When the cell walls' bucking strength is reached, cell collapse begins, and a stress plateau is developed. Eventually opposing cell walls come into contact and further deformation of the material is only possible through deformation of the base material. At this point, referred to as densification, reported stress increases rapidly. It has been postulated that when a single cell of a cellular material is loaded in isolation, it exhibits a different response, characterised by a period of strain-softening once the initial linear elastic period has passed [220].

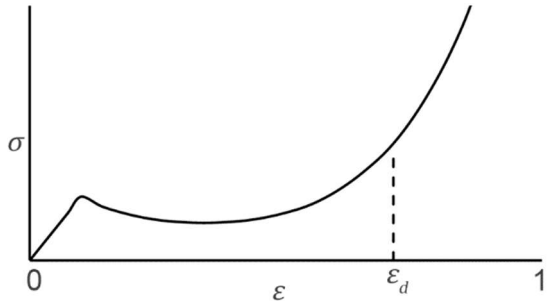

Figure 2-10:Idealised compressive load-deformation characteristics of a single cell

Regardless of type, all cellular materials have standard features that aid in comparing and exploring their mechanisms. Cellular material performance relies on the relative density (ρ^r), the ratio between the density of the cellular material (ρ^c) and the base material (ρ^b) [19]

$$\rho^r = \frac{\rho^c}{\rho^b} \qquad 2\text{-}5$$

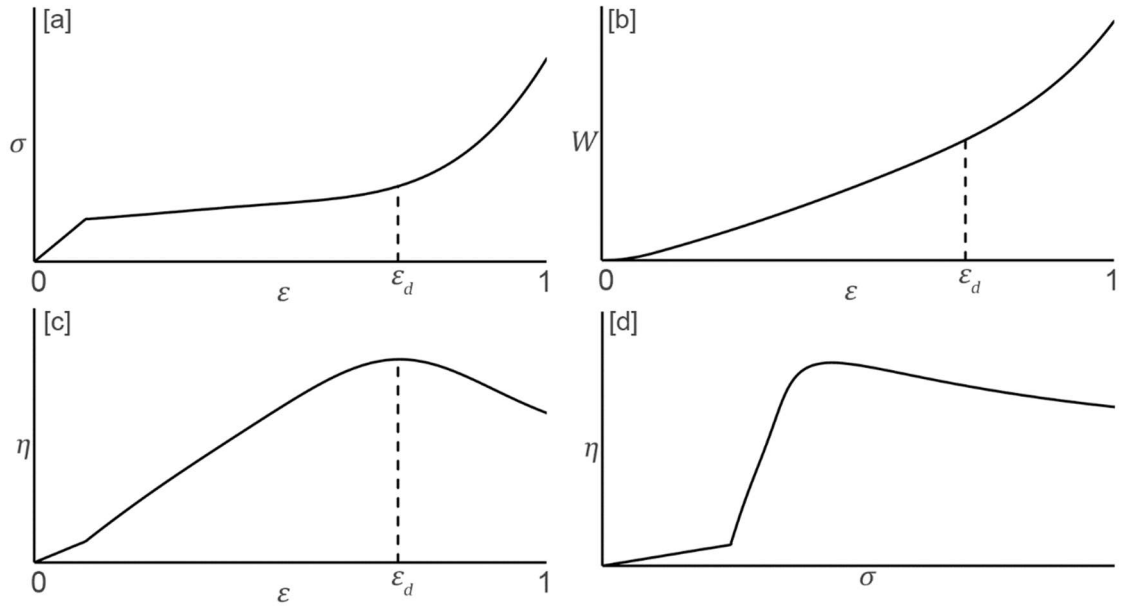

Figure 2-11: Stress-strain response [a] of a hypothetical elastomeric cellular material, with calculated volumetric energy absorption vs strain [b], energy absorption efficiency vs strain [c] and energy absorption efficiency vs stress [d].

For elastomeric foams, the volumetric energy absorbed (W_{ε_n}) for a given strain (ε_n) is given by calculating the area under the stress-strain curve, equation 2-6 [19]. Both the value of W_{ε_n} and its rate of increase naturally rises above the point of densification, as the movement of solid material requires significantly more energy than the simple bending of walls. Figure 2-11 [b].

$$W_{\varepsilon_n} = \int_0^{\varepsilon_n} \sigma d\varepsilon \qquad 2\text{-}6$$

This equation, however, does not account for the effects of the material density. A dense conventional cellular material requires more force and thus more energy, to deform the same distance as a cellular material of lower density. As the design of helmets is a weight-sensitive issue, the performance to weight ratio of the material must be considered. To enable this comparison the normalised energy absorption ($\widetilde{W}_{\varepsilon_n}$) can be used [24].

$$\widetilde{W}_{\varepsilon_n} = \frac{W_{\varepsilon_n}}{\rho^c} \qquad 2\text{-}7$$

The ability of cellular materials to absorb energy whilst reducing the induced forces of an impact can be seriously impinged if it reaches densification before all energy has been successfully dissipated. Therefore, the identification of the densification strain (ε_d) of a candidate material is of paramount importance.

Empirical formulae for foams have been derived, where relationships between ε_d and ρ_r have been drawn, equation 2-8. The exact value of the empirical factor (f) has been found to depend on the geometry of a cell, but a value of 1.4 provides an initial estimate [19].

$$\varepsilon_d = 1 - f\rho^r \qquad 2\text{-}8$$

However, this value can be challenging to validate against real-world data due to factors such as experimental noise. Also, for other classes of cellular material, no such equation exists. It has been proposed that an examination of a material's energy absorption efficiency (η) can be used to provide an absolute value across material type and geometry [221].

$$\eta_{\varepsilon_n} = \frac{1}{\sigma_{m\varepsilon_n}} \int_0^{\varepsilon_n} \sigma d\varepsilon \qquad 2\text{-}9$$

By considering the maximum stress ($\sigma_{m\varepsilon_n}$) at a given strain the efficiency term provides a factor of all available energy a cellular system can absorb. When densification is reached, maximum stress increases quicker than the increase in absorbed energy; hence, the material efficiency reduces, Figure 2-11 [c][d]. Based on this relationship, a cellular material's densification strain can be taken as the maximum efficiency strain.

The reported stress of a material can be normalised similarly to W_{ε_n} so that the influence of cellular geometry can be isolated. W_{ε_n} was normalised using the density of the cellular material accounting for the influence of material volume on the potential for energy absorption, whilst stress is normalised by the modulus of the base material (E^b) as well as the relative density [19].

$$\tilde{\sigma}_{\varepsilon_n} = \frac{\sigma_{\varepsilon_n}}{E^b \rho^r} \qquad 2\text{-}10$$

2.8.1.2. Impact absorption factors.

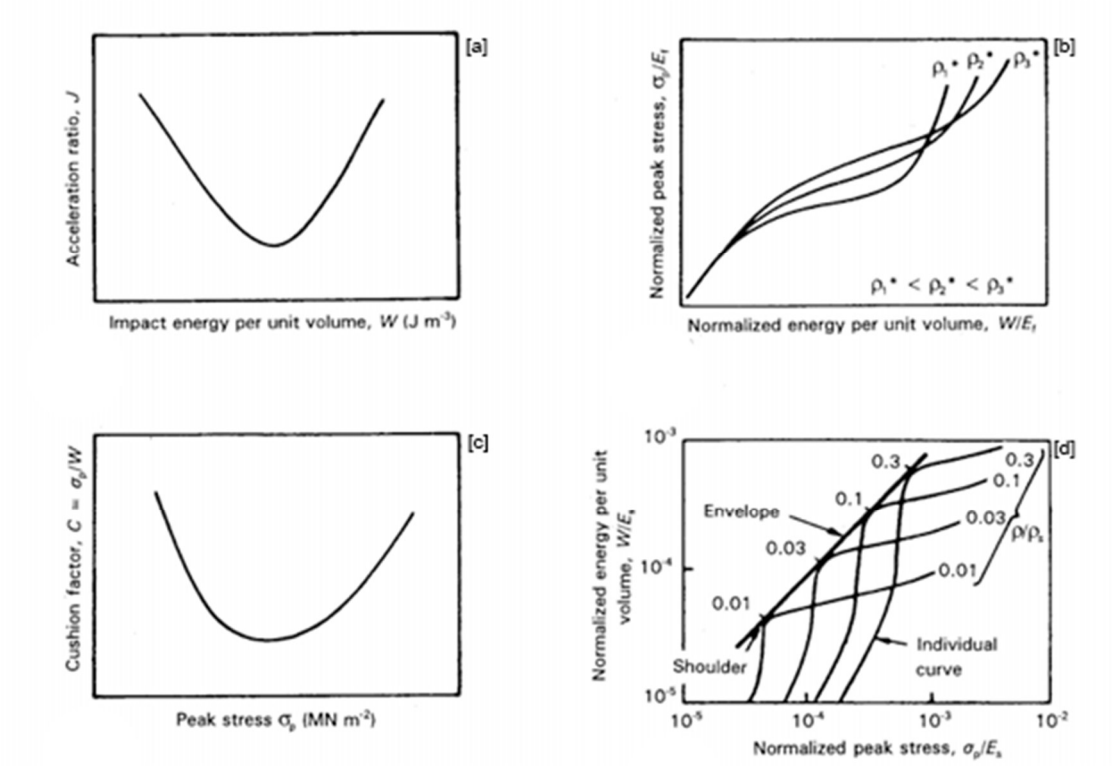

Figure 2-12: Four diagrams that are used to characterise energy absorption: [a] the Janssen factor, J; [b] the Rusch curve, [c] the cushion factor; and [d] the energy-absorption diagram [222]

Various factors to quantify a material's ability to absorb energy have been posited within the literature [222-224]. The Janssen (J) factor relates to the recorded peak acceleration (a_p) of a cellular material to the idealised constant acceleration the material would produce if its entire thickness (t) is utilised for a given impact velocity (v).

$$J = \frac{2ta_p}{v^2} \qquad 2\text{-}11$$

When this factor is calculated for a range of impact velocities and plotted against volumetric energy, a valley shaped trend occurs, Figure 2-12 [a] [19]. The minimal point on this curve identifies the conditions within which the designated foam acts most like an ideal one. This factor's usefulness is limited by the need to conduct a large number of experiments for each new cellular material. As such, it is not well suited as a comparison between factors.

The Cushion (C) factor considers the ratio between the peak stress developed by a cellular material and the volumetric energy. When plotted against peak stress, a curve similar to that of the Janssen factor develops, Figure 2-12 [b] [19]. It has been noted that under dynamic loading conditions, the Cushion factor becomes the equivalent of the Janssen factor [222].

$$C = \frac{\sigma_m}{W} \qquad 2\text{-}12$$

Rusch developed this idea further by identifying that the stress-strain response of cellular materials can be given a shape factor ($\psi(\varepsilon)$), where this shape factor is defined by a series of material constants (m, n, r, s) [19,224].

$$\sigma = E_c \psi(\varepsilon)\varepsilon \qquad 2\text{-}13$$

$$\psi(\varepsilon) = m\varepsilon^{-n} + r\varepsilon^{s} \qquad 2\text{-}14$$

Two additional factors are also defined by Rusch K and I.

$$K = \frac{1}{J} = \frac{v^2}{2ta_p} \qquad 2\text{-}15$$

$$I = \frac{W}{E^c} \qquad 2\text{-}16$$

By plotting I/K against I for a range of material densities, the best material for given allowable stress that maximises the energy absorbed can be identified, Figure 2-12 [c]. It must be acknowledged, however, that despite this analysis being more general than the use of J or C, its empirical basis does not acknowledge the exact mechanics of material behaviour [19].

Maiti et al. (1975) offer a further refinement of Rusch's work [214,222]. Rather than using the apparent modulus of the cellular material, both volumetric energy absorption and peak stress are normalised by the Young's modulus of the base material (E^b). When normalised energy is plotted against normalised peak stress, distinct shoulders form in the materials' response, where energy absorption is maximised. When multiple densities of the same base material are tested at the same strain rate and temperature are plotted together, a performance envelope develops, Figure 2-12 [d]. A performance window can be developed by conducting tests at a range of strain rates, allowing for identifying material densities that can absorb a given amount of energy for given maximum stress [19].

However, it must be noted that all these factors could only be used to identify optimal materials for a single impact scenario and therefore, when the impact environment of football is considered, use may be limited.

2.8.1.3. Honeycombs.

Honeycombs are defined as a nested set of identical prismatic cells that fill a plane and were amongst the first cellular solids to be noted in nature [19]. The behaviour of honeycombs is highly dependent on the direction of loading, with significant increases to material strength when loaded out-of-plane [19,222,225]. However, this increased strength comes at the cost of significant peak stresses when loading, followed by regions of softening [226,227].

2.8.1.4. Lattice Materials.

Lattices are typified by a series of inter-connected trusses and plates, where deformation is controlled through either bending- or stretch-dominated behaviour [218,228]. Wide ranges of lattice structures have been developed, with the trusses' exact configuration being dependent on the loading regime [30,229,230]. Lattice structures offer a large number of variables to control their behaviour, such as truss cross-section, truss angle and if hollow trusses are utilised, their wall thickness [231-234]

2.8.1.5. Surface Materials.

Surface-based materials can refer to structures based on minimal or origami-based structures [233-239].

Minimal surface cellular materials are based on unit cells defined by strict mathematical equations, such that the developed surfaces take up the minimal space [233-235]. The developed surfaces are infinitely expansive and periodic in three dimensions, dividing their volume into two equal spaces. The developed cellular materials offer less scope for variation than latices, with cell size and surface thickness the only changeable variables for any selected surface.

Origami techniques have been applied to the design of energy-absorbing structures, from single sheets of folding patterns to tubes, honeycombs and stacked sheets as honeycombs [236-239]. Their use allows for the designing of bespoke collapse mechanisms which, when leveraged, can increase a structures ability to absorb energy [27,238-242]. Origami-based materials have exhibited lower peak forces while maintaining higher average crushing forces, with the reduction in peak force attributed to the pre folding induced by the origami pattern's design, effectively removing the need for compressive loads to reach the buckling strength of the walls [238,241]. Origami-

based structures can also be designed to fit complex geometries compared to other cellular materials where a series of pads are employed, naturally leading to unprotected areas and compromised cells [22,243,244].

A range of behaviours can be developed in an origami-based material through control of the folding variables, such as bistability and self-locking mechanisms [245,246]. They can also be more readily functionally graded. For instance, the Miura-Ori folding pattern's in-plane behaviour can be altered through the control of a single angle. By varying this angle across a sheet's width, a variety of cell behaviour can be developed without inducing the step changes in performance inherent to wall thickness-based grading [24,247-249].

One consideration in using origami techniques is that they are idealised as two-dimensional solids, whose folding mechanisms are not affected by the thickness of the material from which they have been manufactured [231,248-250]. While this simplification may be justifiable for thin walls, when components are manufactured from rigid materials such as metals, part bending becomes highly reliant on material thickness [242,251].

One of the significant advantages of metamaterials based on origami patterns is that they exhibit a large number of parameters that can be used to optimise the geometry [238,241,251,252].

2.8.1.6. Foams.

Present throughout the world, foams are naturally occurring in examples such as bone and woods and bespoke products of manufacture, formed from metals and polymers [19,253-255]. Two classes of foams exist; open-cell, whose internal structure is, in essence, a microscale lattice, and closed-cell, where thin walls form a connected series of voids [19,253].

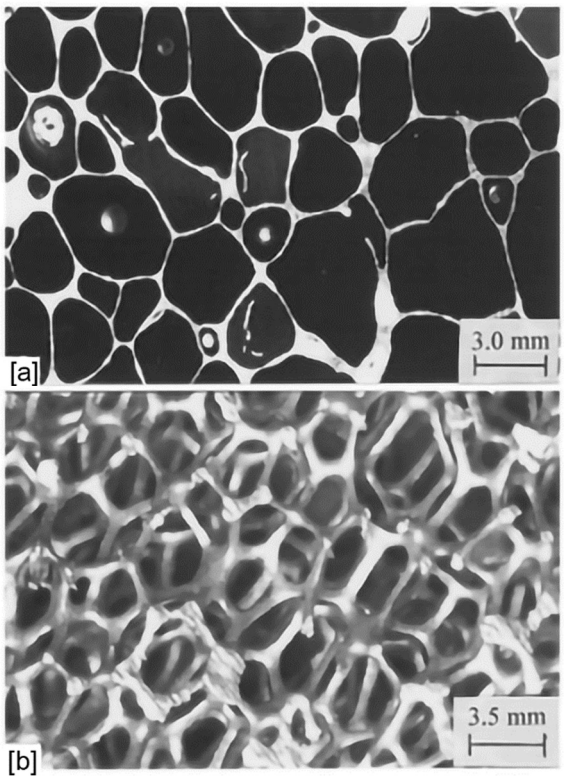

Figure 2-13: Optical micrographs of [a] closed-cell Alporas foam and [b] open-cell Duocel foam [256]

Open-cell foams are typically less dense than their closed-cell counterparts; however, they are also less capable of resisting compressive loads [19,253]. When foams are manufactured from elastic materials, their behaviour under compression is defined by the elastic buckling strength of cell walls [19].

Foams, however, are limited in their ability to be optimised for a given scenario. Assuming that base material is kept constant, Gibson and Ashbey show that for a given impact velocity and therefore strain rate, optimisation of foam can only be conducted by varying its density or thickness [19]. As football helmets inherently have space limits within the design for the energy-absorbing liner, this leaves designers with only the chemical composition of the base polymer and foam density as avenues for optimisation. This is compounded by the limitation of optimisation velocity, as the process described by Gibson and Ashbey utilises a single velocity. If the foam is optimised for the sport's highest velocity impacts, its stiffness may mean it contributes nothing in mitigating lower velocity impacts. In contrast, a foam optimised for the lowest impact velocities may be too soft in higher energy environments and densify before all energy has been absorbed, leading to higher peak accelerations.

2.8.2. Auxetic materials.

Auxetic materials, defined as materials that exhibit a negative Poisson's ratios (υ), Figure 2-14, have been found to exist at a wide range of scales from macro-level cellular structures to nanoscale chemical compositions [231,257-261].

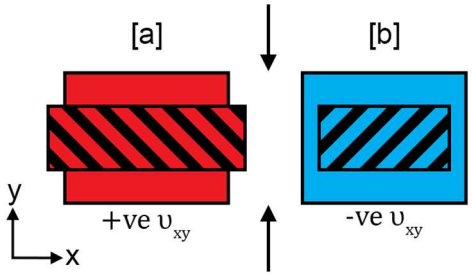

Figure 2-14: Hypothetical [a] non-auxetic and [b] auxetic solids exposed to a compressive force (black arrows) showing uncompressed (solid) and compressed (cross-hatched) states.

A wide range of mechanisms for auxetic behaviour have been developed, such as re-entrance and rotation of rigid units [260,262-264]. The changes to material behaviour due to their negative Poisson's ratios have made auxetic materials an attractive choice for a wide range of potential applications, from aviation to helmets and blast protection [24,31,261,265-267].

Auxetic materials exhibit synclastic curvature, achieving double-curvature and so enabling manufacturing in flat sheets that can then be curved into a helmet, rather than the more complex moulding required for non-auxetic foams, Figure 2-15.

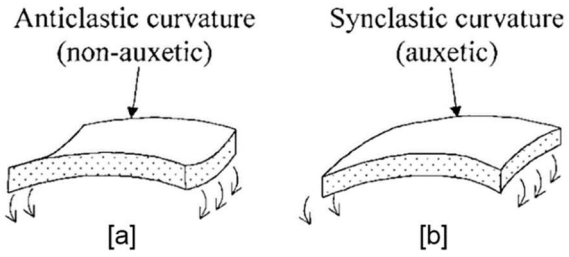

Figure 2-15: Examples of synclastic and anticlastic curvature [268]

More significantly, however, is the perceived ability of the negative Poisson's ratio (υ) to affect various material properties. For example, the shear modulus (G) of an isotropic material is given by equation 2-17.

$$G = \frac{E}{2(1+\upsilon)} \qquad 2\text{-}17$$

The value of υ for an anisotropic material has limits of -1 $\leq \upsilon \leq$ 0.5, thus as υ tends towards the lower limit, the $2(1+\upsilon)$ term becomes zero, and the value of G becomes infinite [269].

Where the optimal material response to linear impact is defined by the choosing the correct stiffness of material such that the plateau stress is minimised while densification is avoided, the optimal response of a material to shearing forces will have an equivalent relationship. The expanded performance range offered by auxetic materials may allow for the ideal shear modulus to be engineered into a helmet liner and, therefore, reduce rotational accelerations induced by common football impacts.

Under impact or indentation, auxetic materials pull additional material into the impact site and thus increase the material's local density, Figure 2-16.

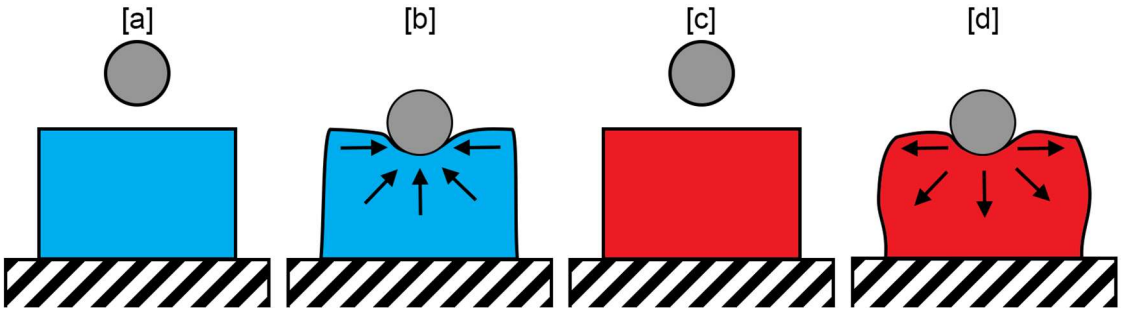

Figure 2-16: Hypothertical [a][b] auxetic and [c][d] non auxetic materials before [a][c] and after [b][d] impact by a sphere. black arrows indicate the local movement of material.

This naturally provides stiffer resistance to deformation in comparison to non-auxetic materials [25,268,270]. In the context of foams, this pre-densification strain stiffening allows for increased energy absorption but lowers perceived efficiency, Figure 2-17. Although the manufacturing methods used to create auxetic foams increase the density compared to the starting foam, the improvements in energy absorption have been found to hold even compared with identical density material over several loading cycles [271].

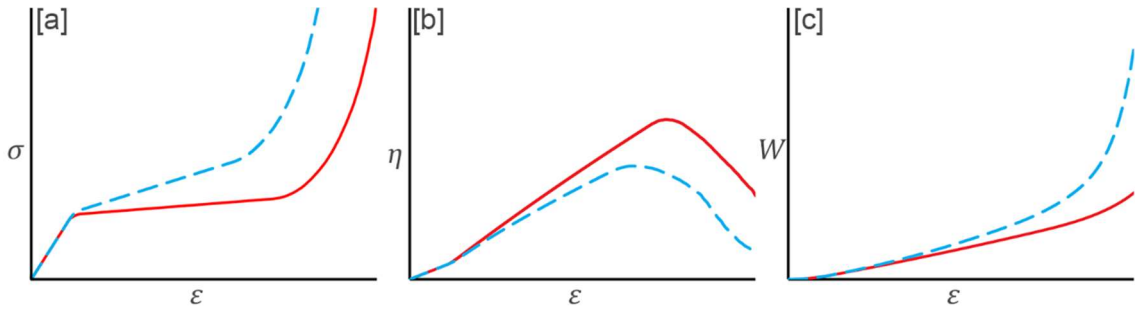

Figure 2-17: Stress-strain [a], energy absorption efficiency [b] and volumetric energy absorption [c] for hypothetical auxetic (blue dash) and non-auxetic (solid red) foams of equivalent density.

Compared to non-auxetic foams, the strain stiffening exhibited by auxetic foams allows them to handle impacts of increasing energy better, but at similar strain rates [20,212,267]. Although this has only been demonstrated at low energy levels, there is nothing to indicate that this trend would continue for auxetic material designed for higher impact energies.

Auxetic materials have also been noted to exhibit load spreading properties, having been shown to reduce peak pressures in shoe soles [272,273]. This is important for helmet applications, where performance is accredited based on managing acceleration and force distribution and is critical in preventing TBIs [274,275]. Auxetic materials may enable safer helmets by more effective force distribution by increasing liner area recruited to dissipate the impact and thus reduce injury risk or severity.

2.8.3. Non-Cellular Liners.

In recent years alternative structures to foams have appeared in a small number of football helmets [1,17,276-279]. Two broad categories of foam alternative systems can be identified: collapsible elastomeric structures and thin-walled pneumatic structures.

The pneumatic systems allow for a duality of energy absorption, wherein addition to wall bending and buckling, airflow is regulated through a vent allowing pressure to build until a specific resistive force is reached [1,21,276]. This allows the structure to exhibit a perfectly flat plateau force under compression, making close to an ideal material. The collapsible elastomeric structures absorb energy in a manner similar to honeycomb structures, where the force required to induce column buckling is the primary driver of energy absorption [280].

2.8.4. Influence of dynamic loading on material response.

The dynamic loading environment of football must also be considered, as changes in strain rate affect how the base material and structural geometry of a cellular material responds to the loading conditions [19,32,281-284]. Many elastic polymers have shown degrees of strain rate sensitivity, with the materials strengthening as strain rate increases [32,282-284]. These properties naturally transfer to the cellular material, where increasing strain rates have been associated with higher plateau stress and earlier densification [285].

Foams have demonstrated degrees of strain rate sensitivity across a variety of material types [19,223,281,285,286]. In open-cell foams, this behaviour is attributed to both the base material's viscoelasticity and the airflow within the cells [287]. In cellular materials based on elastic-plastic materials, two distinct behaviour types have been noted [288].

Type I structures exhibit either a consistent or increasing plateau region, while type II structures exhibit significant softening period under compression. Type I structures have been found to exhibit no noticeable differences in behaviour over an extensive range of strain rates, while Type II structures exhibit 20 – 74 % increases in compressive strength when strain rates are increased from 10^2 - 10^3 s^{-1} [289-292].

It may be possible that similar structure types exist for elastomeric materials, though no study explicitly identifies this. However, it must be noted that football helmet liners are exposed to strain rates from 100 – 400 s^{-1}, depending on impact conditions discussed in section 2.2. The contribution of geometry to dynamic behaviour may be minimal.

2.8.5. Candidate geometries for investigation.

Based on the requirements of a novel helmet liner material presented in section 2.7, the literature was reviewed to identify a series of candidate solutions, focusing on auxetic materials due to the advantages discussed in section 2.8.2.

The in-plane performance of simple auxetic honeycombs has been examined under dynamic and quasistatic loading conditions [372-374]. While these structures have shown promise under loading conditions similar to those identified for American football, this has been from samples either manufactured from elastic-plastic base materials or significantly greater thickness than permissible in the context of American football helmets [372,374]. When these structures have been manufactured from or simulated using hyperelastic base materials, such as TPU's, impact energies have ben orders of magnitude lower than those associated with American football impacts [373]. While further performance could be gained by utilising the structures in a manner that the loading occurs out of plane, this would reduce the structures to simple honeycombs, thus removing some of the perceived benefits of auxetic materials.

Auxetic foams have also been presented as a viable alternative to the elastomeric foams found in sports helmets [266,267, 20]. Compared to the traditional foams they replace, the auxetic foams offered better peak accelerations and, when tested in helmets, GSI values across the range of examined test conditions [267, 20]. However, these foams suffer from the same downside as the conventional counterparts, where the opportunities to optimise the material for a given application is limited.

The family of auxetic-origamis structures have shown promise in a wide range of applications, showing promise in both scope of optimisation and preferable loading response compared to honeycombs [232,238,242,248,252]. However several of these proposed structures may suffer when applied to an American football helmet as they have been examined as single columns or sheets which may not tessellate to offer all-round protection. However, the Miura-Ori folding pattern was consistently used as a base for these structures and thus was identified as a route forward.

A meta-material based upon stacked cores of alternating designs of the Miur-Ori pattern had shown promise under dynamic loads whe manufactured from a variety of materials, both hyper-elastic and elastic-plastic [24,26,39,231,331]. Therefore the metamaterial can be directly employed without changing its loading orientation or reducing its geometrical complexity. These factors make it a preferential option to both the simple auxetic honeycombs and auxetic foams. Additionally, the cellular nature of the metamaterial allows for better scaling of the material to an ideal size for application to American football helmets, which was a problem of other origam based solutions.

2.9. Emerging helmet liner technologies: materials and manufacturing.

With the types of structure of utilised by helmet liners defined, consideration must be given to the materials and methods used to fabricate a novel liner.

2.9.1. Thermoplastic Elastomers.

Thermoplastic elastomers (TPEs) are an exciting subset of polymers, whose combination of thermoplastic and elastomeric properties allow for rubber-like materials to be processed as thermoplastics [213]. TPEs exhibit several favourable material characteristics, such as high flexibility and abrasion resistance [41,42]. These attractive properties mean TPEs have been utilised to produce a wide range of cellular materials, hierarchical structures, and simple geometries for a wide range of energy absorption applications [33,34,292,293].

All TPEs are formed of either microphase separated blocks - where the thermoplastic segments form nanostructures surrounded by a matrix of the softer rubber-like polymer, or in the case of thermoplastic polyurethanes (TPUs) are segmented, with the two chemical compounds forming alternating chains [42,213,294]. It is the balance of these microstructures that give TPEs their properties, although some TPE microstructures are influenced by their thermo-mechanical history [295]. Cast TPE material properties may, therefore, differ versus components produced via injection moulding or additive manufacture (AM). The unique challenges of producing TPE-based components through AM are covered in a later section.

2.9.2. Additive manufacturing

Additive manufacturing enables the manufacture of components through the controlled deposition and binding of material, rather than the subtractive nature of more traditional methods. AM is often referred to as 3D printing and rapid prototyping (RP) [296]. While the argument has been made that these terms serve different functions, for this review, they shall be considered to be synonymous as AM and RP are both enabled by 3D printing [296,297]. As the manufacturing process adds material layer by layer, it enables geometries that are impossible to manufacture through traditional processes [41,296]. Other advantages in component design enabled by AM include optimisation of topology, component customisation, low-cost geometric freedom and the use of lightweight materials [296]. A variety of AM methods have been developed since the inception of the process in 1986, which form 7 broad categories [298]: binder jetting, direct energy deposition, material extrusion, material jetting, powder bed fusion and vat polymerization. Within each of these seven categories, a range of distinct technologies exist [32,39,296,299-314].

The capabilities of these system types were reviewed against the requirements of a novel material for use within football helmets, as discussed in section 2.7. Also, any AM method's ability to utilise a TPE in its manufacturing process, and manufacturing cost and accuracy required evaluation.

The material requirement immediately discounted metal-based techniques such as selective laser melting and electron beam additive manufacturing as well as laminated object manufacturing as this process utilises paper and composite materials exclusively [299,315,316]. Despite material jetting being capable of utilising flexible materials, the process is not capable of producing functional components due to manufactured parts exhibiting low elongation at break under tensile testing, and fatigue life smaller than the expected number of impacts sustained by football athletes [317-319].

Elimination based on material availability left only powder bed fusion, material extrusion and vat polymerisation techniques. From these categories, four manufacturing methods, and their derivatives, Stereolithography (SLA), Selective Laser Sintering (SLS), Multi Jet Fusion (MJF) and Fused Filament Fabrication (FFF) were selected as potential routes to manufacture and thus are covered in greater detail.

2.9.3. Stereolithography

SLA is a form of vat polymerisation where a photosensitive resin is cured by exposure to specific waveforms of light. Traditionally, the system utilised a scanning laser which would trace out a layer of the desired geometry curing the resin. On completion of the layer, the whole build plate was lowered into a vat of resin so that the top surface was refreshed, and the scanning process could begin again. In more recent years, inverted systems have been developed [312,314,320].

By utilising a boundary layer of either glass bubbles or oil at the bottom of the tank, these systems prevent the photopolymerization process and allow for a continual refreshing of material at the build surface. This allows for the continual movement of the build platform, which, when combined with a projector rather than a laser, enables vastly reduced build times [312,320,321].

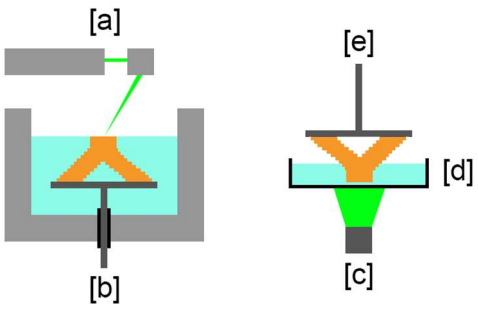

Figure 2-18: Conventional SLA consisting of [a] scanning laser system and [b] moveable platform, and inverted SLA consisting of [c] projector, [d] resin tank with a transparent bottom and moveable platform [e]. In both systems, the curable resin (blue) is polymerised to form a solid component (orange) through the use of a UV light source of a specific wavelength (green).

When SLA manufactured components are subjected to compressive loads, layers perpendicular to the loading direction produce higher strength, although an inverse relationship is displayed when considering tensile loads [35,322]. However, components produced by inverted SLA systems have shown mechanical properties that are almost identical across all build directions [314]. This directional insensitivity has been postulated to be linked to the nanoscale layer heights enabled by the technology [296,312,314]. Parts manufactured with this process have demonstrated mechanical strength equal to parts manufactured from the same base material, via casting and injection moulding processes [312]. Although a wide range of material types is available for SLA, material choice is limited to those that equipment manufacturers provide, with no third party materials available.

2.9.4. Selective laser sintering.

SLS, often referred to as laser sintering or LS, is a form of powder bed fusion, with a wide range of available materials [34,310,323,326]. Unlike other powder bed fusion methods where sufficient energy is provided to the material to melt the powder, SLS only melts the outer layer, allowing the grains of material to bond together [327].

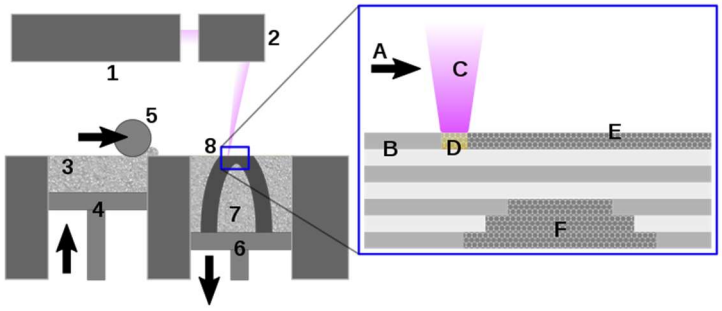

Figure 2-19: 1. Laser 2. Scanner system 3. Powder delivery system 4. Powder delivery piston 5. Roller 6. Fabrication piston 7. Fabrication powder bed 8. Object being fabricated (see inset),A. Laser scanning direction B. Sintered powder particles (brown state) C. Laser beam D. Laser sintering E. Pre-placed powder bed (green state) F Unsintered material in previous layers [328]

SLS components are produced in a manner similar to SLA components, where a layer is melted into the material present in the build bed before it is lowered and refreshed with new material. Unlike SLA, however, the SLS process is inherently self-supporting and as such excess material is not required to produce components with significant overhang. However, internal voids within components can present a challenge as it may be difficult to remove excess powder from the finished component. Much like those manufactured by SLA, the material properties of components manufactured via SLS are sensitive to their orientation within the printer's build volume [35].

2.9.5. Multi Jet Fusion.

Multi Jet Fusion is a powder-based process, much like SLS. However, the critical difference is that the process bonds the powdered material through the use of fusing and detailing agents and IR radiation [316].

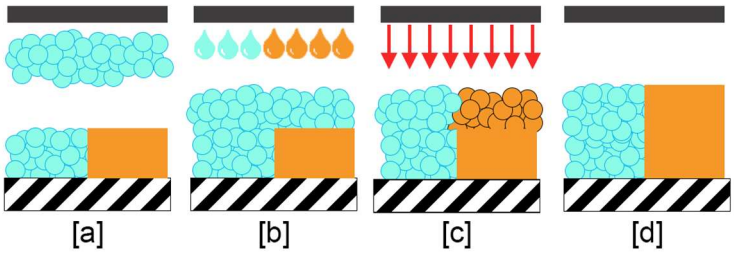

Figure 2-20: Multi Jet Fusion process; [a] new layer of powder is deposited, [b] binding agents are dispensed where new material is to be fused, [c] IR radiation is used to bind powder, [d] new fused material.

By allowing for large areas to be fused simultaneously, MJF allows the creation of parts at a much faster rate than SLS, although due to the novelty of the process the range of materials it can utilise is relatively limited [315,316]. Additionally, MJF allows for the use of transforming agents that can alter the material properties of the deposited powder [316].

2.9.6. Fused Filament Fabrication.

FFF allows for the manufacture of components from a diverse range of thermoplastic polymers, with recent advancements enabling the manufacture of materials containing carbon fibre and metal [36,329,330]. The filament of a specified material is fed into a heated extruder, which is moved in an XY plane to produce a layer of the desired component, Figure 2-21. On completion of the layer, the whole print bed is moved down by a specified height to enable the next layer of manufacture. Because of the nozzle sizes commonly employed by FFF printers, feature size, and a layer height of components produced are typically larger than those of components manufactured using SLS and SLA techniques [36].

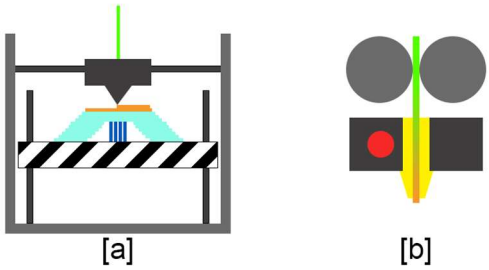

Figure 2-21: [a] Schematic of a FFF printer with [b] a close up of the printing head. Displaying the moveable print bed (cross-hatched), fused material (light blue), molten material (orange), unheated filament (green), support material (dark blue), the heating element (red), nozzle (yellow) and drive wheels (grey circles).

Each layer of components manufactured via FFF are a combination of three primary features: contours, raster and air gaps, Figure 2-22. Contours, or *perimeters*, are extrusion paths that trace the outline of the desired geometry in a concentric pattern. Raster, or *infill*, typically predominates as it extrudes material paths within the perimeter in patterns including rectilinear or hexagonal honeycomb. Air gaps are the intentional spacing between contours and rasters, though these are indirectly defined by the contour and raster parameters.

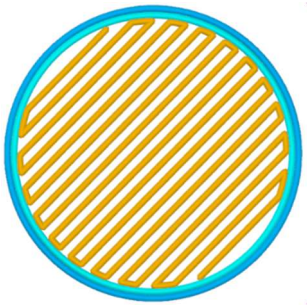

Figure 2-22: Extrusion paths calculated by slicing software showing contours (blue circles), rasters (orange) and air gaps (clear space).

Previous investigations into the influence of FFF process parameters on part quality have focussed on elastic-plastic materials, reporting a broad range of build quality metrics: surface roughness, dimensional accuracy, and mechanical performance in both compressive and tensile loading [308]. These process parameters include but are not limited to print speed, part orientation, extrusion width, layer height, air gap size and temperature [308]. The maximum achievable density of components produced by FFF is less well studied but has been measured at over 99%, with the technique capable of producing components with visually similar fracture sites to cast components [331].

Dimensional accuracy of components has been consistently linked to a part's orientation on the build bed [332-335]. Interestingly, the width of rasters did not have noticeable effects on accuracy, despite the extra material extruded in these printing movements [333]. The relative error of critical dimensions is as low as 4.5% when processing parameters have been adequately controlled [335]. FFF parts are prone to warping, where thermal stresses induced by the deposition of material overcomes the adhesion between the component and the build bed [336].

The orientation of contours and rasters, as well as their interconnectivity, has significant influence over the mechanical strength of produced components, with tensile strength being more sensitive than compressive [337-342]. Layer height has also been linked to mechanical performance, with studies speculating that increased layer height leads to increased pre-stresses within components [343]. Unlike SLA components, however, the mechanical strength of theses specimens is not comparable to that of components manufactured from bulk material. In the case of parts manufactured from TPE, may result from the printing temperature of the filament not being sufficient to overcome the higher glass transition temperature of TPE’s hard segments, leading to the bonding between well-connected rasters formed of the soft segments [340].

In combination with the flexible nature of TPE's, this discrepancy makes it a particularly challenging material to achieve high-quality final parts. Its flexible nature can lead to inconsistent extrusion pressure, while the required print temperatures in comparison to the materials melting point make it prone to oozing, with material extruding unintentionally [40,344]. Specialised extruders have been developed for the printing of flexible materials, which provide significantly more clamping force on the filament to ensure consistent material flow into the heater and nozzle [37].

2.9.7. Comparison of techniques.

FFF printing offers the lowest cost to manufacture of the four systems considered, in terms of both material and machine cost, with both regular and inverted SLA systems costing the most [35,345-348]. Additionally, when one-off prototypes are considered, the cost of manufacture for bed-based systems remain mostly unchanged. As these printers' bed volume remains unchanged, the required volume of base material for manufacture is identical no matter if only 5% or 95% of the volume is filled with components. The filament manufacturing nature of FFF unused build volume in a printer does not affect material costs. Therefore, in experimental development, FFF offers a low-cost solution that enables rapid development of multiple iterations of a design.

However, the manufacturing cost is offset by these systems' abilities to provide the highest dimensional accuracy of the systems reviewed, with FFF naturally being the least accurate [35,346,347,349]. Despite FFF's lesser accuracy, many commercially available printers possess print resolutions capable of producing macrocellular structures [331]. Thus should the minimum feature size of any novel material not be beyond the selected FFF machine's resolution, the system's accuracy would be sufficient for its development.

Print speed and total print time are important considerations for commercial viability but are not necessarily factors for developing a novel material. In both thee regards, FFF can be considered less than ideal as it offers the longest manufacturing time of any of the reviewed techniques [35]. However, as the work presented in this thesis is focused upon developing a novel geometry, manufacturing time of samples can be considered relatively unimportant, so long as it is acknowledged that any further development of the structure in a commercial sense was vai an alternative manufacturing methodology.

FFF offers the broadest range of flexible materials from a range of manufacturers. However, the exact range in material properties is difficult to establish, as not all manufactures state material properties. While MJF is theoretically capable of utilising powders that would form a flexible material, no such material is available at the time of writing. Both SLS and SLA techniques offer flexible materials, but the range of these

materials is limited. This limitation affects the development of a novel material, given the relationship between a cellular materials geometry and base material, as discussed previously.

Consideration must be given to the supporting material used by these techniques, as the method in which this support is generated may impact each system's ability to replicate a novel geometry successfully. Both MJF and SLS utilise powder beds in their manufacturing methodology and provide continuous support to all features, especially overhangs or bridging structures. Comparatively, FFF and SLS must manufacture bespoke support structures for certain geometrical features, such as bridging supports or significant overhangs, which musty be removed upon completion of the print [36]. In the context of cellular geometries, these support structures may be impossible to remove, such as the inner voids of minimally periodic surfaces, or highly reentrant auxetic geometries, without damage to the manufactured component.

For geometries where access to internal surfaces is easy, the use of supports may still lead to issues, mainly where thin walls are utilised, as the relative strength of supports and thin wall sections may be comparable. Thus when this extra material is removed damage to the structure may occur. Therefore, best practice would be to design geometries that do not require support structures, though this naturally hampers the available design space for any novel geometry.

2.10. Experimental Design for Optimisation

The selection of candidate material for study with a high number of geometrical parameters was desirable as this offered the most scope for tailoring the performance of the material under the impact loads commonly seen within American football. However, to ensure that each parameter was examined fairly, a robust methodology for experimental design would have to be selected.

Initially, the design space for any novel geometry had to be established. The minimum and maximum parameter values, and their combinations, that provided functional geometry had to be established to do this. Additional levels could be selected within these established limits to further the study's resolution and identify more complex relationships between parameters and performance metrics, Results of a Hypothetical study of a single parameter, once with only two levels examined (Black Crosses) and a second time with an additional middle level (Blue Cross). The first study suggests that the maximum level would provide the best performance due to the limited linear interpretation of the parameter response relationship (Blue dashed line). In contrast, the second study offers a middle best result due to the quadratic relationship offered.Figure 2-23.

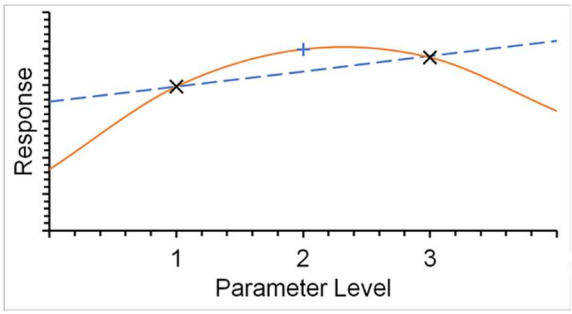

Figure 2-23: Results of a Hypothetical study of a single parameter, once with only two levels examined (Black Crosses) and a second time with an additional middle level (Blue Cross). The first study suggests that the maximum level would provide the best performance due to the limited linear interpretation of the parameter response relationship (Blue dashed line). In contrast, the second study offers a middle best result due to the quadratic relationship offered.

The study of multiple parameters within the same study requires the careful design of samples so that various combinations of parameters can be identified. The most straightforward approach is the full factorial, where all possible combinations of parameters are examined [355]. The total number of samples for this approach is defined by equation 2-18, where N is the number of samples, L is the number of levels of each parameter and m is the number of factors.

$$N = L^m \qquad 2\text{-}18$$

However, as the number of examined parameters and levels increase the number of samples required for study quickly makes a full factorial approach infeasible, in t6erms of both time and monetary expenditure.

Partial factorial experimental designs reduce the number for required samples by defining a subset of samples from the possible design space. However, the selection of samples for a partial factorial method must be carefully considered, as improper selection could have lead to an imbalance in the representation of examined parameters. In turn, this imbalance would in the best case over or understate the importance of a single parameter and in the worst case could have entirely excluded areas of the design space from the examination, Figure 2-24.

		Parameter A				
		1	**2**	**3**	**4**	**5**
Parameter B	**1**	1	2	3	4	5
	2	6	7	8	9	10
	3	11	12	13	14	15
	4	16	17	18	19	20
	5	21	22	23	24	25

Figure 2-24: Sample selection for a hypothetical two-parameter study, with each parameter having five values. The red box demarks samples selected by a full factorial approach, while green cell represents those selected by a partial factorial approach. Note the imbalance between levels 1 and 5 of parameter A, which have 3 and 1 samples respectively, and that level 2 of Parameter B is missed entirely by the selection.

Additionally, while the interpretation of two parameter scenarios is simple, additional parameters add to the complexity of interpreting the results from a partial factorial study [355]. To avoid these experimental design problems from unduly affecting the gathered results, and thus the optimisation of a candidate geometry, a more robust methodology was required.

The Taguchi Method utilises a defined set of Orthnagonal arrays which were designed to minimise the number of samples required to study a process while maintaining the balance of investigated Parameters [355]. Thus the Taguchi method provides a repeatable and consistent experimental design, that is commonly used throughout the literature for a wide range of optimisation tasks [338,355-357]. When used in conjunction with statistical analysis methods, the Taguchi design of experiments allows for identifying each parameter's influence on the process response and any interactions between parameters.

2.11. Conclusions.

Contact sports have a long history with head impacts and injury. American football has been identified as particularly high-risk, due to factors such as the diverse player base and impact environment. On average, the athletes sustain between 250 -1500 impacts above 10g per season, with older players sustaining more impacts due to their participation in a higher number of games and practices each season. The majority of these impacts, between 80 and 90% result in head accelerations below 40g in magnitude and are considered non-injurious. A small number are more violent with the dynamics of these impacts ranging from the low-velocity high mass of linemen, 28 kg at $3ms^{-1}$, to the high-velocity low mass of skill positions, 13 kg at $11ms^{-1}$. These impacts result in changes of head velocity between 4.29 and $7.2ms^{-1}$, with players who sustain injuries receiving higher velocity changes.

The sport has a long history of developments in both rules and PPE in efforts to reduce injury. While these measures have been effective in reducing the worst classes of injury, the prevalence of the most common form of injury, SRC, has remained mostly unchanged in recent years. The years of the high number of impacts that college players and professional athletes sustain during their careers, approximately 6400 impacts for a college athlete, puts them at an elevated risk for a range of neurodegenerative diseases and mental health conditions.

The use of helmets within the sport was initially not enforced, with the protective capabilities of early helmets questionable. Post the introduction of a performance standard helmet safety increased significantly. However, the fundamental design of post standard helmets has remained largely unchanged, with the majority of impact energy being absorbed by an elastomeric foam liner. The testing standards for these helmets employ injury risk metrics based on catastrophic head injury data; thus, the liner's performance is often optimised to worst-case scenarios to achieve the best performance in these tests. Additionally, foams' intrinsic material properties mean that designers must target one loading condition for their helmets, accepting performance degradation outside this scenario. Helmets are also required to operate in a wide range of environmental conditions, whilst still being lightweight and comfortable to wear. Recent years have given rise to a variety of novel structures within football helmets such as flexible cones and air bladders. While these structures have shown promising results in comparison to foams, they have yet to become widely used in the sport.

The advent of flexible materials for use in additive manufacturing processes opens new possibilities in candidate materials for use in helmets. In particular, FFF has demonstrated an ability to manufacture functional components with high levels of dimensional accuracy and part density. This manufacturing technology enables the manufacture of auxetic geometries with new properties that should enable an increase in performance.

To identify a novel geometry for use in football helmets, the literature was reviewed to identify a cellular geometry that satisfied the requirements of a novel material outlined previously. This review identified the Miura-Ori metamaterial (MOM) as a candidate structure for further investigation [31,231]. It is formed by patterned stacking of sheets of the Miura-Ori folding pattern, which in of itself is auxetic. By stacking sheets of differing heights, the material exhibits a double arrowhead's secondary auxetic geometry [231]. This secondary geometry allows for the developed metamaterial to exhibit auxetic properties in all three planes, though only in components with sufficient cells [31,231].

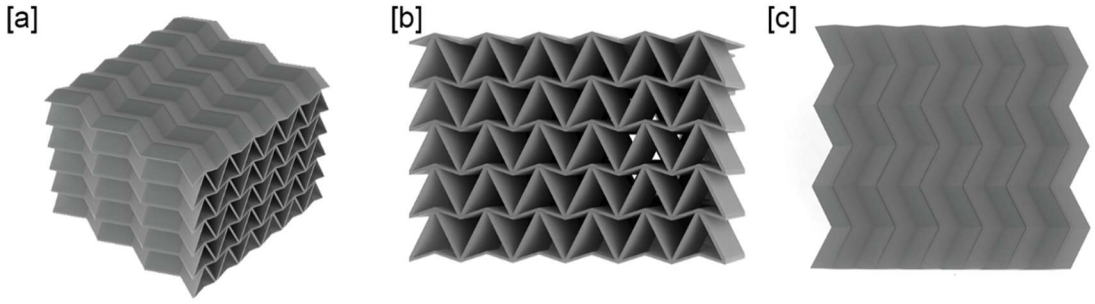

Figure 2-25: Example render of the Miura-Ori metamaterial [a] showing the double arrowhead [b] and Miura-Ori [c] geometries.

Variants of the structure have been examined through computer simulation and physical testing, where both metals and TPEs have been used as base materials [24,26,39,231,331]. When subjected to quasi-static loads, the MOM has shown superior energy absorption performance to equivalent density non-auxetic structures [26]. In dynamic loading conditions, the structure has shown promise in blast mitigation applications and, more importantly, impact regimes equivalent to American football [24, 39]. In all studied cases, the performance of the structure was maximised by the precise control of its geometrical parameters. As the material is based on an origami folding pattern, it is technically possible to develop it from sheets of the chosen base material [31,231]; however, to ensure that the two forming sheets are bonded to each other, many studies have manufactured components using AM.

Thermoplastic polyurethane was identified as a suitable base material due to its attractive material properties, such as high flexibility and abrasion resistance, and structures based on this material class have already found success within football helmets. The combination of FFF and TPUs has previously been used to develop energy-absorbing structures for a range of applications.

The optimisation of this candidate material for use within American football helmets is investigated in this thesis following the outline covered in chapter 1.

Chapter 3: Fine Tuning of Fused Filament Fabrication for TPE Manufacture.

3.1. Introduction.

The use of fused filament fabrication (FFF) to build thermoplastic elastomer (TPE) components is relatively new, with scant literature describing the process when compared to established materials such as ABS and PLA. Although the available process parameters do not alter between the two materials, extra care must be given to the manufacture of TPE filaments due to the FFF process's ability to influence the mechanical performance of the material only by extrusion, as well as the additional challenges arising from maintaining a consistent pressure within the nozzle with a flexible filament [295]. Therefore, identification and control of specific process parameters that enabled high-quality builds was deemed necessary, especially when considering the goal to achieve high-performance components.

The first step of fine-tuning the FFF process was to identify the key metrics on which part quality would be judged. As the intended use of the process developed would be to manufacture cellular materials, aspects of part quality influential to the performance of these structures were given prominence. This led to the identification of three quality metrics: part porosity, dimensional accuracy and mechanical performance.

3.1.1. Part porosity.

As cellular materials' performance is reliant on the deformation behaviour of cell walls, the ability of these walls to transmit forces is of paramount importance [19]. Pores (voids of missing material) inherently weaken walls and change their deformation behaviour, meaning they must be eliminated from manufactured components. This is achieved by identifying processing parameters that enable extrusion of sufficient material at a sufficient temperature, to allow the material to successfully bond to the previous layer across the entire length of the extrusion path.

There are various methods to assess the internal structure of a component through destructive and non-destructive means [350]. Micro-computed tomography (μCT) has been identified as capable of providing an overall level of porosity and identifying the distribution of pores throughout the structure and pore size and orientation [331,350]. The techniques have been used to assess a wide range of geometries manufactured via the FFF process [336,351,352].

3.1.2. Dimensional accuracy.

Optimisation of the MOM is reliant on the ability to control its geometry precisely. Although modern FFF printers are capable of high levels of precision in their movements, improperly controlled extrusion and print speed can lead to unintended material deposition, such strings of material in intended voids, and growth in geometric features where excess material has been deposited.

3.1.3. Mechanical performance.

The performance of any cellular material is derived from the behaviour of its walls to compressive loads [19]. Components manufactured via FFF, have been shown to exhibit apparent anisotropic behaviour, where strength is maximised when uniaxial loads are applied in the direction in which rasters, printing movements that constitute the bulk of the volume of a layer, and contours, the outlines of geometry, have been extruded [35,339,353]. However, the material properties of FFF filaments are often reported from standardised tests conducted on specimens manufactured from bulk material rather than an AM process [40,344]. Thus, a chosen material for use in a cellular structure may have less favourable material properties when the cellular material is constructed via FFF. To avoid a potential loss of performance, the ability of an FFF process to produce parts with mechanical performance similar to that of the base material is desirable.

3.2. Materials and Methods

3.2.1. Materials

A review of currently available flexible filaments, of a 1.75mm diameter, for FFF printers, was conducted. Although the use of a commercial filament would limit the optimisation of the novel protection material as it would restrain the base material properties, the consistent filament diameter would enable more consistent extrusion and enable higher quality components.

Choice of the filament was based upon various factors; presence within the literature, technical detail availability, and the range of other filaments offered by the same manufacturer. Literature presence was determined by the number of papers retuned when academic collections were searched using the filament name, A filament with a higher number of returned papers would be preferable to one with a lower number as more information as to the achievable quality and material performance. Additionally, a comprehensive technical data set would allow for easy comparison between parts manufactured via FFF and injection moulded, or cast components that would be expected to have more isotropic properties, and greater component strength.

Table 3-1: Review of TPE based flexible filaments available for FFF printers.

Manufacturer	Filament	Material	Material Data	Presence in literature (number of Papers)
Ninjatek	Ninjaflex 85A	TPU	Full TDS	1150
	Cheetah 95A	TPU	Full TDS	22
	Armadillo 75D	TPU	Full TDS	1
Polymaker	PolyFlex™ TPU90	TPU	Full TDS	1
	PolyFlex™ TPU95	TPU	Full TDS	0
StrainSmart	StrainSmart TPU	TPU	None	0
eSun	eSun eLastic TPE	TPE	None	18
BASF	Ultrafuse® TPE 60D	TPE	Full TDS	0
	Ultrafuse® TPC 45D	TPC	Full TDS	0
	Ultrafuse TPU80A LF	TPU	Full TDS	0
	Ultrafuse TPU85A	TPU	Full TDS	0
3D Solutech	Flexible Filament	TPU	None	0
Gizmodorks	Flexible TPU Filament	TPU	None	0
Recreus	Filaflex 70A	TPE	Full TDS	1
	Filaflex 82A	TPE	Full TDS	10
	Filaflex 90A	TPE	Full TDS	0

This review identified two filaments, Ninjaflex (Ninjatek, USA) and Cheetah (Ninjatek, USA). These two filaments not only presented with the largest number of returned papers within the literature but also offered comprehensive technical data sheets. Additionally, these filaments offered the broadest range in material behaviour of filaments of the same base material family from a single manufacturer.

Both filaments were manufactured from differing blends of thermoplastic polyurethanes (TPUs), which are a subclass of TPEs. Access to the technical data allowed for the results of the fine-tuning process to be compared to that of a fully dense component manufactured via traditional methods. The data presented in this study was collected using samples manufactured from Ninjaflex.

To enable the maximum control of the printing process a highly capable slicing software, Simplify 3D (Simplify 3D, Cincinnati, US), was used to generate the print files. While there is a wide range of software packages available for printer control, these typically limit the control over a FFF printer, such that modification is made to all movements made by the printer. In contrast, Simplify 3D breaks the printing process into a range of specific actions, such as bridging unsupported gaps and the manufacture of thin-walled sections. This granularity allows the software to alter the printing of contours and rasters for each action, maximising the print's quality.

On review of Simplify 3D, five variables were selected for use in the tuning process:

1. **Extrusion Speed.** The speed at which the print head moves while extruding filament onto the build bed. As speed increases, the software increases the rate at which filament is pulled into the hot end of the printer.

2. **Extrusion Temperature.** The temperature at which the hot end of the printer is maintained during the print process. Higher temperatures produce a less viscous extrusion of material, which may provide superior bonding to previous layers, and elimination of pores.

3. **Outline Overlap.** The percentage of the extrusion width a raster can overlap with a contour, thus increasing the bonding between the contours and rasters. This parameter is critical to consider as previous studies of TPU components identified that the majority of voids appeared at the interface of contour and rasters [331].

4. **Extrusion Multiplier.** A bulk modifier to all extrusions made by the printer. Increasing the value of this parameter increases the amount of material the printer produces and can thus reduce voids.

5. **Inclusion of solid diaphragms.** Simplify 3D enables the use of a different raster pattern for the top and bottom of a part to enable superior surface finish. The use of this different pattern within the part may allow for material to be extruded into locations not directly covered by the regular raster pattern. For this study, three possibilities for the distribution of these solid diaphragms were considered: none, once every three layers, and exclusively.

This sample geometry was designed to enable the uses of advanced analysis techniques, covered in the next section, to measure part quality. The sample contained features that enable measurements of thin-walled accuracy, porosity and z-axis accuracy of a print profile, Figure 3-1. Thin walls were generated in pairs with dimensions ranging from 0.6mm to 1.5mm in thickness in 0.3mm steps. Z-axis steps were placed in three batches 0.6 - 0.9mm, 2.65 - 2.75mm and 4.7 - 5mm with four steps in each group with a rise of 0.1mm per step. Overall sample dimensions were minimised so that the samples could fit within the scanning volume of the µCT equipment, while a solid centre bar was designed to ensure that sufficient material volume was present to be captured by the µCT.

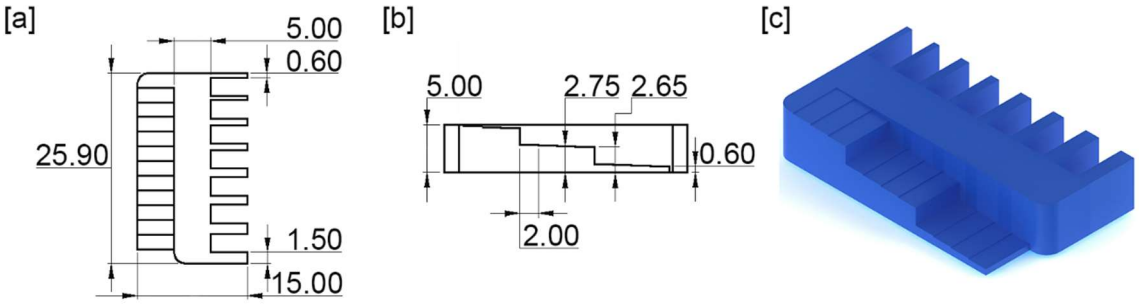

Figure 3-1: Analysis sample developed for the fine-tuning process, a top-down view showing z-axis steps, solid central bar and thin walls [a], side view of z-axis steps [b], and render of geometry [c], all dimensions in mm.

As the analysis sample could not be mechanically tested in a meaningful way, tensile samples matching the geometry specified for type 1 test coupons of BS ISO 37:2017 were produced [354]. Each time a new analysis sample was created, three tensile samples were produced.

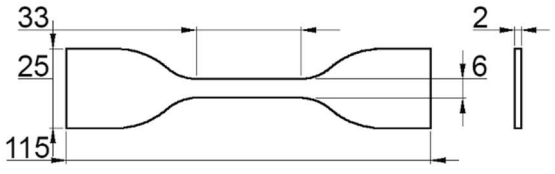

Figure 3-2: Type 1 tensile specimen, all dimensions in mm.

3.2.2. Methods.

3.2.2.1. Sample manufacture.

All samples were manufactured using a modified Flashforge Creator Pro (Zhejiang Flashforge 3D Technology Co, China). This printer was chosen as a cost-effective printing solution that offered direct drive of the filament, heated build plate and allowed the use of and aftermarket print head, a Flexion HT (Diabase Engineering, USA). This print head had been specifically designed to be utilised with flexible filaments and allowed for greater clamping of the filament to ensure consistent extrusion. A piece of borosilicate glass was placed on the build bed and clamped into place. This bed was combined with the use of a specialised adhesive spray to minimise part warping.

The analytical sample was manufactured with the thin wall features perpendicular to the build bed as this would be the orientation of the MOM when printed. Thus any identified issues with manufacturing quality would be expected to carry over to the MOM from the analytical sample when the same profile was used. The mechanical test piece was printed with the maximum surface area in contact with the print bed of the Flashforge to minimise the effects of part warping,

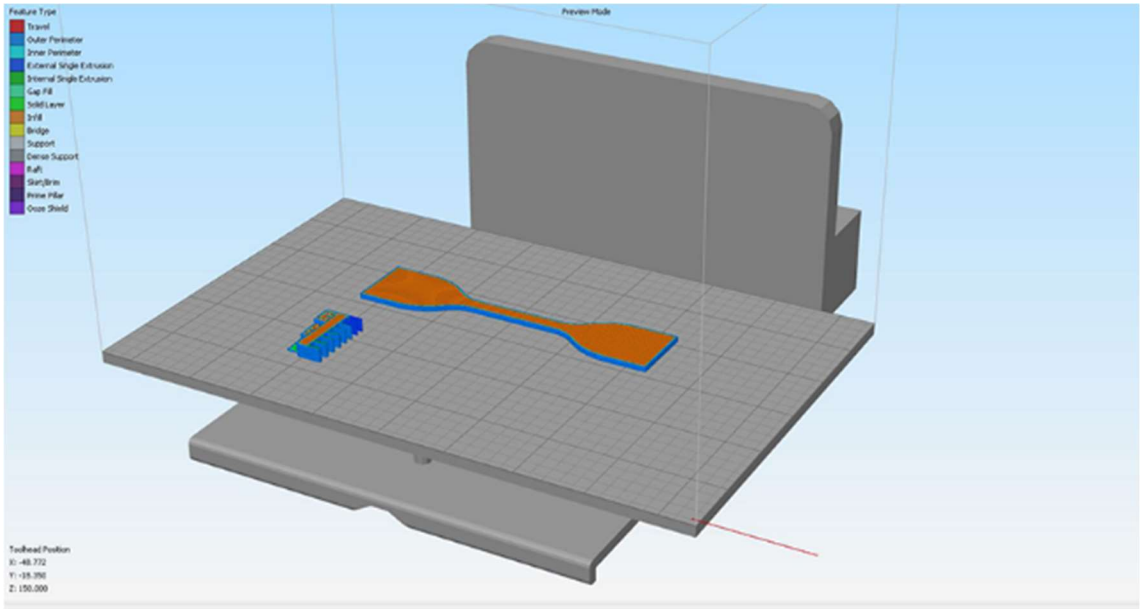

Figure 3-3: Orientation of both the analytical sample and Mechanical Sample within the build volume of the Flashforge. Components were manufactured separately with central placement on the bed.

The first profile used for the iterative process was generated by initially selecting the default settings for a 100% dense ABS print, with print speed and temperature altered to the minimum of the ranges recommended by the filament manufacturer, Table 3-2 [344].

Table 3-2: Initial profile created for Ninjaflex.

Print profile parameter,	Value
Print temperature	225°C
Print speed	900mm/min
Raster Pattern	45°, -45°
Layer height	0.1mm
Interior fill percentage	100%
Bed temperature	40°C
Outline overlap	20%
Extrusion multiplier	1.0
Minimum printing width	50%
Maximum printing width	200%
Solid Diaghaphrams	0
Allowed perimeter overlap	10%

3.2.2.2. Porosity measurements.

Scans were performed using a Skyscan 1272 (Bruker microCT), with a 1344 × 896 resolution and a voxel size of 19.74 µm, in line with previous studies [351]. While this meant that the scan would potentially miss any pores below this voxel sizes, reduction in scan size would have dramatically increased the scan time and potentially induced noise in the scan data which would have influenced the gathered results.

The selected analytical sample was placed in the scanner with the vertical bar placed upright, in line with the centre of the scan area. Due to the sample height in this orientation, over-sized batch scanning was conducted. This resulted in two images being captured one focused on the lower portion of the sample, the second one capturing the upper portion of the sample. These images were retrospectively stitched together to form a single scan image, Figure 3-4[a]. Upon the capture of an image, the sample was rotated by 1°, with the imaging process repeated until the sample had been rotated through 180°.

The raw scan images, Figure 3-4[a], were then imported into dedicated software, (NRecon 1.7.3.1; Bruker microCT, US), allowing for the generation of horizontal slices of the sample spaced in one voxel increments, Figure 3-4 [b]. These horizontal slices were then imported into Mimics Research 20.0 (Materialise NV, Leuven, Belgium) for further analysis. To eliminate noise from each sample's reconstructed images, consistent greyscale values of 28 and 255 were used within the software, Figure 3-4 [c]. These values were based upon the elimination of noise present in the scan volume beyond the boundaries of the examined samples. Top ensure that this process did not remove any material present within each sample, and thus effect the results provided by the scan data the lower limit was set below the point that removed all noise from the reconstructed scan images. Identical thresholds were used across all samples such that the effects of any excess material generated from noise could be expected to be consistent across all

samples, limiting the effects of this phenomenon had upon measured quality metrics. This thresholding allowed for the identification of a solid part within the scan data, Figure 3-4[d]. This solid component was then imported into 3-matic Research 12.0 (Materialise NV, Leuven, Belgium) for further analysis.

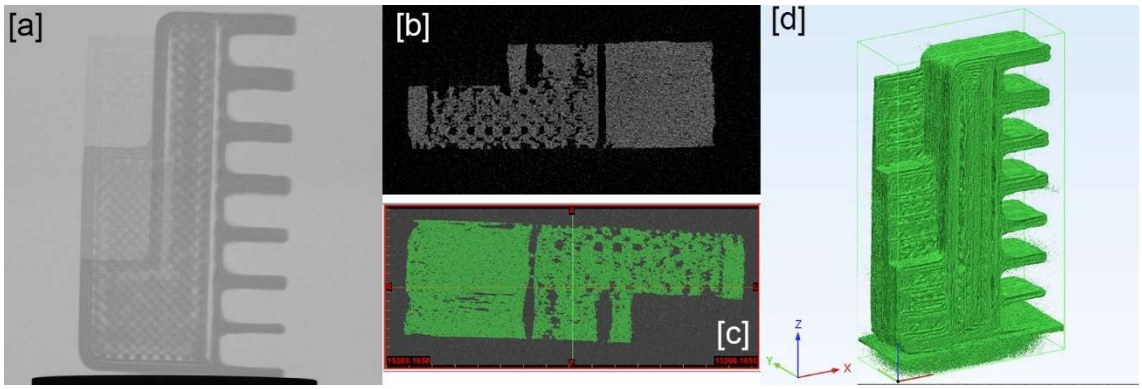

Figure 3-4: Raw image captured by the µCT scanner [a], horizontal slice calculated by NRecon [b], identified solid using greyscale thresholding [c] and imported geometry of 3-Matic.

Standard part healing available in the 3-Matic software suite could not be used to remove the remaining noise evident in Figure 3-4[d], as these processes could unintentionally remove voids within the main part and so effect calculated porosity values. Additionally, to account for interference from the scanner's mounting point, porosity was calculated from a standardised oblong core, measuring 20mm by 3mm by 3mm. Boolean subtraction was used to remove all parts of the identified solid outside of this bounding area. The core was positioned at the centre of the solid bar feature of the manufactured samples.

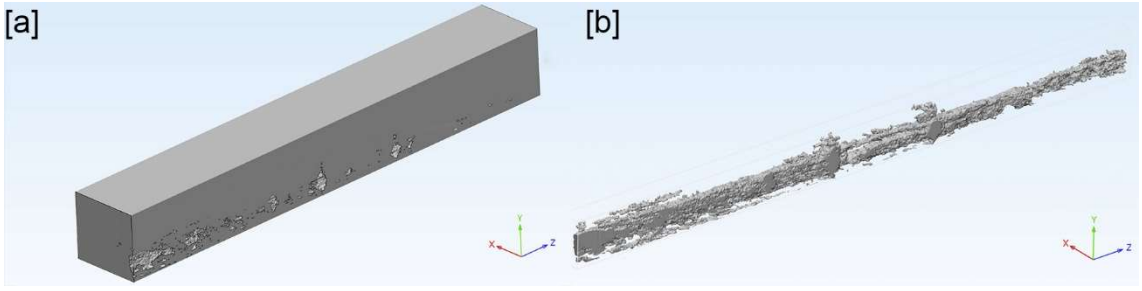

Figure 3-5: µCT core [a] and voids [b] produced by the Boolean subtraction method.

Sample porosity (P) was then calculated by comparing the volume of the core (V_c) to the maximum volume attainable (V_m), equation 3-1.

$$P = 100\frac{V_m - V_c}{V_m} \qquad 3\text{-}1$$

3.2.2.3. Dimensional accuracy.

The elastic nature of TPU materials means contact-based measurements of dimensional components are prone to error, due to part deformation; hence, µCT data was used for measurement acquisition. Scans were imported into 3-matic (Materialise NV, Leuven, Belgium) using the steps described in the previous section. As porosity was not a concern for external measurements, the standardised part repairs within the software were used to remove the san solid noise. Parts were rotated so that critical surfaces were aligned with one of the prescribed planes within the software. This allowed measurements to be taken normal to this plane, through-thickness. Each feature was measured at five randomised points.

Recorded values were converted to absolute measurements (ϵ_a), equation 3-2, calculating the ratio between the prescribed and manufactured dimensions.

$$\epsilon_a = d_m - d_r \qquad 3\text{-}2$$

where $\mathrm{d_m}$ is the measured value of a dimension and $\mathrm{d_r}$ is the reference value of the dimension.

3.2.2.4. Mechanical Performance.

Manufactured tensile samples were clamped in a uniaxial testing machine (Zwick Z50, equipped with a 1kN load cell), with strain measured using a video extensometer (iMETRUM IMT-CAM028 equipped with a GP002 lens). The Z50 and camera were connected to the same data acquisition system so that the data sets they provided were synchronised to the camera's frame rate.

Dots were added to the three mechanical samples produced for each iteration at their midpoint and ends of the test lengths, Figure 3-6.

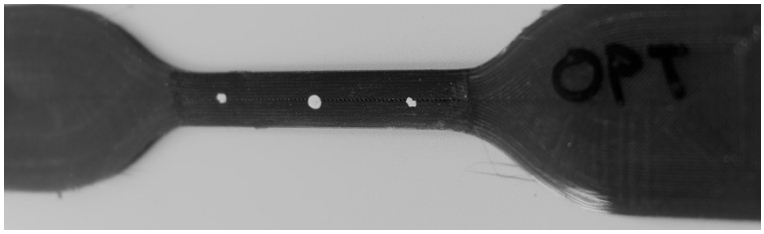

Figure 3-6: Tensile test specimen with a dot array for video exstensometry.

A preload of 5N was applied to each clamped sample to ensure that results would not be affected by displacement caused by either slipping of the sample within the grips, or from a lack of tension in the test sample, which would affect perceived stiffness.

Samples were strained to a recorded value of 200% strain at a constant rate of 500mm/min, in line with the standard [354]. This strain value was well beyond the maximum strain expected to be exhibited by any MOM geometry, though it was intended to cause rupture of a component due to poor build quality.

Stress was calculated under the assumption that the samples were fully dense, with the cross-sectional area of the test length matching design dimensions. Although µCT of the associated analysis sample could be used to estimate the porosity of the tensile bar, accounting for this would remove any influence porosity had on mechanical strength and thus undermine the study. The tensile samples' overall size precluded the use of µCT to measure the dimensions of the test length. Traditional contact methods were utilised, with care being taken to minimise inaccuracies due to part deformation.

A 5^{th} order polynomial curve was fitted to the data for each sample set and used to estimate the stress at 25, 50, 100 and 200% strain, with an average value for each strain used for comparison to previous samples.

3.2.2.5. Iterative tuning process.

As made clear in the literature, the optimisation of FFF printing relies on geometry, filament material and optimisation goal, where a profile optimised for mechanical strength or surface roughness may provide poor dimensional accuracy [308,332]. Rather than retread ground covered by previous studies, the literature's insight was used to iteratively improve the printing profile until an acceptable balance of the quality metrics was met.

The iterative process was conducted in two phases. Initially, efforts were made to increase the density of components. Extrusion multiplier, print temperature and outline overlap were increased to maximise the amount and bonding of extruded material. Once an acceptable degree of porosity had been achieved, the effort's focus went to improving the dimensional accuracy provided by the profile, with a particular focus on thin-walled geometry. Parameters increased during the initial phase were gradually reduced, such that excess material seen on manufactured components was removed without harming achieved density. Throughout this process, print speed was gradually increased to reduce manufacturing time.

For each iteration of the printing process, three tensile samples and two Analysis samples were manufactured. These samples were visually compared to ensure that manufacturing quality was comparable and that defects were caused by incorrect software parameters rather than the printer's physical performance. Where inconsistencies between samples were present, the printer's physical components were inspected, with replacements to components and alterations to the setup made where necessary.

3.3. Results and Discussion.

Table 3-3: Values of variable process parameters for each iteration.

Iteration	Print Speed (mm/min)	Print temperature (°C)	Outline Overlap	Extrusion Multiplier	Distribution of solid layers
Initial	900	225	20%	1	None
First	900	235	20%	1.25	Exclusive
Second	900	235	20%	1.5	Equal
Third	1500	230	40%	1.5	Equal
Fourth	1500	230	20%	1.4	Equal
Final	2100	225	40%	1.4	Equal

Table 3-4: Values of quality metrics for each process iteration.

Iteration	Porosity (%)	Thin wall (mm)	ϵ_a Through thickness (mm)	Stress at 0.5 Strain (MPa)
Initial	27.37	0.052	-0.001	3.12
First	4.46	0.042	-0.001	2.92
Second	1.78	0.761	0.077	3.70
Third	1.76	0.763	0.092	3.73
Fourth	0.60	0.549	0.055	3.28
Final	0.02	0.143	0.047	3.34

Across all the printing profile iterations, the through-thickness absolute error remains mostly unchanged, consistently within one layer thickness, 0.1mm, of the desired value, Table 3-4. The dimensional accuracy of a component perpendicular to the print layers can be assumed to be insensitive to profile settings, and the variation exhibited by the samples is due to changes with the printer's physical setup. However, it must be acknowledged that the samples produced by the second and third iterations produced large amounts of excess material, which degraded the appearance of geometrical features, Figure 3-7 [b].

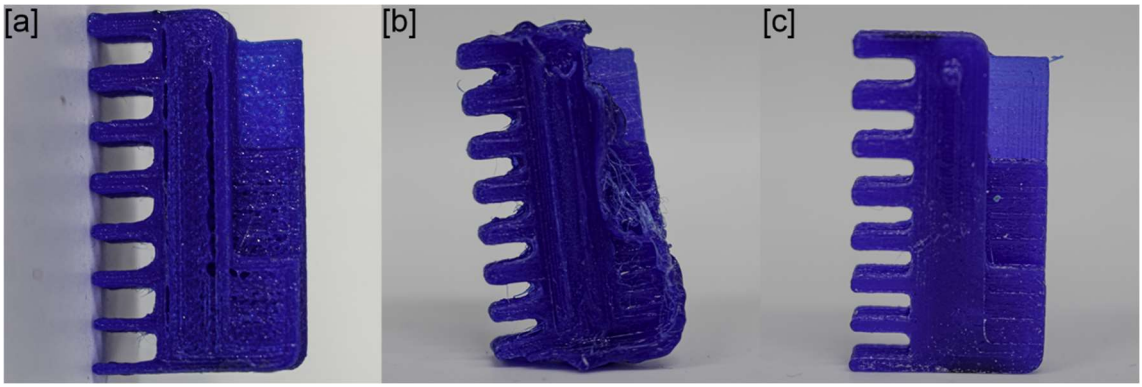

Figure 3-7: Analysis samples produced by the initial FFF profile, showing significant porosity [a], the third iteration of the profile, showing significant amounts of excess material [b] and the final profile iteration presenting as a clean and accurate print [c].

This excess material was deposited in one of two ways, either at the perimeter of a layer leading to lateral expansion or on the final surface where a double ridge feature formed in line with the last printing movement, Figure 3-7 and Figure 3-8. Observing the printing process confirmed that theses iterations extruded sufficient material for a wave to form around the nozzle which was moved around the surface of the print layer and deposited at the edges. Although these components were a single layer different in height from those produced by the initial profile and first iteration, this was sufficient to alter the part significantly.

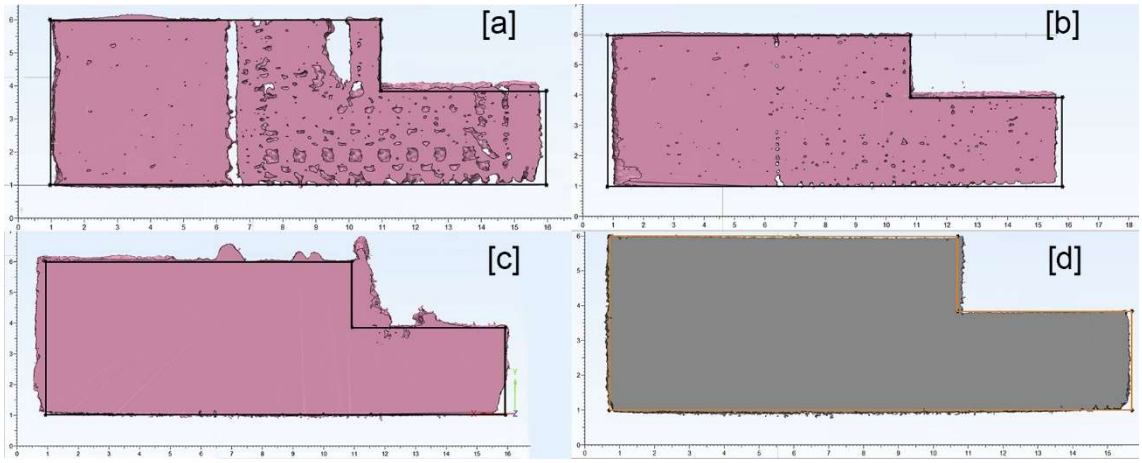

Figure 3-8: µCT cross-sections from Initial profile [a], Iteration 1 [b], Iteration 3 [c] and final iteration [d]. Black and orange lines represent the CAD outline of the analysis geometry. All cross-sections are taken at approximately the same location throughout the geometry.

The initial profile resulted in a component with multiple apparent voids and significant debonding between the contours and rasters within the part, Figure 3-7 to Figure 3-9. A clear checkerboard pattern is seen not only in the cross-section of the component but also the central core.

The pattern's regularity suggests that the rasters within each layer were either incorrectly spaced or that extruded material did not flow as expected. The significant debonding between the contours and rasters is also a symptom of this, as the contraction of cooling material could have pulled the few bonds between these components apart. The small voids linked to the raster pattern appear to have compounded into a more significant build error, where missing material in the previous layer prevents the deposition of the material causing an elongated void to appear, Figure 3-8 [a]. The second iteration managed to increase the deposition of material, and near elimination of the voids. However, some debonding between the contours and rasters was still present, most notably at the sections where thin-wall structures adjoined the central bar, Figure 3-8[b].

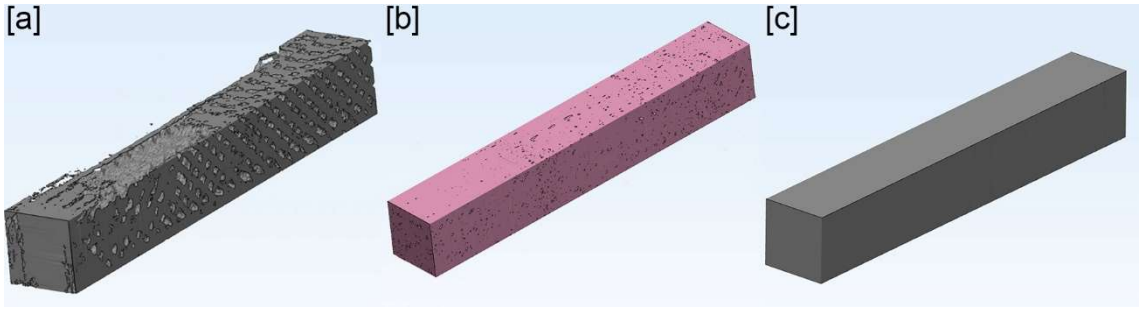

Figure 3-9: µCT cores used to calculate porosity of initial profile [a], iteration 1 [b] and final iteration [c].

When sufficient material was extruded, the produced component's internal structure presented as a monolithic solid, and the part could be considered to be isotropic, Figure 3-9[c]. However, the µCT images cannot provide information as to the distribution of the hard and soft segments of TPE, which would still influence mechanical performance[42,213,294].

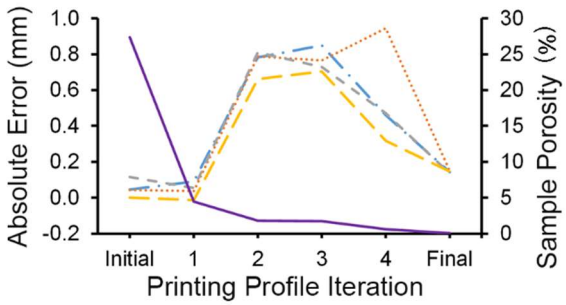

Figure 3-10: Percentage porosity (solid purple) and absolute error for 0.6mm (blue dashed-dot), 0.9mm (orange dot), 1.2mm (short grey dash) and 1.5mm (long yellow dash) thin-wall elements for each iteration of the printing profile.

Throughout the iterative process, a clear tradeoff between dimensional accuracy of thin-walled features and porosity developed, with denser components being less dimensionally accurate, Figure 3-10, consistent with ABS based FFF studies [308]. The average absolute error of thin-wall components was reduced to 0.143mm without negatively impacting density through the management of process parameters. The 1.5mm thin walls consistently reported the lowest error in manufacture across all iterations of the printing profile. The methodology used by 3D-simplify to fill thin wall features is to place an extrusion scaled between 50% and 200%. This type of infill was utilised for the 0.6mm to 1.2mm walls, with the 1.5mm walls receiving the regular infill pattern. The additional growth in the thinner walls' critical dimension may be due to the combination of the extrusion multiplier with the fill multiplier leading to excessive deposition of material.

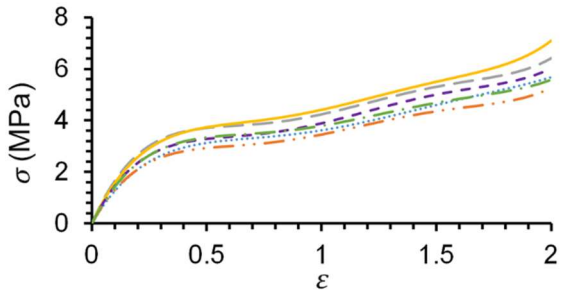

Figure 3-11: Tensile stress vs strain for the Initial profile (blue dot), first iteration (orange dash-double dot), second iteration (long grey dash), third iteration (solid yellow), fourth iteration (short purple dash), and final iteration (green dash-dot).

No clear relationship between porosity and mechanical performance was exhibited by the tensile components produced, with the first and final iterations producing components with almost identical mechanical performance. Although the components manufactured using the second and third iteration appear to provide superior performance, this likely to be an artefact of the assumptions made during the calculation of tensile stress. As the analysis components for these iterations exhibited significant growth, it is likely that the tensile samples also exhibited a similar growth.

When stress at 0.65 strain is compared for all iterations to the reported values of the base material (4MPa), sample strength was between 75.77% (3.031MPa) and 97.72% (3.910MPa), with the final iteration providing a relative strength of 86.33% (3.453MPa) [40]. These values compare favourably to the relative strength of components reported in the literature [340,353].

3.4. Conclusions.

Accurate manufacture of wholly solid components via FFF is vital to any optimisation of the MOM geometry. TPU based filament pose additional challenges to print quality due to their highly elastic nature. A profile for the manufacture of highly dense thin-walled geometry from TPU was achieved through a robust yet straightforward iterative approach. Sample quality was defined as high geometrical accuracy and tensile strength, with low porosity.

The quality of components was measured via the use of μCT imaging to establish porosity and dimensional accuracy, and uniaxial mechanical testing to assess component strength. The iterative process's final profile enabled the construction of a component with less than 0.5% pore volume and average error for thin wall geometry of 0.143mm.

The Iterative approach produced components with comparable performance to those manufactured during studies with more robust optimisation methodologies. Therefore, it stands that this approach offers an alternative where time or cost considerations do not allow for a more comprehensive methodology.

Chapter 4: Validation of the processes used to identify optimal Miura-Ori Metamaterial Geometry.

4.1. Introduction.

The previous chapter established fused filament fabrication as a viable method of producing high-quality functional components from TPU. However, the ability of an optimisation process to generate the best form of the MOM geometry for use in football and provide insight into the geometry relies on the correct selection of a range of decisions around experimental design.

Primarily, the choice and value of geometrical parameters used in the optimisation process are vital to optimisation. Although a simple examination of the structure can identify geometrical parameters, their influence on performance is not so quickly established. A parameter that does not influence performance should not be included in an optimisation process as they will not meaningfully influence results but may hamper the influence of other parameters [355]. The range of parameter values covered in an optimisation process constrains the optimal design produced, as the process can only find the best design in the window specified by this choice. Without study, it is difficult to identify whether geometrical parameters of a structure interact, where altering one parameter influences the performance changes attributed to another factor. Without the presence of the interactions identified and understood optimal geometries may underperform and exhibit worse performance than other geometries [355].

Experimental conditions used to generate data for optimisation must be carefully considered**.** As testing of an experimental PPE system in real-world conditions would be both inefficient and unethical as athlete safety could not be guaranteed, an alternative testing method must be specified. While a range of accepted helmet testing methodologies exists, they are limited in their ability to mimic the dynamics of a real-world impact. The inputs into these systems, in terms of impact masses and velocities, must be carefully considered so that the resultant forces induced on a sample are representative of those it would experience in use.

Finally, although the previous chapter demonstrated that TPUs could be printed via FFF, there is still a wide range of performance in this class of material. Therefore, the selection of an individual TPU to serve as a cellular structures base material is key to its performance [19]. For example, a weak TPU will lead to a structure that is easy to collapse, which in turn will obfuscate any influence that the identified geometrical parameters have over the performance of the material.

While the literature can be used to estimate and identify reasonable values for many of these experimental features, aspects of the optimisation process, most notably the presence of interactions, can only be validated through experimental testing [355]. Experimental design decisions such as optimisation metrics and impact environment are defined by literature and as such, do not need to be validated in a similar manner before optimisation can begin.

This chapter aims to validate the experimental design of the optimisation process to be applied to the MOM. This validation study was conducted using a series of MOM geometries, manufactured from TPU, subjected to both quasi-static and dynamic loading conditions and comparing a selection of performance metrics to comparative materials. As such, this chapter has four objectives:

1. Ensure that the choice of parameter ranges provide sufficient variation in sample response for meaningful optimisation.
2. Determine the exitance of interactions between the primary geometrical parameters.
3. Demonstrate that the dynamic testing environment used provides comparable data to established helmet testing results.
4. Ensure that the performance of developed MOM samples is equivalent to current protection materials.

4.2. Materials and Methods.

The following sections cover the initial inputs for the optimisation method and experimental design used to assess the validity of these decisions. Initially, the choice of parameters for optimisation is covered, followed by the optimisation method chosen and the design and manufacture of samples specified by this method. Finally, the quasi-static and dynamic testing used to validate these choices is covered.

4.2.1. Experimental Design of Optimisation Process.

One of the rationales for selecting the MOM geometry was the high number of parameters that controlled the exact geometry of the unit cell. These parameters were separated into two groups: variable and control.

4.2.1.1. Parameter Identification.

Initially, the parameters of a unit cell were identified. Previous parameterisations of the MOM and other Miura-Ori based cellular materials have been conducted [26,231]. However, these studies based their parameterisation on examination of single sheets of the folding pattern, with parameters duplicated when these sheets were stacked to form metamaterials.

Due to the manufacturing method used, it was deemed more appropriate to base the parameter identification on a single cell of the developed metamaterial. This examination identified a total of seven parameters of the intricate folding geometry of the metamaterial, Figure 4-1.

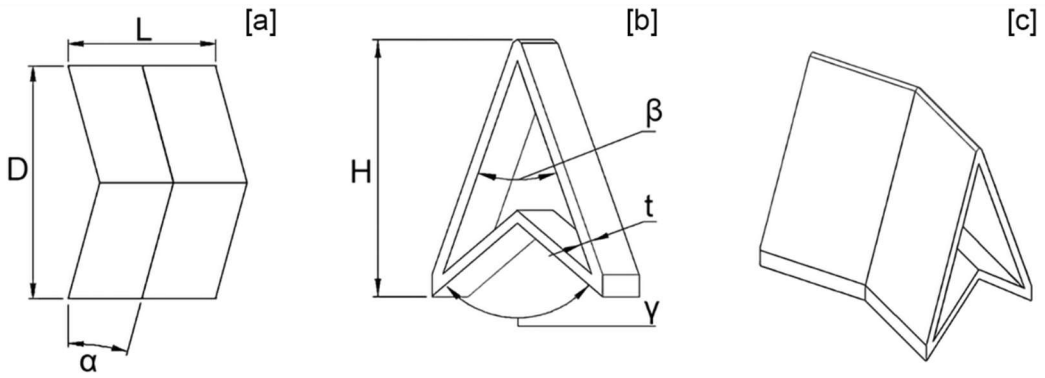

Figure 4-1: Geometrical Parameters Defining a Single Cell of the MOM, [a] front view, [b] top view and [c] isometric projection.

Three parameters, cell depth (D), width (L) and height (H) defined overall cell volume without necessarily changing the geometry and as such, were used as control variables. This left four parameters, angles α, β, γ and wall thickness t, which were deemed to have greater influence in varying the cell structure.

4.2.1.2. Identification of parameter values and ranges.

Cell size was maximised, to aid the manufacture of accurate MOM samples, as the feature size achievable using a FFF printer is linked to the nozzle diameter used in the process [36]. Therefore, to maximise the wall thickness, while maintaining low relative density, a single cell was utilised through the depth of a sample. D was given an equivalent value to the thickness of a sample of the elastomeric foam in a liner pad taken from the side of a Rawlings Impulse (Rawlings Sporting Goods Company, USA) helmet, 25mm. L was kept consistent with the previously reported version of the MOM, 15.8mm [39].

H was not given a defined value as it was defined by its relationship with both L and β, equation 4-1, as a defined value would have removed β as a variable for study.

$$H = \frac{L}{2\tan\left(\frac{\beta}{2}\right)} \qquad 4\text{-}1$$

Initially, a flexible MOM reference geometry was examined, and values of α, γ, β and t were identified [39], Table 4-1.

Table 4-1: Identified parameter values from the reference design.

Parameter	Reference Design Values
α (°)	15
γ (°)	110
β (°)	38
t (mm)	0.9

Maximum and minimum parameter values were centred around these identified values, with the reference design at the centre of a design window. Variation in sample geometry was balanced against both manufacturability of samples and preservation of the underlying geometry of the MOM. For example, the nozzle diameter used in the FFF printer, 0.3mm, informed the choice of 0.6mm and 1.2mm as the limits of wall thickness, maintaining a consistent manufacturing method. Extreme combinations of parameter levels, such as maximum values of α, β and t with a minimum value of γ were checked to see if the combination could be detrimental to the underlying MOM geometry, for instance producing a part that was effectively a solid block of material. Finalised minimum and maximum values for parameters used in this study are presented in Table 4-2, with extreme variations of geometry presented in Figure 4-2.

Table 4-2: Upper and lower bounds of the design space for MOM optimisation.

Parameter	Minimum	Maximum
α (°)	5	25
γ (°)	80	140
β (°)	33	43
t (mm)	0.6	1.2

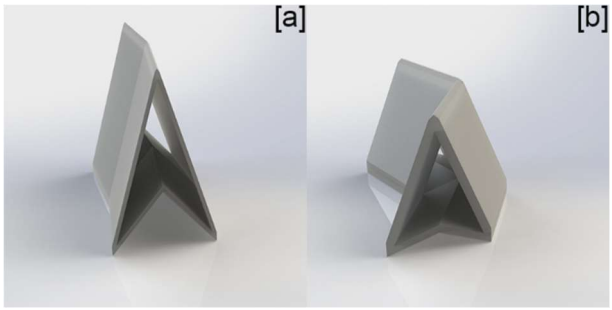

Figure 4-2: Examples of single cells of the MOM geometry based on minimum parameter values [a], and maximum parameter values [b].

4.2.1.3. Experimental Design

Of the available three-level orthogonal arrays utilised by the Taguchi method, the L9 array, was selected for this validation effort, as it allowed for the minimum number of samples which would still generate enough data to validate the optimisation process. To populate the orthogonal array, minimum, middle and maximum parameter values were used as levels one, two, and three, respectively, *Table 4-3*.

Table 4-3: Populated L9 Orthogonal Array

Sample Number	α (°)	t (mm)	β (°)	γ (°)
Baseline	15	0.9	38	110
1_N	5	0.6	33	80
2_N	5	0.9	38	110
3_N	5	1.2	43	140
4_N	15	0.6	38	140
5_N	15	0.9	43	80
6_N	15	1.2	33	110
7_N	25	0.6	43	110
8_N	25	0.9	33	140
9_N	25	1.2	38	80

4.2.2. Design and manufacture of samples.

4.2.2.1. Sample Design.

The parameter combinations specified by the Taguchi array were used to modify an equation driven Solidworks (Dassault Systèmes, France) file to generate sample geometry. The overall sample size was dimensionally controlled to maintain a consistent volume to aid in comparison to contemporary materials. A sample area of 60mm by 60mm was selected, positioned to maximise the number of intact cells in the sample. This sample size was consistent with the previously reported areas of utilised material within helmeted collisions [358,359]

4.2.2.2. Additive Manufacture of Samples.

Generated CAD files were exported from Solidworks as a stereolithography (STL) file at the maximum level of quality in the software. The STL files were then imported to Simplify 3D (Simplify3D, USA), using the profile parameters generated in chapter 3 to process the geometry. Parts were manufactured on the same printer using the same material, Ninjaflex, as presented in chapter 3, with the print bed cleaned and levelled between prints. Before each print, the build bed was sprayed with a water-soluble adhesive spray to minimise part warping.

4.2.2.3. Sample Quality Control.

All manufactured samples were validated against their design in three stages. Firstly, a visual inspection of parts was conducted to identify printing errors such as warping, excess material or under extrusion. If any sample failed this visual inspection printer setup and condition was checked and corrected as necessary, and the sample was reproduced.

Samples were then weighed using a high precision set of scales. Measured weight was then compared against both the nominal weight provided by Solidworks using the material density of Ninjaflex,1190 kg/m^3 and the theoretical weight (m) calculated using equation 4-2, where ρ^b is base material densty, V is sample volume [40,231].

$$m = \frac{2tV\rho^b}{L}\left[\frac{1}{\frac{\Gamma}{\Delta}-1}\sqrt{1+\Gamma^2+[tan\,(\alpha)]^2}+\frac{1}{1-\frac{\Delta}{\Gamma}}\sqrt{1+\Delta^2+[tan\,(\alpha)]^2}\right] \quad 4\text{-}2$$

$$\Delta = tan\left(\frac{\beta}{2}\right) \quad 4\text{-}3$$

$$\Gamma = tan\left(\frac{\gamma}{2}\right) \quad 4\text{-}4$$

Finally, ten measurements of wall thickness were taken at random locations across both sides of the sample using a set of Vernier callipers. Due to the elastic properties of TPU, callipers were pinched into the walls and then allowed to relax before measurements were recorded. Average wall measurements were compared to the designed thickness and other manufactured samples. This comparison was aided via the use of both simple scatter plots and the construction of Bland-Altman plots. These plots allowed for an assessment of both the correlation between designed values and those measured from manufactured samples, as well as the agreement between the two data sets. Bland-Altman plots were constructed using a 95% prediction interval.

To ensure the validity of the optimisation array parameter levels needed to be consistently spaced, therefore if all samples were a consistent difference from their designed value then the whole array could still be considered to be valid.

4.2.2.4. Samples of Contemporary Materials for Comparison to MOM.

The change in boundary conditions between the manufactured pads of isolated MOM geometry and a complete helmet system meant that comparison between the two data sets might have been misleading, despite efforts in the design of the impact methodology, discussed in section 4.2.4. Therefore identically sized samples of contemporary helmet liner materials were required to provide comparison data from identical loading environments. Additionally, this data set would enable the assessment of the impact methodology's accuracy by comparing the accelerations recorded from pad-based testing to the performance reported in the literature.

The two helmets, a Rawlings Impulse and a Riddell Speed(Riddell, USA) were selected from the NFLPA's list of approved helmets, with the Riddell helmet being representative of a recommended helmet and the Rawlings being representative of banned helmets that still passed the NOCSAE performance standards [360]. Samples were cut from the centre of the helmet's front pad. This section of foam was used as it comprised the single largest piece of foam in each helmet and thus a 60mm by 60mm sample area was maintained. The 60mm by 60mm area was measured on the outside surface of these pads, and cuts made radially through the material, with a scale. The foam samples were allowed to rest at least 24 hours before any test was conducted post cutting to allow the foam to relax fully.

4.2.3. Quasi-Static Testing Methodology.

Compressive quasi-static loading was utilised to gain understanding into the MOMs ability to absorb energy as well as identify densification strain (ε_d) and Poisson's ratio of the structures developed.

4.2.3.1. Quasi-Static Protocol.

Compressive loading was carried out using a Zwick Z50 (ZwickRoell, Germany) uniaxial testing machine equipped with a 50kN load cell in line with the crosshead's centre. Samples were positioned between two parallel plates aligned with the centre of the load cell. Contact surfaces were left as bare metal with no effort made to increase or decrease frictional contact, consistent with the impact equipment used. While this differs from the curved and compliant boundary conditions the material would experience if tested as part of a full helmet, efforts were taken to simplify conditions so that material performance, and therefore the significance of geometrical parameters, would be less obscured by other factors influencing performance.

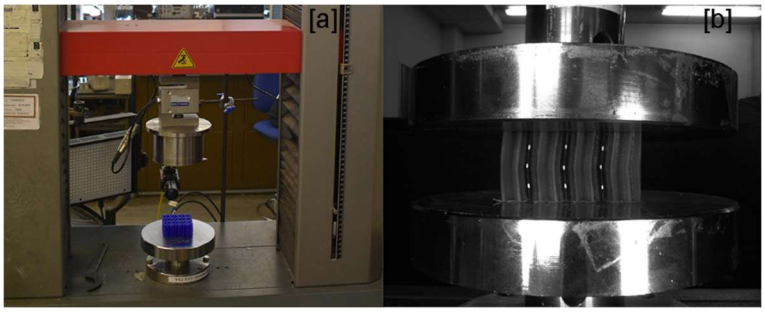

Figure 4-3: Setup of MOM sample in the uniaxial test machine showing Imetrum Camera placement for recording lateral strain [a]. And close up of Sample showing placement between closed plates [b].

The load cell was zeroed between samples to ensure that changes in excitation voltage due to cycling of test equipment did not affect results. Samples were compressed to a preload of 5N to ensure proper contact had been made between the compressive plates and sample geometry. With preload established samples were compressed to 50% compressive strain, 12.5mm, at a displacement rate of 50mm/min.

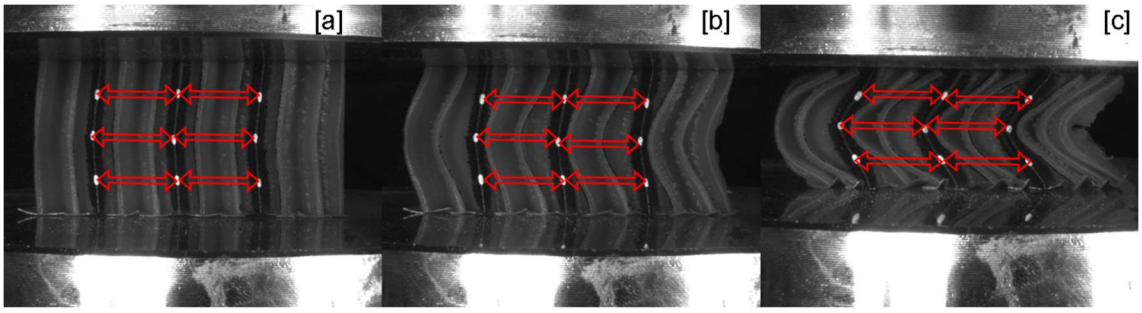

Figure 4-4: Array of dots used to track lateral strain. The image has edited exposure to show the MOM structure better. Original exposure was set to maximise the contrast of tracking dots. Redd arrows represent tarking of software before compression [a], start of compression [b] and nearing compleasion of compression [c].

To allow for calculation of Poisson's ratio, the lateral strain of samples was captured using non-contact video extensiometry. The use of this technique required marking of samples with a three by three array of dots so that virtual strain gauges could track the geometry, Figure 4-4. The array was positioned on prominent ridges so that tracking of the dots was captured successfully throughout the range of compressive strain utilised.

The lateral strain was recorded using an iMetrum CAM028 (iMetrum, Bristol, UK) video strain gauge (VSG) at a refresh rate of 15Hz. To ensure that compressive force and both lateral and compressive strains were captured simultaneously, the Z50 was linked to the VSG.

4.2.3.2. Data Handling.

Quasistatic data was used to calculate engineering stress using the consistent area of $0.0036m^2$ across all samples, with compressive strain calculated from crosshead displacement and sample depth, 25mm.

The three lateral traces captured for each sample were reviewed and complete traces, where the camera did not lose a tracking point, were averaged to provide a single measurement. This data set was converted from the captured percentage values into m/m to be consistent with the captured compressive strain. Strains were normalised so that positive compressive strains represented a reduction in sample depth, and positive lateral strains reduced sample width.

For each sample, densification strain was taken as the value of compressive strain at which lateral strain reported its maximum value. Due to the auxetic nature of the MOM geometry, it was theorised that the point of maximal lateral strain would represent the point at which base material response to compression would override the geometry

response. This would only happen when the geometry could no longer contract under compression due to cell walls contacting and thus be the point of densification.

The instantaneous Poisson's Ratio (IPR) was calculated using equation 4-5, providing a metric for quantifying the effects of the geometrical parameters on the MOM's auxetic properties.

$$\nu_n = \frac{\varepsilon_{ln}}{\varepsilon_{cn}} \quad 4\text{-}5$$

4.2.4. Impact Methodology.

This subsection covers the proposed testing methodology that would be used to optimise the MOM geometry to the impact environment of American football.

4.2.4.1. Impact Method

All impacts were conducted using an Instron Dynatup 9250 HV (Instron, USA), a spring-loaded linear impactor whose impact mass was guided by two solid rails. Impact events were measured using a 500g linear single-axis accelerometer (060-f482-08, Honeywell, USA) that was securely attached to the drop mass. The accelerometer was connected to a StrainStart® 9000 (Micro Measurements, USA) data acquisition system sampling at 50 kHz as so to provide the fullest picture of the impact pulse. Between impact tests, the input signal to the data acquisition system was zeroed to ensure continuity of collected data.

Three distinct impact velocities had been identified as being associated with the onset of SRC in American football players, 9.3ms^{-1}, 7.4ms^{-1} and 5.5ms^{-1} [17,84]. The use of a linear impact rig meant that the complex kinematics of an onfield head impact, where both the player's body and head have a full six of degrees of freedom to expend impact energy, could not be accurately copied. Therefore, a reduction in impact energy was required to recreate the American football impact environment accurately.

Recreations of on-pitch impacts have shown that the heads of struck players effectively undergo a one-dimensional change in head velocity during impact [84]. This one-dimensionality allows for the linear impact rig to recreate these conditions. As a change in head velocity in injurious impacts has been shown to be approximately 60% of the impact velocity, the identified impact velocities were multiplied by a factor of 0.6 [84]. This reduction provided testing velocities of 3.30ms^{-1}, 4.44ms^{-1} and 5.58ms^{-1}.

Although it has been shown that football players are capable of recruiting significant body mass into in-play impacts, the limitations of the test rig meant that the impact mass had to be carefully considered [50]. As the limitations of the impact rig allowed for recreation

of the head kinematics only, impact mass was selected to be representative of the headforms used to assess the performance of AF helmets. As such, an impact mass of 4.8kg was utilised for all test impacts [211]. The Instron's impact mass was made up of a low weight cage (2.2 kg), two low friction drop guides (0.7kg), accelerometer attachment plates and impact surface (0.9kg), spacer blocks (0.2kg) and an additional mass block (0.8kg), all of which were tightly secured to the cage. The impact cage was checked between impacts to ensure all components were secure and not inducing vibrations, which would have presented as spikes of noise in the captured voltage-time data that would have influenced the calculated acceleration values.

For validation of the experimental design, testing of the MOM was only conducted at the lowest velocity as this would provide sufficient data to identify the presence of interactions and the suitability of both parameter ranges and base material choices. The foam samples were tested at all identified velocities so that the response could be compared to American football helmets' previously reported performance [21,22]. If the reductions in impact velocity and mass had successfully accounted for the limitations in the impact rig, in comparison to real-world conditions, test data from the foam samples would be expected to be consistent with reported behaviour of similar liners within the literature. Repeat impacts were 75 ± 15 seconds apart, consistent with helmet testing methodologies, with three impacts conducted for each sample [184].

A large steel block was securely attached to the base of the rig in line with the impact mass to act as an anvil. A test area was marked on the anvil to enable consistent placement of samples, and all samples were impacted under the centre of the load. Test samples were held loosely to the anvil with a piece of tape, which allowed for the sample to deform as usual but prevented the sample from rebounding out from underneath the impact mass, which would result in the mass colliding with the anvil and damaging test equipment.

4.2.4.2. Data Handling.

Raw impact data was reduced to a 30ms period around the recorded peak linear acceleration value (PLA), with 10ms of data before the peak and 20ms after. The reduced impact data was passed to Abaqus (Dassault Systèmes, France) where a Butterworth filter with a cut off frequency of 1000Hz could be applied. This smoothing algorithm is the standardised method present in the NOCSAE helmet testing methodology as an accepted method of removing excess noise [184,361]. Smoothed data sets were passed through Excel, where the first acceleration value exceeding 4g was placed at 1ms for all impacts.

4.2.5. Investigation of Structure Performance

This subsection covers how both quasi-static and impact test data was analysed to calculate key performance metrics. The values for these metrics were then used to analyse the L9 array and gain insight into the structure's performance.

4.2.5.1. Calculation and Identification of Performance Metrics.

Captured quasi-static compression data was used to calculate the normalised stress response of the L-series samples, using equation 2-10, repeated below. The value of E^b was taken as the reported value for the material, 12MPa, [40].

$$\tilde{\sigma}_{\varepsilon_n} = \frac{\sigma_{\varepsilon_n}}{E^b} \qquad 2\text{-}10$$

Using the captured quasi-static compression data, both the volumetric energy absorption and normalise energy absorption values were calculated using equations 2-6 and 2-7. Energy absorption efficiency was also calculated, using equation 2-9, so that the validity of using maximum lateral strain as densification strain could be assessed.

$$W_{\varepsilon_n} = \int_0^{\varepsilon_n} \sigma d\varepsilon \qquad 2\text{-}6$$

$$\widetilde{W}_{\varepsilon_n} = \frac{W_{\varepsilon_n}}{\rho_c} \qquad 2\text{-}7$$

$$\eta_{\varepsilon_n} = \frac{1}{\sigma_{m\varepsilon_n}} \int_0^{\varepsilon_n} \sigma d\varepsilon \qquad 2\text{-}9$$

As this study was conducted to validate the material and experiment choices made before optimising the MOM geometry, only a simplistic examination of impact data was required. Peak linear acceleration (PLA), the maximum acceleration reported by any sample in its data set, was identified as the best metric to enable this initial examination. Although this would not allow for any examination of parameter influence over impact duration, this was to be accounted for in the optimation process via calculation of GSI.

4.2.5.2. Reduction of data.

The Taguchi array allows for a single value per sample to be considered for analysis. Although simple arithmetic means would have achieved this, it would provide no insight into the consistency of a sample, as expressed by the variance of a sample around its mean result. To ensure that both sample performance and consistency were considered, PLAs were used to calculate the mean square difference (MSD) of each tested geometry using equation 4-6, where n is the number of datapoints and x_i is the ith data point.

$$MSD = \frac{\sum_{i=1}^{i=n} x_i^2}{n} \qquad 4\text{-}6$$

For example, consider two data sets of peak acceleration results of two hypothetical samples from five impacts, Table 4-4.

Table 4-4: PLA of two hypothetical samples.

Impact	Sample A	Sample B
1	70	61
2	40	59
3	60	60
4	50	58
5	80	62

While both samples have a mean acceleration of 60g across five impacts, Sample A shows greater variation in performance and thus would be less suitable for use as an energy absorber as its response is less predictable. The Use of MSD expresses this better where the value for sample B,3602, is lower than that of sample A, 3800. The lowest best methodology was used to manufacture a sample with the lowest accelerations to reduce injury risk.

From the MSD, a signal to noise ratio was calculated (S/N) to scale the results for ease of data manipulation, using equation 4-7. This calculation also meant that in an increase in sample performance, a reduction in PLA or head injury metric would be linked to an increased S/N ratio.

$$S/N = -10 \cdot \log_{10}(MSD) \qquad 4\text{-}7$$

4.2.5.3. Analysis of L9 Array.

To establish the influence of the selected geometric parameters and, therefore, the validity of the identified ranges used in this study, each parameter's main effects plots were developed. Initially, the mean response of all samples was calculated to provide a population baseline for the variation in response induced by each geometric parameter to be compared against.

To calculate the variation in response generated by each parameter, samples were grouped by parameter level for the parameter studied, and the average S/N value was calculated. For example, the average response of having an α of 5° would be calculated from the S/N values of samples L1, L2 and L3.

This grouping procedure was carried out for each parameter level in turn, with the average S/N plotted against parameter level. The mean response of all samples is also plotted so that the average response of each parameter level can be placed into context, and comparisons can be drawn between geometrical parameters. This plot allowed for a qualitative assessment of parameter influence with a sample exhibiting a horizontal trend across its predefined range assumed not to influence sample performance. Conversely, a parameter exhibiting significant variation around the mean would be assumed to influence sample response significantly. An example means of means plot for a study consisting of two parameters, A and B, each with two levels is shown in Figure 4-5.

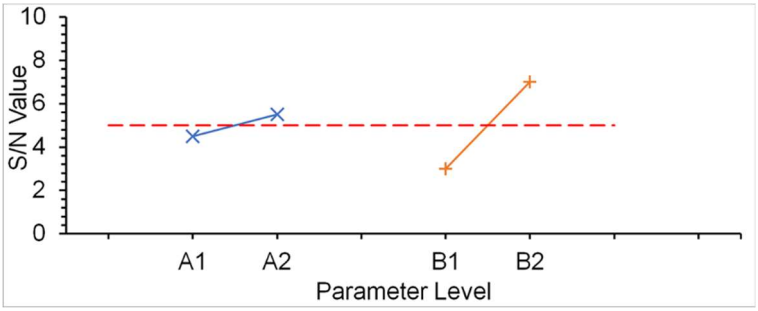

Figure 4-5: Main effects plot for an example study. Showing the mean of all samples (Red) and parameter response lines of Parameter A (Blue) and Parameter B (Orange). Parameter B can be seen to have more significant influence over the response of the samples as the difference between the maximum, and minimum response is larger than that of parameter A. If the study aimed to maximise sample response, the plot suggests that A2 and B2 selection would be optimal.

The mean of means plot also enables examination of the relationship between parameters and the examined response. This relationship can show if maximum performance may be gained by extending or moving the range of parameter values examined. When 3 level parameters are plotted, observed trends may be linear or quadratic in nature, allowing for a better examination of complex geometries.

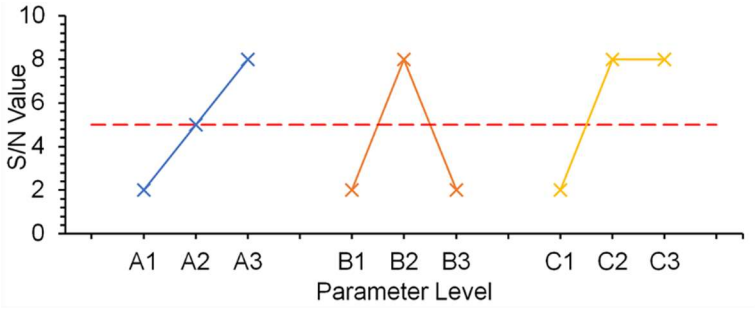

Figure 4-6: Main effects plot for an example study. Showing the mean of all samples (Red Dashed) and parameter response lines for parameter A (Blue), parameter B (Orange) and parameter C (Yellow). If the study aimed to maximise sample response, the plot suggests that A3 and B2 selection would be optimal. For Parameter C, the optimal choice may exist between levels 2 and 3 as these have the same value. For Parameter A, the trend suggests that further performance may be gained by extending beyond level A3.

Surface plots were used to identify the presence of interactions between the geometrical parameters selected for the study. Given two parameters with three levels, nine possible combinations of these parameters could be developed. For each combination, all samples' responses with the combination were averaged, providing 9 data points for each interaction. The surface plot generated by the nine data points described the nature of the relationships between the two parameters studied. A surface with parallel contours denoted no interaction between two parameters, meaning that the effect of varying one parameter did not affect the response of the other, Figure 4-7 [a]. Weak interaction would exhibit as the contours diverging, but an overall slope direction maintained such that one side of the surface is consistently higher than the other Figure 4-7 [b]. Strong interaction exhibited as a complex surface with no consistent directionality to the contours on the plot Figure 4-7 [c].

For the interaction plots, scale values were back-calculated from the range of S/N ratios calculated for the samples, as this allowed for discussion of inter-parameter relationships in terms of acceleration values.

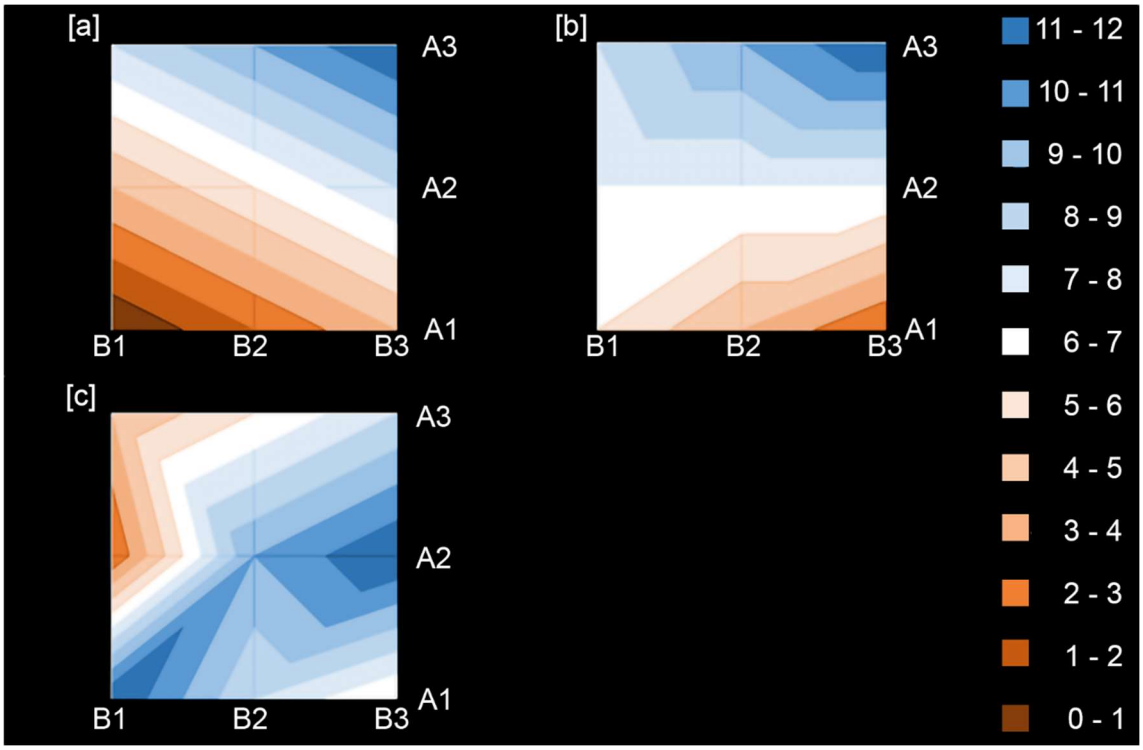

Figure 4-7: Surface plots for interactions between dummy parameters A and B showing [a] no interaction denoted by parallel lines, [b] weak interaction were the contours of the surface gradually converge and [c] strong interaction where complex surface geometry emerges, and the effect of one parameter on the other can significantly influence performance.

4.3. Results

4.3.1. Accuracy of Manufactured Test Samples.

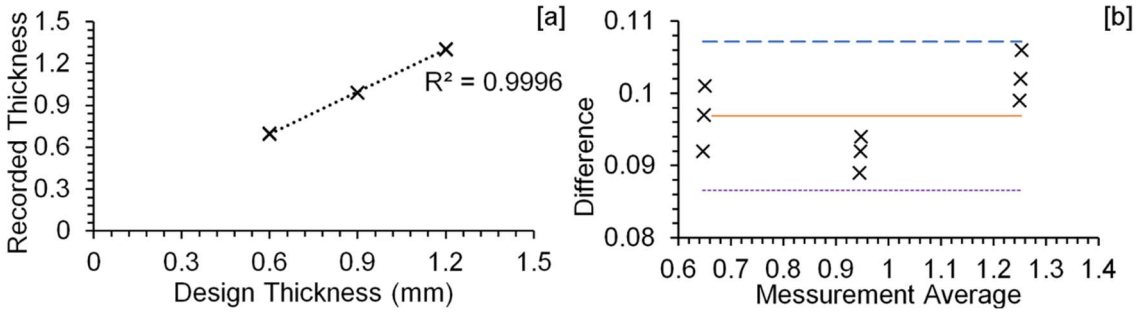

Figure 4-8: Designed wall thickness vs Manufactured component accuracy expressed as a simple scatter plot [a], and Bland-Altman plot [b], with the mean difference (solid Orange), Lower agreement limit (Purple Dotted) and Upper agreement limit (Blue Dashed)

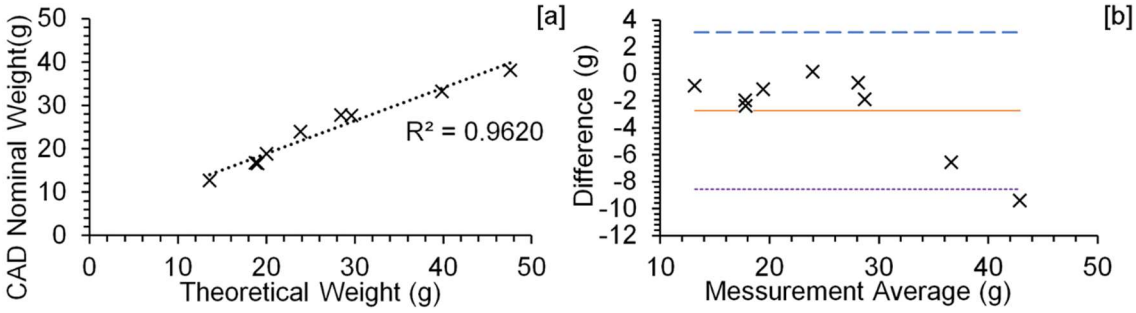

Figure 4-9: Sample weight estimated by CAD vs Theoretical weight expressed as a simple scatter plot [a], and Bland-Altman plot [b], with the mean difference (solid Orange), Lower agreement limit (Purple Dotted) and Upper agreement limit (Blue Dashed)

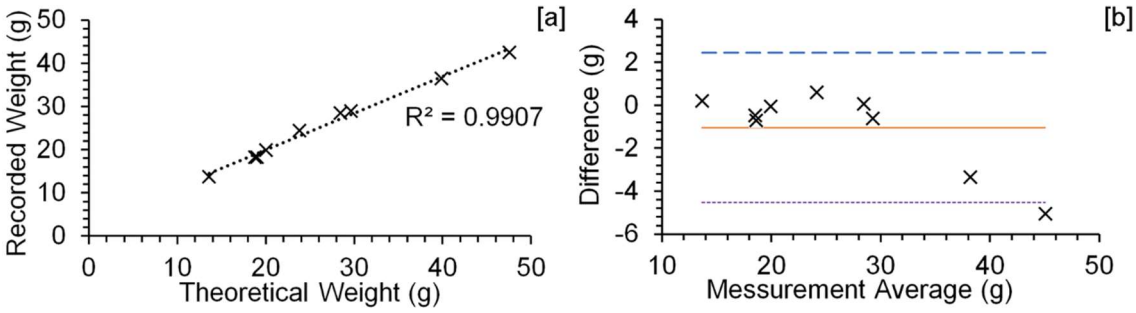

Figure 4-10: Measured sample weight vs Theoretical weight expressed as a simple scatter plot [a], and Bland-Altman plot [b], with the mean difference (solid Orange), Lower agreement limit (Purple Dotted) and Upper agreement limit (Blue Dashed)

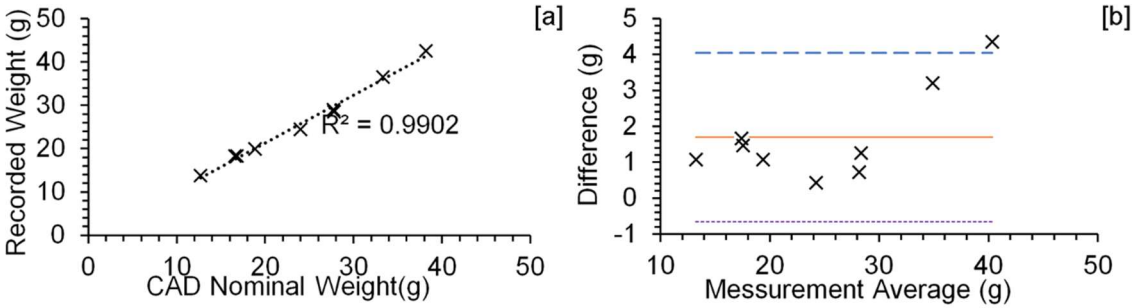

Figure 4-11: Measured sample weight vs Sample weight estimated by CAD as a simple scatter plot [a], and Bland-Altman plot [b], with the mean difference (solid Orange), Lower agreement limit (Purple Dotted) and Upper agreement limit (Blue Dashed)

Measured wall thickness offers both a high degree of correlation and agreement with the designed wall thickness, Figure 4-8. However, some variation in the agreement is noted between sample groups, with 0.9mm wall samples having less difference between design and measurement, while 1.2mm samples typically have a higher difference between the two.

Theoretical sample weight consistently over-estimates actual sample weight when compared to CAD nominal, Figure 4-9[a], and recorded weight, Figure 4-10[a], limiting its use as a metric of quality. Recorded sample weights are consistently above the nominal weight provided by CAD, with the same pattern of good agreement for all but the heaviest two samples, Figure 4-11.

Although good agreement is seen for the majority of samples, Figure 4-9[b], Figure 4-10[b] and Figure 4-11[b], two samples from the group report significant differences between the theoretical weights and both CAD-based estimations and recorded values.

4.3.2. The response of MOM to quasi-static compressive loading.

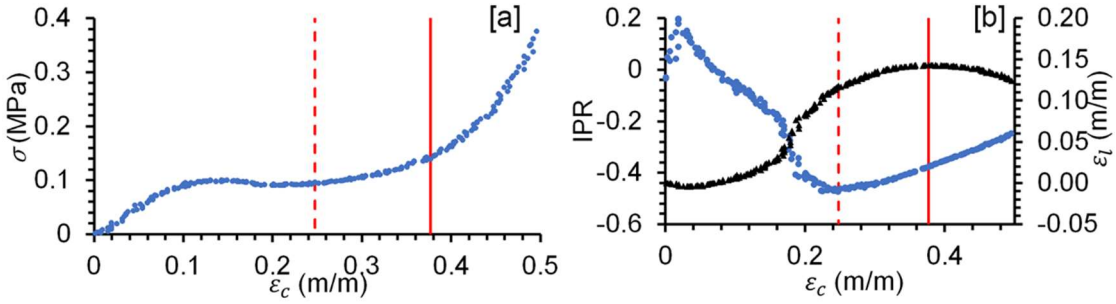

Figure 4-12: Compressive stress (σ) vs compressive strain (ε_c)[a], lateral strain (ε_l)(black triangles) and instantaneous Poisson's ratio (IPR) vs compressive strain [b] for sample 3_N with strain at the onset of densification (red dashed line) and densification strain (solid red line).

The stress-strain response exhibited by the developed MOM geometries is consistent with the classic behaviour of cellular materials, with a rapid rise in reported stress to a plateau followed by another rise in stress once densification is reached, Figure 4-12 [a], [19]. Two notable transition points were exhibited in the recorded data, the compressive strains at which the minimum value of IPR (ε_o) and maximum lateral strain is reported ε_l. The value of ε_o was consistently below both the value of ε_l and strain of maximum efficiency (ε_η) for all samples, Figure 4-13. Given that this point represents the slowing of contraction, it was suspected that at this point, initial cell wall contact is made, which would provide resistance to further cell contraction.

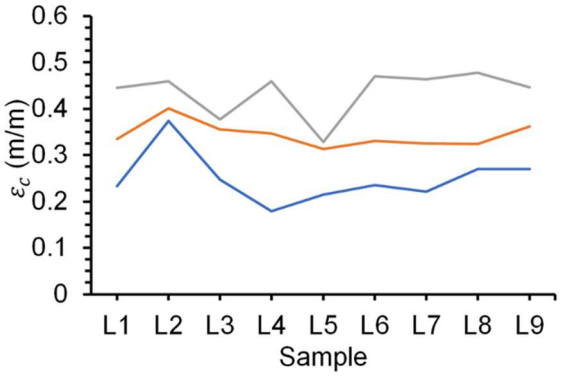

Figure 4-13: Compressive strains for minimum IPR (blue), maximum efficiency (orange), and maximum lateral strain (grey)

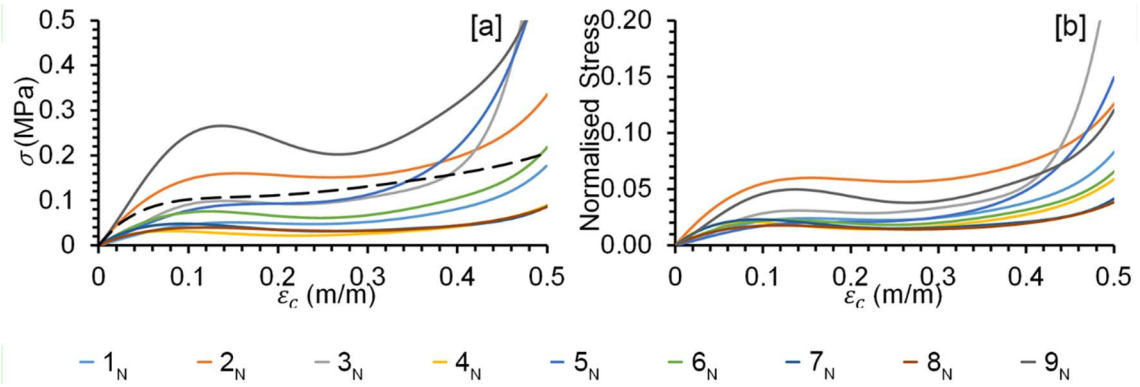

Figure 4-14: Compressive stress vs compressive strain [a] and normalised stress vs compressive strain [b] for all tested geometries, with material data for the Riddell foam for reference [364].

A wide range of stress values was calculated for the developed geometries, with an eightfold increase in stress between the weakest and strongest components. Several samples exhibit a notable drop in the reported compressive stress between strain values of 0.1 and 0.2m/m, Figure 4-12 [a], rather than the strain stiffening response reported for other auxetic materials [25,268,270]. The majority of developed geometries report a weaker response than that of the Riddell foam with two samples, 2_N and 9_N seemingly being responsible for the wide performance window. When the normalised stress response, which accounts for the influence of base material modulus and part density, is examined variation is further reduced, with 2_N providing the stiffest response for its weight, Figure 4-12 [b].

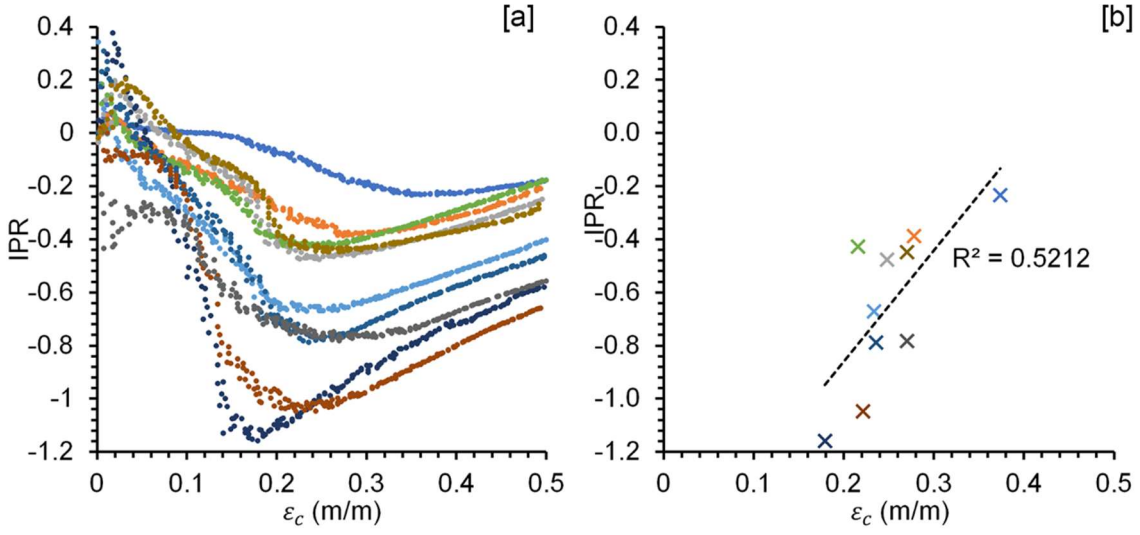

Figure 4-15: IPR vs compressive strain for [a] all tested MOM samples, [b] points of minimum IPR vs compressive strain.

The developed geometries exhibit a wide range of auxetic behaviour, with considerable variation between samples, Figure 4-15 [a]. At higher compressive strain values, 0.4 – 0.5m/m, all samples exhibit a consistent upwards trend in their calculated IPR values. There is a potential relationship between the minimum IPR of a sample and the value of compressive strain at which it is recorded, Figure 4-15 [b]. This suggests that the extent of auxeticity that a given sample exhibits inherently limits the amount of compression that a sample can undergo, increasing the peak acceleration reached.

Table 4-5: Calculated volumetric and normalised energy absorption values for all MOM geometries.

	Volumetric Energy Absorption (kJm^{-3})			Normalised Energy Absorption ($kJkg^{-1}$)		
Sample	ε_o	ε_η	ε_l	ε_o	ε_η	ε_l
Baseline	39.41	50.18	60.89	0.13	0.166	0.201
Riddell Foam	-	652.03	-	-	3.84	-
N1	9.14	14.35	22.95	0.043	0.068	0.109
N2	52.19	57.29	70.22	0.197	0.216	0.265
N3	18.83	30.51	33.35	0.060	0.097	0.191
N4	4.59	8.73	13.73	0.030	0.058	0.091
N5	14.48	24.47	26.33	0.033	0.055	0.059
N6	13.94	20.2	35.62	0.042	0.061	0.108
N7	8.38	11.74	17.93	0.040	0.056	0.086
N8	8.75	10.51	17.76	0.039	0.047	0.080
N9	53.85	74.6	101.99	0.102	0.141	0.193

The nine samples present a considerable variation in the calculated volumetric and normalised energy absorption at the three identified strains in the densification region. The proposed samples develop inferior energy absorption performance when compared to the Riddell foam data, Table 4-5.

4.3.3. The response of MOM geometry to dynamic loading.

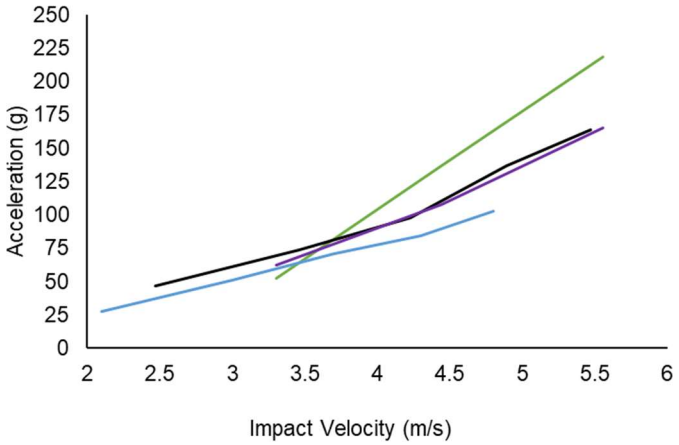

Figure 4-16: Peak linear acceleration vs impact velocity for Riddell (purple) and Rawlings (green) foam samples with values of a tested Riddell Revolution helmet (Black), and VN600 liner (Blue) reported in the literature [22,287].

The recorded values of PLA for the Riddell foam sample aligns well with the reported PLA values for comparable foam liners tested as part of a full helmet, Figure 4-16. Although Rawlings foam shows significantly worse performance as velocity increases, the close alignment of the Riddell foam throughout the velocity range suggests that the lowered impact mass utilised in this study was sufficient to overcome the difference in boundary conditions reduced material volume. Significantly higher or lower recorded accelerations would have suggested that the foam sample was being either overloaded or underloaded, respectively.

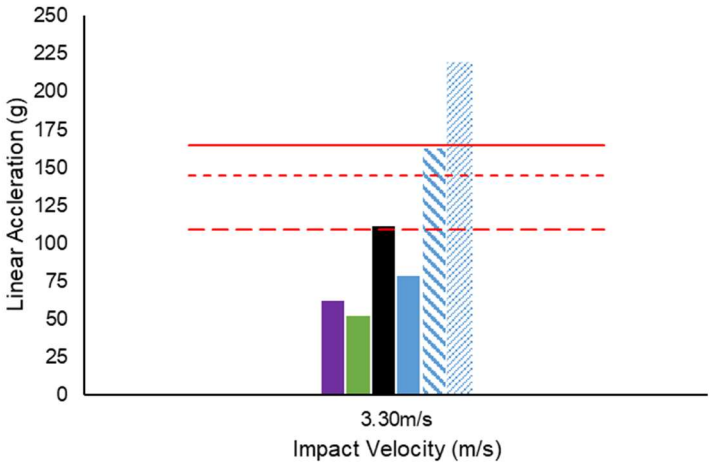

Figure 4-17: Peak linear acceleration vs impact velocity for Riddell foam (purple), Rawlings foam (green), Baseline geometry (black), most (solid blue) and least (thin blue diagonal) favourable L9 samples and average response of the MOM samples (thick blue diagonal), with 1 (red dash), 5 (red dot) and 10% (solid red) SRC risk.

Ninjaflex based MOM geometry demonstrates relatively poor performance compared to the foam samples at the lowest test velocity, with the average response of the nine developed geometries being close to the value of a 10% SRC risk, Figure 4-17.

Both the least favourable and baseline geometries exhibit significant densification, suggesting that most of the impact energy was not absorbed by deformation of the MOM geometry, Figure 4-18. In comparison, the most favourable geometry is closer in performance to the Riddell foam but exhibits dual peaks in recorded acceleration. This shape suggests a period of strain-softening before densification, in keeping with the sample's response to quasi-static loading.

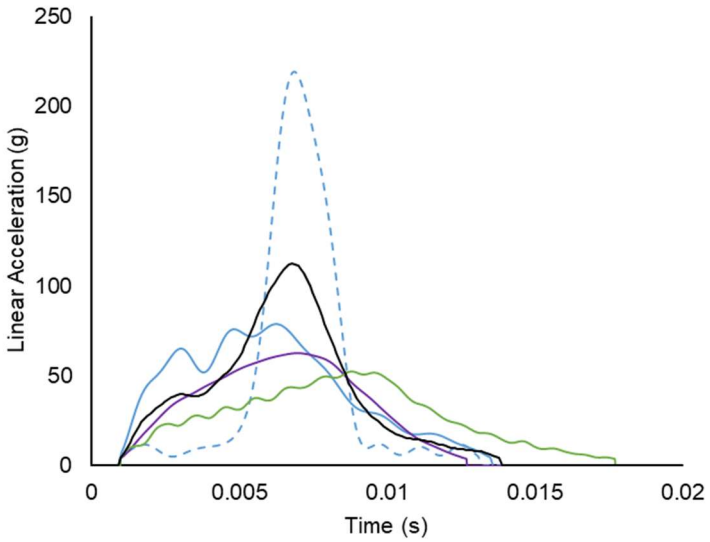

Figure 4-18: Average acceleration vs time for Riddell foam (purple), Rawlings foam (green), IRCOBI geometry (black), most (solid blue) and least (blue dashed) favourable MOM samples.

4.3.4. Analysis of L9 Array.

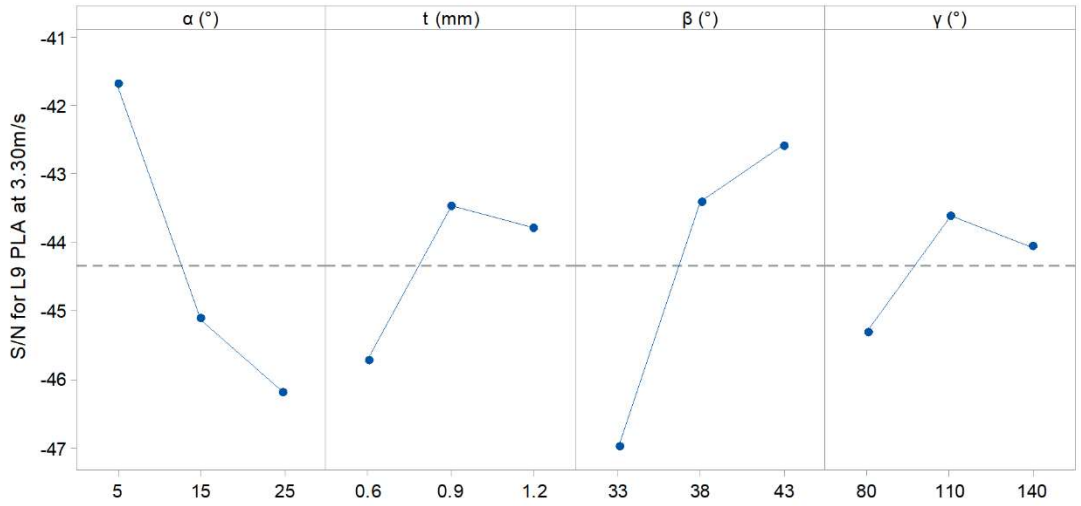

Figure 4-19: Main effects plot for PLA response at 3.30ms^{-1}. S/N scale equates to a PLA range of 112 to 224g. Grey dashed line represents the average response of all MOM samples.

All geometrical parameters show considerable variation around the mean sample response, suggesting that all parameters influenced the PLA response of a sample, Figure 4-19. Two of the fold angles, α and β, seem to exert more change in geometry response than wall thickness, which is dominant in informing the response of foam materials [19]. For two of the parameters, α and β, maximum performance is reached by minimum and maximum values, suggesting that the range of values for these parameters may not contain the value which represents absolute best performance.

Complex interactions between all four of the geometrical parameters are present when considering the PLA values, Figure 4-20. These interactions prevent further analysis of the structure in any meaningful way, as their exact contribution to the structure cannot be ascertained due to the limitations of the L9 array.

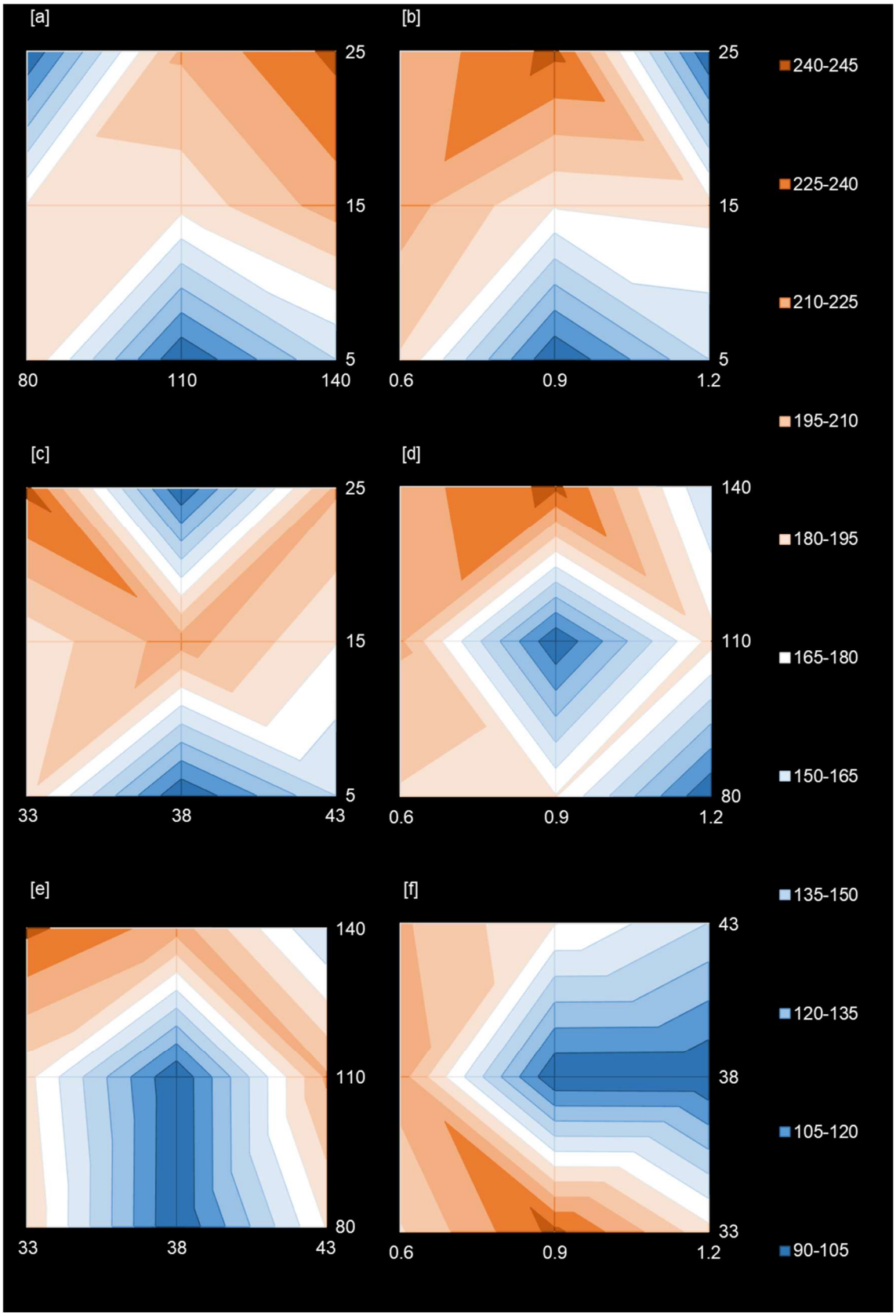

Figure 4-20: Interaction Plots for L9 Samples S/N for 3.30m/s Impacts PLA, v – α [a], t – α [b], β– α [c], t – v [d], β – v [e], t – β [f].

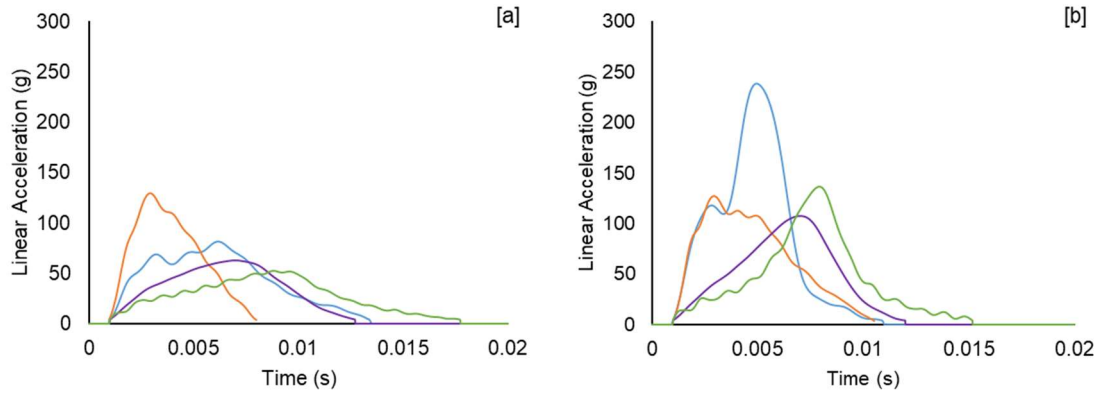

Figure 4-21: Acceleration vs time for 2_N geometry produced in Cheetah (orange) and Ninjaflex (blue), at impact velocities 3.30m/s [a] and 4.4m/s [b]. Comparative traces from Riddell (purple) and Rawlings (green) foam.

Due to identified limitations in the chosen base material sample, 2_N was reproduced from stiffer TPU material and underwent testing across the full range of identified velocities. However, only data from the lowest and middle velocities are presented in this chapter as data had not been captured for the Ninjaflex variant at the highest velocity to avoid overloading the accelerometer and therefore damaging the impact rig, Figure 4-21.

4.4. Discussion

4.4.1. The validity of the experimental design.

Recorded weight of the L9 samples correlates exceptionally well with both CAD nominal and theoretical values, with R^2 figures over 0.99, Figure 4-9 to Figure 4-11. Recorded weight is consistently above the CAD nominal, with a weight increase of 1.69g ± 1.96g on average, representing a growth of 1.8 to 11.4% in mass depending on the sample. This growth was expected as the manufacturing method developed in chapter 3 was noted to over extrude material to ensure the manufacture of dense samples at a loss of geometrical accuracy, most notably in wall thickness.

The overall difference in wall thickness ranges from 0.09mm to 0.11mm, with an average absolute error of 0.01mm, which is less than one-third of the nozzle diameter used in the samples' manufacture and thus could be considered an acceptable level of manufacturing error. Therefore the spacing of sample groups is preserved, and as such, the analysis of the L9 array is not undermined [355].

Interestingly the developed equation, 4-2, for calculating the density of a MOM geometry consistently overestimated its mass when compared to both measured and CAD nominal, Figure 4-8. The developed equation generates a relative density based on the geometrical parameters of a given MOM sample and applies this to the sample's volume. Therefore, it does not account for incomplete geometry present at the edges of developed samples, and orphaned geometry that was removed during the CAD element of sample manufacture. For these reasons, the heaviest sample falls outside the limits of the agreement established the Bland-Altman plots.

The Riddell foam sample's identified response under the dynamic test environment is consistent with the reported performance in the literature, Figure 4-16 [22,287]. Both reported data sets use a different Riddell helmet, Riddell Revolution (Riddell, USA), than the one used in this study. However, these helmets appear to use a similar - if not identical - foam to the Speed helmet.

The similarity between these data sets and the recorded data for the Riddell foam suggests that the reduction factor applied to the impact velocity created an impact environment that provides representative data of material performance in full helmet conditions. Therefore, reported sample performance and subsequent optimisation efforts would provide geometries that should perform well when scaled up to replace helmet liners.

4.4.2. Variation in sample performance.

When subjected to compressive loading, the majority of developed MOM geometries exhibit a strain-softening response with resistive force decreasing during loading, Figure 4-14. This is consistent with variations of the structure previously reported [24,26]. The developed MOM geometries' response is remarkably similar to the posited response of a single cell under compression, Figure 4-14 [220]. This response is at odds with the reported performance of other auxetic materials, which have been shown to exhibit significant strain stiffening [212,362].

The difference in loading response may be due to the relatively few cells in the manufactured MOM geometries that limit the metamaterial's ability to act as a fully auxetic material. However, a single cell through the thickness of a sample was utilised to both better isolate the changes in parameters values from the influence of more complex boundary effects and to maximise print quality of the samples by keeping feature size of the geometry relatively large. As only a single layer of cells is present the metamaterial is limited to drawing in cells to only the lateral direction, whereas auxetic foams have been reported to draw in material radially around the impact site [212,362]. This, in turn, would limit the strain stiffening response of the material, allowing the single-cell response to be dominant. Alternatively, the MOM geometry has been noted to exhibit a type II response for values below 45°, and so the response seen here may be due to the bending and stretching dominated behaviour of material deformation [24].

Many of the developed samples reported positive IPR values at low values of compressive strain, Figure 4-15. This is unlikely to be caused by tracking errors within the VSG system as the system had been allowed to settle, and the consistent traces recorded suggest consistent tracking of the marks on the samples. The initial response of the MOM geometry under low strain rate compression is non-auxetic, suggesting interference in the folding mechanics of the geometry.

When the deformation pattern of the L series sample is observed, Figure 4-22, it is a significant departure from the folding pattern exhibited by previous examples of Miura-Ori based materials [26,31]. Two notable deviations are present. Firstly the chevron deformation appears unbalanced across the face of the cellular geometry with inner chevrons, to the right of Figure 4-22, appearing to have a more acute fold angle that the outer chevrons, to the left of Figure 4-22. Folding of geometry is also less localised to the edges present in the geometry, with the L-series samples presenting with more of a pronounced s-curve.

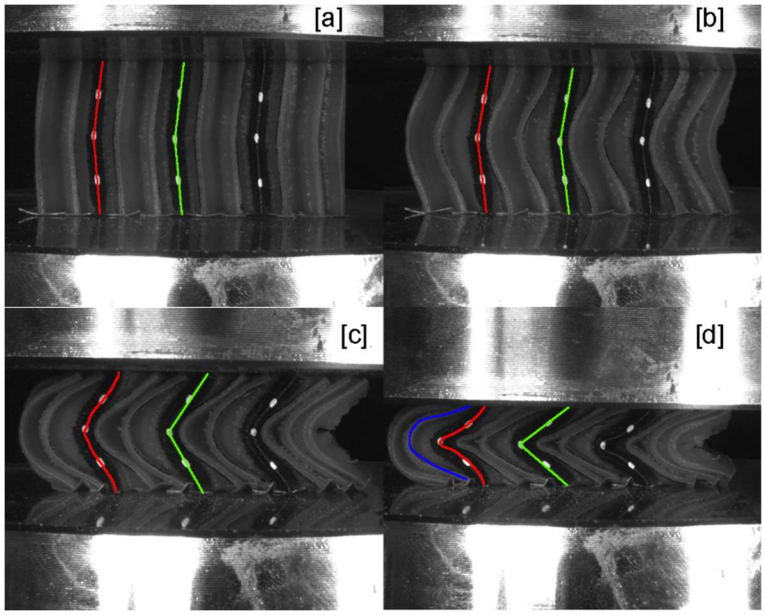

Figure 4-22: Deformation of the MOM under various sategs of compression. showing observed deformation pattern (red), and expected deformation pattern (green), before testing [a], start of compression [b] mid way through compression [c] and at the end of compression [d] where alternating tight and open (blue) curved deformation is exhibated.

No effort had been taken to limit the frictional interference between the top and bottom sample surfaces and the relevant surface of the Z50. This frictional contact may be responsible for both the different deformation and the initially favourable IPR exhibited by the L-series, by removing the contacting surfaces' ability to deform as intended. Although steps could have been taken to minimise friction, such as the use of silicone gel, in a practical application the MOM geometry would be contained within the helmet through the use of a flexible structure, similar to the foam pads. Thus, a frictional boundary condition can be expected to be present, and therefore the conducted testing is more representative of this than a low friction contact surface. Additionally, the boundary conditions used in the quasi-static testing of the geometry mimicked those of the present in the impact test rig. This similarity of boundary conditions eased the comparison of the data captured in both test environments.

The relatively thick walls of the TPU based MOM compared to the reported metal-based variants also could have affected the bending behaviour of the origami-based geometry, where the folding of the plates is less localised to fold lines in the geometry, Figure 4-22 [26,31,363]. The influence of both the boundary conditions and thick walls were considered to be acceptable trade-offs between sample behaviour and experimental accuracy.

At the initial impact velocity, the investigated ranges for the identified geometrical parameters appear to develop considerable variation in parameters response, Figure 4-19. The γ and *t* parameters presented with a maximum S/N response to the 3.30ms^{-1} loading appearing at their middle parameter level. This relationship indicated that the selected parameter levels were appropriate. However, minimising α leads to the vastly superior performance of MOM geometry in comparison to other parameter levels. In comparison, minimisation of β leads to significantly worse performance, Figure 4-19.

Comparatively both α and β present with significant shifts in performance at the extremes of their examined ranges, with a single point being responsible for the considerable variation seen, *Figure 4-19*. The response of α, where performance is improved by minimising the angle, is in keeping with the previous MOM investigation, where α was found to be of critical importance when optimising geometries [24]. Due to the apparent degradation in performance at larger angles the range of α values used in the optimisation process would need to be assessed before any optimisation effort could be conducted so that overall sample performance was not hampered. The value of β was constrained by two factors: the values of γ, and the resultant value of H from the relationship expressed in equation 4-1. Although the range of this parameter could have been narrowed such that the mid-level, 38°, became the lowest value studied, this may have eliminated the influence of this parameter on impact performance, such that it would have been effectively removed from the study altogether. As these conditions had not changed, it was decided not to alter the values of β used with the optimisation process, with the understanding that the presence of the 33° β level may influence the process.

4.4.3. Presence of Parameter Interaction.

Complex interactions between all geometrical parameters are exhibited for the PLA response of the developed geometries under dynamic loading conditions, Figure 4-20. The presence of these interactions makes continued use of the L9 array for the optimisation of the MOM geometry impossible as the array cannot accommodate the study of these interactions. As the presence of interactions is impossible to establish before an investigation, the L9 array had been chosen to minimise the number of samples with enough intersample design variation to examine parameter interactions. It must be noted that the surface plots generated to discover the presence of interactions used the minimal amount of data so the relationships presented in Figure 4-20 may not be an accurate representation of the actual interaction. However, sufficient data was gathered to rule out a lack of interaction which would have appeared even with the minimal data gathered.

4.4.4. Performance of developed MOM in comparison to the contemporary liner materials.

The L9 array produced a series of MOM geometry that exhibited a wide range of behaviour when exposed to both quasi-static and dynamic loading conditions. However, for the majority of samples, the performance of the structure is limited, in terms of energy absorption capability and dynamic performance. Under dynamic loading conditions, many samples exhibit signs of extensive densification, which makes any optimisation effort difficult as actual parameter influence on performance is obfuscated. The majority of developed samples perform unfavourably against both the tested foam samples and novel structure presented in the literature [21,22]. Although an increase in wall thickness may have been capable of increasing part performance, the poor performance of samples with *t* values of 1.2mm suggests that a large amount of additional wall material would be required to bring part performance to a comparable level of contemporary materials.

4.4.5. Alterations to experimental design.

To provide the required increase in sample performance, a new base material for manufacture was needed. A review of available TPU filaments highlighted Cheetah, as a potential replacement, providing higher material strength while retaining the flexibility and other material properties that made Ninjaflex an attractive choice, [40,344]. Due to the presence of interactions between the examined parameters and the required new range of α values, the tested samples were analysed for suitability as a new base geometry. By examining normalised energy absorption, 2_N was identified as a promising geometry capable of absorbing disproportionally large amounts of energy compared to other MOM samples, Table 4-5. Although 9_N had produced a lower PLA than 2_N at the lowest test velocity, 90.26g vs 91.12g, the sample had a relative density twice that of 2_N, 0.444 vs 0.222, meaning that the 0.95% loss in performance was deemed acceptable for the considerable weight saving. Comparative testing of the MOM geometry in an alternative TPU material demonstrated that significant performance could be gained at higher impact velocities, due to the stiffer base material. The Cheetah based component showed no sign of densification at the two presented impact velocities; however, this performance improvement comes at the cost of an increased PLA at the lowest test speed. At the $4.44ms^{-1}$ the Cheetah sample performs favourably against the two foam samples, while the Ninjaflex based sample shows clear evidence of densification. The exhibited performance of the Cheetah based sample suggests that its use as a base material for the optimisation process would yield data driven by sample performance rather than the densification driven data set of the L9 samples.

4.5. Conclusions.

To ensure that the process used to optimise the MOM would provide meaningful results, a validation study was conducted using a small series of samples. Exact sample geometries were specified by the use of an L9 Taguchi array with parameters and levels identified by a study of a single cell of the MOM. Comparison samples were gathered from helmets capable of meeting current standards. All samples underwent both quasi-static and dynamic testing. The results of these tests allowed for the validation of various features of experimental design. A list of the main conclusions of this study are as follows:

1. The identified geometry and examined ranges were found to generate extensive variation in both quasi-static and dynamic performance of the MOM geometry. Three of the parameter ranges were determined to be appropriate for further study, with the range of α angles being repositioned to focus around the lowest angle covered in this study, 5°, which had been linked to reducing PLA.
2. Complex interactions were discovered between all examined parameters.
3. The adapted impact methodology produced results from the foam samples that were comparable to the performance described in the literature. Acquired impact data can be assumed to be representative of sample performance in full helmet conditions.
4. Ninjaflex based samples performed poorly against both reported novel geometries and tested foam samples. However, switching base material to a stiffer TPU (Cheetah) yielded improved performance for identical geometry.

Chapter 5: Optimisation of the Miura-Ori Metamaterial to impact conditions related to sports-related concussions.

5.1. Introduction

The previous chapter validated some of the experimental processes to be used in the optimisation of the Miura-Ori Metamaterial (MOM). However, the experimental design's critical aspects, such as the base material, and the Taguchi array used to generate sample geometry, were deemed unsuitable.

This chapter presents the optimisation of the MOM using the adapted experimental design that addresses these concerns. The adapted design enabled a more in-depth exploration of the MOM's geometrical parameters. This allowed for a determination of the influence parameters had on the dynamic response of the MOM. The geometry had been chosen in part for the expanded performance range offered by its auxetic nature. Therefore, consideration was given to how samples responded across the loading conditions used in the study.

The expanded Taguchi array necessary for this study enabled the use of more complex statistical methods. The analysis that these methods provide aided the balance of parameter values to maximise the structure's performance, thus lowering injury risk.

This chapter's primary aim was to develop MOM geometries that minimised both PLA and GSI at each of the investigated impact velocities. These impact velocities used where a representative of those linked to on-pitch impacts, resulting in a player sustaining an SRC. Thus the reduction in recorded acceleration would represent a reduction in the risk of this category injury.

The work presented in this chapter had the following objectives:

1. Develop a robust set of test data suitable for use in identification of optimal geometry.
2. Establish the contribution to the performance that each identified geometrical parameter and their interaction had through the use of statistical processes.
3. Identify the combination of parameters that are capable of reducing the injury risk.
4. Compare the performance of the developed optimal geometries to existing head impact solutions.

5.2. Materials and Methods.

5.2.1. Test Sample Design.

The previous chapter established that only the levels for α required change for the optimisation effort, as the lowest level of 5° offered substantial performance improvement. To maintain the MOM geometry while maximising the design space, a lower level of 1° was specified. The Taguchi array required all levels of a parameter to be equally spaced, defining a maximum value of 9°. The finalised level values for all parameters used in this study are shown in Table 5-1.

Table 5-1: Finalised Level Values for Geometrical Parameters.

Parameter	Level 1	Level 2	Level 3
α (°)	1	5	9
γ (°)	80	110	140
β (°)	33	38	43
t (mm)	0.6	0.9	1.2

Due to the inclusion of parameter interactions, the available Taguchi arrays were reviewed for a three-level array with a minimum of ten columns. The L27 array was the smallest array that could accommodate the placement of the four parameters and the six interactions. The positioning of the parameters defines the placement of interactions within Taguchi arrays [355]. Thus, the placement of the geometrical parameters was carefully considered. The assigned column for each factor is displayed in Table 5-2.

Table 5-2:Column assignment of each factor and interaction in the L27 Orthogonal Array

Factor	L27 Column
α	1
γ	2
β	5
t	9
α - γ Interaction	3
α - β Interaction	7
α - t Interaction	8
γ - β Interaction	11
γ - t Interaction	12
β - t Interaction	13

To differentiate the results from the L9 samples, all developed geometries were given a label ranging from 1_C to 27_C, with the finalised array used for sample design presented in Table 10-1. Sample cross-section was maintained as a 60mm by 60mm square with overall sample depth increased to 30mm, a better representation of the thickness of the foam samples used for comparison.

5.2.2. Test Sample Manufacture.

All samples were designed and manufactured using the same software packages and equipment covered in chapters 3 and 4. As a new base material had been necessary to improve the performance of the MOM geometry, a new material profile was required. As both Cheetah and Ninjaflex were similar materials from the same manufacturer, the new profile was developed from the Ninjaflex profile established in chapter 3. Both Print Speed and Temperature were increased in line with filament manufacturer recommendations, Table 5-3, with other parameters remaining unchanged.

Table 5-3: Print Profile used to Manufacture Samples.

Print profile parameter,	Value
Print temperature	230°C
Print speed	2000mm/min
Layer height	0.1mm
Interior fill percentage	100%
Bed temperature	40°C
Outline overlap	50%
Infill extrusion width	125%
Extrusion multiplier	1.4
Minimum extrusion length	1mm
Minimum printing width	50%
Maximum printing width	200%
Allowed perimeter overlap	10%

5.2.2.1. Sample Quality Control.

Manufactured samples were assessed against the same quality metrics as the L9 samples, using the same techniques as discussed in chapter 4. Due to the previously discussed inconsistencies between the theoretical mass and manufactured mass, the Cheetah components' measured mass was only compared to the CAD nominal value.

5.2.3. Quasi-static Testing Methodology.

All L27 samples were subjected to the quasi-static loading regimes described in chapter 4. However, the decision was taken to increase the maximum compressive strain reached during testing to a value of 60% due to the relatively high densification strains captured for the L9 samples, so that the densification strain, taken as the strain of maximum lateral strain, was captured for all samples.

5.2.4. Impact Methodology.

The L27 samples were exposed to the full range of identified impact velocities. Impact data was captured and smoothed using the same process as discussed in chapter 4. However, the change in base material meant that the repeatability of MOM samples needed to be established. As the number of repeated impacts each sample is subjected to increases, the influence of experimental error over reported performance decreases. The Cheetah 2_N sample was subjected to seven repeat impacts at each velocity, with impacts spaced at 75 seconds.

PLA and correlation values to the first impact were generated for each subsequent impact to determine when a significant difference in sample performance occurred. At the lowest velocity, the sample exhibited a stable PLA after the second impact. However, at the middle and highest test velocities, PLA increased by over 10% by the 6th impact. Thus, the maximum number of impacts for each velocity was set at 5. Impact spacing was maintained at 75±15 seconds.

Tests were conducted at the reduced velocities presented in chapter 4, 3.30ms^{-1}, 4.44ms^{-1} and 5.58ms^{-1}, in ascending order, with a minimum of 24 hours rest for each sample. This rest period allowed each MOM structure to relax so that the first impact at each velocity could be considered independently of the previous testing.

5.2.5. Optimisation Methodology.

5.2.5.1. Optimisation Metrics

The literature presented two performance metrics that could be calculated from linear impact data sets. Peak linear accelerations thresholds had been identified for the risk of concussions [172]. To avoid an increase in impact duration from reduction in acceleration, the Gadd Severity Index (GSI) was chosen as a second metric. GSI was selected over HIC as it is still the accepted metric of the sole standard for football helmets [184,185,361].

$$GSI = \int_{t=0}^{t=t_{max}} a^{2.5} dt \qquad 5\text{-}1$$

Calculated using equation 5-1, the impact duration is identified as the length of time acceleration is above a value of 4g [361]. It must be acknowledged that lower values of GSI do not represent a proportional reduction in injury risk; a value of 300 does not carry half the risk of an impact with a score of 600.

The Taguchi array can only use a single value for each sample. The previous chapter had used a single PLA score to validate the design of the Taguchi array. However, this was unsuitable for the optimisation of the MOM as it would not allow for consideration of the range of impacts present in American football. Additionally, the sample optimised for single impact conditions using PLA and GSI may only offer superior performance at the design velocity, with substantially worse performance at the other impact conditions. Therefore, a weighted score was required. The weightings utilised in the Biocore testing methodology, discussed in section 2.6.3, were selected as a base for calculating a new metric, as it utilised the same base impact velocities identified for this study [195]. However, as the testing in this chapter was based on material samples rather than full helmets, the weighting factors were adjusted. As the MOM was intended to serve as an all-round protective material, the weighting factors presented in Table 2-3, were combined such that for each velocity, a single weighting factor had been determined. The weighting factors were applied to both PLA and GSI values for each sample using equation 5-2, where M is the currently examined metric.

$$3VS = 0.06737M_{3.3} + 0.04167\mathrm{M}_{4.44} + 0.05442M_{5.58} \quad 5\text{-}2$$

Although 3VS combined data from all investigated scenarios, its use may compromise a developed geometry's performance, as its performance would be balanced between low and high energy impacts. The MOM had been selected as its auxetic properties counteracting this issue via its strain stiffening response. However, to maximise the potential performance of the MOM, impact data captured for this study was used to develop a GSI and PLA optimal at for each velocity tested, producing eight unique optimal geometries.

Impact duration was not considered a standalone metric for optimisation, as pure reduction of value would increase the recorded accelerations, and therefore increases the risk of an athlete sustaining a head injury. However, the impact duration of developed optimal geometries would be considered as part of its performance.

5.2.5.2. Reduction of Data.

Both PLA and GSI values were reduced as per section 4.2.5.2, via the MSD and S/N values calculations, enabling objective performance analysis.

5.2.5.3. Performance metrics not used to optimise geometry.

Gathered data was used to calculate a range of metrics to inform the results of L27 samples and the optimisation process. To ease comparison between the L27 and foam samples an averaged acceleration time curve was developed from each sample at each tested velocity.

Each sample's stress-strain response under dynamic loading was calculated using equations 5-3 and 5-4. Where ε_x and σ_x are the stress and strain at $t = x$ and a is the acceleration value in ms^{-2}.

$$\varepsilon_x = \frac{\iint_{t=0}^{t=x} a\ dt}{0.03} \quad 5\text{-}3$$

$$\sigma_x = \frac{4.8a_x}{0.0036} \quad 5\text{-}4$$

Due to the chosen optimisation metrics, the process was sensitive to sample densification, which results in increased accelerations. To understand the influence of densification, the relative maximum strain (RMS) each sample reached under impact was calculated. This value compared the maximum strain (ε_{dmax}) a sample reached when impacted to its identified densification strain (ε_l) from quasi-static testing.

$$RMS = \frac{\varepsilon_{dmax}}{\varepsilon_l} \quad 5\text{-}5$$

When cellular material theory is considered, the lowest acceleration for a given impact comes from a material with the lowest plateau stress that does not reach densification. Thus, an ideal sample for an impact would be expected to report an RMS of one. An RMS value over one would identify a sample which has reached densification, and thus the base material would have greater influence over its performance. If the average RMS of all L27 samples was above one, the optimisation would be more limited in its scope as the importance of the geometry to performance was lessened.

Quasi-static compression data was used to calculate the normalised stress of the L27 samples, using equation 2-10. The value of E^b was taken as the reported value for the material, 26MPa, [344].

Volumetric and normalised energy absorption and energy absorption efficiency were also calculated from the quasi-static data using equations 2-6, 2-7 and 2-9 respectively.

5.2.5.4. Statistical Calculations and development of optimal geometries.

Both main effect and interaction plots were developed using the techniques discussed in section 4.2.6. These plots allowed for the identification of geometrical parameters and parameter interactions henceforth referred to as factors, that would maximise the performance of samples for each metric.

As the L27 array had not been saturated, an analysis of variance (ANOVA) was performed on the reduced data. This statistical analysis measures the effect of each studied factor on the observed variance in the results. By comparing each factor's variance to the residual variance, ascribed to experimental error, each factor's statistical significance and contribution to sample response could be determined.

Actual analysis was conducted using Minitab 18 (Minitab, Pennsylvania, USA), a statistical processing software. For clarity, the steps of the analysis are presented here.

Initially, a series of key data points are calculated: the degrees of freedom (DoF) of the experiment (f_T), DoF of each Factor ($f_1, f_2,,, f_g$) and the sum of all data (T). These values were then used to calculate the DoF of the experimental error (f_e) and the correction factor (CF) using equations 5-6 and 5-7.

$$CF = \frac{T^2}{n} \tag{5-6}$$

$$f_e = f_T - \sum_{x=1}^{x=g} f_x \tag{5-7}$$

For the L27 array, each factor has a DoF value of 2, and the number of experimental runs (n) is 27. For the L27 array, the value of f_T is 26, meaning that the DoF for the error term ranges from 6, when all factors are considered, to 24, when only one factor is considered.

As the target value for all metrics was zero, the sum of squares (S_T) of all results was calculated using equation 5-8, where Y_i is the recorded value of sample i.

$$S_T = \sum_{i=1}^{i=27} ({Y_i}^2) - CF \tag{5-8}$$

To calculate the sum os squares for each factor (S_g) the results of the L27 samples are first grouped by parameter level, with the sum of these groups calculated. For a generic factor with three levels, g, these values would be referred to as g_1, g_2 and g_3.

The sum of squares for each factor was then determined using, where N_{g_x} is the number of samples with level x of parameter g, and has a value of 9 when the L27 array is considered.

$$S_g = \sum_{x=1}^{x=3} \left(\frac{g_x^2}{N_{g_x}} \right) - CF \quad 5\text{-}9$$

The sum of squares of the error term is calculated using an adapted form of equation 5-7, where the f terms were substituted for the S terms calculated for each factor. The variance (V_g) of each factor was then calculated using equation 5-10.

$$V_g = S_g / f_g \quad 5\text{-}10$$

So long as the error term is non-zero, the variance ratio (F_g) for each factor can be calculated using equation 5-11.

$$F_g = V_g / V_e \quad 5\text{-}11$$

A factor is deemed significant if its variance ratio meets or exceeds a value from a standardised F-table. The comparison value is identified by the degrees of freedom of the factor and error terms, with the row in the table specified by f_e and the column by f_g. The value also varies by the confidence value of the analysis, with the value rising as confidence does. The relevant sections of the standard F-Tables for confidence levels of 90 to 99% are presented in Table 5-4.

Table 5-4: F-Value required for significance at given confidence levels [355].

Degrees of freedom of error term	F-Value for a given confidence level			
	90%	95%	97.5%	99%
6	3.463	5.143	7.260	10.925
8	3.113	4.459	6.060	8.649
10	2.925	4.103	5.456	7.558
12	2.807	3.885	5.096	6.927
14	2.727	3.739	4.857	6.515
16	2.662	3.634	4.687	6.226
18	2.624	3.555	4.560	6.013
20	2.589	3.498	4.461	5.849
22	2.561	3.443	4.383	5.719
24	2.538	3.403	4.319	5.614

To calculate the contribution of each factor (P_g), the sum of square value (S_g) is first corrected by the variance of experimental error, equation 5-12. This corrected term (S'_g) is then used to calculate the contribution percentage, equation 5-13.

$$S'_g = S_g - f_g V_e \quad 5\text{-}12$$

$$\mathrm{P}_g = 100\frac{S'_g}{S_T} \quad 5\text{-}13$$

An initial analysis was conducted for each optimisation metric with all factors considered. Factors the failed to reach significance at any confidence level were pooled with the error term. When a factor is pooled, it is removed increasing the values of S_e and f_e. The analysis is then repeated with the remaining factors, with pooling continuing until all factors were significant, or the value of f_e reached half the value of f_T inline with Taguchi's recommendations [355].

On completion of the ANOVA process, optimal geometries were developed for each of the eight identified metrics. Initially, the relevant main effects plot is reviewed, and parameter values that maximise performance are selected.

The selected parameters are then compared to the ANOVA results and Interaction plots. Factors that have been deemed insignificant at any confidence level are not reviewed, as altering them will not significantly alter performance. If an interaction was deemed to have a higher contribution than either one or both of its geometrical parameters by the ANOVA process, and the interaction plot suggested an alternative combination to improve performance, the relevant geometrical parameter was changed.

With the optimal geometries finalised, their performance was estimated using calculated statistics. The average performance of all samples ($\bar{T}$) and each parameter level were taken from the process used to generate the main effects plot. The estimated performance of an optimal geometry was calculated using equation 5-14, where $\overline{g_m}$ represents the average value of a generic parameter. The interaction was significant, and the interacting parameters were removed and replaced by the value of the interaction.

$$Opt = \bar{T} + \sum(\overline{g_m} - \bar{T}) \quad 5\text{-}14$$

Confidence intervals were calculated for these predictions to allow for the influence of experimental error. Firstly the number of equivalent replications (N_e) is calculated from the number of results (n) and the sum of the DoF of the factors used in the calculation of the estimate ($\sum f_{sig}$) using equation 5-15. This value is then used to determine the confidence interval using the variance of an experimental error (V_e) and a value form an F-table ($F(1, f_e)$) defined by the DoF of the error, equation 5-16.

$$N_e = \frac{n}{1 + \sum f_{sig}} \quad \text{5-15}$$

$$CI = \pm \sqrt{F(1, f_e) \cdot \frac{V_e}{N_e}} \quad \text{5-16}$$

Developed optimal geometries underwent the same testing regime as the L27 samples as described by this chapter, with all performance metrics calculated. The performance of the optimals was verified against the predicted performance. Reported performance outside the estimated range identified either an incorrectly manufactured sample or an issue with the developed geometry.

5.3. Results

5.3.1. Part Quality.

Before the L27 samples were tested, their build quality was validated. Recorded and nominal weight of the L27 samples followed the relationship established by the L9 samples, Figure 5-1. Heavier samples were typically more overweight than the lightest samples designed, Figure 5-1[b] which was not unexpected due to the increase wall thickness and reduced cell size found in these samples, which would make them more sensitive to the increased material extruded using the developed printing profile.

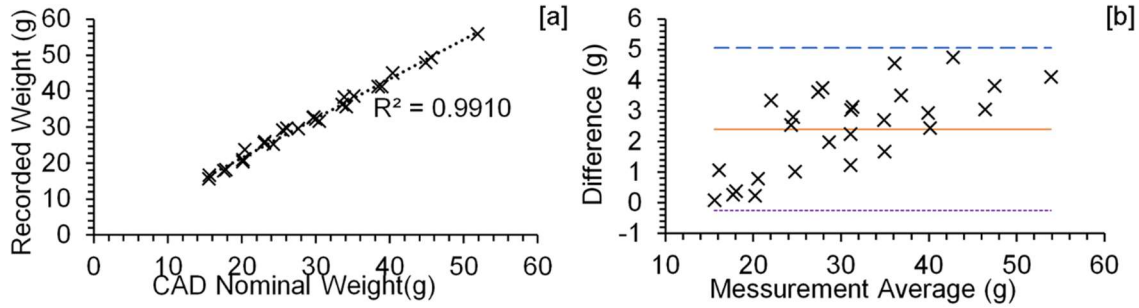

Figure 5-1: Measured sample weight vs Sample weight estimated by CAD as a simple scatter plot [a], and Bland-Altman plot [b], with the mean difference (solid Orange), Lower agreement limit (Purple Dotted) and Upper agreement limit (Blue Dashed)

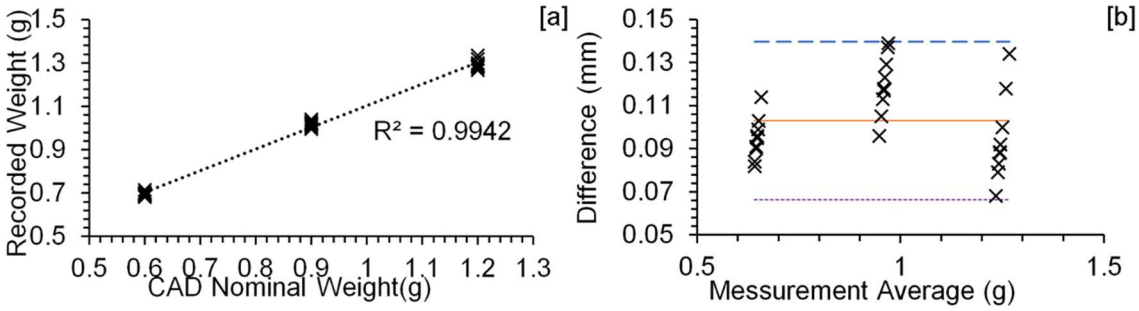

Figure 5-2: Measured wall thickness vs designed thickness a simple scatter plot [a], and Bland-Altman plot [b], with the mean difference (solid Orange), Lower agreement limit (Purple Dotted) and Upper agreement limit (Blue Dashed)

The 0.6mm sample group presents with the lowest variation in measured wall-thickness compared to the two other sample groups, Figure 5-2 [b]. The lowered variation resulted from the FFF process, which manufactured the 0.6mm walls with two extrusion paths, compared to the three paths used for both the 0.9mm and 1.2mm walls. The higher number of paths naturally increased the deposition of excess material for these sample groups, increasing their variance.

No alteration to the manufacturing process could overcome this limitation imposed by the slicing software. Therefore, it was decided to continue with the testing and analysis of L27 samples with the understanding that variation in wall thickness may influence the

results. Thus, the modified printing process can be assumed to provide a comparable level of quality to that used for the L9 samples, and error from manufacture can be assumed to be minimal.

5.3.2. The response of L27 to quasi-static loading.

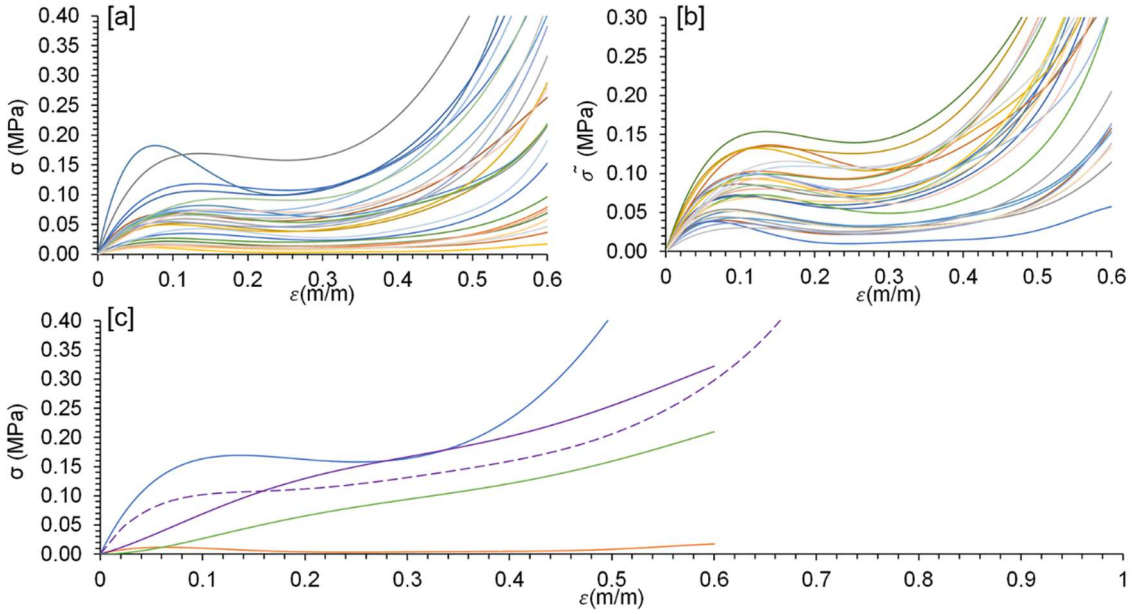

Figure 5-3: Compressive stress vs compressive strain [a] and Normalised Stress vs strain [b] for all L27 samples, and comparison of strongest (blue), weakest (orange) L27 Samples, Rawlings foams (green), Riddell foam sample (purple) and Riddell foam model (Dashed) [364] [c].

The L27 samples exhibited an extensive range of stress responses to the quasi-static loading conditions, Figure 5-3 [a]. Although two samples appear as outliers in pure compressive stress, when normalised stress is considered, sample variation appears consistent across the range of reported response, Figure 5-3 [b]. Since a dominant geometrical factor would form distinct groups within the response, the consistent distribution suggests that all examined factors contribute to performance. The strongest of the L27 samples produces a stiffer initial response and higher plateau stress that either tested foams or material model data Figure 5-3 [c]. The inconsistency between the tested Riddell foam and the material model data is due to the foam's curved form that was not removed by the preloading applied during testing.

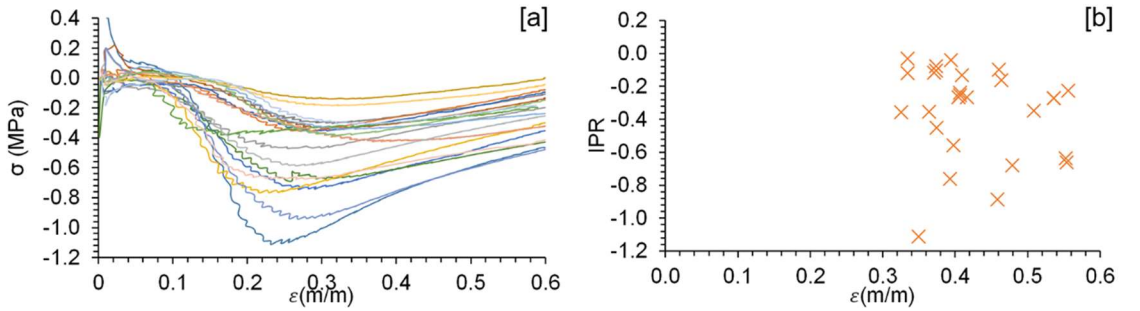

Figure 5-4: Instantaneous Poisson's ratio vs compressive strain for all samples [a], and minimum Instantaneous Poisson's ratio vs compressive strain [b].

The L27 samples IPR response follows the trend of the L9 samples, an initial downwards ramp to a minimum value before rising to a consistent upwards trend at higher levels of compressive strain, Figure 5-4[a]. Some of the L27 samples exhibit IPR trends close to a consistent value of 0 across the full range of compressive strain. Thus, the auxetic nature of the MOM is tailorable, and the potential benefit of auxetic materials is dependent on sample geometry.

The relationship between a samples minimum IPR and compressive strain seen in the results of the L9 samples, no longer hold for the L27 samples with no relationship shown, Figure 5-4 [b]. The lack of a definitive relationship removes a potential limitation to the performance of the MOM geometry, where an increased auxetic response would lower the densification strain, limiting the useable depth of the sample and thus increasing acceleration. The lack of this link between minimum IPR and the onset of densification allows for the leveraging of both the MOMs underlying auxetic nature and a pre-densification response.

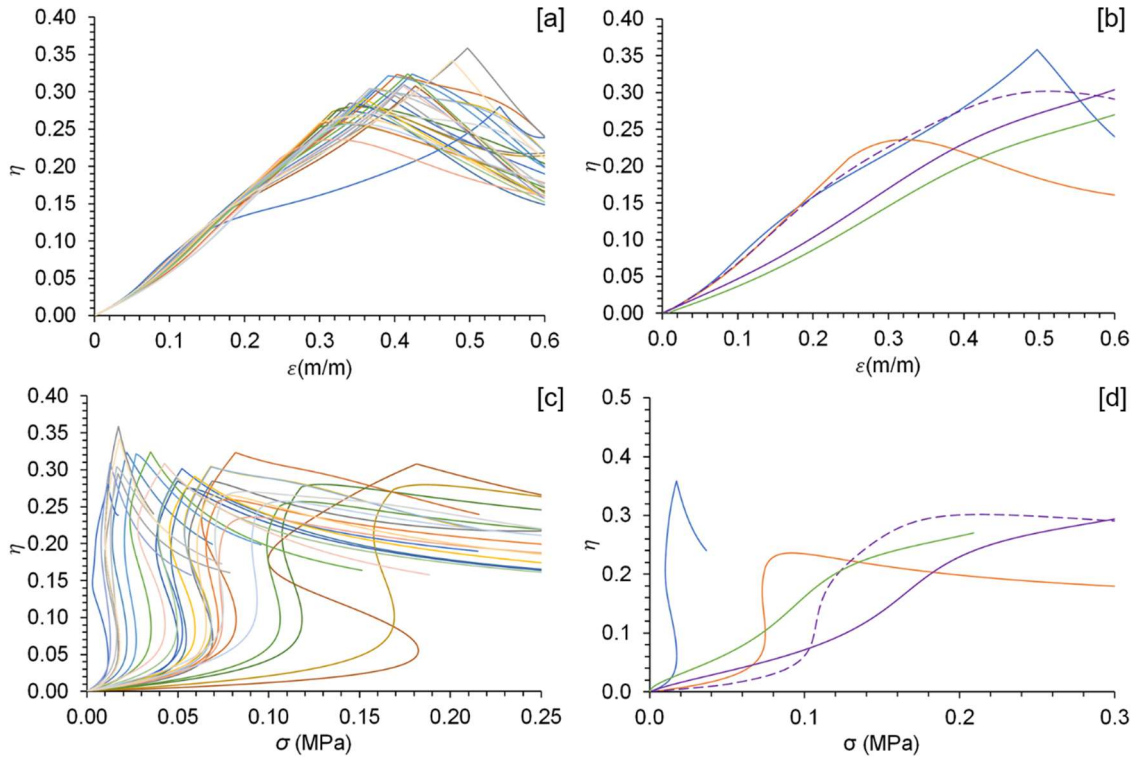

Figure 5-5: Energy absorption efficiency vs compressive strain [a] and energy absorption efficiency vs compressive stress [c] for all L27 samples. Energy absorption efficiency vs compressive strain [b] and energy absorption efficiency vs compressive stress [d] comparison of most (blue) and least efficient (orange) L27Samples, Rawlings foam (green), Riddell foam sample (purple) and Riddell foam model (Dashed) [364].

Almost all L27 samples exhibit similar efficiency curves with only a few notable outliers, Figure 5-5 [a]. The developed geometries have a different response to the foams, with a distinct point of maximum efficiency which quickly drops away, Figure 5-5 [b]. Maximum energy absorption efficiency reported by the L27 samples is comparable to that of the foams, reinforcing the suitability in the change of base material.

Table 5-5: Minimum, maximum and average values from tested L27 samples for volumetric and normalised energy absorption with the Cheetah 2_N sample, tested and theoretical Riddell foam for comparison [364]. Values reported at strains of onset of densification, densification strain and strain of maximum efficiency.

	Volumetric Energy Absorption (kJm^{-3})			Normalised Energy Absorption ($kJkg^{-1}$)		
Sample	ε_o	ε_d	$\varepsilon_{\eta max}$	ε_o	ε_d	ε_{me}
L2-CH	137.55	198.39	155.21	0.378	0.546	0.427
Riddell Foam	-	-	75.82	-	-	0.446
Theoretical Riddell Foam	-	-	67.42	-	-	0.397
L27 Maximum	528.76	613.23	525.00	1.040	1.506	1.087
L27 Minimum	14.50	29.42	32.69	0.103	0.205	0.198
L27 Average	150.37	204.36	170.82	0.450	0.649	0.538

The manufactured L27 samples report favourable energy absorption values, with the range of performance comfortably surrounding the Riddell foam, Table 5-5. Values at ε_o and ε_d were not calculated for the Riddell foam due to its non-auxetic response. No comparison could be made to the Rawlings foam as no data describing its density was available.

The higher normalised energies reported by the maximum L27 components suggests that not only can the MOM outperform the foams in terms of pure performance, but lower density components with equivalent performance were achievable.

5.3.3. The response of L27 samples to dynamic loading.

The L27 samples exhibited a similarly wide range in response to dynamic loads as they had to quasi-static loading. Impact duration ranged wildly from 4ms to 17ms at the lowest test velocity, with the range narrowing as impact velocity increased, Table 5-6. The average impact duration of the L27 samples was Riddell foam, with the Rawlings foam sample exhibiting significantly longer duration.

Table 5-6: Minimum, maximum and average values from tested L27 array samples for relative maximum strains and impact durations with L2-CH and foam data for comparison.

	Relative Maximum Strain			Duration (ms)		
Sample	3.30 m/s	4.44 m/s	5.58 m/s	3.30 m/s	4.44 m/s	5.58 m/s
Cheetah 2_N	0.23	0.39	0.58	7.0	9.6	10.3
Riddell foam	0.94	1.27	1.50	11.7	11.0	9.9
Rawlings foam	-	-	-	16.7	14.2	12.1
L27 Maximum	1.05	1.71	2.37	16.8	15.8	13.5
L27 Minimum	0.39	0.58	0.85	4.1	4.7	5.5
L27 Average	0.67	1.09	1.58	10.1	10.6	9.8

The average RMS values reported for the L27 samples suggest that the majority of samples reached strains exceeding densification at greater impact velocities, Table 5-6. However, the lowest RMS reported by the L27 samples were under one at every impact velocity. As maximised performance could be associated with an RMS of 1, this result suggests that there was sufficient scope in the design space for MOM performance to be maximised.

Interestingly the RMS of the Riddell foam suggests that its performance has been tailored to the lowest impact energy, as significant densification occurs by the higher velocities. This performance may be a result of the NOCSAE standard, which requires a GSI of no more than 300 at the lowest velocity tested.

5.3.3.1. Peak linear acceleration.

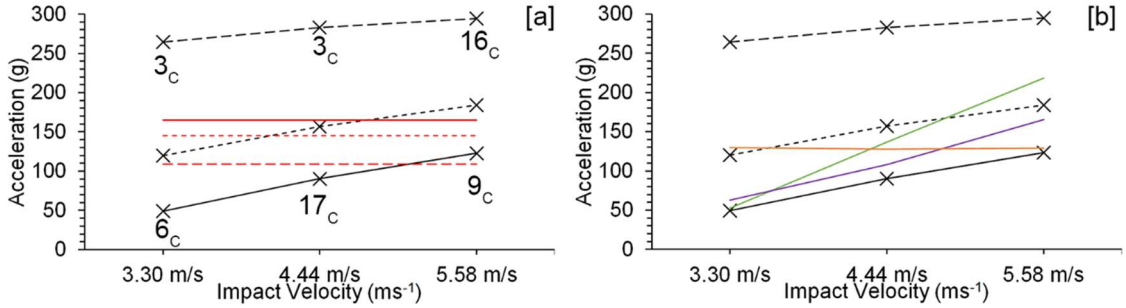

Figure 5-6: Maximum (dashed), minimum (solid) and average (dotted) PLA at each test velocity for the L27 samples, with 1(dashed), 5 (dotted), and 10% (solid) SRC risk thresholds [a][172], and Cheetah 2_N (orange), Rawlings (green) and Riddell (purple) [b] foams for comparison.

The L27 samples exhibit a wide range of performance, with the least favourable components reaching PLA values above those associated with a catastrophic injury, while the most favourable samples reduce the risk of SRC in comparison to the foams, Figure 5-6. At least one sample outperforms both foams at each impact velocity with the performance gap widening as foam performance degrades at higher velocities.

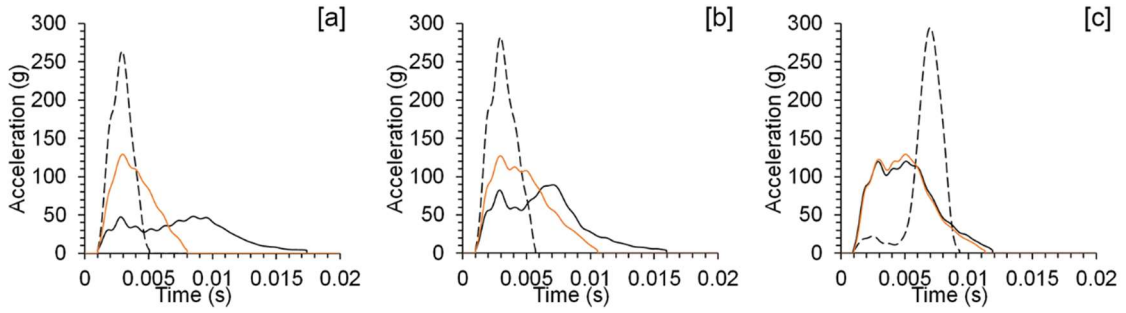

Figure 5-7: Acceleration vs time for the L27 samples with most (solid black) and least (dashed) favourable PLA with the Cheetah 2_N for comparison (orange), at [a] 3.30ms^{-1}, [b] 4.44ms^{-1} and [c] 5.58ms^{-1}.

The highest PLAs of the L27 samples is attributed to sampling 3_C being overly stiff under compression, resulting in the short duration, high acceleration pulses, Figure 5-7[a] and [b], Figure 5-7. It is not until the highest test velocity that a densified sample, 16_C, provides the highest PLA, Figure 5-7[c]. Across the entire range of velocities, the lowest PLAs are given by samples that appear to have just reached densification.

5.3.3.2. Gadd Severity Index

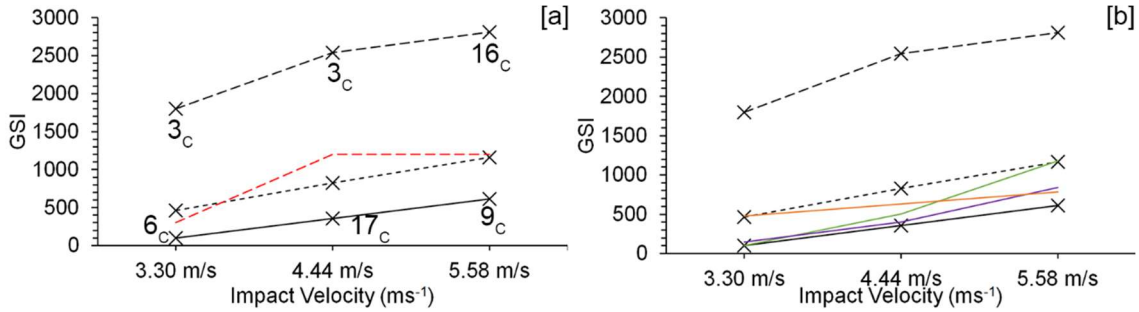

Figure 5-8: Maximum (dashed), minimum (solid) and average (dotted) GSI at each test velocity for the L27 Samples, with NOCSAE GSI limits (red dashed) [a], and the Cheetah 2_N (orange), Rawlings (green) and Riddell (purple) [b] for comparison.

The GSI for the L27 samples exhibits the same trends as the PLA response, with the least favourable components exhibiting responses which would result in catastrophic injury, while the most favourable components reduce GSI in comparison to the foam samples, Figure 5-8.

The positioning of the minimum, average and maximum GSI shows a significant skew to the distribution of the data set, with the worst performing samples significantly further from the average than the best performing ones. This skew suggests that the worst performing samples, 3_C and 16_C, may represent outliers with the data. Thus, the skew was considered when the main effects and interaction plots were created.

5.3.4. Statistics for Optimisation.

5.3.4.1. Peak Linear Acceleration.

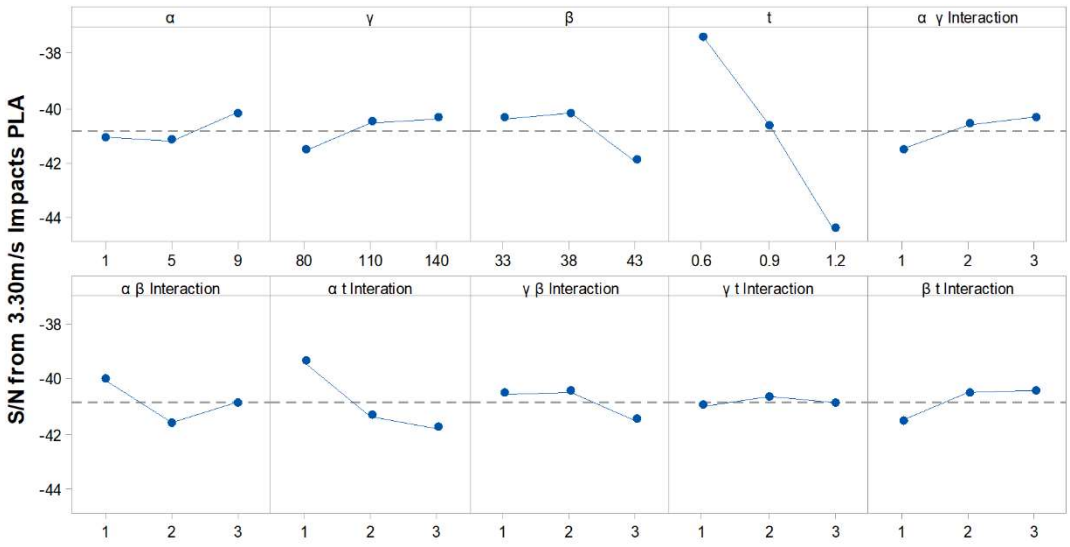

Figure 5-9: Main effects plot for S/N ratio calculated from L27 samples 3.30ms^{-1} impact PLA using the lowest best methodology.

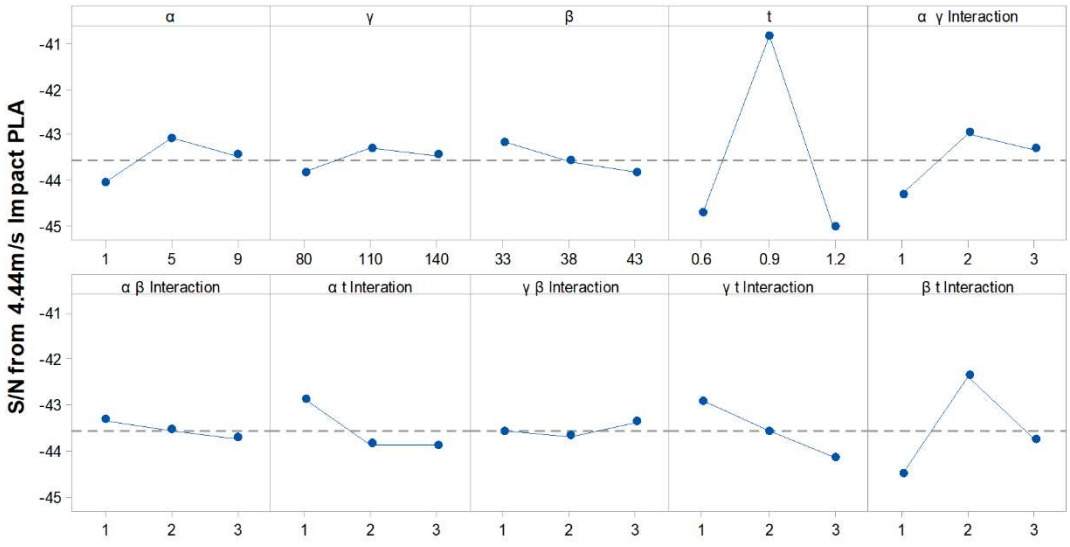

Figure 5-10: Main effects plot for S/N ratio calculated from L27 samples 4.44ms^{-1} impact PLA using the lowest best methodology.

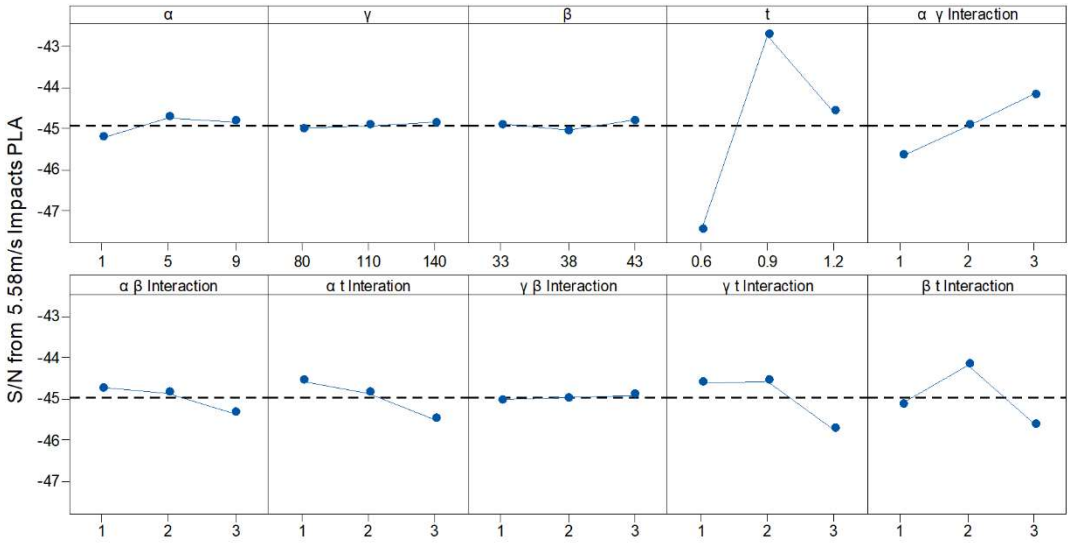

Figure 5-11: Main effects plot for S/N ratio calculated from L27 samples 5.58ms^{-1} impact PLA using the lowest best methodology.

Across all the developed main effects plots wall thickness, *t*, is consistently responsible for the largest sample variation, with 0.6mm walls providing the best performance at the lowest tested velocity, giving way to 0.9mm walls at higher velocities, Figure 5-9, Figure 5-10 and Figure 5-11. The reported S/N values for the 1.2mm group are consistent across the range of impact velocities.

Interactions between the geometrical parameters consistently seem to exert more influence over a sample's PLA than the geometrical parameters, most notably in response to the 5.58ms^{-1} impact where the folding angels, α, β and γ, all exhibit minimal variation around the mean response. This lack of variation indicates that the angles have little control over the MOMs response to impact, contrary to the findings in chapter 4.

Complex interactions are observed for all parameter combinations, across all investigated impact velocities, Figure 5-12, Figure 5-13 and Figure 5-14. Synonyms to the main effect plots, interactions with *t exhibit* more variance across the design space than the interactions between the fold angles. However, interactions between α, β, and γ consistently present more complex relationships, though this may be due to the lower variation seen in these interactions.

The interactions present in the 4.44ms^{-1} impact data exhibit a lower overall variation than those present in the 3.30 and 5.58ms^{-1} impact data, with a 110g range compared to 160g and 150g respectively, Figure 5-12, Figure 5-13 and Figure 5-14. The narrower window would indicate that the interactions have less influence over performance, thus making an optimisation effort more complex.

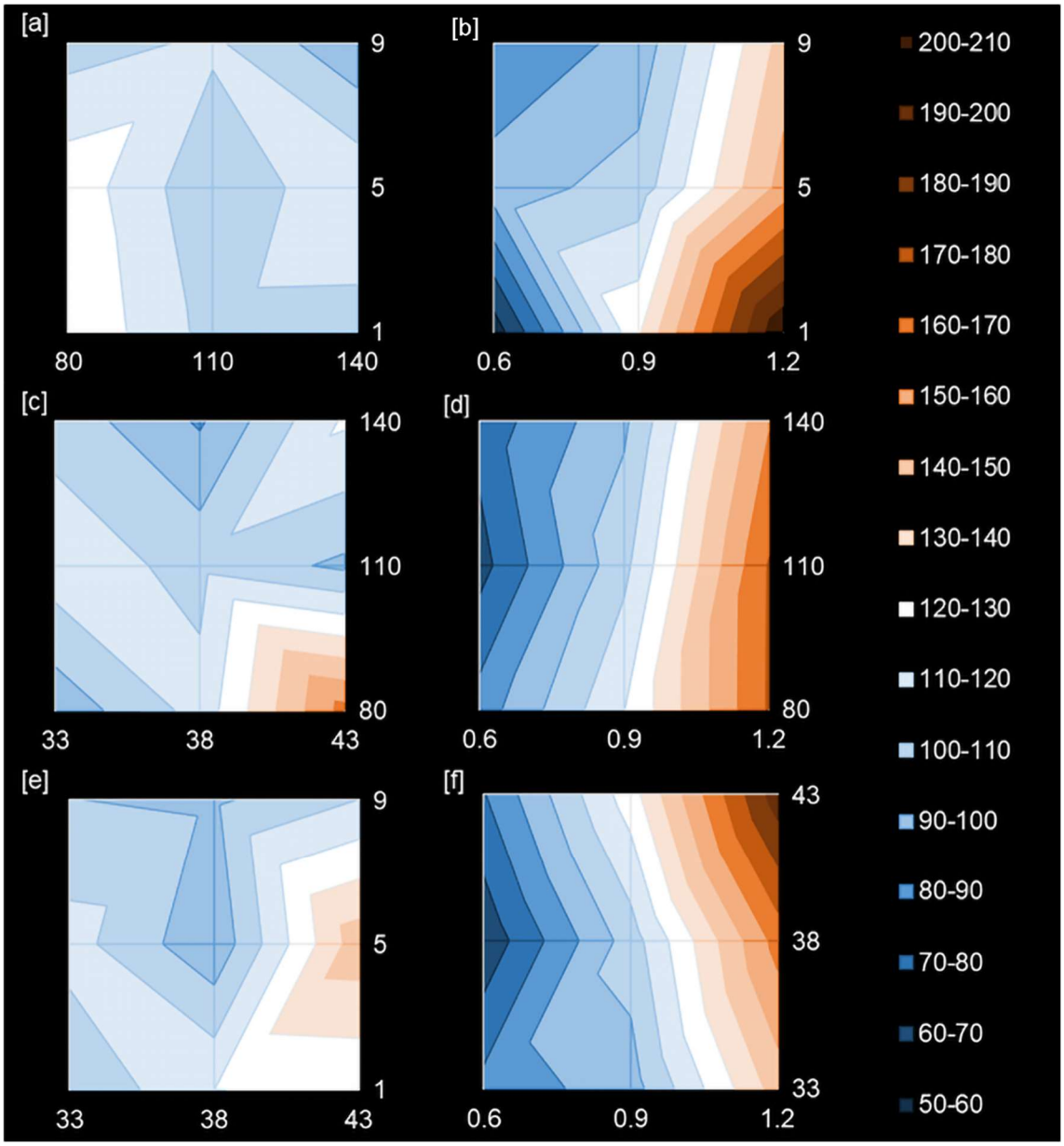

Figure 5-12: Interaction Plots for L27 Samples S/N for 3.30ms^{-1} Impacts PLA, γ – α [a], t – α [b], β– α [c], t – γ [d], β – v [e], t – β [f]. (scale calculated from S/N ranges)

The *t* – β and *t* – γ interactions present in the 3.30 ms^{-1} impact data are minimally complex, with variation within the 0.6mm walls driving the non-parallel nature, Figure 5-12 [d] and [e]. When the *t* – *α* interaction is considered, the apparent dominance of the wall thickness lessens as the angle of α increases, as the surface flattens out, Figure 5-12 [b]. Therefore, the chevron angle, α, allows for a fine-tuning of the wall thickness, for instance, a 0.9mm and 9° combination provide similar performance to 0.6mm and 5°. This relationship allows the optimisation to overcome a limitation of the FFF method.

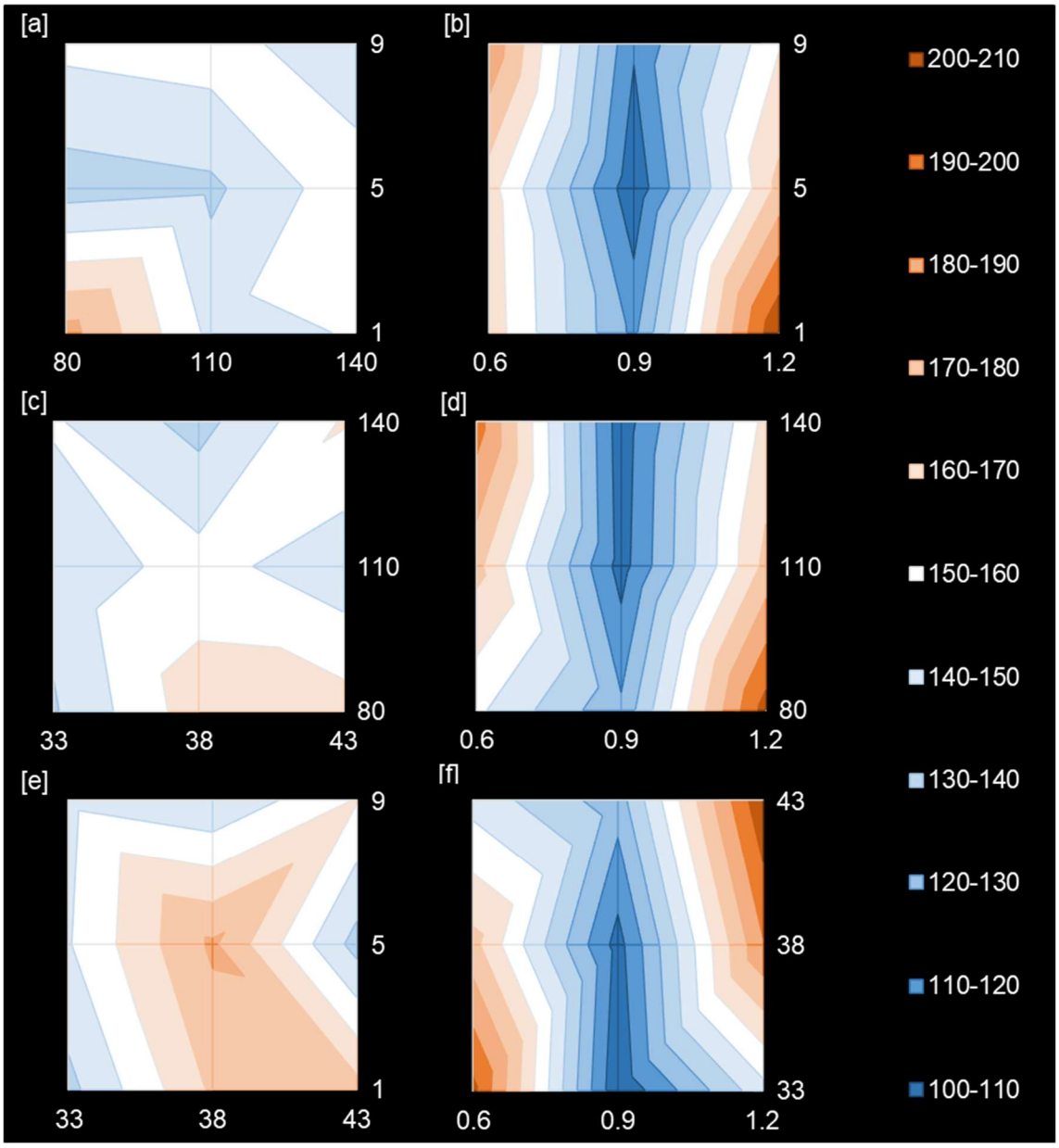

Figure 5-13: Interaction Plots for L27 Samples S/N for 4.44ms^{-1} Impacts PLA, γ – α [a], t – α [b], β– α [c], t – γ [d], β – v [e], t – β [f]. (scale calculated from S/N ranges)

Distinct valleys of best performance are present in the $t - \alpha$, $t - \beta$ and $t - \gamma$ interactions with apparent trade-offs between angle value and wall thickness, Figure 5-13 [b][d] and [f]. The trade-off between the wall thickness and fold angles noted previously is better developed here. For example, the combinations of 0.6mm - 1° and 0.6mm - 80° appear to provide similar performance to 1.2mm - 9° and 1.2mm – 140° respectively. However, these areas of equivalent performance exist only in high acceleration zones, and thus cannot be leveraged to improve performance.

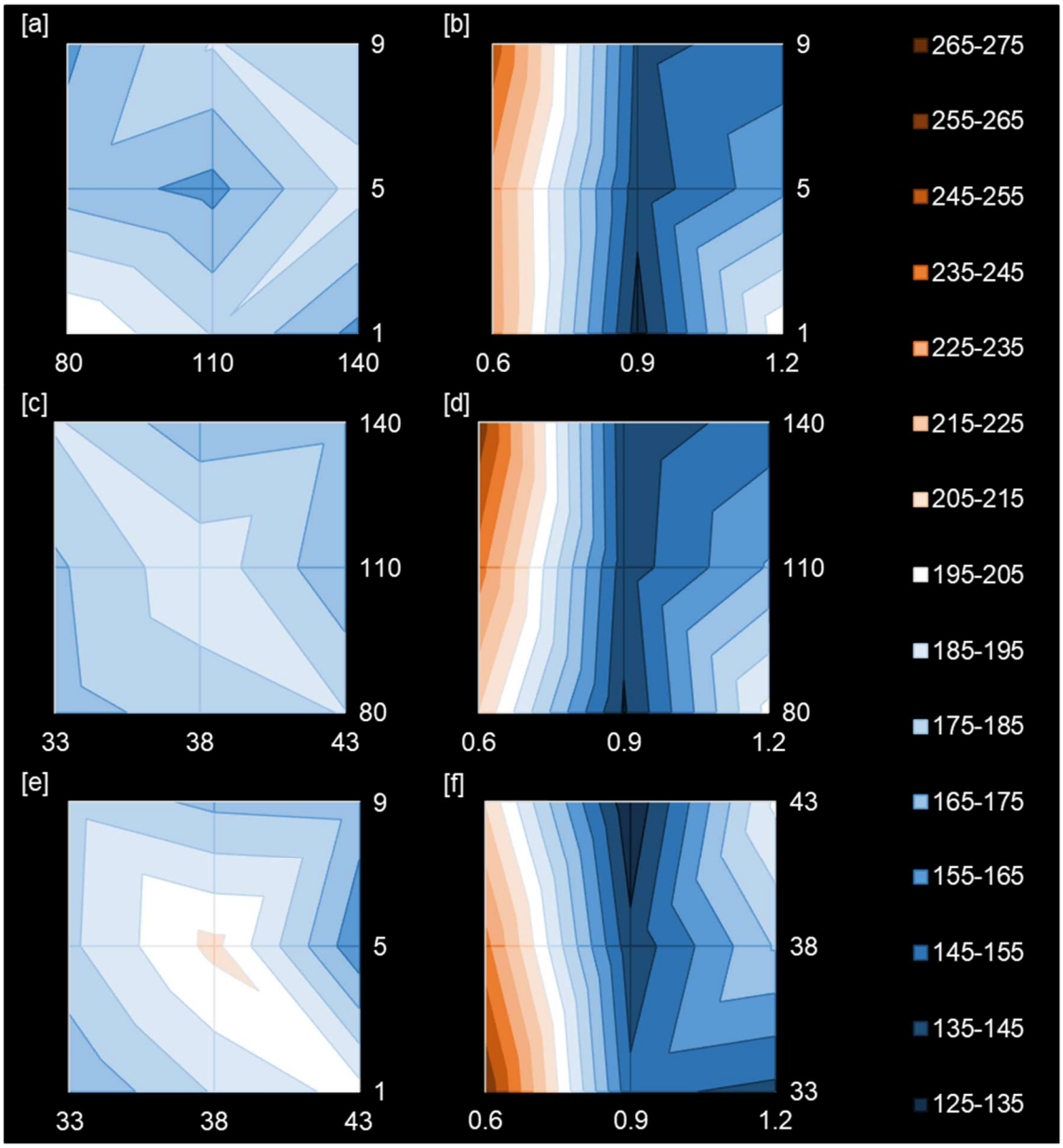

Figure 5-14: Interaction Plots for L27 Samples S/N for 5.58ms^{-1} Impacts PLA, γ – α [a], t – α [b], β– α [c], t – γ [d], β – v [e], t – β [f]. (scale calculated from S/N ranges)

The relationships in the $t - \alpha$, $t - \beta$ and $t - \gamma$ interactions of lower velocity impacts are less notable in the interaction plots for the 5.58ms^{-1} impact data, Figure 5-14. However, the diminished relationships are due to the high accelerations reported by all structures with 0.6mm walls.

At the lowest impact velocity only t and the α – t interaction were deemed significant to a samples PLA by ANOVA, Table 5-7. The dominance of t *to* sample performance is apparent, with it responsible for 63% of sample variation. The significance of the α – t interaction reinforces the relationship seen in the interaction plot, Figure 5-12.

Table 5-7: ANOVA results for 3.30ms^{-1} impact PLA S/N post pooling

Factor	f_g	S_g	V_g	P_g(%)	F_g	Confidence Level
Γ	2	7.45	3.73	2.12	0.90	-
B	2	16.02	8.01	4.56	1.93	-
T	2	221.59	110.80	63.08	26.75	99%
α - γ Interaction	2	6.93	3.47	1.97	0.84	-
α - β Interaction	2	11.53	5.77	3.28	1.39	-
α - t Interaction	2	29.74	14.87	8.47	3.59	90%
Error	14	57.99	4.14	16.51	-	-
Total	26	351.27	-	100.00	-	-

Table 5-8: ANOVA results for 4.44ms^{-1} impact PLA S/N post pooling.

Factor	f_g	S_g	V_g	P_g(%)	F_g	Confidence Level
α	2	4.30	2.15	2.62	1.77	-
t	2	99.17	49.58	60.46	40.88	99.0%
α - γ Interaction	2	8.96	4.48	5.46	3.69	90.0%
α - t Interaction	2	5.97	2.99	3.64	2.46	-
γ - t Interaction	2	7.03	3.51	4.28	2.90	90.0%
β - t Interaction	2	21.61	10.81	13.18	8.91	97.5%
Error	14	16.98	1.21	10.35	-	-
Total	26	164.01	-	100.00	-	-

More factors were deemed to influence PLA at the two higher test velocities significantly, Table 5-8 and Table 5-9. The α – t interaction was no longer deemed to be significant at these test velocities, meaning what fine-tuning the angle offered to wall thickness would not be available to optimal geometries for this condition. However, both the β – t and γ – t interactions are significant at these velocities. The significance of these interactions suggests that the cross-section of the MOM geometry influences the performance of the geometry.

Table 5-9: ANOVA results for 5.58ms^{-1} impact PLA post pooling of insignificant factors.

Factor	f_g	S_g	V_g	P_g(%)	F_g	Confidence Level
t	2	104.75	52.37	67.87	46.28	99%
α - γ Interaction	2	10.16	5.08	6.58	4.49	95%
α - β Interaction	2	1.79	0.89	1.16	0.79	-
α - t Interaction	2	4.10	2.05	2.65	1.81	-
γ - t Interaction	2	7.95	3.98	5.15	3.51	90%
β - t Interaction	2	9.75	4.88	6.32	4.31	95%
Error	14	15.84	1.13	10.27	-	-
Total	26	154.34	-	100.00	-	-

The analysis of the PLA response consistently found the three identified angles to be insignificant to sample performance, Table 5-7 to Table 5-9. However, the interactions containing these angles were often significant, and so they cannot be discounted from the design of optimal geometry.

5.3.4.2. Gadd Severity Index.

The main effects plot for GSI response display similar trends to those developed for PLA response, Figure 5-15 to Figure 5-17. Wall thickness again demonstrates the most extensive variation in GSI response, with interactions exhibiting more variation than geometrical parameters.

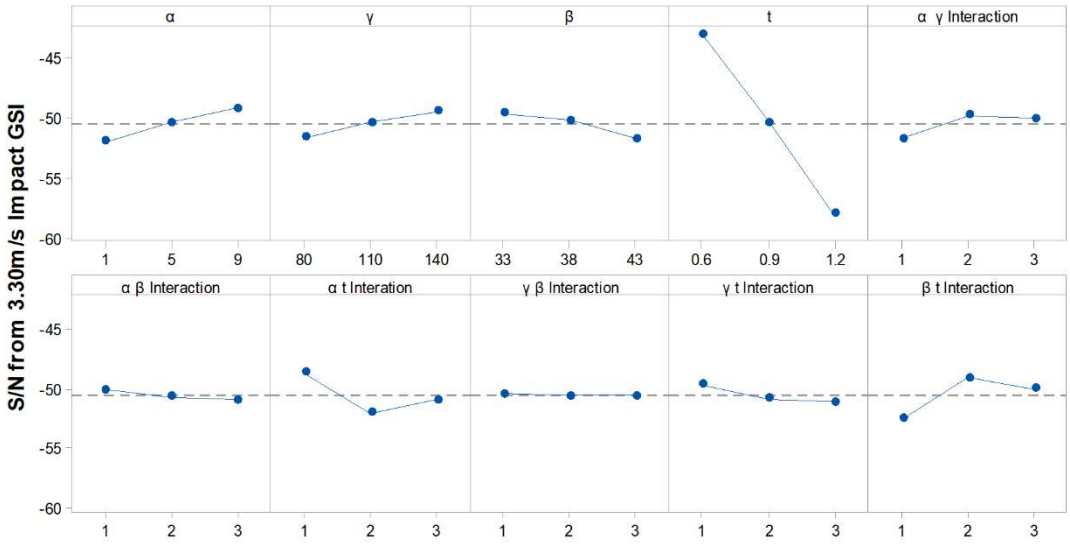

Figure 5-15: Main effects plot for S/N ratio calculated from L27 samples 3.30ms^{-1} impact GSI using the lowest best methodology.

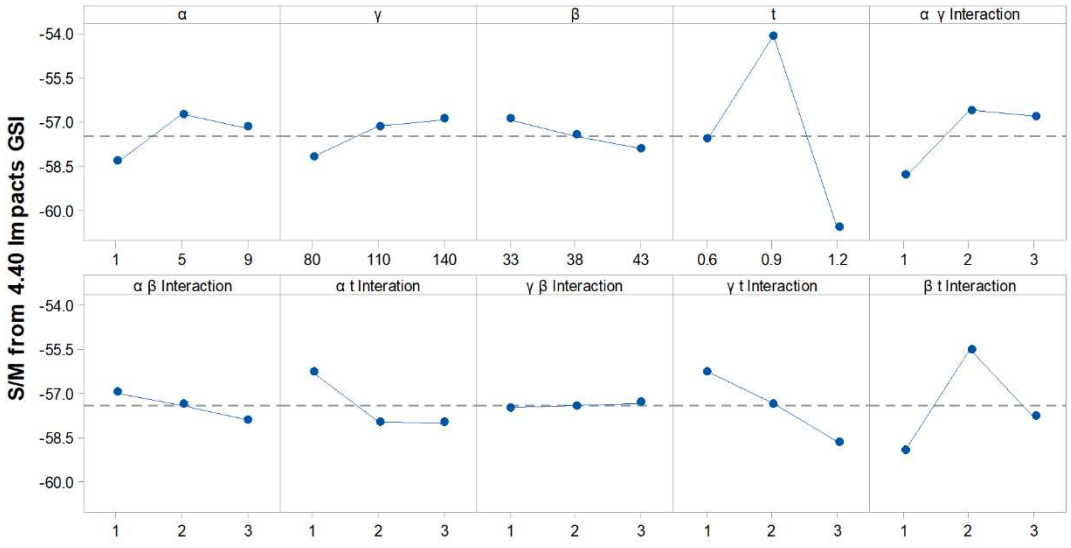

Figure 5-16: Main effects plot for S/N ratio calculated from L27 samples 4.44ms^{-1} impact GSI using the lowest best methodology.

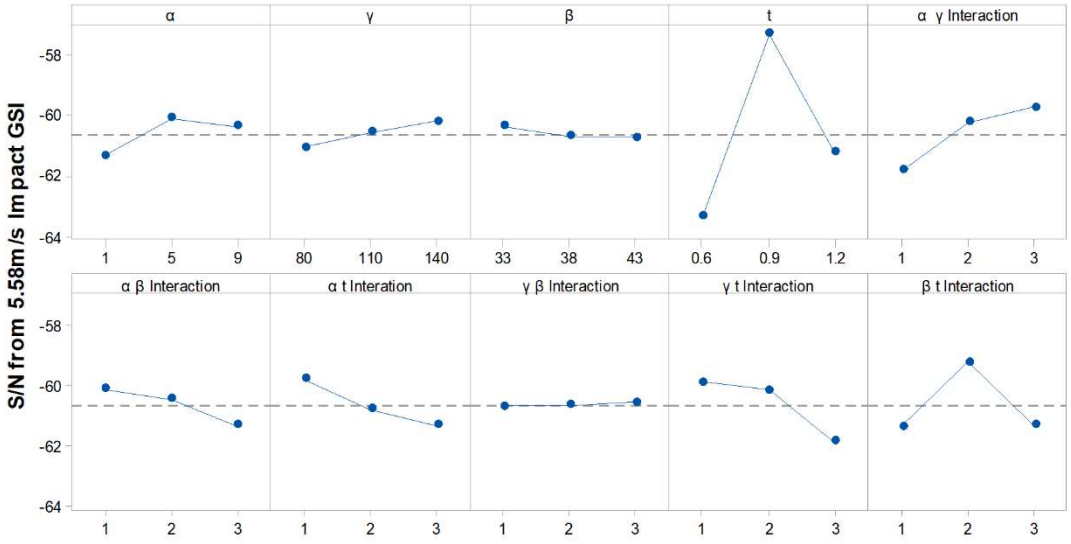

Figure 5-17: Main effects plot for S/N ratio calculated from L27 samples 5.58ms^{-1} impact GSI using the lowest best methodology.

Both β and γ show minimal variation across all impact velocities, with their interaction showing effectively no variation, suggesting that these angles had minimal influence on GSI, despite an apparent ability to affect cell geometry.

Across all GSI interaction plots, the divergence between t based interactions and those not containing t in the noted in the PLA response is repeated, Figure 5-18 to Figure 5-20. This similarity was expected due to the GSIs reliance on acceleration data, equation 5-1.

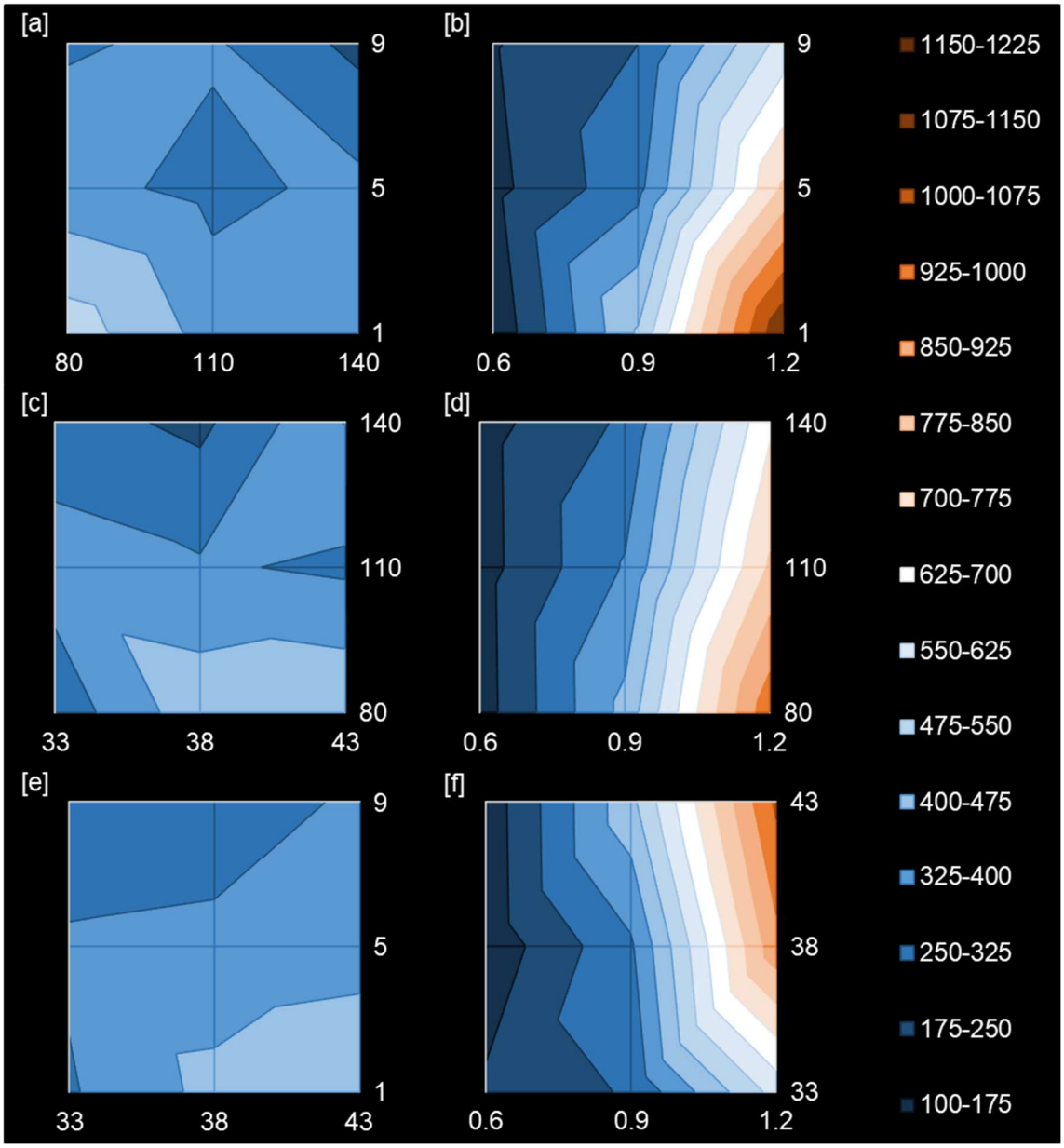

Figure 5-18: Interaction Plots for the L27 Samples S/N for 3.30ms^{-1} Impacts GSI, γ – α [a], t – α [b], β– α [c], t – γ [d], β – v [e], t – β [f]. (scale calculated from S/N ranges)

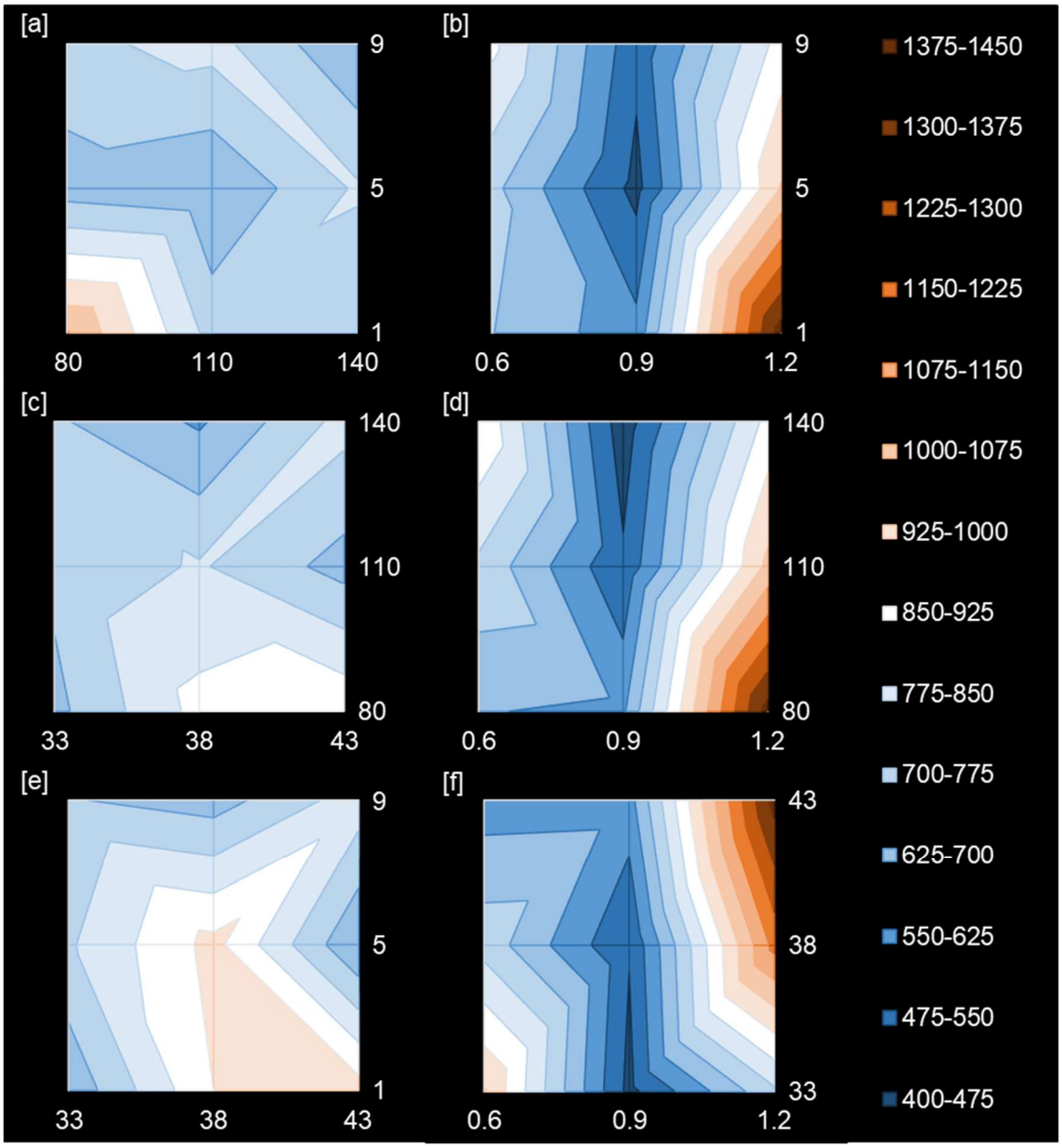

Figure 5-19: Interaction Plots for the L27 Samples S/N for 4.44ms^{-1} Impacts PLA, γ – α [a], t – α [b], β– α [c], t – γ [d], β – v [e], t – β [f]. (scale calculated from S/N ranges)

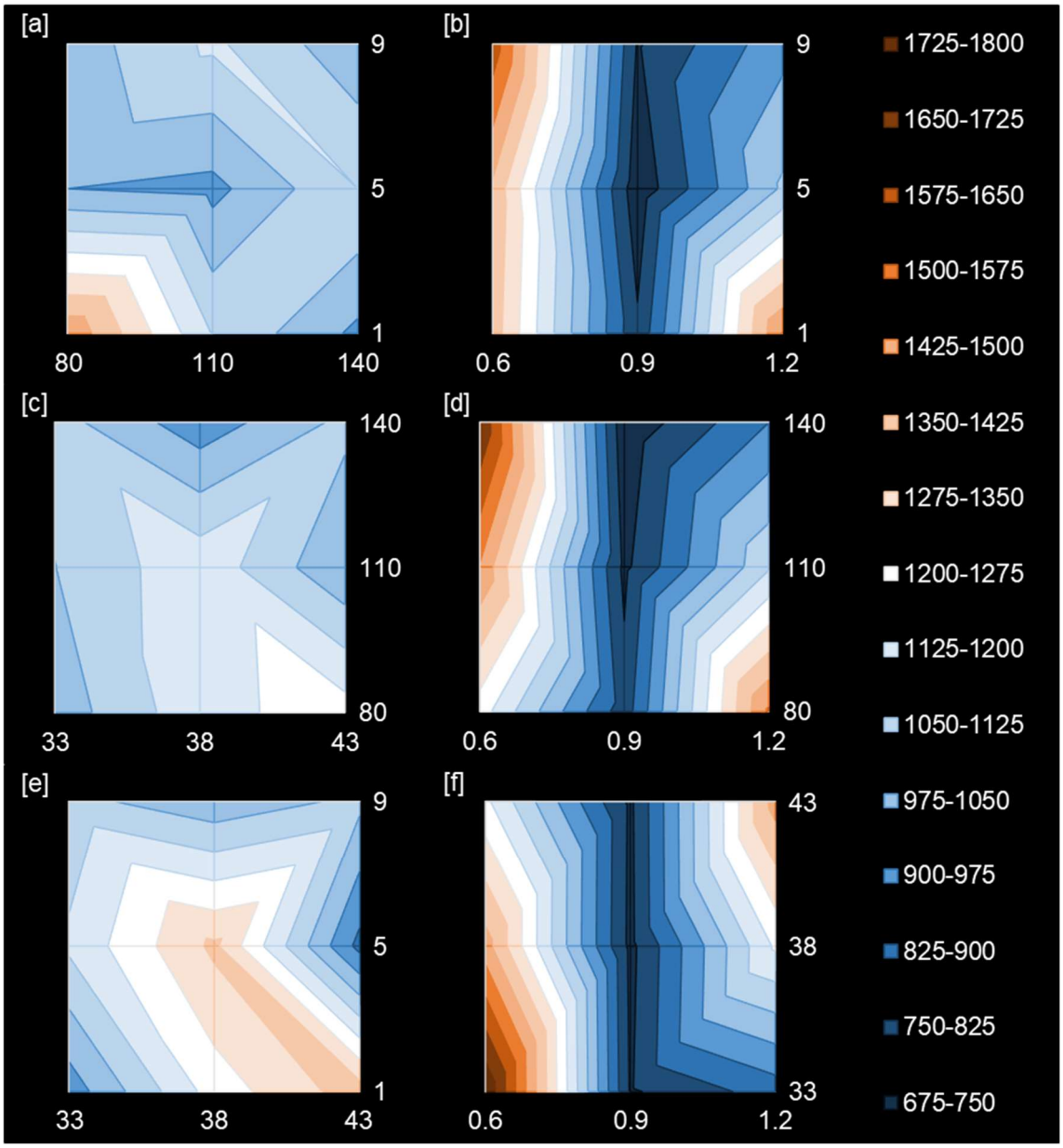

Figure 5-20: Interaction Plots for the L27 Samples S/N for 5.58ms^{-1} Impacts PLA, γ – α [a], t – α [b], β– α [c], t – γ [d], β – v [e], t – β [f]. (scale calculated from S/N ranges)

The analysed GSI response of the L27 samples reconfirmed the importance of t to sample performance, with its contribution ranging from 51 to 79%, Table 5-10 to Table 5-12. Interestingly α is deemed to influence GSI at the lowest impact velocity significantly, Table 5-10. As this factor as not significant to the PLA response, it could be assumed that the angle plays a role in determining the duration of an impact. Again, the fold angles provide less contribution to sample performance than their interactions with the wall thickness.

Table 5-10: ANOVA results for 3.30ms^{-1} impact GSI post pooling of insignificant factors.

Factor	f_g	S_g	V_g	P_g(%)	F_g	Confidence Level
α	2	34.59	17.293	2.69	3.03	90%
γ	2	22.94	11.470	1.78	2.01	-
t	2	1016.70	508.349	79.01	89.00	99%
α - γ Interaction	2	21.46	10.731	1.67	1.88	-
α - t Interaction	2	54.05	27.025	4.20	4.73	95%
β - t Interaction	2	57.09	28.543	4.44	5.00	99%
Error	14	79.97	5.712	6.21	-	-
Total	26	1286.79	-	100.00	-	-

Table 5-11: ANOVA results for 4.44ms^{-1} impact GSI post pooling of insignificant factors.

Factor	f_g	S_g	V_g	P_g(%)	F_g	Confidence Level
α	2	12.37	6.186	3.21	1.70	-
t	2	195.48	97.738	50.75	26.92	99%
α - γ Interaction	2	27.77	13.886	7.21	3.82	95%
α - t Interaction	2	17.56	8.779	4.56	2.42	-
γ - t Interaction	2	25.81	12.903	6.70	3.55	90%
β - t Interaction	2	55.34	27.668	14.37	7.62	99%
Error	14	50.83	3.630	13.20	-	-
Total	26	385.15	-	100.00	-	-

Table 5-12: ANOVA results for 5.58ms^{-1} impact GSI post pooling of insignificant factors.

Factor	f_g	S_g	V_g	P_g(%)	F_g	Confidence Level
α	2	7.552	3.776	2.49	1.14	-
t	2	168.698	84.349	55.51	25.50	99%
α - γ Interaction	2	21.975	10.987	7.23	3.32	90%
α - t Interaction	2	11.163	5.581	3.67	1.69	-
γ - t Interaction	2	21.281	10.641	7.00	3.22	90%
β - t Interaction	2	26.905	13.452	8.85	4.07	95%
Error	14	46.304	3.307	15.24	-	-
Total	26	303.878	-	100.00	-	-

5.3.4.3. 3VS

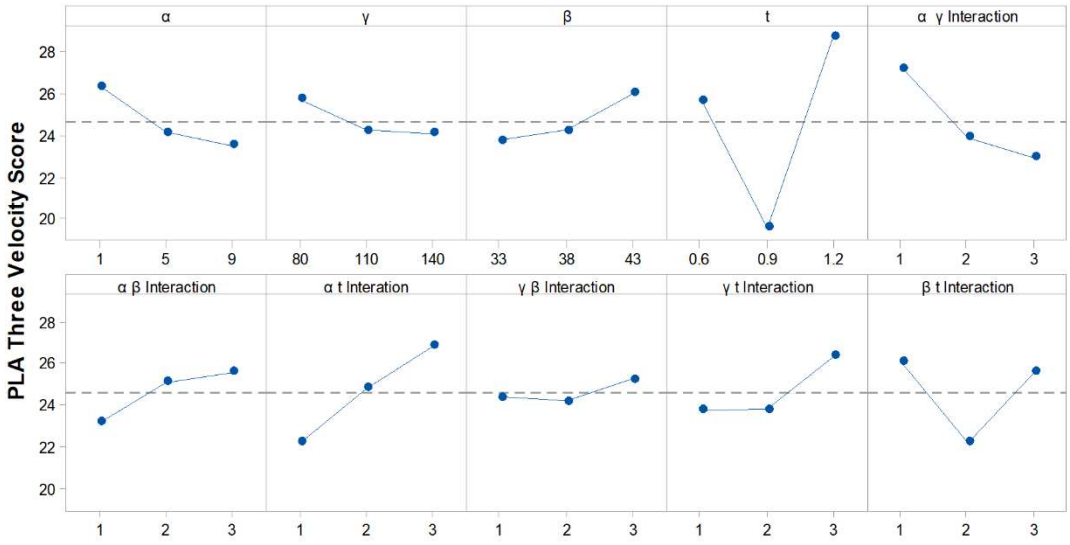

Figure 5-21: Main effects plot for 3VS calculated from the L27 samples PLA.

The developed main effects plots for the PLA and GSI three velocity scores diverge from the paters seen in the individual velocity plots, Figure 5-21 and Figure 5-22. The primary fold angles exhibit similar variation to the interactions, suggesting they are of similar importance. Although wall thickness still shows the most significant variation in response, its dominance is lessened in comparison to the plots developed for PLA and GSI.

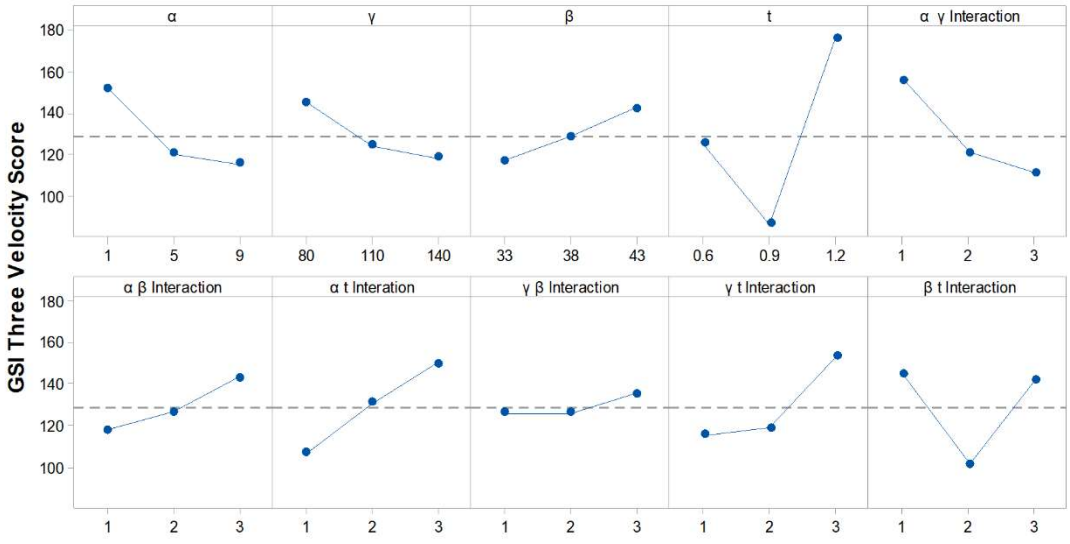

Figure 5-22: Main effects plot for 3VS calculated from L27 samples GSI.

The MOM was chosen in part due to its auxetic nature, potentially increasing the range of velocities at which a material can provide preferable performance. As the fold angles

are responsible for giving the metamaterial its auxetic properties, the increased sample variation they appear to influence is likely a result of the velocity range considered by the 3VS calculation.

Both GSI and PLA based 3VS best performance is driven by the maximisation of α and γ while minimising β, suggesting that further performance for these metrics may have been gained by increasing the range of these values studied.

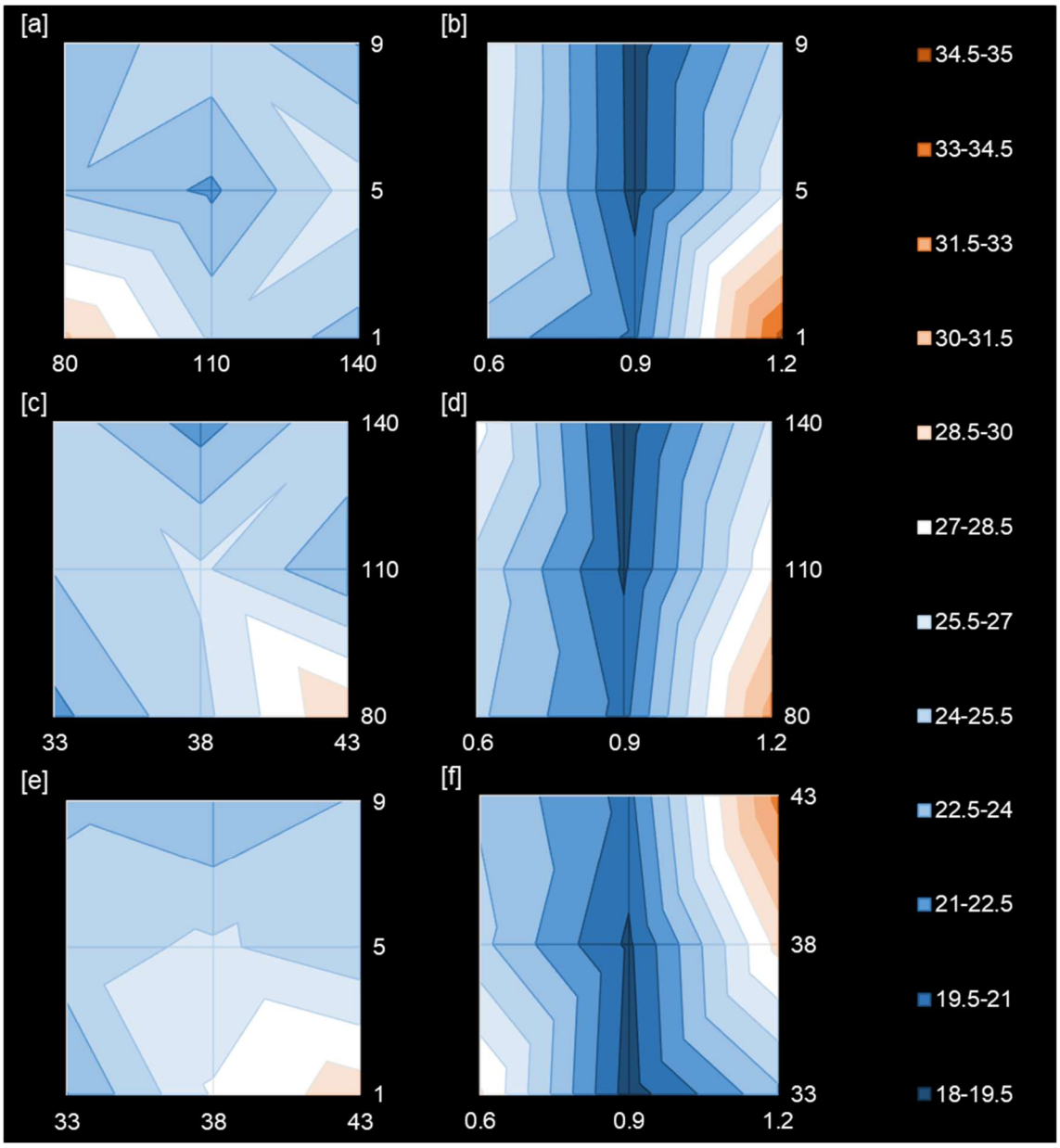

Figure 5-23: Interaction Plots for the L27 Samples 3VS for PLA results at all impacts, γ – α [a], t – α [b], β– α [c], t – γ [d], β – v [e], t – β [f]. (scale calculated from S/N ranges)

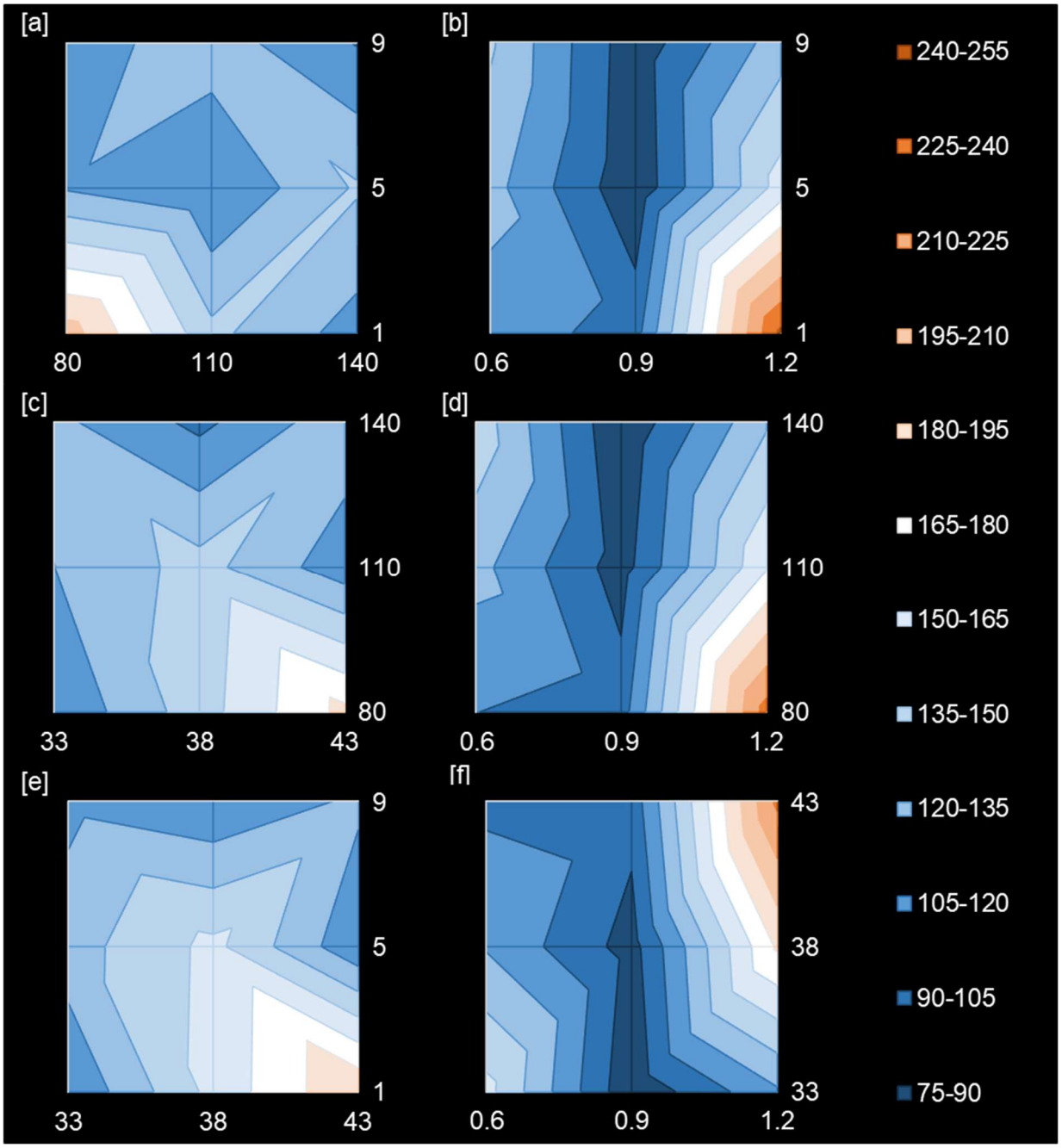

Figure 5-24: Interaction Plots for the L27 Samples 3VS for GSI results at all impacts, γ – α [a], t – α [b], β– α [c], t – γ [d], β – v [e], t – β [f]. (scale calculated from S/N ranges)

Table 5-13: ANOVA results for 3VS based on sample PLA post pooling of insignificant factors.

Factor	f_g	S_g	V_g	$P_g(\%)$	F_g	Confidence Level
α	2	40.04	20.02	4.30%	1.47	-
t	2	394.82	197.41	42.37%	14.54	99%
α - γ Interaction	2	91.13	45.57	9.78%	3.36	90%
α - t Interaction	2	96.82	48.41	10.39%	3.56	90%
γ - t Interaction	2	39.71	19.86	4.26%	1.46	-
β - t Interaction	2	79.23	39.61	8.50%	2.92	90%
Error	14	190.12		20.40%	-	-
Total	26	931.86	-	100.00%	-	-

Table 5-14: ANOVA results for 3VS based on sample GSI post pooling of insignificant factors.

Factor	f_g	S_g	V_g	$P_g(\%)$	F_g	Confidence Level
α	2	7120	3560	6.65%	1.93	-
t	2	36889	18445	34.48%	9.98	99%
α - γ Interaction	2	10116	5058	9.45%	2.74	90%
α - t Interaction	2	8472	4236	7.92%	2.29	-
γ - t Interaction	2	7980	3990	7.46%	2.16	-
β - t Interaction	2	10547	5273	9.86%	2.85	90%
Error	14	25871	1848	24.18%	-	-
Total	26	106995	-	100.00%	-	-

The analysis of the 3VS values confirms the lessened importance of wall thickness to samples performance noted in the main effects plots, Table 5-13 and Table 5-14. Despite the increased variance of the fold angles, none were found to be significant by the analysis. Additionally, other factors were found to be significant only at the lowest level of confidence considered. As different factor combinations provided the best performance at each impact velocity when the weighted score is considered, this difference in performance can be obfuscated.

For example, 2_C and 6_C have similar PLA based 3VS values, 21.88 and 21.5 respectively, which would suggest that changes between the two samples geometries are inconsequential to performance, Table 10-5. However, while 2_C maintains a consistent PLA at each velocity, 6_C has far better performance at the lowest velocity but much worse at the highest tested velocity. Therefore, the design of optimals for these metrics must be carefully considered.

5.3.5. Optimal Geometry Performance.

Following the method outlined in section 5.2.5, the parameter combinations for optimal performance for each condition were identified. Six of the eight optimal geometries were contained within the L27 array, more than was expected as the array contained only one-third of all possible designs, Table 5-15.

Table 5-15: Optimal Geometry Parameter Values

Metric	Optimal Velocity (ms^{-1})	α (°)	β (°)	γ (°)	t (mm)	L27 array equivalent geometry.
PLA	3.30	1	38	140	0.6	8_C
	4.44	5	33	110	0.9	-
	5.58	1	43	140	0.9	9_C
	3VS	9	33	140	0.9	25_C
GSI	3.30	1	38	140	0.6	8_C
	4.44	5	33	140	0.9	-
	5.58	5	38	140	0.9	17_C
	3VS	5	33	110	0.9	-

All optimal geometries were manufactured using the same process covered in section 5.2.2, including those with an equivalent geometry in the L27 array. This was done to avoid sample wear or differences in material properties in batches of the cheetah filament from affecting the results. Where parameter combinations were identical, a single sample was manufactured.

Table 5-16: Predicted vs experimental values of designed metrics for optimal geometries. Prediction limits representative of a 95% confidence level.

	Predicted Acceleration (g)			Experimental result	Relative to Predicted
Velocity (ms^{-1})	Value	Lower Limit	Upper Limit	(g)	(%)
3.30	57.66	45.58	72.94	54.62	94.73
4.44	88.39	77.98	100.18	98.14	111.03
5.58	127.35	111.94	144.87	120.31	94.47
3VS	17.31	13.61	21.01	17.26	99.71

	Predicted SI				Relative to Predicted
Velocity (ms^{-1})	Value	Lower Limit	Upper Limit	Experimental result	(%)
3.30	106	80	140	101	95.28
4.44	382	307	475	384	100.52
5.58	666	543	817	611	91.74
3VS	42.3	-0.22	84.82	92.54	218.77

The majority of samples performed within the 95% confidence interval of their predicted result, Table 5-16. Only the 3VS GSI optimal performed outside of this range, with its experimental result twice that of its predicted. The broad range of its confidence interval suggests that a large amount of sample variation was not accounted for by the optimisation process.

5.3.5.1. Stress-Strain Response.

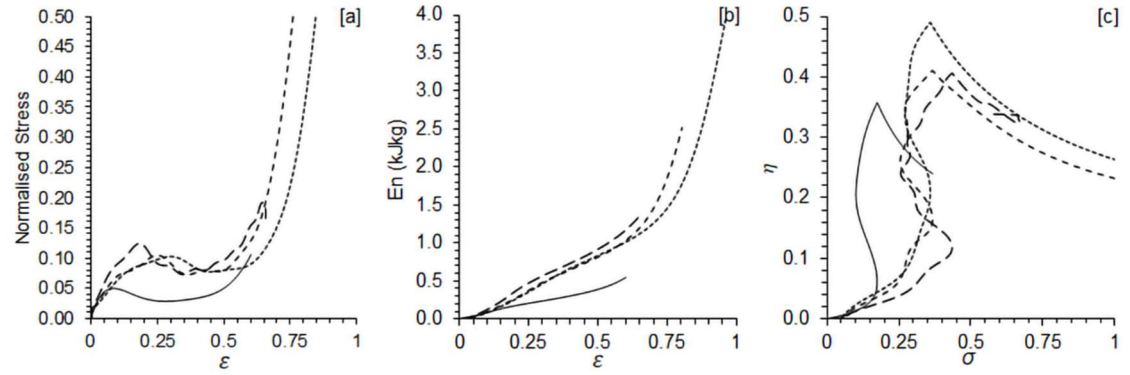

Figure 5-25: Normalised stress [a], and normalised energy absorption vs compressive strain [b] and efficiency vs compressive stress [c] for the 3.30ms^{-1} optimum geometry (black), for quasi-static (solid), 3.30ms^{-1}(long dash), 4.44ms^{-1} (short dash) and 5.58ms^{-1} (dotted) loading conditions.

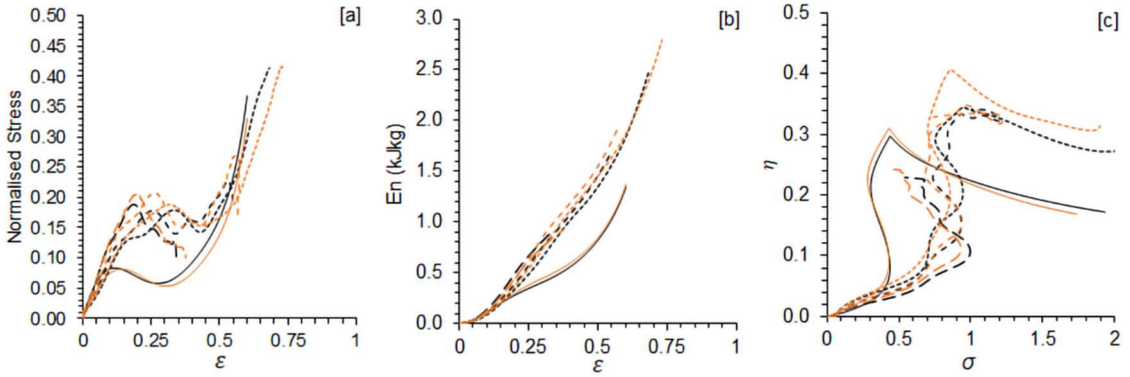

Figure 5-26 Normalised stress [a], and normalised energy absorption vs compressive strain [b] and efficiency vs compressive stress [c] for the 4.44ms^{-1} PLA (black) and GSI (Orange) optimum geometries, for quasi-static (solid), 3.30ms^{-1}(long dash), 4.44ms^{-1} (short dash) and 5.58ms^{-1} (dotted) loading conditions.

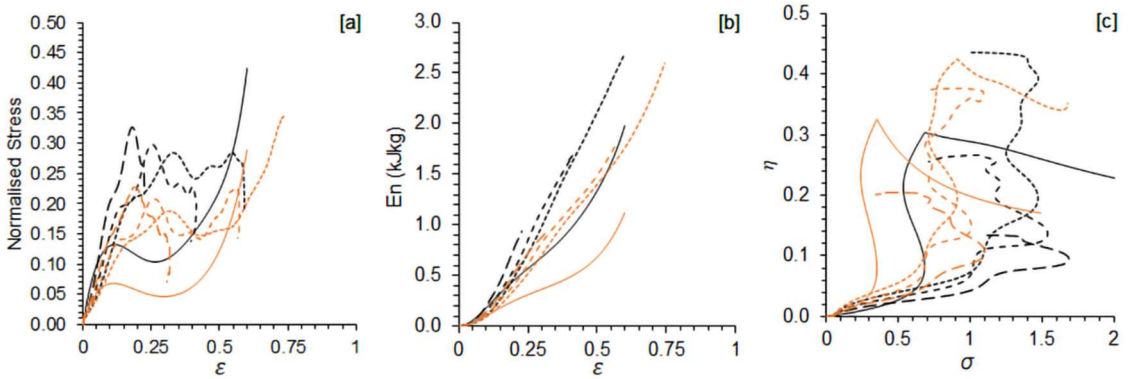

Figure 5-27: Normalised stress [a], and normalised energy absorption vs compressive strain [b] and efficiency vs compressive stress [c] for the 5.58ms^{-1} PLA (black) and GSI (Orange) optimum geometries, for quasi-static (solid), 3.30ms^{-1}(long dash), 4.44ms^{-1} (short dash) and 5.58ms^{-1} (dotted) loading conditions.

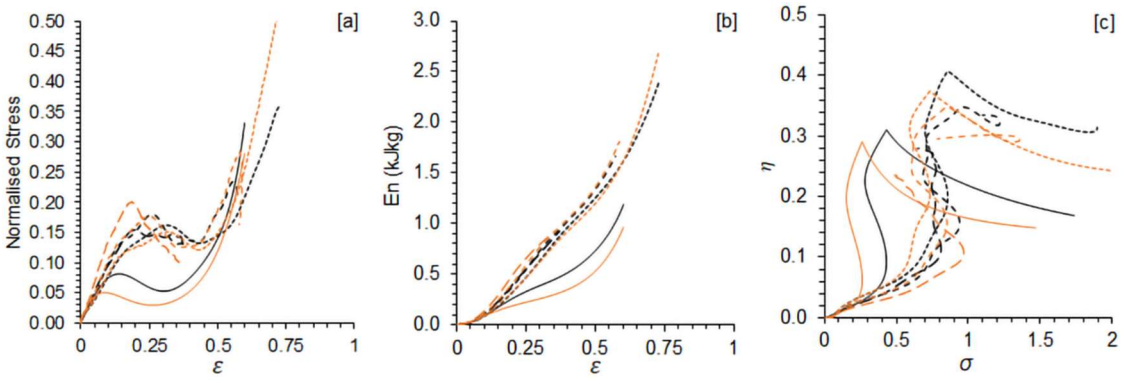

Figure 5-28: Normalised stress [a], and normalised energy absorption vs compressive strain [b] and efficiency vs compressive stress [c] for the 3VS PLA (black) and GSI (Orange) optimum geometries, for quasi-static (solid), 3.30ms^{-1}(long dash), 4.44ms^{-1} (short dash) and 5.58ms^{-1} (dotted) loading conditions.

All the developed optimal geometries exhibit an increased stiffness when subjected to dynamic loads, with plateau stresses approximately twice that of those seen under quasi-static loading, Figure 5-25 to Figure 5-28. Samples also undergo an increase in peak absorption efficiency when impacted.

5.3.5.2. Peak Linear Acceleration.

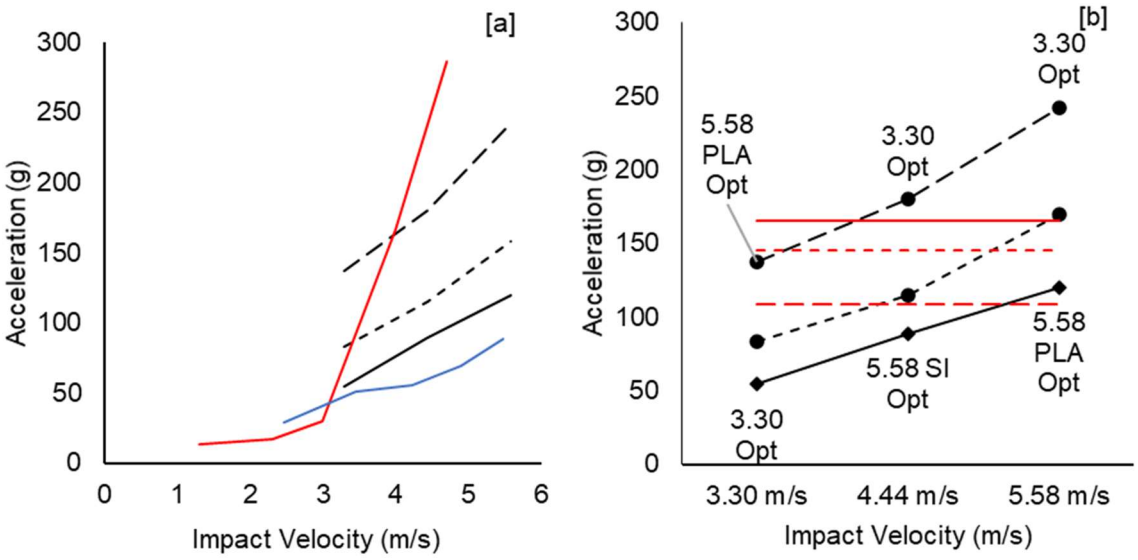

Figure 5-29: Best (solid), average (dotted) and worst (dashed) Optimal Geometries (black) performance at all tested velocities, with Awareflow shock absorber [21] and Schutt Ion 4D [22][a], and SRC risk thresholds [172][b] for comparison.

The devised optimal MOM geometries fit comfortably within the range of performance of novel AF impact systems presented in the literature, Figure 5-29 [a]. The derived geometries reduce SRC risk below the 1% PLA threshold at the two lowest velocities, only crossing this threshold at higher values, Figure 5-29 [b].

Neither 3VS optimal geometry provides the best performance at any single speed, not unexpected due to the data handling methods used to derive these geometries. Both the 4.44ms^{-1} samples are outperformed at the mid-velocity impact condition by the 5.58ms^{-1} SI optimal.

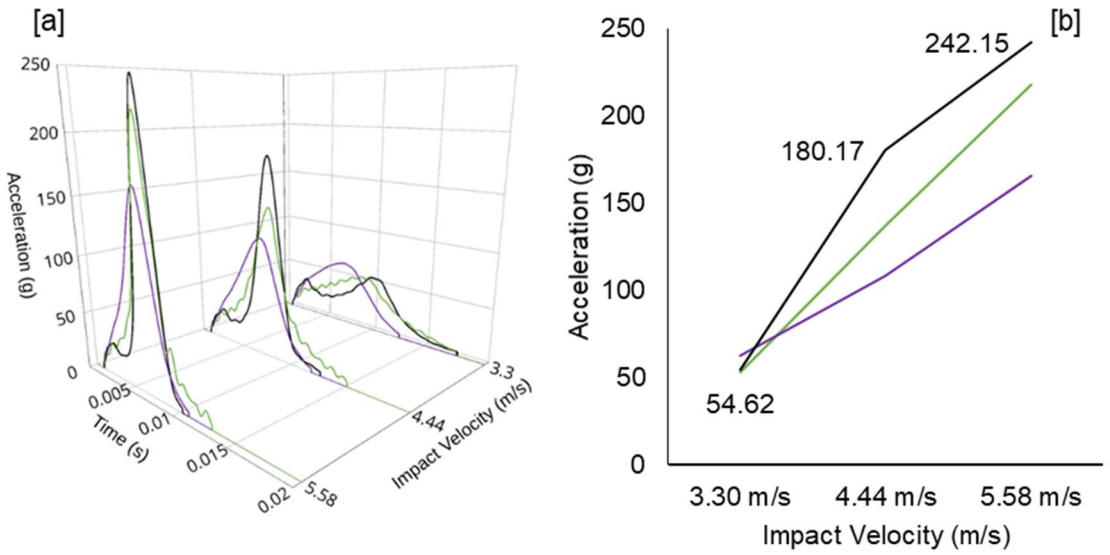

Figure 5-30: Acceleration Time Curves for 3.30 m/s, 4.44 m/s and 5.58 m/s impacts [a] and peak acceleration values [b] for 3.30 m/s Optimal Geometry (Black) with Riddell (purple) and Rawlings (Green) foams for comparison.

The 3.30ms^{-1} optimal geometry presents remarkably similar trends to the two tested foam samples across the range of impact velocities. There is evidence of the onset of densification at the lowest velocity, with the associated spike in acceleration increasing in prominence as impact velocity rises, Figure 5-30 [a]. The severity of this spike is a result of the single cell present through the depth of the sample, thus limiting the energy absorption post the collapse of this cell. By comparison, the foams have multiple cells through the thickness of the sample, with cells collapsing in distinct patterns rather than uniformly across the sample, [19,365].

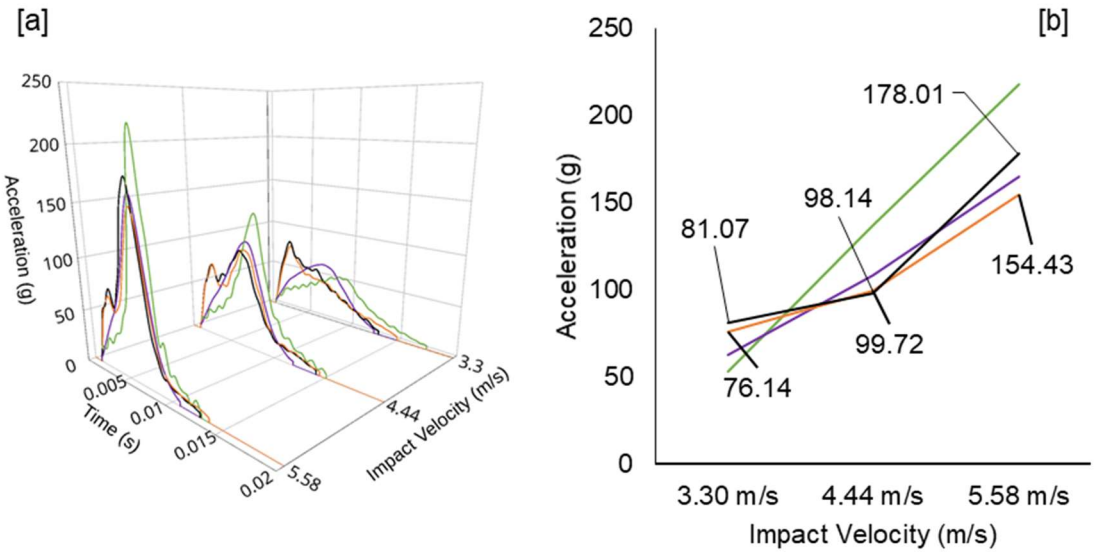

Figure 5-31: Acceleration Time Curves for 3.30 m/s, 4.44 m/s and 5.58 m/s impacts [a] and peak acceleration values [b] for 4.44 m/s PLA (Black) and GSI (Orange) optimal geometries with Riddell (purple) and Rawlings (Green) foams for comparison.

The two developed 4.44ms^{-1} optimal geometries have remarkably similar acceleration time pluses, with the SI optimal appearing to have a marginally lower plateau region at the expense of increased impact duration, Figure 5-31. Although the PLA optimal provides a lower acceleration at the middle impact velocity, the difference is marginal. The worse performance at the lowest and highest impact velocities result from the samples increased stiffness and lower densification strain, respectively, Figure 5-26.

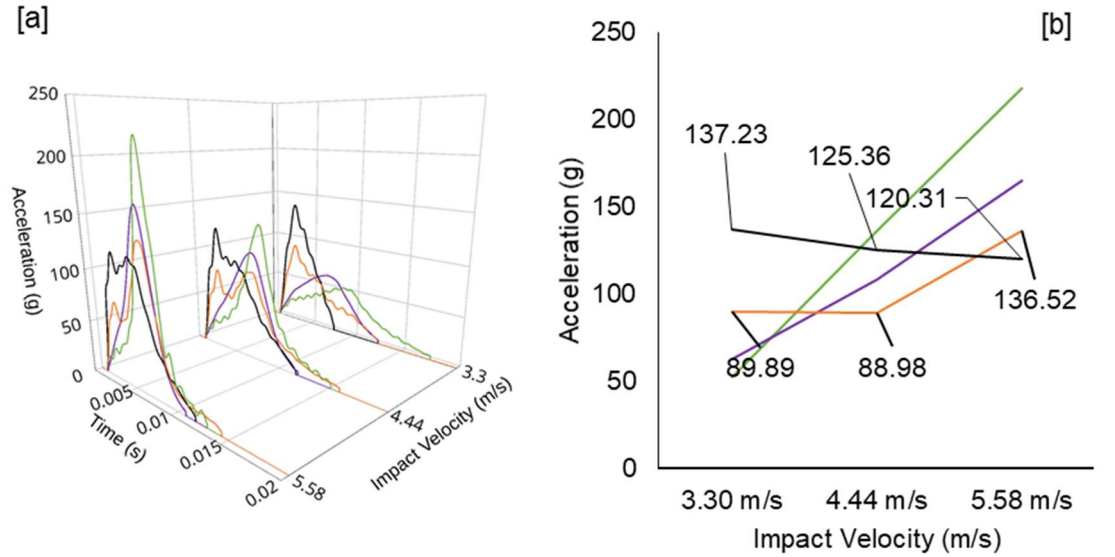

Figure 5-32: Acceleration Time Curves for 3.30 m/s, 4.44 m/s and 5.58 m/s impacts [a] and peak acceleration values [b] for 5.58 m/s PLA (Black) and GSI (Orange) optimal geometries with Riddell (purple) and Rawlings (Green) foams for comparison.

The 5.58ms^{-1} optimal geometries show the same trade-off between duration and acceleration seen in the results for the 4.44ms^{-1} optimals, Figure 5-32. Here the disparity is increased, with a 50g separation in pre-densified accelerations the highest impact velocity. The GSI appears to have densified at the middle test velocity, resulting in worse peak acceleration at the highest velocity.

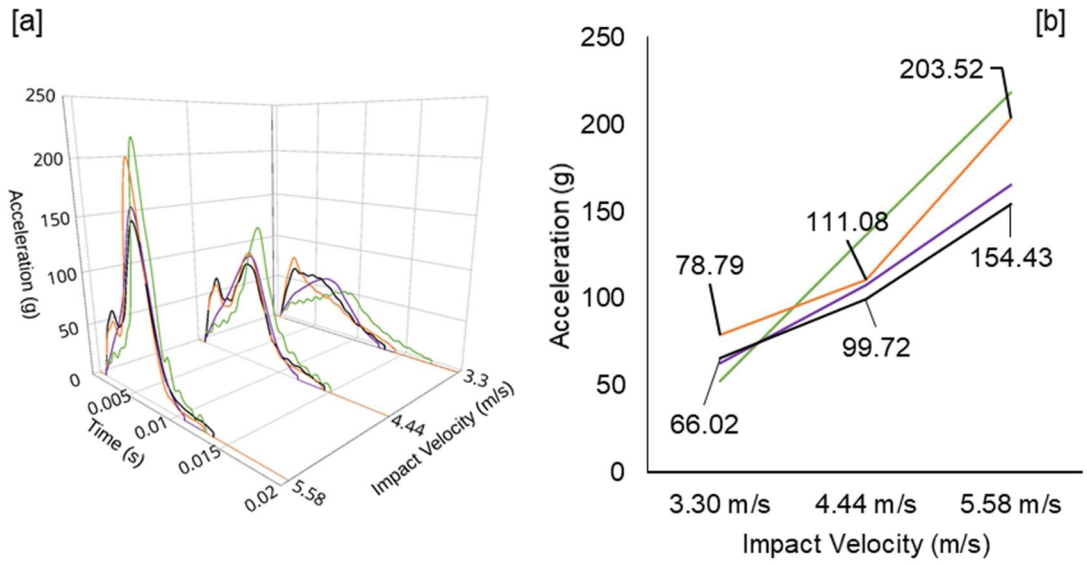

Figure 5-33: Acceleration Time Curves for 3.30 m/s, 4.44 m/s and 5.58 m/s impacts [a] and peak acceleration values [b] for 3VS PLA (Black) and GSI (Orange) optimal geometries with Riddell (purple) and Rawlings (Green) foams for comparison.

The GSI based 3VS reports inferior performance across the board to both the PLA based optimal and Riddell foam sample, with performance comparable to the Rawlings foam at the highest velocity.

5.3.5.3. Severity Index.

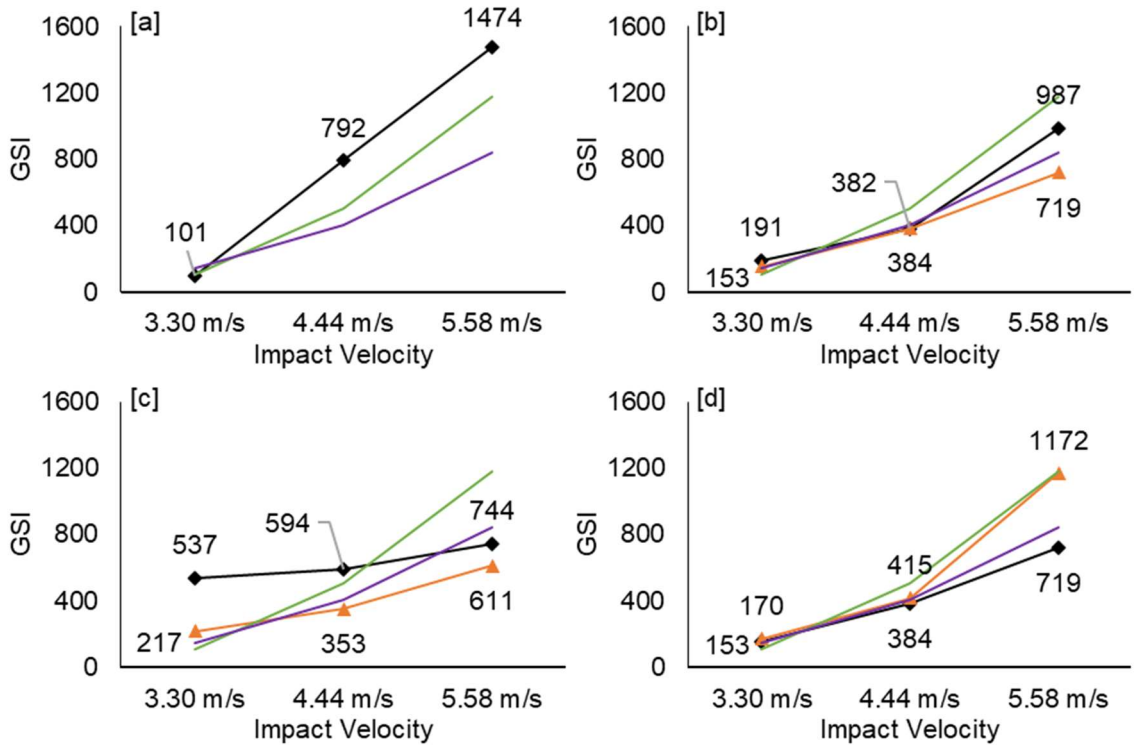

Figure 5-34: Calculated GSI values for 3.30ms^{-1}[a], 4.44ms^{-1}[b], 5.58^{-1}[c] and 3VS [d] PLA (black) and GSI (orange) optimal geometries with Riddell (purple) and Rawlings (green) foams for reference.

The lower acceleration plateaus of the GSI based optimal geometries resulted in lowered GSI values across the entire impact range, Figure 5-34 [b][c]. Notably, the gap between the GSI and PLA optimals is smaller at the optimal velocities for the PLA based sample. It is at these velocities where the GSI optimals lower acceleration plateau is offset by the spike in acceleration caused by densification.

Table 5-17: PLA, GSI and 3VS values for all tested optimal geometries.

Optimisation Condition		Optimal						
		3.30ms^{-1}	4.44ms^{-1}		5.58ms^{-1}		3VS	
Metric	Velocity		PLA	GSI	PLA	GSI	PLA	GSI
PLA	3.30	54.62	81.07	76.14	137.23	89.89	66.02	78.79
	4.44	180.17	98.14	99.72	125.36	88.98	99.72	111.08
	5.56	242.15	178.01	154.43	120.31	136.52	154.43	203.52
	3VS	24.37	19.24	17.69	21.02	17.19	17.01	21.01
GSI	3.30	100.56	190.85	153.13	537.11	216.90	153.13	170.31
	4.44	791.62	381.70	383.93	593.67	352.67	383.93	415.00
	5.56	1473.68	986.54	719.07	743.82	611.34	719.07	1171.79
	3VS	119.96	82.45	65.45	101.40	62.58	65.45	92.54

5.4. Discussion

5.4.1. Quasi-static performance of MOM geometry.

The developed L27 samples report a similar range of auxetic behaviour to the L9 samples, with a minimum IPR value of -1.11 being common to both sample groups, *Figure 4-15* and Figure 5-4. Therefore, the lateral strain response of a MOM sample is apparently entirely reliant on its geometry, with the base material having no influence, although new material families may alter this result. Although the developed theory for this metamaterial stipulates that the Poisson's ratio can be calculated from key parameters, in practice, the developed geometries exhibit a far more complex behaviour [231]. The departure from established theory is perhaps caused by TPUs effect on the deformation of the MOM, as discussed in chapter 4. Additionally, the uses of a single cell may exaggerate the observed IPR under compression.

Many of the L27 samples report IPR values that are above -0.2 for the entire range of compressive strains examined with 26_C, displaying behaviour that would suggest a Poisson's ratio of 0, Figure 5-4. No common geometric trait is observed in this selection of samples, meaning that the exact cause of this behaviour is difficult to establish.

Both the optimal geometries and the L27 samples exhibit stress-strain behaviour closer to that of an ideal foam than the behaviour of auxetic materials reported in the literature, Figure 5-3 and Figure 5-25 to Figure 5-28. As discussed in chapter 4, this is suspected to be the effect of the limited number of cells present within each sample, combined with the single cell present through sample depth.

A difference between the MOM samples and foams in seen in the shape of the efficiency curve, Figure 5-3 and Figure 5-25 to Figure 5-28. The MOMs efficiency-strain relationship has a unique peak, with a steep rise and fall in efficiency before and after this point. In comparison, foams tend to report a more gradual curving near the peak in energy absorption efficiency [27,366-368]. The singular points of maximum efficiency result from the densification of the single cell. As further energy absorption comes from deformation of the base material, significantly more force, and thus stress is required. Therefore the efficiency rapidly decreases as the $\sigma_{m\varepsilon_1}$term of equation 2-9 rapidly increases in value. The non-uniform collapse of cells in foams spreads the increase in required stress over a greater strain range, resulting in the curve response seen.

5.4.2. Optimal Geometries

The developed optimal geometries provided favourable performance compared to both elastomeric foams and novel solutions presented in the literature, Figure 5-29 to Figure 5-34. The optimals consistently perform as well as the best performing L27 samples, with only the 3.30ms^{-1} optimal being outperformed in terms of average PLA response, Figure 5-6 and Figure 5-29. The chosen optimisation methodology is the root of this discrepancy. The use of MSD accounted for both performances, in terms of low PLA, and repeatability. Although 6_C provided a lower average PLA, the optimal geometry provided more consistent performance across the five impacts. Due to the demands of the football environment, this was seen as an acceptable trade-off.

5.4.2.1. Main effects, Interactions and ANOVA.

Wall thickness was consistently determined to be the primary source of the performance of a sample, with contribution ranging from 34 to 79%. Although this response indicates that the developed MOM samples act as honeycombs, the continued significance of parameter interactions indicates a more complex behaviour. The effects of the single cell present in sample depth influenced the importance of wall thickness due to the effects of densification. Therefore, the significance of all parameters may be subject to change if cell size was to be reduced.

The insignificance of the fold angles across all examined metrics can be linked to their variability under deformation. Consider, for example, two variants of MOM with all parameters equal aside from α angles of 1° and 9°. During deformation the sample with an α of 1° would reach an apparent α value of 9°, assuming the deformation patterns discussed in chapter 4 remained. Both β and γ would decrease as the sample contracts, as the double arrowhead deforms. Therefore, increasing α or decreasing γ and β values of a sample would in effect define a level of pre-compression, assuming that wall thickness and overall cell size are consistent. If the 1° sample reached an α of 9°, its performance would be expected to be near-identical to the 9°sample due to the apparent similarity in geometry. Therefore, variation caused by the angle change would be minimal, and its contribution could be deemed as insignificant.

The captured data is sufficient to speculate on the location and physical effects of the significant interactions. Neither the α-β and β-γ interactions are discussed as they were not found to have any significant effect on any of the optimisation metrics studied.

If the α angle is viewed as a designated level of pre-bending of a double arrowhead honeycomb, the α-t interaction would indicate the effectiveness of this pre-bending. This pre-bending eliminates the high initial peak force seen in singular cells and type-II geometries, as the whole structure is effectively deformed beyond the initial buckling [220,289-292]. Thus, the effect of the alpha angle is to fine-tune the wall thicknesses, allowing for the use of a thicker wall without the pre-buckling resistance breaching limits associated with head injuries. In the context of MOM geometries, a variant with an increased α could be seen as a more deformed, and therefore softer, version of an identical sample with a reduced α.

The β-t and γ-t interactions have two possible interpretations within the MOM geometry. They could refer to the space in which the walls are free to deform. However, the more likely interpretation is that they indicate the locations where the two sheets join. Previous analysis has shown that peak stress develops as the ridges of the MOM geometry [24]. The combination of angles and wall thickness defines the quantity of material at these joining locations and therefore influences the strength of the structure, Figure 5-35.

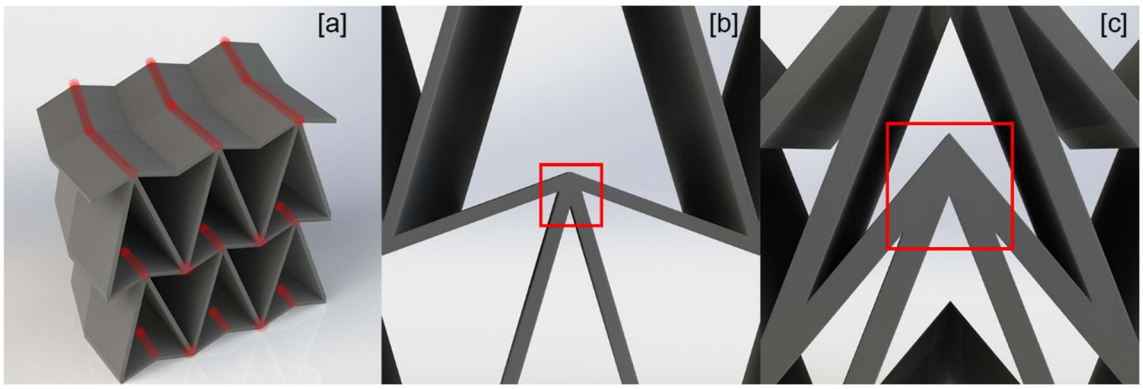

Figure 5-35:[a] Locations of sheets joins within geometry, shown in red, [b] smallest join and [c] larges join achievable in the L27 array design space.

The β-t and γ-t interactions are not consistently significant, which results from the limited number of cells, and therefore connections, within the tested samples.

The α-γ interaction is the most challenging interaction to place within the structure. The interaction may indicate that the γ based Miura-Ori sheets play a larger role in sample performance that the β based sheets. However, the β based sheets cannot be replaced as they help inform the in-plane deformation of the double arrowhead cross-section, and therefore overall sample response.

Throughout the derived main effects and interaction plots, the best performance is found by maximising β and minimising γ, Figure 5-9 to Figure 5-24. This consistent relationship suggests a compact and proportionally more re-entrant cell geometry improves performance. Smaller cells naturally maximise the number of cells within a sample, increasing the amount of material under the impact site. However, the increased cell count would increase the relative density. Thus, performance would need to be balanced against density due to the weight limitation of head protection.

5.4.2.2. Performance of the 4.44ms^{-1} Optimals.

The optimal geometries generated for the middle impact velocity are outperformed in terms of PLA and GSI by the 5.58ms^{-1} GSI optimal, Figure 5-29 and Figure 5-34. The three geometries only differ in β and γ angles, neither of which significantly affect sample performance, Table 5-8, Table 5-11 and Table 5-15.

Both the contribution of wall thickness and variation in parameter interactions are lower at the medium test velocity in comparison to the lowest and highest velocities, Table 5-8, Table 5-11, Figure 5-13 and Figure 5-19. Combined with the transition in the dominant wall thickness from 0.6 to 0.9mm; these results suggest that the middle impact velocity is close to a threshold energy where optimal design becomes more complicated. For example, both the γ- *t* and α-γ interactions significantly contribute to PLA response at a similar level Table 5-8. As α and α – *t* are not significant, the optimisation process is free to select the best combination of α and γ, 5°and 80° respectively, Figure 5-13 [a]. However, the γ- *t interaction*, which is constrained by the optimal thickness of 0.9mm, suggest an optimal γ of 140°. For the performance again of the first interaction to be leveraged, the second must be sacrificed and vice versa. Thus, the performance of the optimal geometry is hampered.

The levels used for wall thickness and α may also play a role. For instance, if a thickness between 0.6 and 0.9mm was available, an intermediate stiffness of geometry may have been possible, allowing for the better performance to be extracted from the array.

5.4.2.3. GSI 3VS poor performance.

The 3VS GSI optimal also failed to meet its predicted performance, Table 5-16. The difference between prediction and experimental result results from the samples poor performance at the 5.58ms^{-1} impact velocity, which led to a rapid increase in reported GSI, Figure 5-33 and Figure 5-34.

Developed GSI optimal geometries were consistently softer than their PLA based counterparts, with lower plateau stresses observed, Figure 5-25 to Figure 5-28. The softer response produced lower pre-densification accelerations and therefore a lower GSI, Figure 5-30 to Figure 5-34. The weightings used to generate 3VS prioritised the lowest test velocity. Therefore, the optimisation process would have favoured parameter combinations that minimised GSI at this velocity, lowering part stiffness. The low stiffness offered by this component resulted in poor performance at the highest velocity as it was unable to absorb sufficient energy prior to densification. The challenge of this metric is noted in the conducted ANOVA, where wall thickness reported its lowest contribution, Table 5-14.

5.5. Conclusions.

The successful optimisation of the MOM geometry to football impacts required a robust and varied data set. Using the learnings from chapter 4, a series of 27 samples were designed using the Taguchi method. The samples were exposed to both quasi-static forces and impacts scenarios representative of those seen within the sport.

The stress-strain response of the developed samples differed from the expected strain - stiffening of auxetic materials. This difference in performance was linked to the limited number of cells present in each MOM samples. Cell size had been maximised to aid both manufacturing accuracy and expand the range of achievable wall thicknesses. The captured Impact data was used to generate a series of statistical plots, to enable the choice of parameters that would lower the PLA and GSI values seen when the MOM geometry was impacted. Additional analysis was conducted so that the significance of each geometrical parameter and its contribution to performance could be established. This approach was used to define an optimal for both PLA and GSI at each velocity tested. A weighted score allowed for the design of geometries that considered the entire velocity range.

Throughout the analysis, wall thickness was the dominant factor in sample performance, responsible for 34 to 79% of the variation seen in sample response. This dominance was linked to the limited number of cells present within each sample. The identified fold angles were rarely significant to sample performance. Unlike wall thickness, the angles were not constant through sample compression, which may have limited their ability to inform sample collapse. In comparison, interactions between the angles and wall thickness were consistently significant, which allowed for the fine-tuning of the dominant walls.

When tested the majority of the optimal geometries performed favourably to the elastomeric foams and novel materials presented in the literature. However, the performance was commonly only better at the impact for which the sample had been optimised. For three of the developed geometries, the performance was worse than different variants of the MOM geometry. The underperformance was linked to limitations of the array, and manufacturing process, which prevented designs between the levels defined in the array.

Various limitations in performance had been linked to the number of cells present within each sample. This suggested that further performance may be gained for the MOM geometry by reducing overall cell size, and therefore increasing the number of cells within a sample.

Chapter 6: The Effects of Cell Scaling on MOM Geometry Performance.

6.1. Introduction.

The previous chapter established that the MOM geometry when manufactured from thermoplastic polyurethane, was capable of absorbing impact energies seen within American football. Using the Taguchi method, a range of optimal geometries were developed that achieved superior performance versus elastomeric foams.

Throughout the analysis used to generate the optimal geometries, the cell wall thickness was the dominant factor in a sample's response to impact. Additionally, the loading response of the tested geometries mimicked that of a single cell, rather than the strain stiffening of an auxetic material. It was concluded that the utilised cell size potentially limited the performance of the tested geometries.

Previous examination of the MOM geometry has included a comparative study of samples with different scales of parametrically identical geometry [24]. J Harris maintained the number of cells present within a sample; thus, its results cannot be easily used to establish if cell size affects energy absorption. The influence of relative cell size needs to be established, as smaller cells may better leverage the auxetic nature of the MOM. Achieving this aim would increase the potential of the MOM to reduce injury risk in comparison to contemporary materials when used as a helmet liner.

Increased cell size was not examined in chapter 5, as a scaled-up version of the optimal geometries presented would not fit within the available volume of a helmet liner. Additionally, the increase in cell size would not alter the limitation of the single-cell response seen in chapter 5.

The primary aim of this chapter is to investigate if the reduction in cell size increased the energy absorption capability of the MOM geometry, and to identify a suitable candidate for use within an American football helmet.

1. Determine the minimum achievable cell size, given the manufacturing constraints of fused filament fabrication.
2. Explore how the change in cell size affects a range of previously established performance metrics.
3. Examine if the introduction of more cells within a sample volume reduces injury risk from American football impacts, by better leveraging the geometries underlying auxetic properties.
4. Identify the optimal geometry with the greatest potential to reduce injury risk when employed as a helmet liner replacement.

6.2. Materials and Methods

6.2.1. Cell size reduction.

To maintain the geometry of the developed optimals, the identified parameters of a single cell were assessed for their sensitivity to scaling. While the fold angles would be insensitive to scaling, wall thickness needed to be adapted to maintain the relative density of the walls. As such, the wall thickness for each optimal was expressed as a non-dimensional ratio ($\emptyset$), equation 6-1. The updated geometric parameters for the seven optimal geometries are provided in Table 6-1.

$$\emptyset = \frac{t}{D} \qquad 6\text{-}1$$

Table 6-1: Optimal Geometry Nondimensional Parameter Values

Optimal Design Velocity	Metric	α (°)	β (°)	γ (°)	$\emptyset$
3.30	Both	1	38	140	0.02
4.44	PLA	5	33	110	0.03
	GSI	5	33	140	0.03
5.58	PLA	1	43	140	0.03
	GSI	5	38	140	0.03
3VS	PLA	9	33	140	0.03
	GSI	5	33	110	0.03

So that a complete number of MOM cells were present through the thickness of any developed samples, scaling levels were developed by reducing the value cell depth, D, Figure 4-1.

Three values of D were identified, 30mm, 15mm and 10mm, which equated to scaling levels of 100%, 50% and 33% respectively. Cell width, L, was scaled by the same amount as D to maintain cell geometry. Overall sample dimensions were maintained at 60 x 60 x 30 mm.

Although the FFF printer could have achieved a smaller cell scale in terms of its resolution, the sample size was limited by manufacturability of the thin walls. The 3.30ms^{-1} optimal had the thinnest wall, 0.6mm, Table 5-15. A 33% scale variant would require a wall thickness of 0.2mm. Test prints with the 0.3mm diameter nozzle used in previous chapters were unable to achieve this dimension, despite the software's attempt to reduce the flow of material. For the manufacture of this sample, a 0.2mm nozzle was utilised. While this would have enabled the manufacture of 25% scale variants of the other optimal geometries, these were not manufactured to maintain a full set of scaled variants.

One full size and two downscaled variants were manufactured for each of the seven developed optimal geometries, providing a total of 21 samples for this study. Renders of the three samples designed using the PLA 3VS parameters, Table 6-1, are shown in Figure 6-1. Full scale samples were remanufactured so that any change in base material would not affect performance. Although the 3VS GSI and 4.44 PLA optimal geometries shared parameters, a full set of samples was generated for both. This was done to increase the number of samples studied at each scale, and therefore the robustness of the statistical analysis that would be performed on the results.

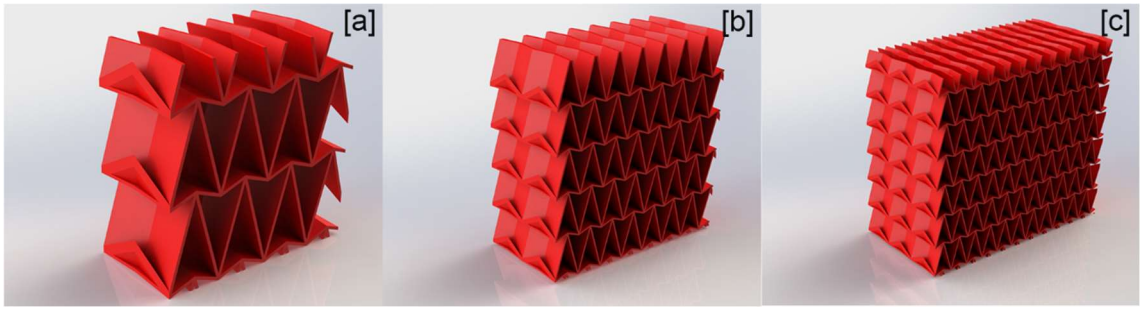

Figure 6-1: Example renders of full-scale geometry [a], 50% scale [b] and 33% scale [c].Sample presented here have exterior dimensions of 60mm by 60mm by 30mm.

The print profile developed for the L27 components, Table 5-3, was utilised for the production of the reduced cells, with the nozzle diameter setting changed where appropriate. Samples were manufactured on the same printer used in previous chapters and subjected to the same quality controls as in Chapters 4 and 5.

6.2.2. Quasi-static and dynamic loading.

The reduced scale samples were subjected to the same quasi-static, and dynamic testing used to develop the optimal geometries, the full details of which are covered in chapters 4 and 5, respectively. For clarity, the critical aspects of each test are covered here.

For quasi-static testing samples were initially preloaded to 5N, before being compressed at a rate of 50mm per minute to a maximum strain of 0.6m/m. Samples were then unloaded at the same rate. The same pattern used in chapter 4 to capture lateral strain measurements was placed on the manufactured samples and tracked through testing via the use of a visual strain gauge.

Impact testing was conducted at 3.30ms^{-1}, 4.44ms^{-1} and 5.58ms^{-1} with a mass of 4.8kg. Five impacts were conducted at each velocity, with impacts spaced 75s apart. Samples were given 24 hours between each velocity to relax and were inspected for damage. This rest period minimised the influence of the previous testing on each velocity.

6.2.3. Analysis of performance.

Captured quasi-static and dynamic data sets underwent the same data-handling process discussed in previous chapters to provide the necessary stress-strain and acceleration-time curves for further analysis.

From acceleration-time data, PLA, GSI and 3VS values for the scaled cell geometries were calculated using the relevant equations presented in chapter 5.

Using averaged acceleration time traces an estimation of a samples stress response to dynamic strain was calculated using equations 5-3 and 5-4.

Both quasi-static compression and calculated dynamic stress-strain data was used to calculate the normalised stress response of the scaled samples, using equation 2-10, repeated below. The value of E^b was taken as the reported value for the material, 26Mpa, [344].

Using the captured quasi-static compression data, both the volumetric energy absorption and normalised energy absorption values were calculated using equations 2-6 and 2-7. Energy absorption efficiency was also calculated, using equation 2-9, so that the validity of using maximum lateral strain as densification strain could be assessed.

To investigate the effect of cell scaling on sample performance, each metric (M_s) was normalised to the relevant value of the 100% scale sample (M_f) using equation 6-2. Normalised values (M_n) were calculated for PLA, GSI and 3VS from the dynamic data, as well as $\tilde{\sigma}_{\varepsilon_n}$, $\widetilde{W}_{\varepsilon_n}$ and ε_η from the gathered quasi-static data

$$M_n = \frac{M_s}{M_f} \qquad 6\text{-}2$$

To determine the significance of any effect cell size had on performance, M_n values were used to conduct ANOVA, following the methodology presented in chapter 5. Normalised values were used to reduce variation caused by the differing geometries performance across the investigated range of impact energies as this study was only concerned with the variation caused by the reduction in cell volume.

The use of 21 samples specified the value of n, the number of experimental runs used in the analysis. This resulted in a value of 20 for the experimental degrees of freedom (f_t). As three cell scales had been used, as a factor it was considered to have 2 degrees of freedom, (f_x). Thus the value of f_e was 18, as dictated by equation 5-7. For cell size to be considered statistically significant at a 95% confidence interval the critical F_x value was 3.5546 [355].

6.2.4. Identification of best performing geometry.

To identify the geometry with the most potential to reduce injury risk, a hierarchy of dynamic performance metrics needed to be established. As any future helmet would be required to pass the standard NOCSAE testing, any optimal geometry, either full size or downscaled, that was unable to meet the specified linear requirements would be discounted from use, [184].

As noted in the literature, PLA was a better predictor of SRC risk than GSI [72,83]. Therefore, the selection of the most favourable geometry would be based on this metric. However, a fundamental limitation of the studied elastomeric foams was their inability to be optimised to more than one impact condition, due to the limited control over their material properties, [19]. Therefore, samples were selected based on the lowest PLA based 3VS presented. The use of this metric would select the geometry that lowered injury risk across the entire range of examined geometries.

Sample density was also considered during selection, with lower density components given preference over higher density ones.

6.3. Results

6.3.1. Quasi-static performance

Across all examined optimal geometries the 50% and 33% scale cells exhibit little to no strain-softening with some samples, such as the 4.44ms^{-1} PLA optimal, even exhibiting signs of strain stiffening behaviour, Figure 6-2.

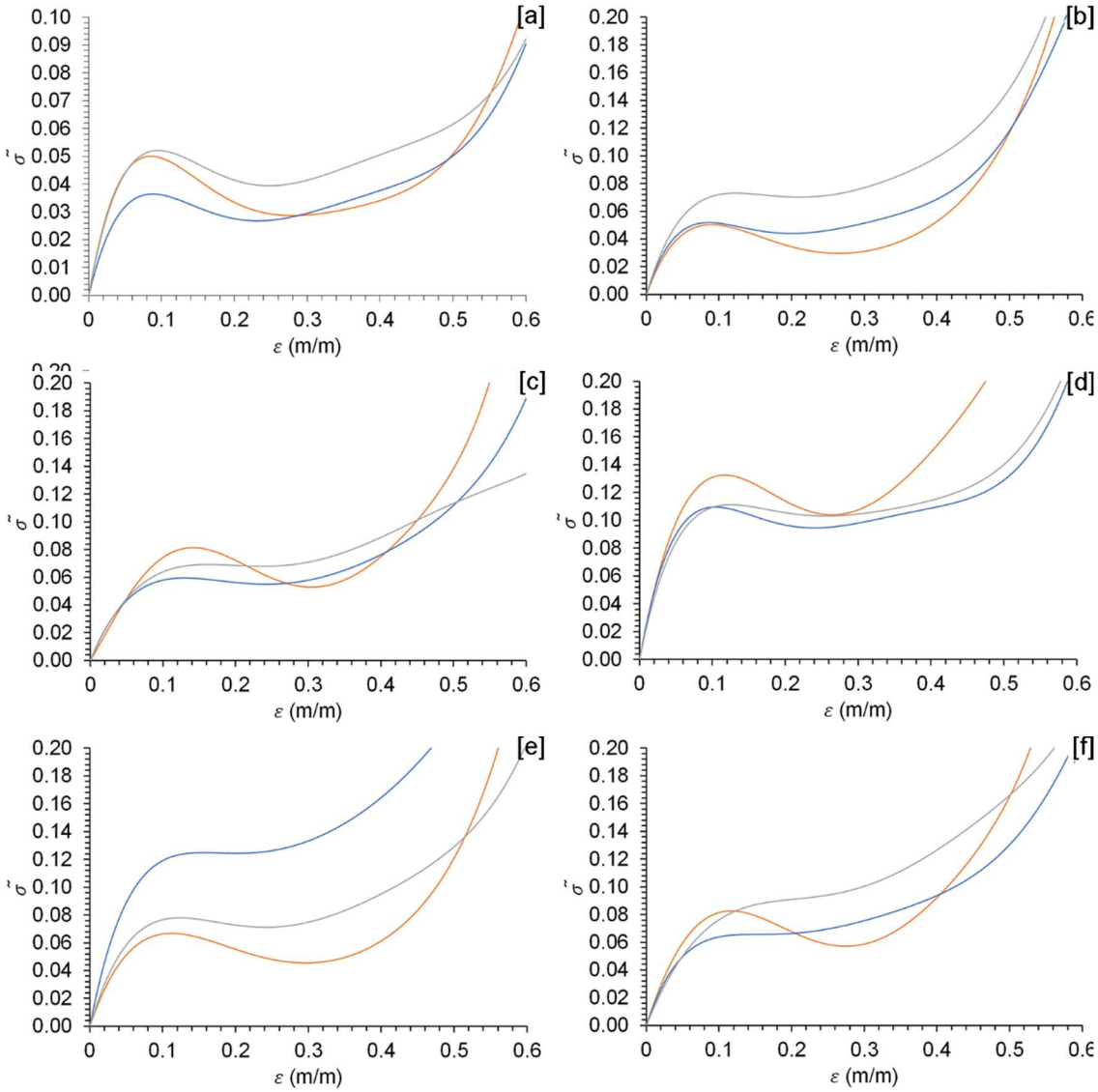

Figure 6-2: Normalised stress vs strain for [a] 3.30ms^{-1} optimal, [b] 4.44ms^{-1} PLA / 3VS GSI optimals, [c] 4.44ms^{-1} GSI optimal, [d] 5.58ms^{-1} PLA optimal, [e] 5.58ms^{-1} GSI optimal and [e] 3VS GSI optimal, for cell scale of 100% (orange), 50% (blue) and 33% (grey).

Aside from the 5.58ms^{-1} GSI optimal, the 50% scale cells offer an initially softer response to loading than the 100% and 33% scale geometries. Interestingly, the smaller scale geometries also exhibit much later densification, denoted by a significant rise in stress, than their full-scale counterparts.

On examination, the 50% scale 5.58ms^{-1} GSI optimal was found to have an average wall thickness over 0.15mm thicker than designed, Figure 6-3. This wall thickness placed it well above both the design thickness, 0.45mm, and the average for samples with the same design thickness, 0.48mm.

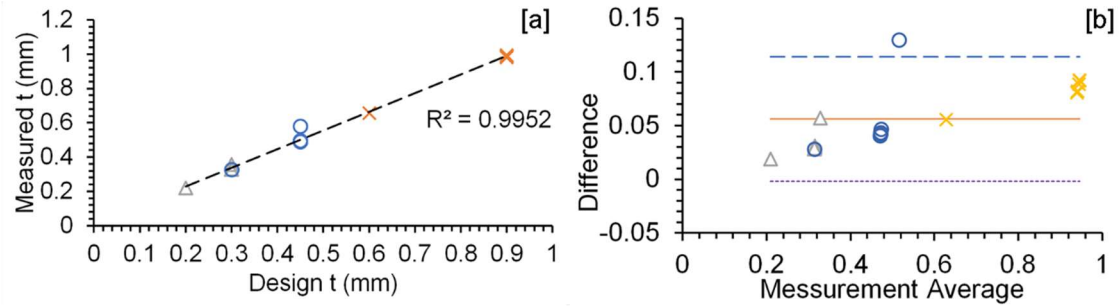

Figure 6-3: Measured thickness vs designed thickness for 100% scale (Orange Cross), 50% scale (Blue circle)and 33% scale (grey triangle) geometries as a simple scatter plot [a], and Bland-Altman plot [b]. With the mean difference (solid Orange), Lower agreement limit (Purple Dotted) and Upper agreement limit (Blue Dashed)

Attempted reprints of this sample were unable to compensate for this growth in geometry. The issue was unique to this sample, with the other 50% scale samples presenting with wall thickness consistent with other manufactured samples, Figure 6-3. While its trace is included in this section for completeness, data derived from this sample was not included in any further analysis. This naturally reduced the value of n to 20 when ANOVA was conducted. The observed tend seen in previous chapters of parts with the largest designed wall thicknes exhibiting the most growth in measured wall thickness contiused across all manufactured scales.

A significant difference in normalised stress at the strain of maximum efficiency, $\tilde{\sigma}_{\varepsilon_n}$, was found at a 95% confidence level, Table 6-2. Cell size was deemed responsible for 37% of the variation seen between the sample groups. The remaining variation is attributed to the differing performance of the optimal geometries, which, although minimised by the use of normalised data was not completely removed.

Table 6-2: ANOVA results for normalised stress at strain of maximised efficiency.

Factor	f_g	S_g	V_g	P_g(%)	F_g
Cell Scale	2	4.8294	2.4147	36.87	5.3794
Error	17	7.6310	0.4489	63.13	
Total	19	12.4603		100.00	

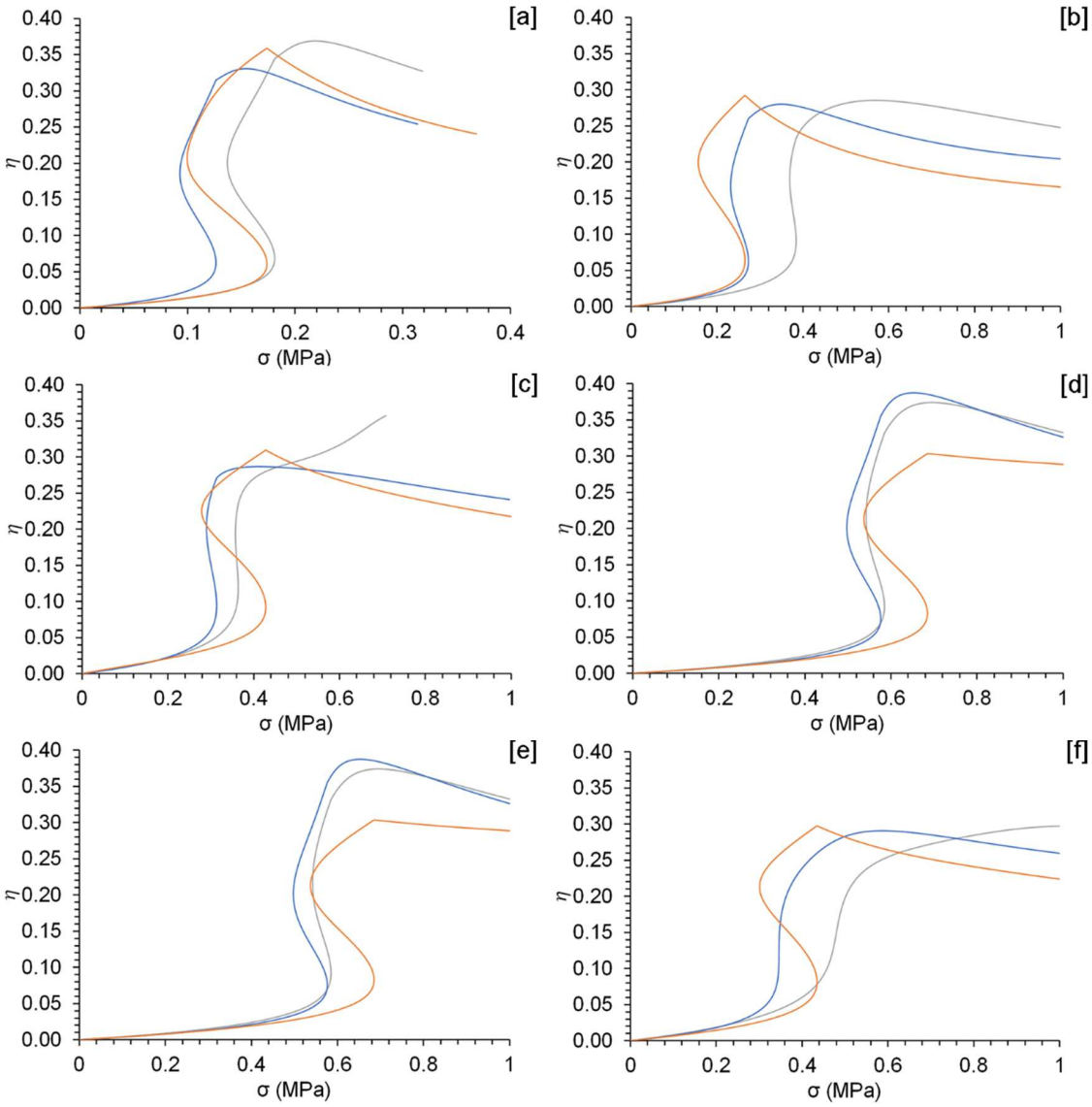

Figure 6-4: Efficiency vs compressive stress for [a] 3.30ms^{-1} optimal, [b] 4.44ms^{-1} PLA / 3VS GSI optimals, [c] 4.44ms^{-1} GSI optimal, [d] 5.58ms^{-1} PLA optimal, [e] 5.58ms^{-1} GSI optimal and [f] 3VS PLA optimal, for cell scale of 100% (orange), 50% (blue) and 33% (grey).

The developed efficiency curves of the 50% and 33% scale optimals show a significant change in how peak efficiency is reached in comparison to the full-scale samples, Figure 6-4. In contrast to the full-scale samples, the 50% and 33% samples exhibit a curved response around the point of maximum efficiency, similar to that seen in the response of elastomeric foams [27,366-368].

The difference in response is attributed to the presence of more cells in the direction of loading. These cells were observed to collapse non-uniformly; thus, the peak efficiency reached by each cell was present at a different strain value, which leads to the presented curve.

Table 6-3: Values of ε_η identified for each optimal design.

Optimal Geometry	100% Scale	50% Scale	33% Scale
3.30ms^{-1}	0.50	0.47	0.51
4.44ms^{-1} PLA	0.38	0.46	0.56
4.44ms^{-1} GSI	0.41	0.41	0.60
5.58ms^{-1} PLA	0.37	0.49	0.48
5.58ms^{-1} GSI	0.42	0.42	0.60
3VS PLA	0.41	0.41	0.60
3VS GSI	0.39	0.39	0.43
Average ± 1 Standard Deviation	0.412 ± 0.039	0.433 ± 0.034	0.539 ±0.064

The 33% scale cells consistently reported higher strains of maximum efficiency, than their 100% scale counterparts, Table 6-3. The behaviour of the 50% scale cells is more complex, with ε_η not consistently between that reported for the 100% and 33% scale variants. Therefore, the improvement in performance exhibited by reducing cell size, may not be consistently present until a specific scale of cell size is reached. The change in densification strain was found to be significant at a 95% confidence level, Table 6-4.

Table 6-4: ANOVA results for the strain of maximum efficiency.

Factor	f_g	S_g	V_g	$P_g(\%)$	F_g
Cell Size	2	0.3813	0.1906	54.15	9.8577
Error	17	0.3288	0.0193	45.85	-
Total	19	0.7101	-	100.00	-

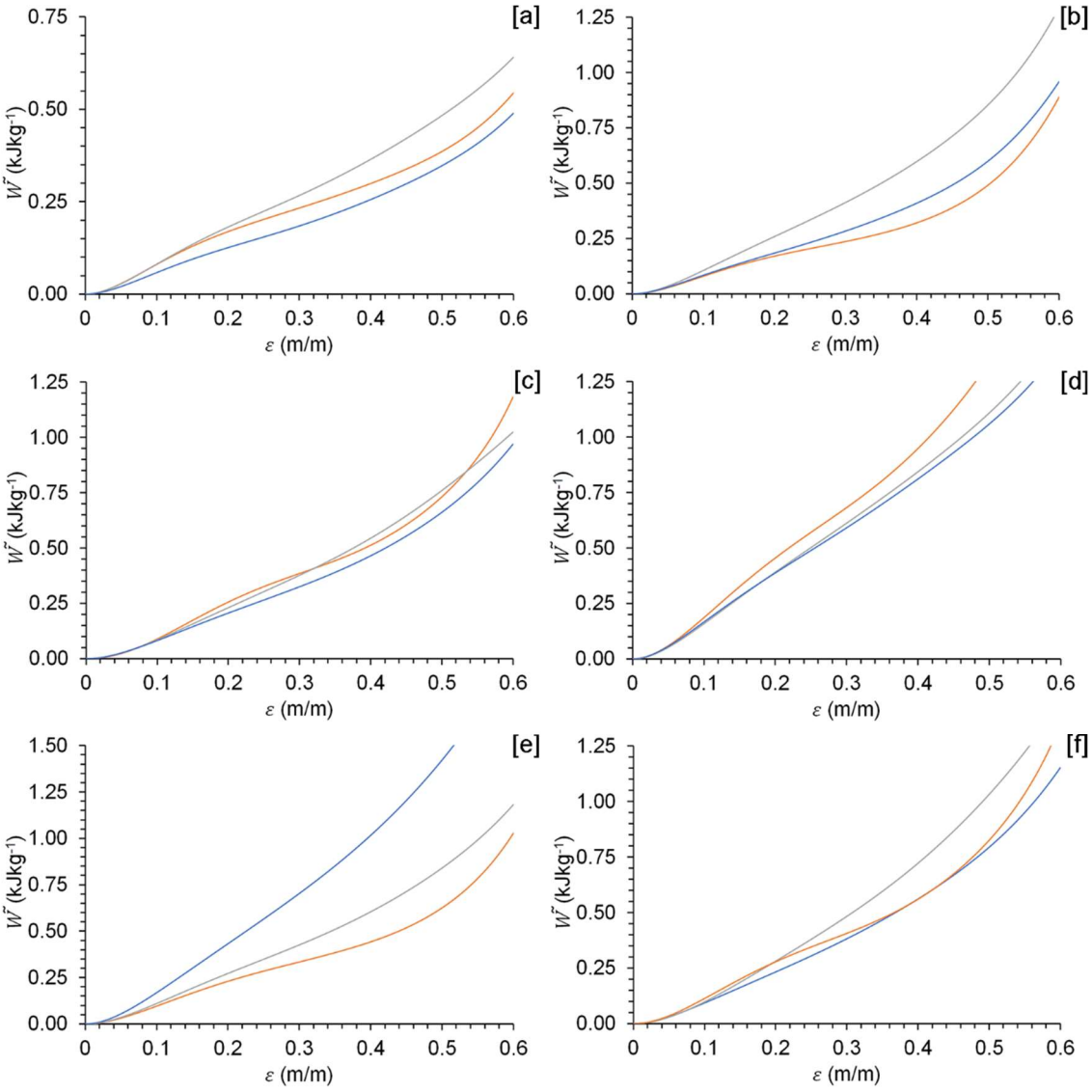

Figure 6-5: Normalised energy absorption vs strain for [a] 3.30ms^{-1} optimal, [b] 4.44ms^{-1} PLA / 3VS GSI optimals, [c] 4.44ms^{-1} GSI optimal, [d] 5.58ms^{-1} PLA optimal, [e] 5.58ms^{-1} GSI optimal and [f] 3VS PLA optimal, for cell scale of 100% (orange), 50% (blue) and 33% (grey).

The full-scale samples exhibit a slowing in normalised energy absorption around a strain of 0.2, which is not present in the response of the reduced scale samples, Figure 6-5. As the reduced scale samples exhibit little or no strain-softening the rate of energy absorption is maintained, resulting in greater energy absorbed for an equivalent deformation. The influence of the delayed densification can be seen here again when the 100% scale samples all exhibit a notable uptick in energy absorption towards the higher levels of strain, due to the higher forces needed to deform the base material. Again the influence of cell size was found to be significant at a 95% confidence interval, Table 6-5.

Table 6-5: ANOVA results for normalised energy at strain of maximised efficiency.

Factor	f_g	S_g	V_g	$P_g(\%)$	F_g
Cell Size	2	5.7330	2.8665	46.78	7.5935
Error	17	6.4174	0.3775	53.22	-
Total	19	12.1504	-	100.00	-

6.3.2. Dynamic Performance.

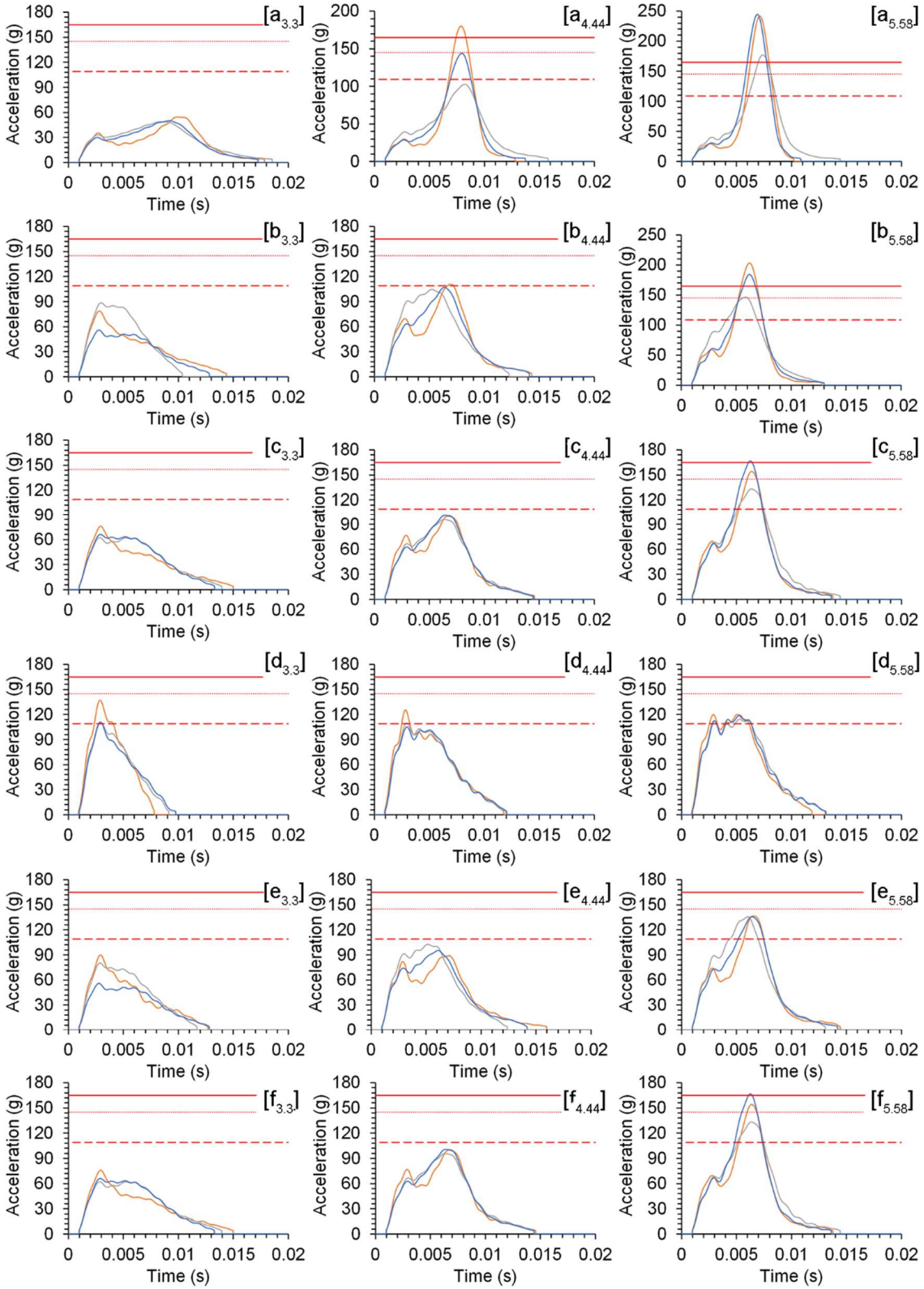

Figure 6-6: Acceleration vs time for [a] 3.30ms^{-1} optimal, [b] 4.44ms^{-1} PLA / 3VS GSI optimals, [c] 4.44ms^{-1} GSI optimal, [d] 5.58ms^{-1} PLA optimal, [e] 5.58ms^{-1} GSI optimal and [f] 3VS PLA optimal, for cell scale of 100% (orange), 50% (blue) and 33% (grey). Label subscript denotes impact velocity. 1%(red dash), 5% (red dot) and 10% (Red line) SRC risk for comparison [172].

The strain-stiffening response of the downscaled samples noted in their quasi-static performance influences their dynamic response across all tested velocities. Whereas the full scale samples have a definitive dual peak response when densified, Figure 6-6[$b_{4.44}$] [$e_{4.44}$][$f_{4.44}$], the downscaled samples show a slowing in the rate of acceleration gain until they reach a single peak value. The extra energy absorption predesification allows for a lower PLA when impacted, Figure 6-6 [a][f].

Although the increased plataue strength of downscaled samples could be expected to hamper their reported PLAs, this does not appear to be the case, with either consistent performance with the 100% scale samples, Figure 6-6[$d_{5.58}$], or showing a slight reduction in PLA, Figure 6-6[$c_{3.3}$], due to the initial peak in stress presented by the full scale samples being equivalent to the plataue of the downscaled samples.

Although cellular theory indicates that non-densified samples offer superior performance, and therefore a reduction in injury risk, this improved performance is limited to the impact condition for which the material is specified. For example, although no scale variant of the 5.58 PLA optimal densifies at any tested velocity, it reports PLA twice that of the 3.30 optimal when impacted at 3.30ms, despite the 3.30 optimal exhibiting signs of densification at this velocity.

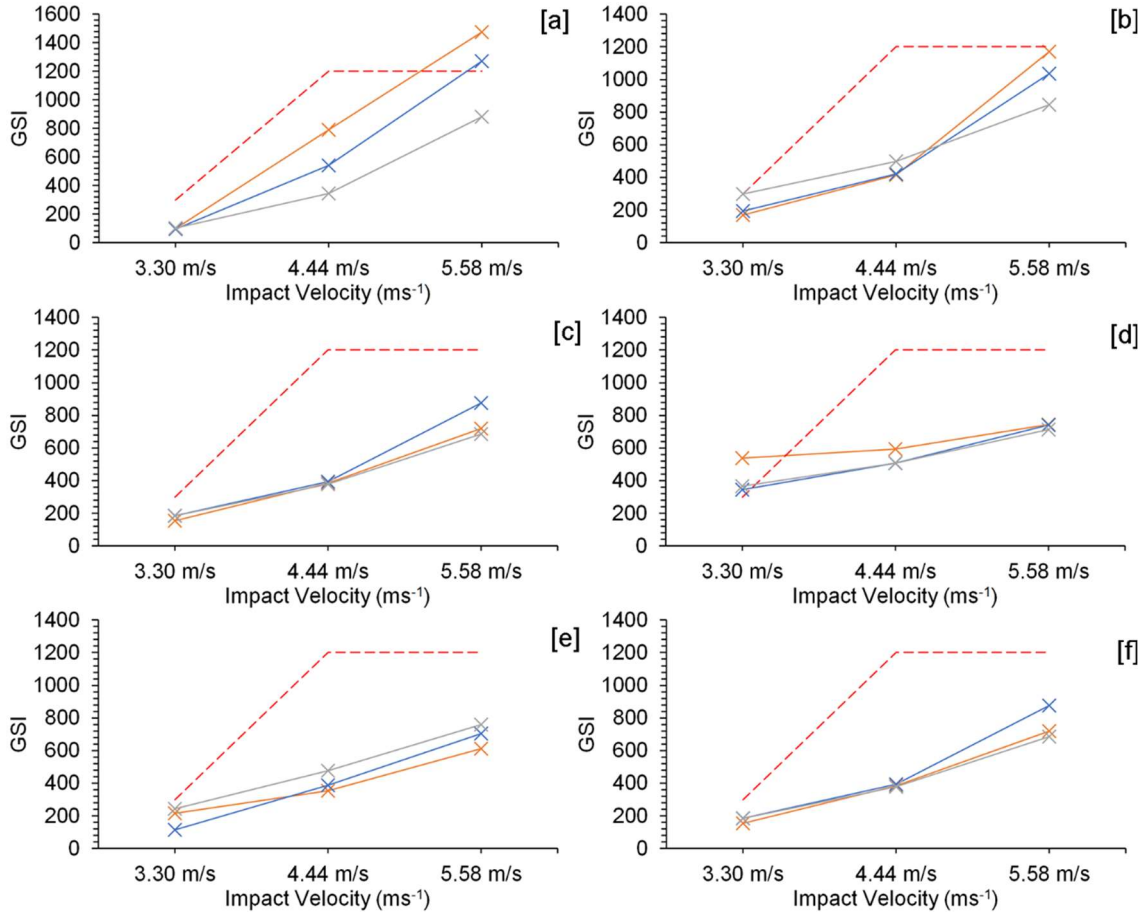

Figure 6-7: Calculated GSI vs impact velocity for [a] 3.30ms^{-1} optimal, [b] 4.44ms^{-1} PLA / 3VS GSI optimals, [c] 4.44ms^{-1} GSI optimal, [d] 5.58ms^{-1} PLA optimal, [e] 5.58ms^{-1} GSI optimal and [f] 3VS PLA optimal, for cell scale of 100% (orange), 50% (blue) and 33% (grey). NOCSAE GSI limits (dashed red) for comparison.

The downscaled geometries do not exhibit a comparable improvement in GSI response as seen in the PLA data, Figure 6-7, with downscaled samples not consistently offering improved or worse performance than the full scale samples. This results from the strain-stiffening response of the downscaled samples, which results in elongated periods of increased accelerations, in comparison to the full-scale geometries.

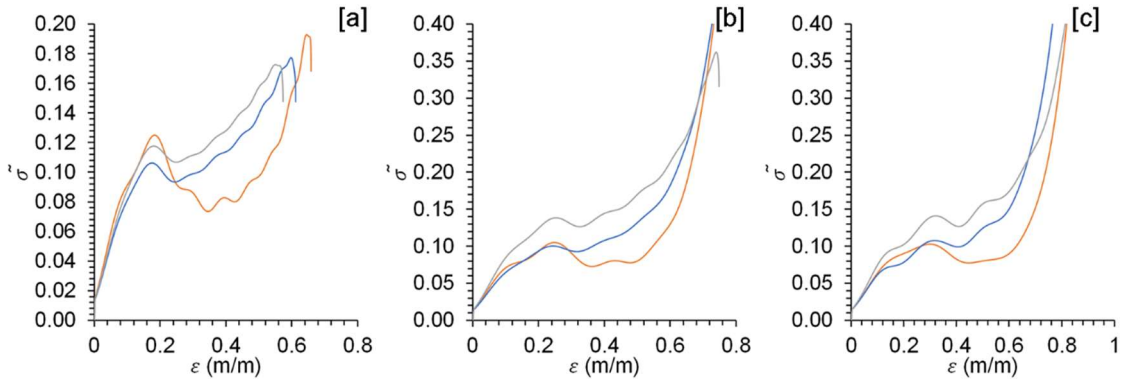

Figure 6-8: Normalised stress vs strain for the 3.30ms^{-1} optimal 100% scale (orange), 50% scale (blue) and 33% scale (grey) samples, for the 3.30ms^{-1} [a], 4.44ms^{-1} [b] and 5.58ms^{-1} [c] velocity impacts.

The change in stress-strain behaviour seen in the quasi-static data is present within the dynamic data for the scaled optimals, where 100% scale samples exhibit signs of strain-softening, with the scaled variants showing strain-stiffening behaviour, Figure 6-8.

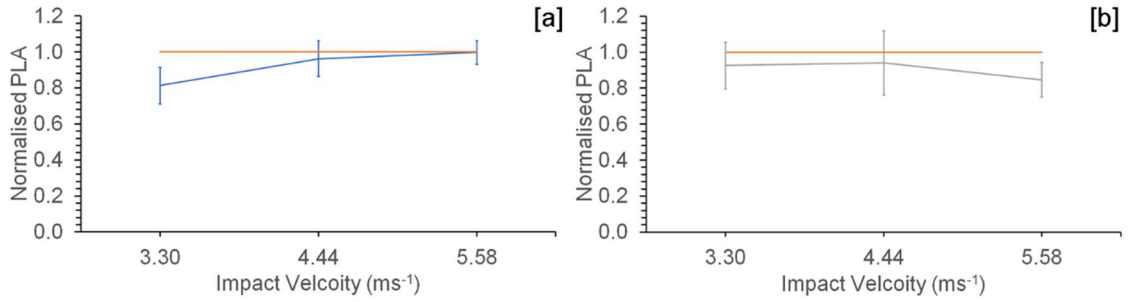

Figure 6-9: Average normalised PLA vs impact velocity for the 50% scale samples [a] and 33% scale samples [b], with 100% scale cells (blue) for reference. Error bars represent one standard deviation.

The 50% and 33% scale samples exhibit different behaviour across the full range of examined velocities. The 50% scale samples behave more like their full-scale counterparts as impact energy increases. In comparison, the 33% scale samples display more divergent behaviour, Figure 6-9.

The 33% scale samples on average provide worse performance, in terms of GSI, at the lowest impact velocity than their full-scale counterpart, Figure 6-10, with a marginal improvement in performance at the highest tested velocity. In comparison, the 50% scale sample produced an almost identical response.

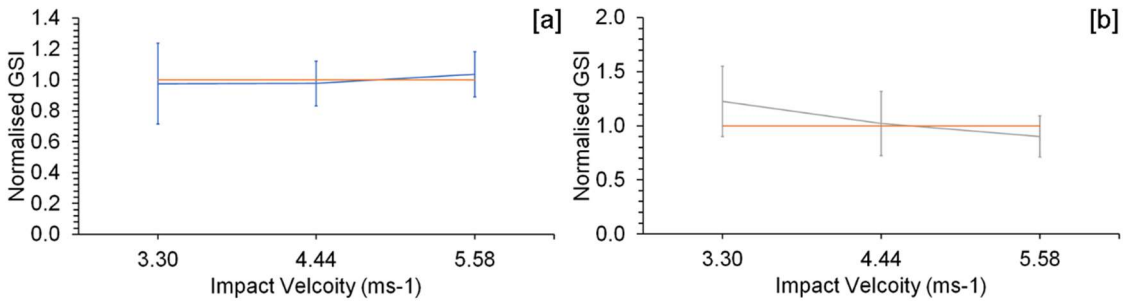

Figure 6-10: Average normalised GSI vs impact velocity for the 50% scale samples [a] and 33% scale samples [b], with 100% scale cells (blue) for reference. Error bars represent one standard deviation.

Cell size was found to significantly affect the PLA based 3VS values developed by the tested geometries, Table 6-6. However, the GSI 3VS was not significantly affected, Table 6-7. As the 50% scale sample average GSI response was virtually identical to that of the 100% scale samples, an additional ANOVA was conducted with this selection of samples removed from the analysis. This

Table 6-6: ANOVA results for normalised peak linear acceleration 3VS.

Factor	f_g	S_g	V_g	$P_g(\%)$	F_g
Cell Size	2	0.0480	0.0240	37.92	5.5818
Error	17	0.0730	0.0043	62.08	-
Total	19	0.1210	-	100.00	-

Table 6-7: ANOVA results for normalised Gadd severity index 3VS.

Factor	f_g	S_g	V_g	$P_g(\%)$	F_g
Cell Size	2	0.0142	0.0071	-	0.3444
Error	17	0.3497	0.0206	-	-
Total	19	0.3638	-	-	-

While the influence of cell size was found to be statistically significant to the difference in the PLA based 3VS values, it was not significant in the difference in the normalised GSI values. To ensure that the behaviour of the 50% scale samples was not hiding any significance of the 33% scale samples behaviour an additional ANOVA was run, comparing only the 100% and 33% scale samples. This run also determined that the influence of the cell scale on normalised GSI was also insignificant.

6.4. Discussion.

The FFF process was capable of accurately manufacturing the downscaled optimal geometries. However, the manufacture of the extremely thin wall samples, notably the 33% scale 3.30ms^{-1} optimal, presented the process's minimum achievable feature size. While this provided sufficient scope to explore the effects of cell scale, further exploitation of the cell size to reduce injury risk would only be possible through an alternative manufacturing method. Additionally, the reduction of sample geometry feature size increases the risk of manufacturing failure due to the increased friability of manufactured geometry and difficulty in bonding material.

For all examined performance metrics, with the exclusion of normalised GSI 3VS, a reduction in cell size produced a statistically significant change ins sample response. Reduction in cell size was associated with a reduction in PLA, while the strain of peak efficiency, normalised stress and normalised energy absorption typically rose.

The downscaled geometries responded to both quasi-static and dynamic loading with a strain stiffening response, typically associated with auxetic materials, meaning that the inclusion of more cells had overcome the strain-softening response of a single cell, Figure 6-2 and Figure 6-8 [25,220,268,270]. The reduced cell size resulted in thinner cell walls, which inherently had lower buckling strengths [19]. As each cell was weaker, the significant softening post wall buckling would be less influential in the overall response of the sample.

Overall sample performance was not hampered by the weakening of cells, due to the proportional increase in the number of cells within each sample. For example, the 100% 3VS PLA optimal, contained six complete cells. In comparison, 50% and 33% scale variants contained 56 and 198 complete cells, respectively. This non-perfect scaling results from downscaled samples being able to fit more complete cells in their width. The number of cells within a plane has already been linked to the presence of auxetic behaviour in one plane, and it stands that this relationship could be present in the other planes of the material [31,231]. This transition point appears to be at 33% scale where three cells were present in the loading direction of the sample. It was at this scale where a range of performance metrics, such as densification strains and PLA, significantly and continuously diverged from the full-scale variants, Figure 6-4, Figure 6-5, Figure 6-9 and Table 6-3. The validity of this threshold, however, could only be established through the testing of a 25% scale cell samples, via the utilisation of alternative additive manufacturing technology.

Interestingly some of the downscaled samples reported a stress-strain response indicative of an ideal cellular material, i.e. no strain-softening or strain-stiffening, Figure 6-2 [d]. This suggests that it may be possible to balance the single-cell and auxetic effects to maximise performance for a single impact scenario by providing the ideal response of a cellular material. However, the varied impact environment of American football, where liner materials are expected to dissipate a wide range of energies limited the use of exploiting this phenomenon.

Statistical analysis quasi-static data noted that cell size had a greater influence on the strain of maximum efficiency, 54%, that it did on either normalised stress, $\tilde{\sigma}_{\varepsilon_n}$, or normalised energy absorption, $\widetilde{W}_{\varepsilon_n}$, 37% and 47% respectively. As both $\tilde{\sigma}_{\varepsilon_n}$ and $\widetilde{W}_{\varepsilon_n}$ values were reliant on the value of ε_η for their calculation, it may be that some of the increased performance for these metrics results from the delay of densification. The increased densification strain would have formed part of the error term in the ANOVA conducted for both $\tilde{\sigma}_{\varepsilon_n}$ and $\widetilde{W}_{\varepsilon_n}$ thus reducing the perceived contribution provided by the analysis.

The reduction in cell size allowed for more cells in the loading direction. The MOM geometry exhibited an unbalanced deformation when compressed, with deformed cell shape ranging from a V shape to a C shape depending on the presence of other cells, *Figure 4-22*. This pattern was exhibited within each row of cells present in the downscaled geometry, with the pattern mirroring between layers. The alternating pattern allowed a greater degree of sample folding before the densification of the most compacted cell limited the overall densification of the sample. Additionally, the thinner walls present in the downscaled samples enabled greater localisation of the geometries folding, overcoming the thick origami problem noted in previous chapters.

Although statistical analysis suggested a significant reduction in PLA, and thus SRC risk, was achieved, the actual reduction was reliant on the response of a sample to impact, Figure 6-6. Where impact energy was not sufficient to cause densification PLA values were either consistent across all scales of a geometry, Figure 6-6[$d_{5.58}$], or downscaled samples offers a slight reduction in acceleration, Figure 6-6[$c_{3.3}$]. Full scale samples typically recorded their highest accelerations during region associated with the initial stiffness phase of the sample's compressive response. Several of the downscaled samples reported either reduced initial stiffness, or entered their plateau region at lower stress, Figure 6-2. This resulted in the slightly reduced PLAs seen as less force was required to deform the structure.

In comparison, when a sample has reached densification during impact, the PLA reached is dictated by the amount of impact energy that must be dissipated through deformation of the base material. The additional energy absorption that the downscaled samples are capable of before densification alongside the delayed densification of these samples enables them to reduce the amount of energy to be absorbed by the base material.

In either case, the reduction in cell size improves the meta-materials ability to reduce the risk of SRCs in comparison to the full scale variants, Figure 6-6. For example, the 33% scale 3.30ms^{-1} optimal geometry maintained acceleration below 1% injury risk, while the full scale variant of the geometry reported accelerations over 10% risk of injury. As the full scale variants of the optimal geometries had been shown to offer preferential performance to contemporary foam materials, Chapter 5, reducing cell size clearly makes the MOM a more promising material to be used as a replacement for these foams.

Despite the reduced PLA exhibited by the downscaled samples, no significant reduction in GSI response is seen, Figure 6-10 and Table 6-7. Although there is some variation in the impact duration, the 33% scale samples typically have shorter durations than their 100% scale counterparts, with the 50% scales samples typically being consistent in duration with the 100% scale samples, Figure 6-6. Where the impact duration of the full-scale samples is longer, it is in a region of relatively low acceleration values, and thus contributes little to the overall GSI score of a sample. For example, an extra period of consistent acceleration of 30g for 5ms adds only 24.65 to a samples GSI value. Therefore, the cause of insignificant GSI change cannot be due to duration compensating for reductions in acceleration.

Both groups of downscaled samples report wide variation in their normalised GSI response, Figure 6-10, which is primarily driven by the inconsistent relationship between cell scale and GSI performance, Figure 6-7. For some geometries cell scaling greatly improved GSI. In contrast, for other geometries, it increased the calculated response, and therefore injury risk.

At the lowest velocities, 33% scale sample reported worse GSI than their full scale counterparts, with a minor improvement in performance at the maximum tested velocity, Figure 6-10. At the lowest tested velocities, the strain-stiffening response of downscaled samples resulted in a period of sustained higher accelerations, in comparison to the full scale and 50% scale samples. It is this period that is responsible for the increased GSI. As this period reduced post-densification accelerations at the higher velocities however, performance of the 33% samples improved in comparison to the full scale samples.

The insignificance of the GSI response is not detrimental to the overall ability of the MOM to minimise injury. As noted previously, changes in GSI do not induce an equivalent change in the risk of injury, so long as the value is below 1200. Therefore, the trade-off in perceived performance exhibited by the 33% samples is acceptable.

Two of the developed geometries deviate from the discussed behaviour the 3.30ms^{-1} and 5.58ms^{-1} PLA optimal geometries, Figure 6-6 [a][d]. The downscaled 3.30ms^{-1} samples continually improved on both GSI and PLA across all three examined velocities, Figure 6-6and Figure 6-7. In comparison, the 5.58ms^{-1} PLA geometry exhibits minimal change when downscaled. These samples are at the extremes of the developed samples stiffness, with the 3.30ms^{-1} optimal being the softest and the 5,58 ms^{-1} optimal being the stiffest, Figure 6-2.

The 3.30ms^{-1} optimal experiences densification, as noted by the double peak response, at the lowest tested velocity. Therefore, the previously discussed advantages of downscaling are leveraged for all impacts. While the full scale sample performs worse than the tested Rawlings geometry, the 33% scale samples provide comparable performance to the Riddell foam, Table 10-17. Both the 100% and 50% scale geometries were still incapable of producing a GSI below the threshold for catastrophic injury, 1200 GSI, Figure 6-7 [184], which invalidated their use in football helmets. The 33% scale geometry offers similar performance to the Riddell foam with a lower density, 150.88kgm^{-3} and 170kgm^{-3}, respectively, Figure 6-6, Figure 6-7 and Table 10-17.

In comparison, the 5.58ms^{-1} PLA optimals stiffness prevents densification at every tested velocity, which prevents the benefits of downscaling from influencing performance. Both the developed 50% and 33% scale samples for this geometry provide a slightly lowered plateau stress versus the 100% scale sample, Figure 6-2[d]. Therefore, the elongated accelerations exhibited by other samples are not present here, preventing loss of GSI performance. However, all scaled variants of this geometry reported GSI value over the limit specified for the lowest velocity, 300 GSI [184]. Therefore, these samples were discounted from further use.

Of the remaining samples, the 33% scale PLA 3VS optimal presented with the lowest PLA 3VS of any tested sample, 15.45 g, Table 10-19. This improved on both tested foams, 17.72 g for the Riddell foam and 21.13 g for the Rawlings foam, suggesting an increased ability to reduce injury. This samples GSI 3VS, 65.56, was outperformed by the 100% scale 5.58 GSI optimal, 62.58, but was highly competitive versus the recorded scores for the tested foam samples, 72.52 and 92.34 for the Riddell and Rawlings foams respectively again highlighting its potential to reduce injury risk. Ths improved performance comes at the cost of increased density, 213.51kgm^{-3}, making this a heavier alternative. Full PLA, GSI and 3VS results are available in Table 10-17 and Table 10-19.

6.5. Conclusions

The limited number of cells in the direction of loading had been noted in chapter 5 as a potential limitation to the performance of the MOM geometry. To investigate this possibility, downscaled variants of the optimal geometries developed in chapter 5 were manufactured. These downscaled variants were subjected to the same quasi-static and dynamic loading as the optimals. Statistical analysis was conducted on collected results to determine if the scaling of cell size provided significant performance.

Reducing the cell size was found to transition the stress-strain response of the MOM geometry from strain-softening to strain-stiffening, a response consistent with other auxetic materials. This was attributed to the reduced strength of individual cells, while sample strength was maintained by the increased number of cells within each sample.

The smaller cells prolonged the densification of samples, by enabling better folding of geometry. This delayed densification, combined with the strain-stiffening of samples improved the energy absorption capability of the geometry prior to densification.

Under dynamic loading, the reduction in cell size provided significantly lower PLA while GSI was not significantly affected. Closer examination of sample performance identified that PLA reductions came from sample exhibiting signs of densification, where the improved pre-densification energy absorption could be leveraged. Samples that did not densify maintained consistent PLA across all sample sizes.

Therefore, reducing the scale of the MOM cells was determined to aid in the reduction of injury risk. The majority of downscaled geometries maintained GSI values below the accepted thresholds of catastrophic injury, and offered lower SRC risk, based on linear acceleration, to the geometries developed in chapter 5 and contemporary liner materials.

The 33% scale variant of the PLA 3VS optimal geometry was identified had the best potential to provide superior performance to foam liners, in terms of reducing the risk of SRC. This geometry offered the best performance when all impact velocities were considered, which was beneficial due to the complex impact environment of American football, although it was outperformed at each velocity by one other variant of the MOM geometry.

Chapter 7: Implementation of MOM to helmet conditions.

7.1. Introduction.

The previous chapter established that the performance of the optimal geometries developed in Chapter 5 could be further improved by downscaling the cells within each sample. However, all testing thus far had been conducted utilising material samples isolated from the boundary conditions present within football helmets. Therefore it was vital to examine the performance of the MOM when tested as part of a completer helmet, using the methodology present within performance standards [184].

The introduction of the helmet changes fundamental aspects of how the developed metamaterial is loaded. These boundary conditions included curvature of the sample geometry and the larger volume of useable material present in the helmet liner.

The ability of liner material to conform to the curvature of both the helmet shell and the athletes head is a vital aspect to the correct fit of a helmet. Incorrect helmet fit has been shown to increase the risk of injury [201]. Although the auxetic material displays synclasticity and so allows a flat sheet of material to fill the curved design space, this curving compresses the layer of cells closest to the head and cause the cells close to the helmet to expand. This distortion will likely influence the collapse of the cells under loading and so affect performance.

All testing on the MOM geometry thus far has been conducted using samples with a 60 x 60 mm cross-sectional area. This provided a contact area for the impact similar to that reported in the literature [358,359]; however, the actual contact area the MOM may exhibit when contained in a helmet is unknown. A smaller area would result in higher accelerations under densification, while a larger area would lead to higher pre-densification accelerations.

The optimisation of the MOM geometry was conducted utilising impact masses representative of established headforms. The use of this mass had ensured that the impact response of tested foams was consistent with their performance reported in the literature. Therefore, the MOM samples used to generate optimal geometry were exposed to loads equivalent to the ones present in standard helmet testing. The use of helmeted headform for this study would naturally increase the mass, and therefore the impact energy required to be absorbed.

Some of the increased energy would be absorbed by the use of the MEP pad thick circular rubber pad, which has a specified impact response [361]. As this material is more compliant than a steel anvil, changes in recorded accelerations were expected.

Football players sustain a large number of head impacts in each play session, between 3.31 and 37.42 depending on session type and player cohort [73,74]. Therefore, the ability of liner materials to provide a consistent response was vital.

American football athletes expose themselves to a large number of head impact throughout their careers [48,49,60,64-78]; therefore, even small reductions in injury severity will reduce head injury risk and numbers of head injuries, within the sport.

Therefore, the identified potential of the MOM to reduce injury offered in comparison to elastomeric foams needed to be validated. This chapter aims to demonstrate the improved player safety that could be gained by using a MOM based liner. In aid of this aim, the chapter has the following objectives:

1. Develop a replacement front pad for a football helmet from the identified best performing MOM geometry.
2. Demonstrate the ability of a MOM liner to reduce injury risk in comparison to elastomeric foams.
3. Determine the ability of the metamaterial to maintain performance when impacted multiple times in quick succession.
4. Establish the effects of the changes in boundary conditions between the sample and helmet testing protocols.

7.2. Methods and Materials.

7.2.1. Replacement Pad Design and Manufacture.

The Riddell Speed was selected as a comparator helmet, being representative of the National Football Leagues and National Football League Players Association's recommended helmets [360].

As the pad performance is partially reliant on its fit within a helmet, the optimal MOM pad was designed to match the dimensions of the foam pad it was replacing. Doing so enabled the adoption of the same retention system that secured the original pad within the helmet. Initially, a CAD geometry of the pad was taken from a finite element analysis model of the helmet, Figure 7-1 [364].

Figure 7-1: Render of the Front pad of a Riddell Speed helmet (2016) isolated from CAD geometry, side view[a], front view [b] and top view [c].

The outer surface of the pad was measured to develop a flat surface projection. Although the FFF method could produce curved geometries, this would have required the use of support structures. Due to the limitations of the printer, the support structures and thin walls of the optimal MOM geometry would have been of the same dimensions, meaning damage to the functional geometry may have occurred when separating it from the supports. While this approach was a viable solution for the manufacture of a one-off component for developmental purposes, future manufacturing of components in a commercial setting would require an alternative manufacturing process such as DLS or SLS.

The flat projection was used as the perimeter of a sheet of optimal MOM geometry. Grooves were placed at 60mm intervals, both horizontally and vertically across the pad to a depth of 20mm. These groves aided in the curving of geometry while minimising individual cells' distortion, thus retaining performance. Groove angles were calculated from the curves present in the foam geometry.

The replacement pad was manufactured using the same printer and process discussed in Chapter 5, Figure 7-2. The manufacture of a replacement front pad from MOM geometry posed a unique challenge to the FFF process. While cellular geometry remained unchanged from previous chapters, the sample's increased volume meant that the entirety of the available print volume was used. The increased print time, from 11 hours for a 60mm sample to 72 hours for a full pad, meant that prints were prone to more errors that would fail the print. This print time again represents the upper limit of the FFF process's viability, when full-scale manufacturing is considered. While alternative methods would have potentially reduced cots and manufacturing time, this would have required a change in base material which was considered non-viable.

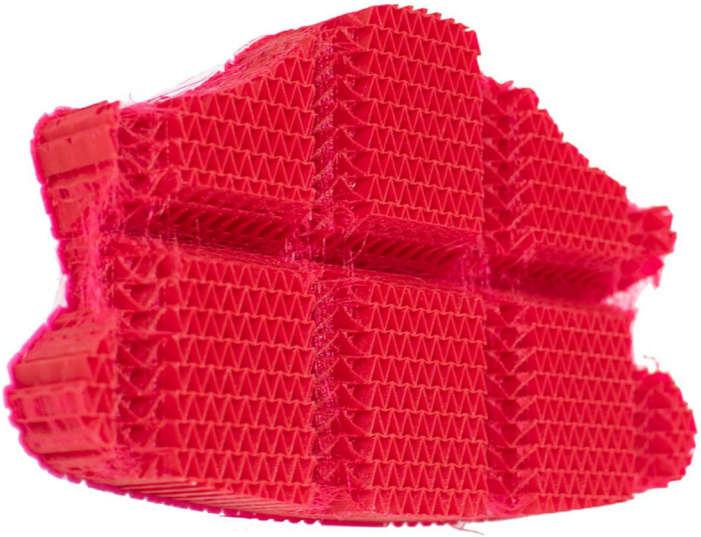

Figure 7-2: Manufactured replacement front pad based on 3VS PLA geometry.

7.2.2. Impact testing protocol.

The Instron impact rig used for impact testing in previous chapters could not accommodate both the headform and helmet within its test volume. Testing was conducted at a dedicated helmet testing facility using an MAU 1026/2w combination impact rig (AD engineering, Italy), which was specifically designed to meet the requirements of the NOCSAE helmet standards [184,361]. The MAU was wire-guided rather than rail-guided during freefall, which enabled comparatively more lateral movement of the headform and drop cage post-impact.

The biofidelic NOCSAE headform was selected based on helmet fit, in line with the testing standard [184], with the selected 7 1/4 headform's weight, 4.9 kg, being the closest match to the weight of the 95th percentile human male head, 4.55 kg [211, 361].

The Headform was attached to the MAUs lightweight drop cage, using the friction pins specified. The combined mass of the head form helmet and drop cage was 8.8 kg.

Accelerations were captured using the 356AO2 triaxial accelerometer (PCB, Depew USA) which was securely fixed at the centre of gravity of the headform. This accelerometer was rated to 500g and was sampled at a rate of 50kHz via a DLS 9000 62502014 (AD engineering, Italy) data acquisition system.

Unlike the StrainStart® 9000 system used in previous chapters, the DLS 9000 used a physical filter circuit to clean data as it was recorded. The filter circuit imposed the equivalent of a 1kHz Butterworth filter, in line with testing standards [361], and thus no post-processing of captured data was required.

Impact tests were conducted at the same identified velocities utilised for the optimisation effort, 3.30ms^{-1}, 4.44ms^{-1} and 5.58ms^{-1}. Each front pad was subjected to 5 impacts at each velocity, with impacts spaced at 75s intervals with 15 minutes rest between impact velocities.

7.2.3. Performance metrics.

From acceleration-time data, PLA, GSI and 3VS values for the front pads were calculated using the relevant equations preented in chapter 5.

To allow for insight into the impact behaviour of the tested pads, the densification strains identified in previous chapters from single pad testing were used to calculate the relative maximum strains for each impact, using equation 5-5.

To allow exploration of the MOM's ability to maintain performance when subjected to multiple impacts, the GSI and PLA from the second to fifth impacts at each velocity were normalised to the first impact. This normalisation was conducted for both the foam and MOM liners. The reduced rest between test velocities allowed for the creation of a worst-case scenario, where a single pad was subjected to multiple extreme impacts. This worst-case scenario would highlight any shortcomings in either material.

7.3. Results.

The optimal MOM geometry provides both lower PLA and impact duration at the two highest impact velocities while maintaining comparable performance to the foam liner at lower velocities, Figure 7-3.

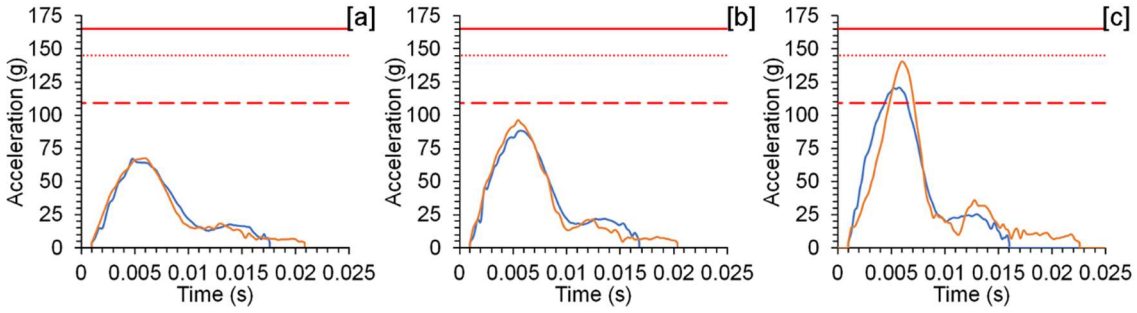

Figure 7-3: Linear acceleration vs time for Riddell foam pad (orange) and MOM replacement (blue) at 3.30ms^{-1}[a], 4.44ms^{-1}[b] and 5.58ms^{-1}[c] with 1(dashed), 5 (dotted), and 10% (solid) SRC risk thresholds[172].

Both materials maintain accelerations below identified SRC risks for the first two impact velocities. At the highest velocity, the accelerations recorded for the MOM liner represented a 1% risk of injury. In contrast, the foam liner reached a PLA close to the established risk threshold of 5%, Figure 7-3 and Figure 7-4[b][172].

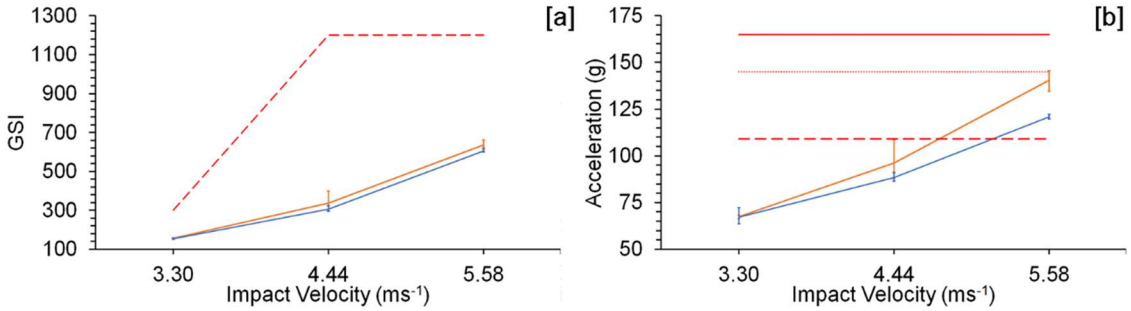

Figure 7-4:Average GSI [a] and PLA [b] for Riddell foam (Orange) and MOM geometry (Blue), with 1% (red dashed) 5% (red dotted) and 10% (red solid) SRC risk. Error bars represent the range of performance over 5 impacts.

Both the optimal MOM and foam liners report GSI values significantly below established injury risk thresholds, Figure 7-4 [a] [184], with the MOM liner offering a slight improvement on the foam.

The Riddell foam undergoes an apparent instability in its response at 4.44ms^{-1}, where the range of GSI response, 104, is 30% of the average response, 336. The PLA response is similar, with the range, 20.76g, being just under a quarter of the average, 88.31g, Figure 7-4. In comparison, the MOM liner offers a consistent response across the range of impact velocities with the range of performance being around 10% of the average.

When all three impact velocities are considered, the MOM geometry offers a 9% improvement in the PLA based score, and a 5% improvement in the GSI based score, Table 7-1, highlighting its ability to reduce injury severity and thus, risk.

Table 7-1: Calculated 3VS scores for the Riddell and MOM front pads, with 60mm pad performance for reference.

Sample	PLA (g)				GSI			
	Helmet	60mm	Pad %	Foam %	Helmet	60mm	Pad %	Foam %
Riddell Foam	16.19	17.72	91.41	100.00	59.05	72.52	81.43	100.00
Optimal MOM	14.78	15.46	95.57	91.21	56.04	65.56	85.48	94.90

Table 7-2:Average Strain and RMS for the Riddell and MOM front pads at each impact velocity. Brackets contain one standard deviation.

Sample		3.30ms^{-1}	4.44ms^{-1}	5.58ms^{-1}
Riddell Foam	Average Strain	0.456 (0.010)	0.689 (0.055)	0.834 (0.022)
	RMS	0.867 (0.019)	1.312 (0.105)	1.587 (0.042)
Optimal MOM	Average Strain	0.454 (0.013)	0.615 (0.015)	0.727 (0.013)
	RMS	0.756 (0.022)	1.025 (0.024)	1.211 (0.022)

Both the Riddell foam and optimal MOM have started to densify at the middle velocity, Table 7-2. However, the Riddell foam has reached a comparatively higher level of densification than the MOM, as noted by average RMS. Due to the limitations of foam optimisation, it appears that the performance of the foams was designed to maximise performance at the lowest velocity, whilst maintaining sufficient energy absorption ability to keep impact performance within the NOCSAE standards envelope, [184].

In comparison, the MOM geometry was designed to limit PLAs, which rapidly increase during densification. This design consideration results in the lower RMS values seen. Notably, the structure has only just begun densifying at the middle velocity.

The optimal MOM geometry provided a similar response when tested as part of a helmet in comparison to is performance as an isolated material, Figure 7-5. Reported peak accelerations were within 10g and total duration within 5ms across the range of tested velocities.

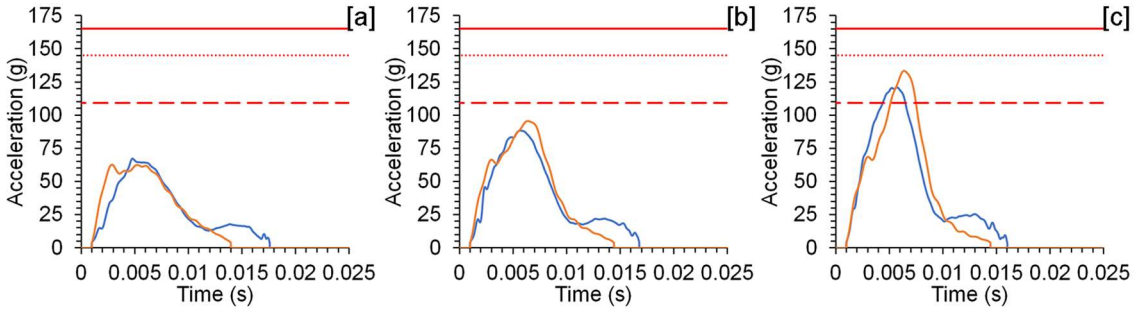

Figure 7-5: Linear acceleration vs time for 60mm MOM sample (orange) and full helmet MOM pad (blue) at 3.30ms^{-1}[a], 4.44ms^{-1}[b] and 5.58ms^{-1}[c] with 1(dashed), 5 (dotted), and 10% (solid) SRC risk thresholds[172].

One notable change is the loss in the clear demarcation between non densified and densified responses, in the response of the full helmet test, Figure 7-5 [c], which was seen as a short plateau in the reported accelerations of the pad samples, typically 1-2ms in duration. Additionally, the accelerations from the helmet testing reported a consistent secondary pulse where the pad accelerations tailed off.

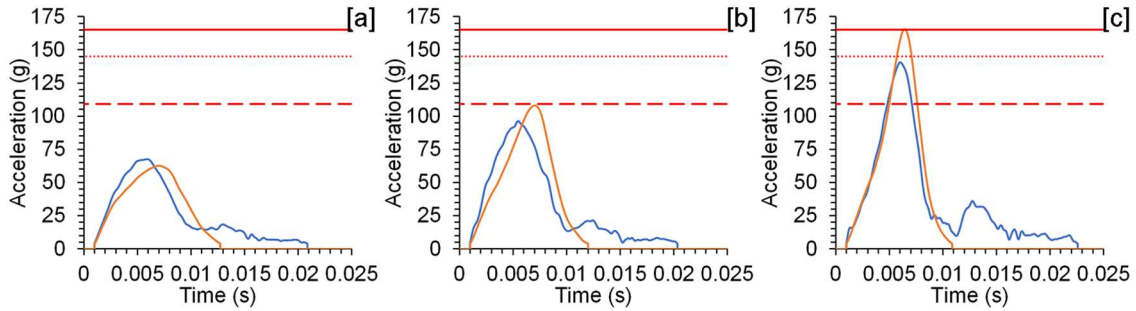

Figure 7-6: Linear acceleration vs time for 60mm Riddell foam sample (orange) and full helmet (blue) at 3.30ms^{-1}[a], 4.44ms^{-1}[b] and 5.58ms^{-1}[c] with 1(dashed), 5 (dotted), and 10% (solid) SRC risk thresholds[172].

The foam liner also reported a similar response between full helmet testing and the previously reported sample testing. Helmet testing provided worse performance at the lowest tested velocity but offered a substantial performance increase at the higher velocities, Figure 7-6. A substantial increase in impact duration was seen, with a tail of low accelerations ranging in length from 8ms to 13ms. The shape of this pulse was less consistent than the one seen in the response of the MOM liner.

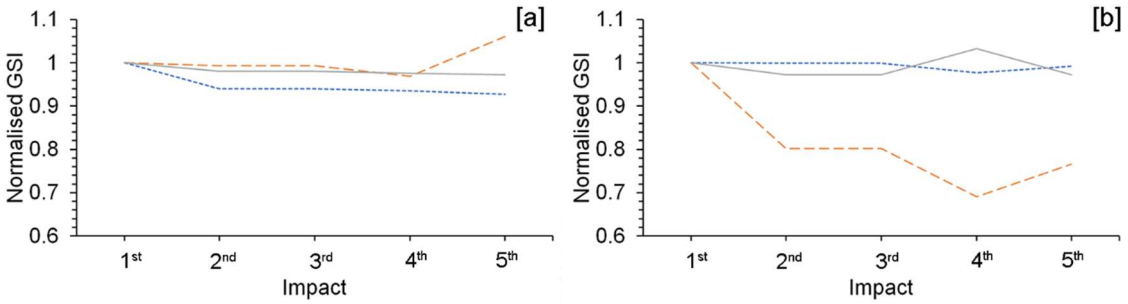

Figure 7-7: Normalised GSI for MOM liner [a] and foam liner [b], at 3.30ms^{-1} (dotted blue), 4.44ms^{-1} (dashed orange) and 5.58ms^{-1} (soild grey)

When compared to the first reported impact, both the MOM and Riddell front pads typically report lower GSI values for subsequent impacts; however, this reduced response is within 5% of the first impact performance, Figure 7-7. The Riddell pad experience significant reduction during the 4.44ms-1 impact testing, suggesting a significant softening in sample response.

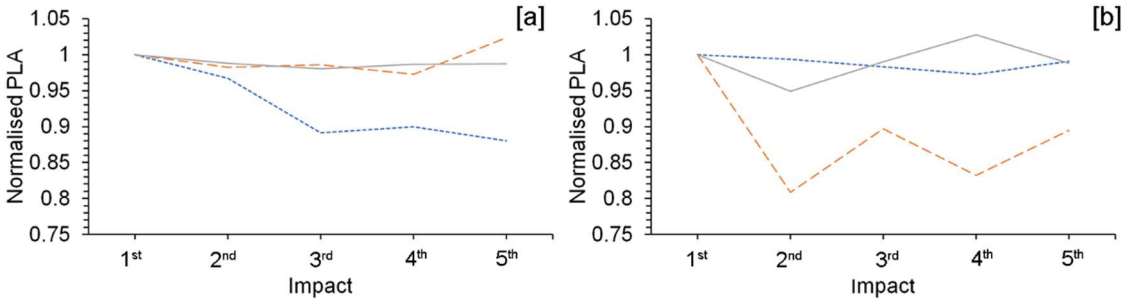

Figure 7-8: Normalised PLA for MOM liner [a] and foam liner [b], at 3.30ms^{-1} (dotted blue), 4.44ms^{-1} (dashed orange) and 5.58ms^{-1} (soild grey)

The normalised PLA response of the Riddell and MOM front pads is similar, but with more considerable variation in response, Figure 7-8. Most notably, the MOM geometry shows significant reduction at the lowest measured velocity, with the 5th impact reporting a PLA under 90% of the first impact. Again, the foam liner exhibits an unstable response at the middle velocity, indicating a change in material behaviour.

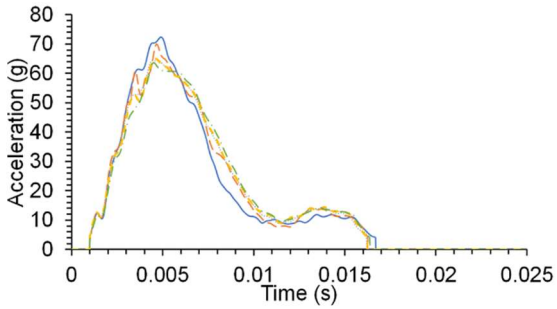

Figure 7-9: Acceleration vs time for the first (solid blue), second (long orange dash), third (grey dot), fourth (short yellow dash) and fifth (green dash-dot) impacts for the optimal MOM pad under the 3.30ms^{-1}impact conditions.

The drop in acceleration noted in the MOM liners PLA response between the first and subsequent impacts results from a softening of the material as it is exposed to further impact, Figure 7-9. This likely results from the incomplete recovery of the liner material.

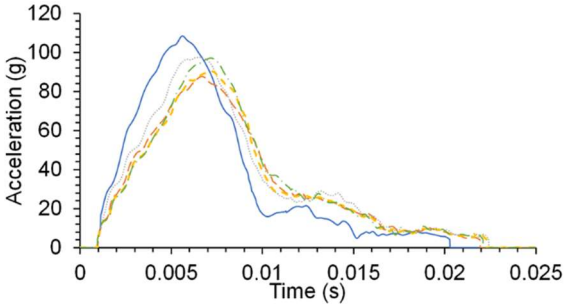

Figure 7-10: Acceleration vs time for the first (solid blue), second (long orange dash), third (grey dot), fourth (short yellow dash) and fifth (green dash-dot) impacts for the Riddell foam under the 4.44ms^{-1}impact conditions.

The first impact response of the foam liner at the middle velocity presents a significantly different response to the second to fifth impacts, Figure 7-10, with a faster ramp to a higher PLA, with an overall lower impact duration.

7.4. Discussion.

The MOM liner reduced measured headform accelerations in comparison to the original foam material when impacted at the average speed of impact linked to a concussion, 5.58ms^{-1}, Figure 7-3 [17,84]. At lower velocities, the performance was either consistent with or a small improvement on the foam liner. This means that this novel solution provides an opportunity to reduce head injury severity, especially during high-energy collisions.

The lowered accelerations reduced risk of injury by approximately 4% when established thresholds are considered, Figure 7-3 [172]. An athlete in their 5th year of professional play can be expected to have experienced approximately ten thousand head impacts at that point in their career, depending on their onfield position [48,49,60,64-78]. The two highest tested impact velocities studied in this chapter resulted in accelerations that would place them as 99th percentile events in terms of resultant acceleration. Therefore the hypothetical athlete would have been exposed to approximately 100 impacts with sufficient accelerations to cause an SRC [60,66,75]. The foam liner's performance suggests that if the athlete's helmet had used such a liner, they could have experienced four or more concussions.

In comparison, the use of a MOM liner reduced the average PLA by up to 20g. This represented a 4% reduction in the risk of an impact resulting in an SRC. Therefore, this liner's use suggests that the hypothetical athlete would be likely to endure only a single concussion in the same period. In addition, the apparent link between the number of concussions an athlete sustains and neurodegenerative diseases, the use of a MOM liner could be expected to reduce the risk of an athlete being diagnosed with one of these conditions [139,148,152,153,155,156]. However as no oblique impact testing was conducted, and therefore no rotational accelerations were collected, it must be acknowledged that is the reduction in injury risk for both SRC, and thus the occurrence of neurodegenerative diseases is tentative at best.

The MOM based liner offers a more consistent response to impact than the foam liner, with substantially reduced ranges, Figure 7-4, Figure 7-7 and Figure 7-8. This is an essential consideration in the design of football helmets, which regularly undergo multiple collisions in quick succession. The ability of MOM to sustain multiple impacts without significant loss in performance would provide better player protection throughout a game or full-contact practice session.

The small range in performance presented by the optimal MOM resulted from sample softening, indicated by the lower PLA and GSI results for the majority of the repeated impacts at each velocity, Figure 7-7 to Figure 7-9. This is most apparent in the results for the 3.30ms^{-1} impact, where the most extensive variation in PLA is seen. The acceleration time traces of the first and fifth impact at this velocity show a flattening of the acceleration curve, Figure 7-9.

Most likely, the exhibited softening in response results from the incomplete recovery of the sample geometry. As noted in previous chapters, the origami nature of the MOM geometry provides it with a predictable folding deformation. Incomplete recovery of the geometry from an impact results in an increased α angle, which was established in previous chapters to soften the geometry overall.

The flattening of the curve maintains the observed GSI despite the reduction in accelerations, as post-peak accelerations are increased in subsequent impacts in comparison to the first impact, Figure 7-9. The last test conducted on the optimal MOM at 4.4ms^{-1} is the only result to break the observed trend, reporting both higher PLA and GSI in comparison to the first test, Figure 7-7 and Figure 7-8. As the optimal geometry has reached densification during these impacts, as noted by the RMS, the softening of sample geometry would naturally lead to greater densification on each impact, and therefore higher accelerations are achieved.

The response of the foam pad at the middle test velocity shows a significant difference between the first and fifth impact for both the PLA and GSI response Figure 7-7 and Figure 7-8. As the foam pad had reached and surpassed its densification strain under this impact condition, Table 7-2, any softening of material due to incomplete recovery would be expected to lead to an increase in both PLA and GSI, due to the higher resistive forces from densified material. However, both PLA and GSI are vastly reduced beyond the first test, meaning that some other factor must be at play.

Examination of the acceleration time curves shows that beyond the first impact, the foam pad responds as expected, with severity increasing with repeated impacts, Figure 7-10. While this may suggest that the result of the first impact could be considered erroneous, the lack of change in test conditions between impacts makes this unlikely. Additionally, the data set did not contain any drops in recording or long periods of consistent accelerations, that would suggest an issue with the data recorder.

The foam pad was not visibly damaged when removed from the helmet. While the impact velocities used in testing were representative of those that cause mTBIs within the sport, these events are still in the 99th percentile in terms of severity [17,60,66,75,84]. Therefore, the repetition of these impacts may have caused internal damage within the foam, or on the border area between the utilised foam and uncompressed foam. Additionally, the area of material used to absorb impact energy has been noted to slightly increase on repeated impacts [274].

Both the MOM and Riddell foam exhibited changed acceleration response to impact loading when tested as a helmet liner rather than as an isolated material. Both materials exhibited reductions in PLAs, while a secondary pulse was seen during the later portions of impact, Figure 7-5 and Figure 7-6.

However, the performance gap between the optimal MOM geometry and the Riddell foam samples closed considerably under full helmet testing, Figure 7-4 and Table 7-1. The foam had a notably greater improvement in performance, with a 9% and 19% reduction in its PLA and GSI base 3VS scores, Table 7-1. In comparison, the optimal MOM reported 4% and 15% improvements in the PLA and GSI 3VS, respectively.

These improvements in performance came despite the higher impact energies, which increased by a factor of 1.83 due to the higher mass present. Some of the excess energy was dissipated by the helmet shell, which is reported to be responsible for 18 to 34% of impact energy [15,16,204]. This, however, cannot account for all the additional energy present. Although previous work established the area of material utilised in an impact, this was based on expanded polystyrene foam [358,359]. Therefore, both the Riddell Foam and optimal MOM were possibly able to utilise a greater quantity of material when the full helmet was tested. The increased material would naturally increase the energy absorption capability, resulting in the lowered PLA and GSI values seen.

If additional material volume had been utilised, the grooves used in the MOM pad to aid curving would have inhibited the materials ability to recruit material into the impact site successfully. This would partially explain the less improved response of the optimal MOM in comparison to the Riddell foam.

It should also be noted that both the testing in this chapter and previous studies do not contain the metal facemask of American football helmets, which itself has been linked to increased acceleration under impact, with a 36% increase in recorded PLAs [369,370]. Therefore, the onfield response of the developed materials may be closer to the 60mm square samples in terms of performance. However, the chosen MOM geometry significantly outperformed the Riddel foam in the 60mm sample testing. Therefore, the previously discussed improvement in injury prevention that the MOM offers would still be present.

The second notable change in the liners' response is the second pulse and longer tail in the acceleration- time response to loading, Figure 7-5 and Figure 7-6. However, as this extra acceleration is below 20g in magnitude, it adds little to the injury risk presented by either material.

7.5. Conclusions.

Previous testing had identified an optimal MOM geometry that had the most potential to reduce injury when impacted at velocities linked to SRCs. This geometry was used to manufacture a replacement pad for a helmet recommended by the governing body of professional American football. Both the replacement pad and original foam were tested as part of a helmet at the previously identified impact velocities, using industry-standard equipment.

The MOM geometry presented superior performance, in terms of PLAs and GSI responses, compared to the Riddell foam at the two highest velocities, with a comparable performance at the lowest velocity. Both materials reported accelerations below identified injury risk thresholds at the two lowest tested velocities. At the highest tested velocity, the optimal MOM geometry outperformed the foam liner, with its response suggesting a drop in injury risk. This drop, combined with the MOM liners consistent performance across all examined velocities, indicated its use in American football would potentially reduce the number of SRC a player might sustain in the course of their career.

Chapter 8: Conclusions and Further Work.

8.1. Conclusions.

This thesis aimed to develop a novel cellular metamaterial for use within American football helmets that would reduce the risk of injury present in the sport. To achieve this aim, the study had the following objectives:

- Define the impact environment and injury risks associated with American football.
- Identify a suitable candidate geometry, base material and enabling technology for use in a football helmet.
- Demonstrate the ability to manufacture the chosen metamaterial to a high degree of accuracy.
- Develop a testing environment that was representative of injury-causing impacts within the sport.
- Utilise a validated optimisation process to revise the geometry of the candidate material to maximise its performance.
- Test the candidate material versus contemporary liner materials to quantify its ability to reduce injury.

Athletes who play contact sports, especially those who play American football, place themselves at considerably increased risk of sustaining a head injury, ranging from mild injuries such as sports-related concussions to more catastrophic injuries, such as subdural haematomas. Although concussions typically present with limited neurological symptoms, repeated instances of this injury have been linked to increased prevalence of a range of neurodegenerative conditions in retired athletes. The higher rate of injury results from the large number of head impacts that athletes are exposed to, with professional players sustaining tens of thousands of impacts by the end of their playing careers, page 7. The vast majority of these impacts are mild, with resultant accelerations typically being below 40g in magnitude, page 10. Previous studies identified a range of impact velocities that were linked to the presence of SRCs and acceleration thresholds that established risk of injury, page 22.

The defined impact environment of American football provided a five-point specification for a new candidate geometry, page 34. Origami-based materials offered a wide range of parameters for optimisation, page 41, while auxetic materials were identified as an opportunity for expanding performance over a range of impact energies, page 44. A novel stacked origami structure which combined these properties was identified as having great potential for use within American football helmets. TPEs were seen as a promising family of materials, which combined a range of desired properties, page 49. Additive manufacturing was identified as a technology space that would allow for the design and manufacture of the novel geometry, which could not be realised by more traditional manufacturing technologies, page 49. Fused Filament Fabrication was identified as a technique that would be capable of producing geometrically accurate functional components, page 53.

The accuracy of any optimisation was reliant upon the accuracy of manufactured components. Therefore an exploratory study utilising micro-computed tomography was conducted to develop the FFF process with consideration given to density, accuracy and mechanical strength, page 67. Part density of 99.98% was achieved with an absolute error of thin walls of less than 0.15mm, page 73. Although the tensile strength of components was only 86% of that reported in the materials technical data, this level of strength was comparable to the reported strength of other TPEs within the literature.

The impact environment identified in the literature provided velocities and acceleration thresholds for SRCs, while industry-standard criteria were selected for catastrophic injury assessment. Impact weight was chosen to be representative of testing headforms. The Taguchi method was used to develop nine samples of the stacked origami, measuring 60mm by 60mm by 25mm, varied by four geometric parameters, page 83. The impact environment was validated based on the measured performance of two samples of elastomeric foams, taken from two helmets, one banned and one recommended, compared to reported performance in the literature, page 101. Testing of the nine samples revealed complex interactions between the parameters, page 108, and a need to alter both the base material and parameter ranges, page 109.

These findings allowed for a redesign of the optimisation study, with the minimum number of required samples being increased from nine to twenty-seven. Samples were manufactured from a stiffer TPE, with a Young's modulus of 26 MPa in comparison to the 12 MPa of the material used in the scoping study, page 114. The developed samples produced a wide range of sample performance that enveloped the performance of the comparative foam materials, page 122.

Through the use of ANOVA, the influence of the geometrical parameters and interactions was established with wall thickness being found to be responsible for 34 – 79% of a sample's PLA and GSI response to impact. No other geometrical parameters were consistently significant at a 95% confidence level across all impact conditions and optimisation metric. However, the several interactions between these parameters were, and thus the development of optimal geometries had to be carefully considered. Using ANOVA data and develop statistical plots, a range of seven optimal geometries were developed to provide maximum performance for a range of conditions and metrics. The developed optimals consistently outperformed the best foam at each condition, although no sample was capable of outperforming the foam consistently across the range of conditions developed. The middle impact velocity optimals did not provide the best performance. However, this was due to the optimisation process struggling to deal with an apparent transition between optimal wall thicknesses, page 145.

The performance of both the 27 array samples and the developed optimals all demonstrated quasi-static performance with distinct strain softening, page 146. As the literature suggested that this may be due to a single cell present through the thickness, scaled variants of the optimal geometries were developed to see if better performance could be gained, page 160. The smaller scale cell variants were found to reduce PLA values by 10 to 20% at a 95% confidence level. However, due to weaker recovery past the point of maximum deflection, causing longer impact durations, the scaled variations did not significantly affect GSI, page 164. Performance of the downscaled cells was used to identify the stacked origami geometry which had the greatest potential to reduce the risk of injury, page 180.

As all testing conducted so far had been carried out on small samples, a final round of testing was conducted to validate the performance of the novel geometry under full helmet testing conditions. A replacement front pad for the recommended helmet was created to match the geometry of the original foam and secured to the helmet using the same restraints as the foam pad, page 183. Testing was conducted at the same test velocities as previous, using industry-standard equipment. The replacement pad presented significant performance improvements over the original foam liner, page 186. This performance increase represented a reduction in risk that when expanded over the course of a player's career had the potential to reduce the number of concussions experienced by that player by 3. Due to the link between SRCs and neurodegenerative disease, use of the MOM may be able to protect players from developing these conditions.

8.2. Further work.

The work conducted in this study highlighted the possibility of utilising an origami-based metamaterial for use within sports protective equipment, with a prototype structure meeting the performance of a mature technology solution. Based on the work presented in this study, there are three possible routes of additional study which may further improve the performance of the metamaterial.

Firstly, the employment of alternative AM techniques such as inverted SLA would allow for further reductions in cell size, which was limited in this study by nozzle diameter. As explored in this study, smaller cells would allow for the material response to be less dominated by single-cell and boundary edition effects and would allow for the underlying auxetic nature of the metamaterial to become apparent. Once minimum feature size has been achieved a further parametric study on the material could be warranted to see if the findings in this study were representative of the geometry. Use of more advanced techniques would also allow for increased complexity of manufactured geometry. This would allow for features such as pre-curving of helmet pads for a better fit, weight-saving holes in the geometry, and employment of functionally grading principals. While sample curvature would only be significant for further helmet testing, both the functional grading and weight-saving would need to be proved and refined through a small sample number study.

The second route forward would be to develop a bespoke thermoplastic polyurethane or thermoplastic elastomer to be used as the base material for the developed metamaterial. As the performance of any cellular structure is reliant on its base material, the work presented in this study is limited as only commercially available materials were used. Some efforts have been made to produce bespoke TPUs within the literature, and a higher strength TPU would allow for thinner walls to be manufactured, thus lowering overall sample mass, an essential consideration in helmet design.

Although the metamaterial had undergone extensive testing in this study, all impact forces were linear, and thus so was all data collected. Therefore, the potential ability of an auxetic material to reduce brain injury risk by lowering rotational accelerations due to their lower shear resistance has not been established. To enable insight into the rotational performance of the candidate material there are two possible solutions for testing, either the use of a combined compression shear rig to load samples in isolation, as was done in chapters 5 and 6, or full helmet testing utilising a pneumatic ram or pendulum test rig, both of which allow for more degrees of freedom in the movement of the testing headform. Both of these techniques come with their drawbacks, such as time and cost of helmet testing and non-representative boundary conditions for combined compression shear, and thus the choice of techniques must be carefully considered.

At the conclusion of these developments, the metamaterial would be ready for use within a football helmet. However, design considerations such as how the metamaterial would be mounted to the shell would need to be solved before the material could be considered on the shelf solution.

Chapter 9: Reference List.

1. Piland SG., Gould T E., Jesunathadas M., Wiggins J.S., McNair O., Caswell S. V. Protective Helmets in Sports – Chapter 3. 2nd ed. Woodhead Publishing; 2019. p. 71–121.
2. McKeag D, Moeller J L. ACSM's primary care sports medicine. 2nd ed. Philadelphia: Lippincott Williams & Wilkins; 2007.
3. Winterstein AP. Athletic training student primer: A foundation for success. Thorofare: Slack Incorporated; 2009.
4. Koh J O, Cassidy JD, Watkinson EJ. Incidence of concussion in contact sports: A systematic review of the evidence. Brain Inj. 2003;17(10):901–17. doi: 0.1080/0269905031000088869
5. Zuckerman S L, Kerr Z Y, Yengo-Kahn A, Wasserman E, Covassin T, Solomon G S. Epidemiology of sports-related concussion in NCAA athletes from 2009-2010 to 2013-2014. Am J Sports Med. 2015;43(11):2654–62. doi: 10.1177/0363546515599634
6. Yau R K, Kucera K L, Thomas LC, Price HM, Cantu R C. Catastrophic Sports Injury Research - Twenty-Fifth Annual Report - Fall 1982 - Spring 2017. 2018. [accessed 2019-09-24]. Available from: https://nccsir.unc.edu/files/2013/10/Annual-Football-2017-Fatalities-FINAL.pdf
7. Lehman E J, Hein M J, Baron S L, Gersic C M. Neurodegenerative causes of death among retired national football league players. Neurology. 2012;79(19):1970–1974. doi: 10.1212/WNL.0b013e31826daf50
8. Gavett BE, Stern R A, McKee A C. Chronic Traumatic Encephalopathy: A Potential Late Effect of Sport-Related Concussive and Subconcussive Head Trauma. Clinics in Sports Medicine. 2011;30: 179–188. doi: 10.1016/j.csm.2010.09.007
9. McAllister T W, Ford J C, Flashman L A, Maerlender A, Greenwald RM, Beckwith J G, Bolander R P, Tosteson, T D, Turco J H, Raman R, Jain S. Effect of head impacts on diffusivity measures in a cohort of collegiate contact sport athletes. Neurology. 2014;82(1):63–69. doi: 10.1212/01.wnl.0000438220.16190.42
10. Rabadi MH, Jordan BD. The cumulative effect of repetitive concussion in sports. Clin J Sport Med. 2001;11(3):194–198. doi: 10.1097/00042752-200107000-00011
11. Spiotta AM, Shin JH, Bartsch AJ, Benzel EC. Subconcussive impact in sports: A new era of awareness. World Neurosurgery. 2011;75(2):175–178. doi: 10.1016/j.wneu.2011.01.019
12. Hoshizaki T B, Post A, Oeur R A, Brien S E. Current and future concepts in helmet and sports injury prevention. Neurosurgery. 2014;75(4):136–148. doi:10.1227/NEU.0000000000000496
13. Benson B W, Hamilton G M, Meeuwisse W H, Mccrory P, Dvorak J. Is protective equipment useful in preventing concussion? A systematic review of the literature. Br J Sports Med. 2009;43(1): i56-i67. doi: 10.1136/bjsm.2009.058271
14. McIntosh AS, Andersen TE, Bahr R, Greenwald R, Kleiven S, Turner M, et al. Sports helmets now and in the future. Vol. 45, Br J Sports Med. 2011;45(16):1258–1265. doi: 10.1136/bjsports-2011-090509
15. Di Landro L, Sala G, Olivieri D. Deformation mechanisms and energy absorption of polystyrene foams for protective helmets. Polymer Testing. 2002;21(2):217–228. doi: 10.1016/S0142-9418(01)00073-3
16. Hoshizaki T B, Brien S E, Bailes J E, Maroon J C, Kaye A H, Cantu R C. The science and design of head protection in sport. Neurosurgery. 2004;55(4):956–967. doi: 10.1227/01.NEU.0000137275.50246.0B
17. Viano D C, Halstead D. Change in size and impact performance of football helmets from the 1970s to 2010. Ann Biomed Eng. 2012;40(1):175–184. doi: 10.1007/s10439-011-0395-1
18. Bonfield C M, Shin S S, Kanter A S. Helmets, head injury and concussion in sport. Phys Sportsmed. 2015;43(3):236–46. doi: 10.1080/00913847.2015.1039922
19. Gibson L J, Ashby M F. Cellular solids: Structure and properties, 2nd ed. Cambridge. Cambridge University Press; 2014.
20. Foster L, Peketi P, Allen T, Senior T, Duncan O, Alderson A. Application of Auxetic Foam in Sports Helmets. Appl Sci. 2018;8(3):354. doi: 10.3390/app8030354

21. Krzeminski D E, Goetz J T, Janisse A P, Lippa N M, Gould T E, Rawlins J W, Piland S G. Investigation of linear impact energy management and product claims of a novel American football helmet liner component. Sport Technol. 2011 Feb 26;4(1–2):65–76. doi: 10.1080/19346182.2012.691508
22. Johnston J M, Ning H, Kim J E, Kim Y H, Soni B, Reynolds R, et al. Simulation, fabrication and impact testing of a novel football helmet padding system that decreases rotational acceleration. Sport Eng. 2015;18(1):11–20. doi: 10.1007/s12283-014-0160-4
23. Ahsanfar M, Galehdari S A. Optimum Design for Graded Honeycomb as Energy Absorber Device in Elevator Cabin. Procedia Eng. 2017; 173:1291–1298. doi: 10.1016/j.proeng.2016.12.163
24. Harris J A. Additively Manufactured Metallic Cellular Materials for Blast and Impact Mitigation [PhD]. Cambridge: Cambridge University;2018.
25. Duncan O, Shepherd T, Moroney C, Foster L, Venkatraman P D, Winwood K, Allen T, Alderson A. Review of auxetic materials for sports applications: Expanding options in comfort and protection. Applied Sciences. 2018;8(6):941-974. doi: 10.3390/app8060941
26. Zhang J, Karagiozova D, You Z, Chen Y, Lu G. Quasi-static large deformation compressive behaviour of origami-based metamaterials. Int J Mech Sci. 2019;153–154:194–207. doi: 10.1016/j.ijmecsci.2019.01.044
27. Townsend S, Adams R, Robinson M, Hanna B, Theobald P. 3D printed origami honeycombs with tailored out-of-plane energy absorption behavior. Mater Des. 2020 Oct 1; 195:108930. doi: 10.1016/j.matdes.2020.108930
28. Landrock A H. Handbook of plastic foams: types, properties, manufacture and applications – Chapter 3. Park Ridge, NJ: William Andrew Publishing; 1995. p. 221–45
29. Wadley H N G, Fleck N A, Evans A G. Fabrication and structural performance of periodic cellular metal sandwich structures. Compos Sci Technol. 2003;63(16):2331–2343. doi: 10.1016/S0266-3538(03)00266-5
30. Wadley H N G. Multifunctional periodic cellular metals. Philos Trans R Soc A Math Phys Eng Sci. 2006;364(1838):31–68. doi: 10.1098/rsta.2005.1697
31. Schenk M, Guest SD, McShane GJ. Novel stacked folded cores for blast-resistant sandwich beams. Int J Solids Struct. 2014;51(25–26):4196–4214. doi: 10.1016/j.ijsolstr.2014.07.027
32. Adams R, Soe S P, Santiago R, Robinson M, Hanna B, McShane G, et al. A novel pathway for efficient characterisation of additively manufactured thermoplastic elastomers. Mater Des. 2019;180. doi: 10.1016/j.matdes.2019.107917.
33. Kumar A, Verma S, Jeng J Y. Supportless lattice structures for energy absorption fabricated by fused deposition modeling. 3D Print Addit Manuf. 2020;7(2):85–96. doi: 10.1089/3dp.2019.0089
34. Yuan S, Shen F, Bai J, Chua C K, Wei J, Zhou K. 3D soft auxetic lattice structures fabricated by selective laser sintering: TPU powder evaluation and process optimization. Mater Des. 2017;120:317–27. doi: 10.1016/j.matdes.2017.01.098
35. Kim G D, Oh Y T. A benchmark study on rapid prototyping processes and machines: Quantitative comparisons of mechanical properties, accuracy, roughness, speed, and material cost. Proc Inst Mech Eng Part B J Eng Manuf. 2008;222(2):201–15. doi: 10.1243/09544054JEM724
36. Redwood B, Schffer F, Garret B. The 3D printing handbook: technologies, design and applications. Amsterdam: 3D Hubs; 2017.
37. Diabase. Why the Cam Dial for compression control?. Longmont, Diabase Engineering. 2016 [accessed 2020-06-20] Available from: https://flexionextruder.com/why-the-cam-dial-for-compression-control/
38. Soe S P, Martin P, Jones M, Robinson M, Theobald P. Feasibility of optimising bicycle helmet design safety through the use of additive manufactured TPE cellular structures. Int J Adv Manuf Technol. 2015;79(9–12):1975–1982. doi: 10.1007/s00170-015-6972-y
39. M. Robinson, S. Soe, G. McShane, R. Celeghini, R. Burek, M. Alves, B. Hanna PT. Developing Elastomeric Cellular Structures for Multiple Head Impacts. M. In: IRCOBI; 2017 Sep 13 – 15 Antwerp, Belgium. p. 182-189
40. Ninjatek. Technical Specifications Ninjaflex 3D Printing Filament. Available at: https://ninjatek.fppsites.com/wp-content/uploads/2018/10/NinjaFlex-TDS.pdf [Accessed 28 November 2018].
41. Bates S R G, Farrow I R, Trask R S. 3D printed elastic honeycombs with graded density for tailorable energy absorption. In: SPIE Smart Structures and Materials + Nondestructive

Evaluation and Health Monitoring; Active and Passive Smart Structures and Integrated Systems 2016 March 20-24. Las Vega USA. doi: 10.1117/12.2219322
42. Qi H J, Boyce M C. Stress-strain behavior of thermoplastic polyurethanes. Mech Mater. 2005;37(8):817–39. doi: 10.1016/j.mechmat.2004.08.001
43. Dompier T P, Kerr Z Y, Marshall S W, Hainline B, Snook E M, Hayden R, et al. Incidence of concussion during practice and games in youth, high school, and collegiate American football players. JAMA Pediatr. 2015;169(7):659–665. doi: 10.1001/jamapediatrics.2015.0210
44. Peterson AR, Kruse AJ, Meester SM, Olson TS, Riedle BN, Slayman TG, et al. Youth football injuries: A prospective cohort. Orthop J Sport Med. 2017;5(2). doi: 10.1177/2325967116686784
45. National Federation of State High School Associations. 2018-19 High School Athletics Participation Survey. 2019; [accessed 2020-07-06] Available from: https://www.nfhs.org/media/1020412/2018-19_participation_survey.pdf
46. Irick E. Student-athlete participation. NCAA® Sports Sponsorship and Participation Rates Report. 2019. [accessed 2020-07-06] Available from: https://ncaaorg.s3.amazonaws.com/research/sportpart/2018-19RES_SportsSponsorshipParticipationRatesReport.pdf
47. Grashow R G, Roberts A L, Zafonte R, Pascual-Leone A, Taylor H, Baggish A, et al. Defining Exposures in Professional Football: Professional American-Style Football Players as an Occupational Cohort. Orthopaedic Journal of Sports Medicine. 2019;7(2). doi: 10.1177/2325967119829212
48. Ocwieja K E, Mihalik J P, Marshall S W, Schmidt J D, Trulock S C, Guskiewicz K M. The effect of play type and collision closing distance on head impact biomechanics. Ann Biomed Eng. 2012;40(1):90–96. doi: 10.1007/s10439-011-0401-7
49. Broglio S P, Sosnoff J J, Shin S H, He X, Alcaraz C, Zimmerman J. Head impacts during high school football: A biomechanical assessment. J Athl Train. 2009;44(4):342–349. doi: 10.4085/1062-6050-44.4.342
50. Zanetti K, Post A, Karton C, Kendall M, Hoshizaki T B, Gilchrist M D. Identifying injury characteristics for three player positions in American football using physical and finite element modeling reconstructions. In: IRCOBI. Gothenburg; Sweden: 2013 Sep 11-13. p. 525-535
51. Iguchi J, Yamada Y, Ando S, Fujisawa Y, Hojo T, Nishimura K, et al. Physical and Performance Characteristics of Japanese Division 1 Collegiate Football Players. J Strength Cond Res. 2011;25(12):3368–77. doi: 10.1519/JSC.0b013e318215fc19
52. Kraemer WJ, Torine JC, Silvestre R, French DN, Ratamess NA, Spiering BA, et al. Body size and composition of National Football League players. J Strength Cond Res. 2005;19(3):485–9. doi: 10.1519/18175.1
53. Anzell AR, Potteiger JA, Kraemer WJ, Otieno S. Changes in height, body weight, and body composition in american football players from 1942 to 2011. Vol. 27, J Strength Cond Res. 2013;27(2). p. 277–84. doi: 10.1519/JSC.0b013e31827f4c08
54. Willigenburg N W, Borchers J R, Quincy R, Kaeding C C, Hewett T E. Comparison of Injuries in American Collegiate Football and Club Rugby. Am J Sports Med. 2016;44(3):753–760. doi: 10.1177/0363546515622389
55. Marar M, McIlvain N M, Fields S K, Comstock R D. Epidemiology of concussions among united states high school athletes in 20 sports. Am J Sports Med. 2012;40(4):747–55. doi: 10.1177/0363546511435626
56. Zuckerman SL, Kerr ZY, Yengo-Kahn A, Wasserman E, Covassin T, Solomon GS. Epidemiology of sports-related concussion in NCAA athletes from 2009-2010 to 2013-2014. Am J Sports Med. 2015;43(11):2654–62. doi: 10.1177/0363546515599634
57. Bishop P J, Norman R W, Kozey J W. An evaluation of football helmets under impact conditions. Am J Sports Med. 1984;12(3):233–6. doi: 10.1177/036354658401200313
58. Sidman J. From Helmte to Sideline, Device Measures Impacts to Head. USA Today. 2006 [accessed 2019-11-14] Available from: https://usatoday30.usatoday.com/news/health/2006-07-26-helmets_x.htm
59. Duma SM, Manoogian SJ, Bussone WR, Brolinson PG, Goforth MW, Donnenwerth JJ, et al. Analysis of real-time head accelerations in collegiate football players. Clin J Sport Med. 2005;15(1):3–8. doi: 10.1097/00042752-200501000-00002

60. Eckner JT, Sabin M, Kutcher JS, Broglio SP. No evidence for a cumulative impact effect on concussion injury threshold. J Neurotrauma. 2011;28(10):2079–90. doi: 10.1089/neu.2011.1910
61. Beckwith JG, Greenwald RM, Chu JJ. Measuring head kinematics in football: Correlation between the head impact telemetry system and hybrid III headform. Ann Biomed Eng. 2012 Jan;40(1):237–48. doi: 10.1007/s10439-011-0422-2
62. Siegmund GP, Bonin SJ, Luck JF, Bass CRD. Validation of a skin-mounted sensor for measuring in-vivo head impacts. In: IRCOBI Lyon; France: 2015. p182–3.
63. Lennon A. Measurement of Head Impact Biomechanics: A Comparison of the Head Impact Telemetry [MA]. Chaple Hill. University of Noth Carolina. 2015
64. Daniel RW, Rowson S, Duma SM. Head impact exposure in youth football. Ann Biomed Eng. 2012;40(4):976–81. doi: 10.1007/s10439-012-0530-7
65. Cobb BR, Urban JE, Davenport EM, Rowson S, Duma SM, Maldjian JA, et al. Head impact exposure in youth football: Elementary school ages 9-12 years and the effect of practice structure. Ann Biomed Eng. 2013;41(12):2463–73. doi: 10.1007/s10439-013-0867-6
66. Campolettano ET, Rowson S, Duma SM. Drill-specific head impact exposure in youth football practice. J Neurosurg Pediatr. 2016;18(5):536–41. doi: 10.3171/2016.5.PEDS1696
67. Campolettano ET, Gellner RA, Rowson S. High-magnitude head impact exposure in youth football. J Neurosurg Pediatr. 2017;20(6):604–12. doi: 10.3171/2017.5.peds17185
68. Kelley ME, Kane JM, Espeland MA, Miller LE, Powers AK, Stitzel JD, et al. Head impact exposure measured in a single youth football team during practice drills. J Neurosurg Pediatr. 2017;20(5):489–97. doi: 10.3171/2017.5.PEDS16627
69. Schnebel B, Gwin JT, Anderson S, Gatlin R. In vivo study of head impacts in football: A comparison of National Collegiate Athletic Association Division I versus high school impacts. Neurosurgery. 2007;60(3):490–5. doi: 10.1227/01.NEU.0000249286.92255.7F
70. Greenwald RM, Gwin JT, Chu JJ, Crisco JJ. Head Impact Severity Measures for Evaluating Mild Traumatic Brain Injury Risk Exposure. Neurosurgery. 2008;62(4):789–98. doi: 10.1227/01.NEU.0000311244.05104.96
71. Broglio SP, Eckner JT, Martini D, Sosnoff JJ, Kutcher JS, Randolph C. Cumulative head impact burden in high school football. J Neurotrauma. 2011 Oct 1;28(10):2069–78. doi: 10.1089/neu.2011.1825
72. Broglio SP, Schnebel B, Sosnoff JJ, Shin S, Feng X, He X, et al. Biomechanical properties of concussions in high school football. Med Sci Sports Exerc. 2010;42(11):2064–71. doi: 10.1249/MSS.0b013e3181dd9156
73. Urban JE, Davenport EM, Golman AJ, Maldjian JA, Whitlow CT, Powers AK. Head impact exposure in youth football: High school ages 14 to 18 years and cumulative impact analysis. Ann Biomed Eng. 2013;41(12):2474–87. doi: 10.1007/s10439-013-0861-z
74. Broglio SP, Williams RM, O'Connor KL, Goldstick J. Football players' head-impact exposure after limiting of full-contact practices. J Athl Train. 2016;51(7):511–8. doi: 10.4085/1062-6050-51.7.04
75. Rowson S, Brolinson G, Goforth M, Dietter D, Duma S. Linear and angular head acceleration measurements in collegiate football. J Biomech Eng. 2009;131(6). doi: 10.1115/1.3130454
76. Crisco JJ, Fiore R, Beckwith JG, Chu JJ, Brolinson GP, Duma S, et al. Frequency and location of head impact exposures in individual collegiate football players. J Athl Train. 2010;45(6):549–59. doi: 10.4085/1062-6050-45.6.549
77. Crisco JJ, Wilcox BJ, Beckwith JG, Chu JJ, Duhaime AC, Rowson S, et al. Head impact exposure in collegiate football players. J Biomech. 2011;44(15):2673–8. doi: 10.1016/j.jbiomech.2011.08.003
78. Crisco JJ, Wilcox BJ, Machan JT, McAllister TW, Duhaime AC, Duma SM, et al. Magnitude of head impact exposures in individual collegiate football players. J Appl Biomech. 2012 May;28(2):174–83. doi: 10.1123/jab.28.2.174
79. Fukuda T, Koike S, Miyakawa S, Fujiya H, Yamamoto Y. Magnitude and frequency of head impact among university American football players. J Phys Fit Sport Med. 2019;8(1):1–13. doi: 10.7600/jpfsm.8.1
80. Fukuda T, Koike S, Miyakawa S, Fujiya H, Yamamoto Y. Impact on the head during collisions between university American football players - focusing on the number of head

impacts and linear head acceleration -. J Phys Fit Sport Med. 2017;6(4):241–9. doi: 10.7600/jpfsm.6.241
81. Reynolds BB, Patrie J, Henry EJ, Goodkin HP, Broshek DK, Wintermark M, et al. Comparative Analysis of Head Impact in Contact and Collision Sports. J Neurotrauma. 2017;34(1):38–49. doi: 10.1089/neu.2015.4308
82. Houck Z, Asken B, Bauer R, Pothast J, Michaudet C, Clugston J. Epidemiology of sport-related concussion in an NCAA division i football bowl subdivision sample. Am J Sports Med. 2016;44(9):2269–75. doi: 10.1177/0363546516645070
83. Pellman EJ, Viano DC, Tucker AM, Casson IR, Waeckerle JF, Maroon JC, et al. Concussion in professional football: Reconstruction of game impacts and injuries. Neurosurgery. 2003 Oct 1;53(4):799–814. doi: 10.1093/neurosurgery/53.3.799
84. Viano DC, Withnall C, Halstead D. Impact performance of modern football helmets. Ann Biomed Eng. 2012;40(1):160–74. doi: 10.1007/s10439-011-0384-4
85. Beckwith JG, Greenwald RM, Chu JJ, Crisco JJ, Rowson S, Duma SM, et al. Head impact exposure sustained by football players on days of diagnosed concussion. Med Sci Sports Exerc. 2013;45(4):737–46. doi: 10.1249/MSS.0b013e3182792ed7
86. Elkin BS, Gabler LF, Panzer MB, Siegmund GP. Brain tissue strains vary with head impact location: A possible explanation for increased concussion risk in struck versus striking football players. Clin Biomech. 2019;64:49–57. doi: 10.1016/j.clinbiomech.2018.03.021
87. King A. The Biomechanics of Impact Injury. Springer International Publishing. 2018
88. Hurt W. The Scalp. England and Wales, TeachMe Series, 2020-05-20, [Accessed: 2020-06-30] Available from: https://teachmeanatomy.info/head/areas/scalp/
89. Jones, O. The Meniges. England and Wales, TeachMe Series, 2020-02-07, [Accessed: 2020-06-30] Available from: https://teachmeanatomy.info/head/areas/scalp/
90. Parikh S, Kock M, Narayan RK. Traumatic Brain Injury. Int Anesthesiol Clin. 2007;45(3):119–1135. doi: 10.1097/AIA.0b013e318078cfe7
91. Shankar P R, Fields S K, Collins C L, Dick R W, Comstock R D. Epidemiology of high school and collegiate football injuries in the United States, 2005-2006. Am J Sports Med. 2007;35(8):1295–1303. doi: 10.1177/0363546507299745
92. McCrory P, Meeuwisse W, Dvořák J, Aubry M, Bailes J, Broglio S, Cantu R C,Cassidy D, Echemendia, R J, Castellani, R J, Davis, G A, Ellenbogen R, Emery C, Engebretsen L, Feddermann-Demont N, Giza C G, Guskiewicz K M, Herring S, Iverson G L, Johnston K M, Kissick J, Kutcher J, Leddy J J, Maddocks D, Makdissi M, Manley G T, McCrea M, Meehan W P, Nagahiro S, Patricios J, Putukian M, Schneider K J, Sills A, Tator C H, Turner M, Vos P E. Consensus statement on concussion in sport—the 5th international conference on concussion in sport held in Berlin, October 2016. Br J Sports Med. 2017;51(11):838–847. doi: 10.1136/bjsports-2017-097699
93. Choe MC. The Pathophysiology of Concussion. Curr Pain Headache Rep. 2016;20(6) doi: 10.1007/s11916-016-0573-9
94. Jordan BD. The clinical spectrum of sport-related traumatic brain injury. Nature Reviews Neurology. 2013;9(4):222–230. doi: 10.1038/nrneurol.2013.33
95. Alexander MP. Mild traumatic brain injury: Pathophysiology, natural history, and clinical management. Neurology. 1995;45(7):1253–1260. doi: 10.1212/WNL.45.7.1253
96. Brunger H, Ogden J, Malia K, Eldred C, Terblanche R, Mistlin A. Adjusting to persistent post-concussive symptoms following mild traumatic brain injury and subsequent psycho-educational intervention: A qualitative analysis in military personnel. Brain Inj. 2014;28(1):71–80. doi: 10.3109/02699052.2013.857788
97. Guskiewicz K M, Marshall S W, Bailes J, Mccrea M, Cantu R C, Randolph C, Jordan B D. Association between Recurrent Concussion and Late-Life Cognitive Impairment in Retired Professional Football Players. Neurosurgery. 2005;57(4):719–26. doi: 10.1227/01.NEU.0000175725.75780.DD
98. Janssen PH, Mandrekar J, Mielke MM, Ahlskog JE, Boeve BF, Josephs K, et al. High School Football and Late-Life Risk of Neurodegenerative Syndromes, 1956-1970. Mayo Clin Proc. 2017;92(1):66–71. doi: 10.1016/j.mayocp.2016.09.004
99. Solomon G. Chronic traumatic encephalopathy in sports: a historical and narrative review. Vol. 43, Developmental Neuropsychology. 2018;53(4):279–311. doi: 10.1080/87565641.2018.1447575
100. Kucera K L, Klossner D, Cantu R C. Annual Survey of Catastrophic Football Injuries 1977 - 2018. National Center for Catastrophic Sport Injury Research 2019. [accessed

202-01-15]. Available from: https://nccsir.unc.edu/files/2013/10/Annual-Football-2014-Fatalities-Final.pdf
101. Boden BP, Tacchetti RL, Cantu RC, Knowles SB, Mueller FO. Catastrophic head injuries in high school and college football players. Am J Sports Med. 2007;35(7):1075–81. doi: 10.1177/0363546507299239
102. Munro D, Merritt HH. Surgical pathology of subdural hematoma: based on a study of one hundred and five cases. Archives of Neurology & Psychiatry. 1936;35(1):64-78. doi: 10.1001/archneurpsyc.1936.02260010074005
103. Gurdjian ES, Lissner HR, Patrick LM. Protection of the Head and Neck in Sports. JAMA J Am Med Assoc. 1962;182(5):509–12. doi: 10.1001/jama.1962.03050440001001
104. Kucera K L, Klossner D, Colgate B, Cantu RC. annual survey of football injury research 1931 - 2018. National Center for Catastrophic Sport Injury Research. 2019. [accessed 202-01-15]. Available from: https://nccsir.unc.edu/files/2013/10/Annual-Football-2014-Fatalities-Final.pdf
105. Cantu R C, Mueller F O, Maroon J C, Day A L, Theodosopoulos P, Bailes J E. Brain injury-related fatalities in American football, 1945-1999. Neurosurgery. 2003;52(4):846–853. doi: 10.1227/01.NEU.0000053210.76063.E4
106. Page E, Sant J, Paverd J, Adair J, Culache D, Jackson M, et al. Serum Neurofilament Light in American Football Athletes Over the Course of a Season. J Neurotrauma. 2016;33(19):1784–9.
107. Verweij BH, Amelink GJ, Muizelaar JP. Current concepts of ce- rebral oxygen transport and energy metabolism after severe trau- matic brain injury. Prog Brain Res. 2007;161:111–24.
108. Bergsneider M, Hovda DA, McArthur DL, Etchepare M, Huang SC, Sehati N, et al. Metabolic recovery following human traumatic brain injury based on FDG-PET: time course and relationship to neurological disability. J Head Trauma Rehabil. 2001;16(2):135–48.
109. Meier TB, Brummel BJ, Singh R, Nerio CJ, Polanski DW, Bellgowan PSF. The underreporting of self-reported symptoms following sports-related concussion. J Sci Med Sport. 2015 Sep 1;18(5):507–11. doi: 10.1016/j.jsams.2014.07.008
110. Marshall CM. Sports-related concussion: A narrative review of the literature. J Can Chiropr Assoc. 2012;56(4):299–310.
111. Ashman TA, Gordon WA, Cantor JB, Hibbard MR. Neurobehavioral consequences of traumatic brain injury. Mount Sinai Journal of Medicine. 2006;73(7):999–1005.
112. Guskiewicz KM, McCrea M, Marshall SW, Cantu RC, Randolph C, Barr W, et al. Cumulative Effects Associated with Recurrent Concussion in Collegiate Football Players: The NCAA Concussion Study. J Am Med Assoc. 2003 Nov 19;290(19):2549–55. doi: 10.1001/jama.290.19.2549
113. Kerr ZY, Hayden R, Dompier TP, Cohen R. Association of equipment worn and concussion injury rates in national collegiate athletic association football practices: 2004-2005 to 2008-2009 academic years. Am J Sports Med. 2015;43(5):1134–41. doi: 10.1177/0363546515570622
114. Churchill NW, Hutchison MG, Richards D, Leung G, Graham SJ, Schweizer TA. The first week after concussion: Blood flow, brain function and white matter microstructure. NeuroImage Clin. 2017;14:480–9. doi: 10.1016/j.nicl.2017.02.015
115. Cantu RC. Posttraumatic Retrograde and Anterograde Amnesia: Pathophysiology and Implications in Grading and Safe Return to Play. J Athl Train. 2001 Sep;36(3):244–248.
116. Echemendia RJ, Meeuwisse W, McCrory P, Davis GA, Putukian M, Leddy J, et al. The Sport Concussion Assessment Tool 5th Edition (SCAT5): Background and rationale. Br J Sports Med. 2017;51(11):848–50. doi: 10.1136/bjsports-2017-097506
117. Cournoyer J, Hoshizaki TB. Biomechanical comparison of concussions with and without a loss of consciousness in elite American football: implications for prevention. Sport Biomech. 2019. doi: https://doi.org/10.1080/14763141.2019.1600004
118. Buckley WE. Concussions in college football: A multivariate analysis. Am J Sports Med. 1988;16(1):51–6. doi: 10.1177/036354658801600109
119. Albright JP, McAuley E, Martin RK, Crowley ET, Foster DT. Head and neck injuries in college football: An eight-year analysis. Am J Sports Med. 1985;13(3):147–52. doi: 10.1177/036354658501300301.

120. Nathanson JT, Connolly JG, Yuk F, Gometz A, Rasouli J, Lovell M, et al. Concussion Incidence in Professional Football: Position-Specific Analysis With Use of a Novel Metric. Orthop J Sport Med. 2016;4(1). doi: 10.1177/2325967115622621
121. Baugh CM, Kiernan PT, Kroshus E, Daneshvar DH, Montenigro PH, McKee AC, et al. Frequency of Head-Impact–Related Outcomes by Position in NCAA Division I Collegiate Football Players. J Neurotrauma. 2015;32(5):314–26. doi: 10.1089/neu.2014.3582
122. Pellman EJ, Viano DC, Casson IR, Tucker AM, Waeckerle JF, Powell JW, et al. Concussion in professional football: Repeat injuries - Part 4. Neurosurgery. 2004;55(4):860–76. doi: 10.1227/01.NEU.0000137657.00146.7D
123. Harmon KG, Clugston JR, Dec K, Hainline B, Herring S, Kane SF, et al. American Medical Society for Sports Medicine position statement on concussion in sport. Br J Sports Med. 2019;53(4):213–225. doi: 10.1136/bjsports-2018-100338
124. Goodwin Gerberich S, Priest JD, Boen JR, Straub CP, Maxwell RE. Concussion Incidences and Severity in Secondary School Varsity Football Players. 1983;73(12):1370-1375. doi: 10.2105/AJPH.73.12.1370
125. Wilberger JE. Minor Head Injuries in American Football. Sport Med. 1993;15(5):338–43. doi: 10.2165/00007256-199315050-00005
126. Barth JT, Alves WM, Ryan T V, Macciocchi SN, Rimel RW, Jane JA, Nelson WE. Mild head injury in sports: neuropsychological sequelae and recovery of function. In: Levin HS, Esinberg HM, Benton AL. Mild head Injury. Oxford: Oxford University Press; 1989. 257–75.
127. Powell JW, Barber-Foss KD. Traumatic brain injury in high school athletes. J Am Med Assoc. 1999 Sep 8;282(10):958–63. doi: 10.1001/jama.282.10.958
128. Guskiewicz KM, Weaver NL, Padua DA, Garrett WE. Epidemiology of concussion in collegiate and high school football players. Am J Sports Med. 2000;28(5):643–50. doi: 10.1177/03635465000280050401
129. Casson IR, Viano DC, Powell JW, Pellman EJ. Twelve years of National Football League concussion data. Sports Health. 2010;2(6):471–83. doi: 10.1177/1941738110383963
130. Rosenthal JA, Foraker RE, Collins CL, Comstock RD. National high school athlete concussion rates from 2005-2006 to 2011-2012. Am J Sports Med. 2014;42(7):1710–5. doi: 10.1177/0363546514530091
131. Kilcoyne KG, Dickens JF, Svoboda SJ, Owens BD, Cameron KL, Sullivan RT, et al. Reported Concussion Rates for Three Division I Football Programs: An Evaluation of the New NCAA Concussion Policy. Sports Health. 2014;6(5):402–5. doi: 10.1177/1941738113491545
132. Pellman, E. J., Powell, J. W., Viano, D. C., Casson, I. R., Tucker, A. M., Feuer, H., … Robertson, D. W. (2004). Concussion in Professional Football: Epidemiological Features of Game Injuries and Review of the Literature - Part 3. *Neurosurgery*, *54*, 81–96. https://doi.org/10.1227/01.NEU.0000097267.54786.54
133. National Football League. Injury Data. USA. 2019 [accessed 2020-06-20] Available from: https://www.playsmartplaysafe.com/newsroom/reports/injury-data/
134. McCrea M, Hammeke T, Olsen G, Leo P, Guskiewicz K. Unreported Concussion in High School Football Players. Clin J Sport Med. 2004;14(1):13–7. doi: 10.1097/01.jsm.0000181438.48892.1b
135. Register-Mihalik JK, Guskiewicz KM, McLeod TCV, Linnan LA, Mueller FO, Marshall SW. Knowledge, attitude, and concussion-reporting behaviors among high school athletes: A preliminary study. J Athl Train. 2013;48(5):645–53. doi: 10.4085/1062-6050-48.3.20
136. Llewellyn T, Burdette GT, Joyner AB, Buckley TA. Concussion reporting rates at the conclusion of an intercollegiate athletic career. Clin J Sport Med. 2014;24(1):76–9. doi: 10.1097/01.jsm.0000432853.77520.3d
137. Lincoln AE, Caswell S V, Almquist JL, Dunn RE, Norris JB, Hinton RY. Trends in concussion incidence in high school sports: A prospective 11-year study. Am J Sports Med. 2011;39(5):958–63. doi: 10.1177/0363546510392326
138. Robbins C, Daneshvar D, Picano J, Gavett B, Baugh C, Riley D, et al. Self-reported concussion history: impact of providing a definition of concussion. Open Access J Sport Med. 2014;99. doi: 10.2147/oajsm.s58005
139. Clark MD, Varangis EML, Champagne AA, Giovanello KS, Shi F, Kerr ZY, et al. Effects of Career Duration, Concussion History, and Playing Position on White Matter

Microstructure and Functional Neural Recruitment in Former College and Professional Football Athletes. Radiology. 2017;286(3):967–77. doi: 10.1148/radiol.2017170539
140. Kerr ZY, Evenson KR, Rosamond WD, Mihalik JP, Guskiewicz KM, Marshall SW. Association between concussion and mental health in former collegiate
141. Schulz MR, Marshall SW, Mueller FO, Yang J, Weaver NL, Kalsbeek WD, et al. Incidence and risk factors for concussion in high school athletes, North Carolina, 1996-1999. Am J Epidemiol. 2004 Nov 15;160(10):937–44. doi: 10.1093/aje/kwh304
142. Alosco ML, Kasimis AB, Stamm JM, Chua AS, Baugh CM, Daneshvar DH, et al. Age of first exposure to American football and long-term neuropsychiatric and cognitive outcomes. Transl Psychiatry. 2017 Sep 19;7(9):e1236. doi: 10.1038/tp.2017.197
143. Schultz V, Stern RA, Tripodis Y, Stamm J, Wrobel P, Lepage C, et al. Age at First Exposure to Repetitive Head Impacts Is Associated with Smaller Thalamic Volumes in Former Professional American Football Players. J Neurotrauma. 2018;35(2):278–85. doi: 10.1089/neu.2017.5145
144. Stamm JM, Bourlas AP, Baugh CM, Fritts NG, Daneshvar DH, Martin BM, et al. Age of first exposure to football and later-life cognitive impairment in former NFL players. Neurology. 2015 Mar 17;84(11):1114–20. doi: 10.1212/WNL.0000000000001358
145. Kerr ZY, Thomas LC, Simon JE, McCrea M, Guskiewicz KM. Association Between History of Multiple Concussions and Health Outcomes Among Former College Football Players: 15-Year Follow-up From the NCAA Concussion Study (1999-2001). Am J Sports Med. 2018;46(7):1733–41. doi: 10.1177/0363546518765121
146. Hart J, Kraut MA, Womack KB, Strain J, Didehbani N, Bartz E, et al. Neuroimaging of cognitive dysfunction and depression in aging retired national football league players. JAMA Neurol. 2013;70(3):326–35. doi: 10.1001/2013.jamaneurol.340
147. Didehbani N, Cullum CM, Mansinghani S, Conover H, Hart J. Depressive symptoms and concussions in aging retired NFL players. Arch Clin Neuropsychol. 2013 Aug;28(5):418–24. doi: 10.1093/arclin/act028
148. Montenigro PH, Alosco ML, Martin BM, Daneshvar DH, Mez J, Chaisson CE, et al. Cumulative Head Impact Exposure Predicts Later-Life Depression, Apathy, Executive Dysfunction, and Cognitive Impairment in Former High School and College Football Players. J Neurotrauma. 2017;34(2):328–40. doi: 10.1089/neu.2016.4413
149. Fields L, Didehbani N, Hart J, Cullum CM. No Linear Association Between Number of Concussions or Years Played and Cognitive Outcomes in Retired NFL Players. Arch Clin Neuropsychol. 2019; doi: 10.1093/arclin/acz008
150. Kerr ZY, DeFreese JD, Marshall SW. Current physical and mental health of former collegiate athletes. Orthop J Sport Med. 2014;2(8). [accessed 14 Oct 2019] Available from: http://www.sagepub.com/journalsPermissions.nav.
151. Manley G, Gardner AJ, Schneider KJ, Guskiewicz KM, Bailes J, Cantu RC, et al. A systematic review of potential long-term effects of sport-related concussion. Vol. 51, British Journal of Sports Medicine. BMJ Publishing Group; 2017. p. 969–77. doi: 10.1136/bjsports-2017-097791
152. Marchi N, Bazarian JJ, Puvenna V, Janigro M, Ghosh C, Zhong J, Zhu T, Blackman E, Stewart D, Ellis J, Butler R, Janigro D. Consequences of Repeated Blood-Brain Barrier Disruption in Football Players. PLoS One. 2013;8(3). doi: 10.1371/journal.pone.0056805
153. Kerr ZY, Littleton AC, Cox LM, DeFreese JD, Varangis E, Lynall RC, et al. Estimating Contact Exposure in Football Using the Head Impact Exposure Estimate. J Neurotrauma. 2015;32(14):1083–9. doi: 10.1089/neu.2014.3666
154. Bailes JE, Petraglia AL, Omalu BI, Nauman E, Talavage T. Role of subconcussion in repetitive mild traumatic brain injury. J Neurosurg. 2013;119(5):1235–45. doi: 10.3171/2013.7.JNS121822
155. Omalu BI, DeKosky ST, Minster RL, Kamboh MI, Hamilton RL, Wecht CH. Chronic traumatic encephalopathy in a National Football League player. Neurosurgery. 2005 Jul 1;57(1):128–33. doi: 10.1227/01.NEU.0000163407.92769.ED
156. Omalu BI, DeKosky ST, Hamilton RL, Minster RL, Kamboh MI, Shakir AM, et al. Chronic traumatic encephalopathy in a National Football League player: Part II. Neurosurgery. 2006;59(5):1086–92. doi: 10.1227/01.NEU.0000245601.69451.27
157. McKee AC, Stein TD, Nowinski CJ, Stern RA, Daneshvar DH, Alvarez VE, et al. The spectrum of disease in chronic traumatic encephalopathy. Brain. 2013;136(1):43–64. doi: 10.1093/brain/aws307

158. Boston University Center for the for the Study of Traumatic Encephalopathy. 2014. [Accessed 2019-10-22] Available from: https://www-cache.pbs.org/wgbh/pages/frontline/art/progs/concussions-cte/h.png
159. Bieniek KF, Ross OA, Cormier KA, Walton RL, Soto-Ortolaza A, Johnston AE, et al. Chronic traumatic encephalopathy pathology in a neurodegenerative disorders brain bank. Acta Neuropathol. 2015 Dec 1;130(6):877–89. doi: 10.1007/s00401-015-1502-4
160. Mez J, Daneshvar DH, Kiernan PT, Abdolmohammadi B, Alvarez VE, Huber BR, et al. Clinicopathological evaluation of chronic traumatic encephalopathy in players of American football. JAMA - J Am Med Assoc. 2017 Jul 25;318(4):360–70. doi: 10.1001/jama.2017.8334
161. Casson IR, Viano DC, Haacke EM, Kou Z, LeStrange DG. Is There Chronic Brain Damage in Retired NFL Players? Neuroradiology, Neuropsychology, and Neurology Examinations of 45 Retired Players. Sports Health. 2014;6(5):384–95. doi: 10.1177/1941738114540270
162. Gessel LM, Fields SK, Collins CL, Dick RW, Comstock RD. Concussions among United States high school and collegiate athletes. J Athl Train. 2007;42(4):495–503.
163. Lessley DJ, Kent RW, Funk JR, Sherwood CP, Cormier JM, Crandall JR, et al. Video Analysis of Reported Concussion Events in the National Football League During the 2015-2016 and 2016-2017 Seasons. Am J Sports Med. 2018;46(14):3502–10. doi: 10.1177/0363546518804498
164. Forbes JA, Awad AJ, Zuckerman S, Carr K, Cheng JS. Association between biomechanical parameters and concussion in helmeted collisions in American football: a review of the literature. Neurosurg Focus. 2012;33(6). doi: 10.3171/2012.9.focus12288
165. Mckee AC, Abdolmohammadi B, Stein TD. The neuropathology of chronic traumatic encephalopathy. In: Handbook of Clinical Neurology. Elsevier B.V.; 2018. p. 297–307. doi: 10.1016/B978-0-444-63954-7.00028-8
166. McKee AC, Cantu RC, Nowinski CJ, Hedley-Whyte ET, Gavett BE, Budson AE, et al. Chronic traumatic encephalopathy in athletes: Progressive tauopathy after repetitive head injury. Vol. 68, Journal of Neuropathology and Experimental Neurology. 2009. p. 709–35. doi: 10.1097/NEN.0b013e3181a9d503
167. Horstemeyer MF, Berthelson PR, Moore J, Persons AK, Dobbins A, Prabhu RK. A Mechanical Brain Damage Framework Used to Model Abnormal Brain Tau Protein Accumulations of National Football League Players. Ann Biomed Eng. 2019 Aug 1; doi: 10.1007/s10439-019-02294-1
168. Kleiven S. Why Most Traumatic Brain Injuries are Not Caused by Linear Acceleration but Skull Fractures are. Front Bioeng Biotechnol. 2013;1. doi: 10.3389/fbioe.2013.00015
169. Huang H-M, Lee M-C, Chiu W-T, Chen C-T, Lee S-Y. Three-Dimensional Finite Element Analysis of Subdural Hematoma. J Trauma Inj Infect Crit Care. 1999;47(3):538–44.
170. Depreitere B, Van Lierde C, Vander Sloten J, Van Audekercke R, Van Der Perre G, Plets C, et al. Mechanics of acute subdural hematomas resulting from bridging vein rupture. J Neurosurg. 2006;104(6):950–6. doi: 10.3171/jns.2006.104.6.950
171. Forbes JA, Zuckerman S, Abla AA, Mocco J, Bode K, Eads T. Biomechanics of subdural hemorrhage in American football: Review of the literature in response to rise in incidence. Child's Nervous System. 2014;30(2):197–203. doi: 10.1007/s00381-013-2318-y
172. Funk JR, Duma SM, Manoogian SJ, Rowson S. Biomechanical risk estimates for mild traumatic brain injury. In: Annual Proceedings - Association for the Advancement of Automotive Medicine. Melbourne; Australia: 2007. p. 343–61.
173. Zhang, L., Yang, K. H., & King, A. I. (2004). A Proposed Injury Threshold for Mild Traumatic Brain Injury. *Journal of Biomechanical Engineering*, *126*(2), 226–236. https://doi.org/10.1115/1.1691446
174. Campolettano ET, Gellner RA, Smith EP, Bellamkonda S, Tierney CT, Crisco JJ, et al. Development of a Concussion Risk Function for a Youth Population Using Head Linear and Rotational Acceleration. Ann Biomed Eng. 2019; doi: 10.1007/s10439-019-02382-2
175. Beckwith JG, Greenwald RM, Chu JJ, Crisco JJ, Rowson S, Duma SM, et al. Timing of concussion diagnosis is related to head impact exposure prior to injury. Med Sci Sports Exerc. 2013;45(4):747–54. doi: 10.1249/MSS.0b013e3182793067
176. Stemper BD, Shah AS, Wild A, Humm JR, Pintar FA, Broglio SP, et al. Role of repetitive head impact exposure in the onset of concussion: Evidence of a possible

second mechanism of concussion for contact sports. In: IRCOBI. Athens; Greece: 2018. p. 334–5
177. Post A, Hoshizaki TB. Mechanisms of brain impact injuries and their prediction: A review. Vol. 14, Trauma. 2012. p. 327–49. doi: 10.1177/1460408612446573
178. Fernandes FA, Sousa RJA de. Head injury predictors in sports trauma – A state-of-the-art review. Proc Inst Mech Eng Part H J Eng Med. 2015 Aug 3;229(8):592–608. doi: 10.1177/0954411915592906
179. Hoshizaki TB, Post A, Kendall M, Cournoyer J, Rousseau P, Gilchrist MD, et al. The development of a threshold curve for the understanding of concussion in sport. Trauma (United Kingdom). 2017;19(3):196–206. doi: 10.1177/1460408616676503
180. Gadd CW. Use of a weighted-impulse criterion for estimating injury hazard. SAE Tech Pap. 1966; doi: 10.4271/660793
181. Saboori P, Mansoor-Baghaei S, Sadegh AM. Evaluation of head injury criteria under different impact loading. In: ASME International Mechanical Engineering Congress and Exposition, Proceedings (IMECE). 2013. doi: 10.1115/IMECE2013-65125
182. Fédération Internationale de Motocyclisme. FRHPhe-01.FIM Racing Homologation Programme for Helmets (FRHPhe)Switzerland: FIM; 2017
183. Snell Foundation. M2020. Standard for Protective Headgear for Use With Motorcycles and Other Motorized Vehicles. North Highlands CA: Snell Foundation; 2019.
184. National Operating Committee on Standards for Athletic Equipment. (ND)002-17m19a. Standard Performance Specification for Newly Manufactured Football Helmets. NOCSAE:2019.
185. National Operating Committee on Standards for Athletic Equipment. (ND)022-18. Standard Performance Specification for Newly Manufactured Baseball/Softball Batter's Helmets. NOCSAE:2018.
186. Chancellor SE, Franz ES, Minaeva O V., Goldstein LE. Pathophysiology of Concussion. Semin Pediatr Neurol. 2019;30:14–25. doi: 10.1016/j.spen.2019.03.004
187. Van Lierde C. Biomechanics of Head injury. Damage criteria for skull and brain lesions [PhD]. Leuven: KU Leuven; 2005
188. Yanaoka T, Dokko Y, Takahashi Y. Investigation on an Injury Criterion Related to Traumatic Brain Injury Primarily Induced by Head Rotation. SAE Tech Pap. 2015;. doi: 10.4271/2015-01-1439
189. Takhounts EG, Craig MJ, Moorhouse K, McFadden J, Hasija V. Development of Brain Injury Criteria (BrIC). SAE Tech Pap. 2013. doi: 10.4271/2013-22-0010
190. Takhounts EG, Hasija V, Ridella SA, Rowson S, Duma SM. Kinematic Rotational Brain Injury Criterion. SAE Tech Pap. 2008;53(9):287. doi: 10.1017/CBO9781107415324.004
191. Kimpara H, Iwamoto M. Mild traumatic brain injury predictors based on angular accelerations during impacts. Ann Biomed Eng. 2012;40(1):114–26. doi: 10.1007/s10439-011-0414-2
192. Kleiven S. Predictors for Traumatic Brain Injuries Evaluated through Accident Reconstructions. SAE Tech Pap. 2007;2007-Octob(October). doi: 10.4271/2007-22-0003
193. Newman JA, Shewchenko N. A proposed new biomechanical head injury assessment function-the maximum power index. SAE Technical Paper; 2000 Nov 1.
194. Gabler LF, Crandall JR, Panzer MB. Development of a Second-Order System for Rapid Estimation of Maximum Brain Strain. Ann Biomed Eng. 2019;47(9):1971–81. doi: 10.1007/s10439-018-02179-9
195. Biocore. Helmet Test Protocol. Charlottesville: Biocore; 2019.
196. Mueller FO. Fatalities from head and cervical spine injuries occurring in tackle football: 50 years' experience. Clin Sports Med. 1998;17(1):169–82. doi: 10.1016/S0278-5919(05)70071-5
197. National Football League. New NFL rules designed to limit head injuries. NFL. 2010. [accessed 2019-11-05] Available from: https://www.nfl.com/news/new-nfl-rules-designed-to-limit-head-injuries-09000d5d81990bdf
198. ESPN.com Staff. NFL rulebook: Unnecessary roughness. ESPN. 2010. [accessed 2019-11-06] Available from: https://www.espn.com/blog/nflnation/post/_/id/29969/nfl-rulebook-unnecessary-roughness
199. Hanson A, Jolly NA, Peterson J. Safety regulation in professional football: Empirical evidence of intended and unintended consequences. J Health Econ. 2017;53:87–99. doi: 10.1016/j.jhealeco.2017.01.004

200. Ruestow PS, Duke TJ, Finley BL, Pierce JS. Effects of the NFL's Amendments to the Free Kick Rule on Injuries during the 2010 and 2011 Seasons. J Occup Environ Hyg. 2015;12(12):875–82. doi: 10.1080/15459624.2015.1072632
201. Greenhill DA, Navo P, Zhao H, Torg J, Comstock RD, Boden BP. Inadequate Helmet Fit Increases Concussion Severity in American High School Football Players. Sports Health. 2016;8(3):238–43 doi: 10.1177/1941738116639027
202. Mertz HJ, Prasad P, Nusholtz G. Head injury risk assessment for forehead impacts. SAE Technical Papers. 1996;105:26–46. doi: 10.4271/960099
203. Riddell. History of Riddell. Riddell 2019. [accessed 2020-01-15] Available from: https://content.riddell.com/history/#slide0
204. Gilchrist, A., & Mills, N. J. (1994). Modelling of the impact response of motorcycle helmets. *International Journal of Impact Engineering*, *15*(3), 201–218. https://doi.org/10.1016/S0734-743X(05)80013-2
205. Post A, Oeur A, Hoshizaki B, Gilchrist MD. An examination of American football helmets using brain deformation metrics associated with concussion. Mater Des. 2013;45:653–62. doi: 10.1016/j.matdes.2012.09.017
206. Sproule DW, Rowson S. Comparison of impact performance between youth and varsity football helmets. Proc Inst Mech Eng Part P J Sport Eng Technol. 2017;231(4):374–80. doi: 10.1177/1754337117731989
207. Whyte T, Stuart CA, Mallory A, Ghajari M, Plant DJ, Siegmund GP, Cripton PA. A review of impact testing methods for headgear in sports: Considerations for improved prevention of head injury through research and standards. Journal of Biomechanical Engineering. 2019;141(7). doi: 10.1115/1.4043140
208. Bina AJ, Batt GS, DesJardins JD. A review of laboratory methods and results used to evaluate protective headgear in American football. Proceedings of the Institution of Mechanical Engineers, Part P: Journal of Sports Engineering and Technology. 2018; 232(4):360-8. doi: 10.1177/1754337118759360
209. Virginia Tech Helmet Lab. Adult Football STAR Methodology. Blacksburg, Virginia Tech. [accessed 2020-02-01] Available from: https://vtechworks.lib.vt.edu/bitstream/handle/10919/82953/Adult%20Football%20STAR%20Methodology.pdf?sequence=1&isAllowed=y
210. Hoshizaki TB, Karton C, Oeur RA, Kendall M, Dawson L, Post A. An examination of the current National Operating Committee on Standards for Athletic Equipment system and a new pneumatic ram method for evaluating American football helmet performance to reduce risk of concussion. Proc Inst Mech Eng Part P J Sport Eng Technol. 2017;231(2):83–90. doi: 10.1177/1754337116633376
211. Cobb BR, Zadnik AM, Rowson S. Comparative analysis of helmeted impact response of Hybrid III and National Operating Committee on Standards for Athletic Equipment headforms. Proc Inst Mech Eng Part P J Sport Eng Technol. 2016;230(1):50–60. doi: 10.1177/1754337115599133
212. Allen, T., Shepherd, J., Hewage, T. A. M., Senior, T., Foster, L., & Alderson, A. (2015). Low-kinetic energy impact response of auxetic and conventional open-cell polyurethane foams. Physica Status Solidi (B), 252(7), 1631–1639. https://doi.org/10.1002/pssb.201451715
213. Spontak, R. J., & Patel, N. P. (2000). Thermoplastic elastomers: Fundamentals and applications. Current Opinion in Colloid and Interface Science, 5(5–6), 333–340. https://doi.org/10.1016/s1359-0294(00)00070-4
214. Maiti SK, Gibson LJ, Ashby MF. Deformation and energy absorption diagrams for cellular solids. Acta Metall. 1984;32(11):1963–75. doi: 10.1016/0001-6160(84)90177-9
215. Viano DC. Head impact biomechanics in sport. Solid Mech its Appl. 2005;124:121–30. doi: 10.1007/1-4020-3796-1_12
216. Viano DC, Pellman EJ. Concussion in professional football: Biomechanics of the striking player - Part 8. Neurosurgery. 2005;56(2):266–78. doi: 10.1227/01.NEU.0000150035.54230.3C
217. Viano DC, Casson IR, Pellman EJ. Concussion in professional football: Biomechanics of the struck player - Part 14. Neurosurgery. 2007;61(2):313–27. doi: 10.1227/01.NEU.0000279969.02685.D0
218. Ashby MF. The properties of foams and lattices. Philos Trans R Soc A Math Phys Eng Sci. 2006;364(1838):15–30. doi: 10.1098/rsta.2005.1678

219. Yoo DJ. New paradigms in cellular material design and fabrication. Int J Precis Eng Manuf. 2015;16(12):2577–89. doi: 10.1007/s12541-015-0330-8
220. Shim VPW, Tay BY and Stronge WJ. Dynamic crushing of strain-softening cellular structures—a one-dimensional analysis. *J. Eng. Mater. Technol*. 1990;112(4):398-405. doi: 10.1115/1.2903349
221. Tan PJ, Harrigan JJ and Reid SR. Inertia effects in uniaxial dynamic compression of a closed cell aluminium alloy foam. Mat Sci and Tech. 2002;18(5):480–488. doi:10.1179/026708302225002092
222. Zhang J, Ashby MF. Mechanical selection of foams and honeycombs used for packaging and energy absorption. J Mater Sci. 1994;29(1):157–63. doi: 10.1007/BF00356587
223. Woolam WE. A Study of the Dynamics of Low Energy Cushioning Materials Using Scale Models. J Cell Plast. 1968;4(2):79–83. doi: 10.1177/0021955X6800400204
224. Rusch KC. Energy-absorbing characteristics of foamed polymers. J Appl Polym Sci. 1970;14(6):1433–47. doi: 10.1002/app.1970.070140603
225. Timoshenko SP, Gere JM. Theory of Elastic Stability, 2nd ed. New York: McGraw-Hill Book Company: 1961.
226. Khan MK, Baig T, Mirza S. Experimental investigation of in-plane and out-of-plane crushing of aluminum honeycomb. Mater Sci Eng A. 2012 Mar 30;539:135–42. doi: 10.1016/j.msea.2012.01.070
227. Aktay L, Johnson AF, Kröplin BH. Numerical modelling of honeycomb core crush behaviour. Eng Fract Mech. 2008 Jun 1;75(9):2616–30. doi: 10.1016/j.engfracmech.2007.03.008
228. Safar A, Mihai LA. The nonlinear elasticity of hyperelastic models for stretch-dominated cellular structures. Int J Non Linear Mech. 2018;106:144–54. doi: 10.1016/j.ijnonlinmec.2018.08.006
229. Zok FW, Latture RM, Begley MR. Periodic truss structures. J Mech Phys Solids. 2016;96:184–203. doi: 10.1016/j.jmps.2016.07.007
230. Soe S, Ryan M, McShane G, Theobald P. Energy absorption characteristics of additively manufactured TPE cellular structures. In: KES International Conference on Sustainable Design and Manufacturing. Serville; Spain 12th -14th April 2015. p 145-158.
231. Schenk M, Guest SD. Geometry of Miura-folded metamaterials. Proc Natl Acad Sci. 2013 Feb 26;110(9):3276–81. doi: 10.1073/pnas.1217998110
232. Liu S, Lu G, Chen Y, Leong YW. Deformation of the Miura-ori patterned sheet. Int J Mech Sci. 2015 Aug 1;99:130–42. doi: 10.1016/j.ijmecsci.2015.05.009
233. Sychov MM, Lebedev LA, Dyachenko S V., Nefedova LA. Mechanical properties of energy-absorbing structures with triply periodic minimal surface topology. Acta Astronaut. 2018 Sep 1;150:81–4. doi: 10.1016/j.actaastro.2017.12.034
234. Zhang L, Feih S, Daynes S, Chang S, Wang MY, Wei J, et al. Energy absorption characteristics of metallic triply periodic minimal surface sheet structures under compressive loading. Addit Manuf. 2018 Oct 1;23:505–15. doi: 10.1016/j.addma.2018.08.007
235. Abueidda DW, Bakir M, Abu Al-Rub RK, Bergström JS, Sobh NA, Jasiuk I. Mechanical properties of 3D printed polymeric cellular materials with triply periodic minimal surface architectures. Mater Des. 2017;122:255–67. doi: /10.1016/j.matdes.2017.03.018
236. Li S, Fang H, Sadeghi S, Bhovad P, Wang KW. Architected Origami Materials: How Folding Creates Sophisticated Mechanical Properties. Adv Mater. 2019;31(5):1–18. doi: 10.1002/adma.201805282
237. Silverberg JL, Evans AA, McLeod L, Hayward RC, Hull T, Santangelo CD, et al. Using origami design principles to fold reprogrammable mechanical metamaterials. Science (80-). 2014;345(6197):647–50. doi: 10.1126/science.1252876
238. Ma J, Hou D, Chen Y, You Z. Quasi-static axial crushing of thin-walled tubes with a kite-shape rigid origami pattern: Numerical simulation. Thin-Walled Struct. 2016;100:38–47. Available from: http://dx.doi.org/10.1016/j.tws.2015.11.023
239. Song J, Chen Y, Lu G. Axial crushing of thin-walled structures with origami patterns. Thin-Walled Struct. 2012;54:65–71. doi: 10.1016/j.tws.2012.02.007
240. Ma J, You Z. Energy absorption of thin-walled square tubes with a prefolded origami pattern - Part I: Geometry and numerical simulation. J Appl Mech Trans ASME. 2014;81(1):1–11. doi: 10.1115/1.4024405

241. Abramowicz W, Jones N. Dynamic axial crushing of circular tubes. Int J Impact Eng. 1984;2(3):263–81. doi: 10.1016/0734-743X(84)90010-1
242. Chen Y, Feng H, Ma J, Peng R, You Z. Symmetric waterbomb origami. Proc R Soc A Math Phys Eng Sci. 2016 Jun 30;472. doi:10.1098/rspa.2015.0846
243. Dudte LH, Vouga E, Tachi T, Mahadevan L. Programming curvature using origami tessellations. Nat Mater. 2016;15(5):583–8. doi: 10.1038/nmat4540
244. Nassar H, Lebée A, Monasse L. Curvature, metric and parametrization of origami tessellations: Theory and application to the eggbox pattern. Proc R Soc A Math Phys Eng Sci. 2017;473(2197). doi: 10.1098/rspa.2016.0705
245. Silverberg JL, Na JH, Evans AA, Liu B, Hull TC, Santangelo CD, et al. Origami structures with a critical transition to bistability arising from hidden degrees of freedom. Nat Mater. 2015;14(4):389–93. doi: 10.1038/nmat4232
246. Fang H, Li S, Wang KW. Self-locking degree-4 vertex origami structures. Proc R Soc A Math Phys Eng Sci. 2016;472(2195). doi: 10.1098/rspa.2016.0682
247. Ma J, Song J, Chen Y. An origami-inspired structure with graded stiffness. Int J Mech Sci. 2018 Feb 1;136:134–42. doi: 10.1016/j.ijmecsci.2017.12.026
248. Xie R, Hou D, Ma J, Chen Y, You Z. Geometrically graded origami tubes. In: Proceedings of the ASME Design Engineering Technical Conference. Charlotte; 2016. p. 1–8. doi: 10.1115/DETC2016-59487
249. Ma J, Song J, Chen Y. An origami-inspired structure with graded stiffness. Int J Mech Sci. 2018;136:134–42. doi: 10.1016/j.ijmecsci.2017.12.026
250. Chen Y, Peng R, You Z. Origami of thick panels. Science. 2015;349(6246):396-400. doi: 10.1126/science.aab2870
251. Yasuda H, Yein T, Tachi T, Miura K, Taya M. 2013 Folding behaviour of Tachi–Miura polyhedron bellows. Proc R Soc A 469: 20130351. http://dx.doi.org/10.1098/rspa.2013.0351
252. Wei ZY, Guo ZV, Dudte L, Liang HY, Mahadevan L. Geometric mechanics of periodic pleated origami. Physical review letters. 2013 May 21;110(21):215501.
253. Mills N. Polymer foams handbook: engineering and biomechanics applications and design guide. Elsevier; 2007.
254. Davies, G.J., Zhen, S. Metallic foams: their production, properties and applications. J Mater Sci 1983;18:1899–1911 doi: https://doi.org/10.1007/BF00554981
255. Reid SR, Peng C. Dynamic uniaxial crushing of wood. Int J Impact Eng. 1997;19(5–6):531–70. doi: 10.1016/s0734-743x(97)00016-x
256. Harte AM, Fleck NA, Ashby MF. Fatigue failure of an open cell and a closed cell aluminum alloy foam. Acta Mater. 1999;47(8):2511–24. doi: 10.1016/S1359-6454(99)00097-X
257. Lakes R. Foam Structures with a Negative Poisson's Ratio. Science 1987;235:1038–41. doi: 10.1126/science.235.4792.1038
258. Evans KE, Nkansah MA, Hutchinson IJ, Rogers SC. Molecular network design. Vol. 353, Nature. 1991. p. 124. doi: 10.1038/353124a0
259. Alderson KL, Alderson A, Evans KE. The interpretation of the strain-dependent Poisson's ratio in auxetic polyethylene. J Strain Anal Eng Des. 1997;32(3):201–12. doi: 10.1243/0309324971513346
260. Evans KE, Alderson A, Christian FR. Auxetic two-dimensional polymer networks. An example of tailoring geometry for specific mechanical properties. Journal of the chemical society, Faraday transactions. 1995;91(16):2671-80.
261. Saxena KK, Das R, Calius EP. Three Decades of Auxetics Research − Materials with Negative Poisson's Ratio: A Review. Adv Eng Mater. 2016;18(11):1847–70. doi: 10.1002/adem.201600053
262. Masters IG, Evans KE. Models for the elastic deformation of honeycombs. Compos Struct. 1996;35(4):403–22. doi: 10.1016/S0263-8223(96)00054-2
263. Grima JN, Gatt R, Alderson A, Evans KE. On the auxetic properties of 'rotating rectangles' with different connectivity. J Phys Soc Japan. 2005;74(10):2866–7. doi: 10.1143/JPSJ.74.2866
264. Grima JN, Gatt R, Farrugia PS. On the properties of auxetic meta-tetrachiral structures. Phys Status Solidi Basic Res. 2008;245(3):511–20. doi: 10.1002/pssb.200777704
265. Budarapu PR, Sudhir Sastry YB, Natarajan R. Design concepts of an aircraft wing: composite and morphing airfoil with auxetic structures. Front Struct Civ Eng. 2016;10(4):394–408. doi: 10.1007/s11709-016-0352-z

266. Sanami M, Ravirala N, Alderson K, Alderson A. Auxetic materials for sports applications. Procedia Eng. 2014;72:453–8. Available from: http://dx.doi.org/10.1016/j.proeng.2014.06.079
267. Duncan O, Foster L, Senior T, Allen T, Alderson A. A Comparison of Novel and Conventional Fabrication Methods for Auxetic Foams for Sports Safety Applications. In: 11th conference of the International Sports Engineering Association Elsevier, Jansen AJ. Delft; Netherlands: 11-14 July 2016. 384-389.
268. Evans KE, Alderson A. Auxetic materials: Functional materials and structures from lateral thinking! Adv Mater. 2000;12(9):617–28.
269. Yang W, Li ZM, Shi W, Xie BH, Yang MB. Review on auxetic materials. Journal of materials science. 2004;39(10):3269-79. doi: https://doi.org/10.1023/B:JMSC.0000026928.93231.e0
270. Allen, T., Duncan, O., Foster, L., Senior, T., Zampieri, D., Edeh, V., & Alderson, A. (2017). Auxetic Foam for Snow-Sport Safety Devices. In: Scher I, Greenwald R. and Petrone N. Snow Sports Trauma and Safety. Springer International Publishing: 2017, 145-159.
271. Bezazi A, Scarpa F. Mechanical behaviour of conventional and negative Poisson's ratio thermoplastic polyurethane foams under compressive cyclic loading. Int J Fatigue. 2007;29(5):922–30. doi: 10.1016/j.ijfatigue.2006.07.015
272. Stojmanovski Mercieca LA, Formosa C, Grima JN, Chockalingam N, Gatt R, Gatt A. On the Use of Auxetics in Footwear: Investigating the Effect of Padding and Padding Material on Forefoot Pressure in High Heels. Phys Status Solidi Basic Res. 2017;254(12):1–5. doi: 10.1002/pssb.201700528
273. Duncan O, Naylor G, M JG, Allen T, Foster L, Hart J, et al. Plantar Pressure Distribution under Uniform and Gradient Foam during Running and Jumping †. Proceedings. 2020;49(116):1–6. doi: 10.3390/proceedings2020049116
274. Ouckama R, Pearsall DJ. Evaluation of a flexible force sensor for measurement of helmet foam impact performance. J Biomech. 2011;44(5):904–9. Available from: http://dx.doi.org/10.1016/j.jbiomech.2010.11.035
275. Ouckama R, Pearsall DJ. Impact performance of ice hockey helmets: Head acceleration versus focal force dispersion. Proc Inst Mech Eng Part P J Sport Eng Technol. 2012;226(3–4):185–92. doi: 10.1177/1754337111435625
276. Lamb L, Hoshizaki TB. Deformation mechanisms and impact attenuation characteristics of thin-walled collapsible air chambers used in head protection. Proc Inst Mech Eng Part H J Eng Med. 2009;223(8):1021–31. doi: 10.1243/09544119JEIM573
277. Gokhale V V., Marko C, Alam T, Chaudhari P, Tovar A. Design of an Advanced Layered Composite for Energy Dissipation using a 3D-Lattice of Micro Compliant Mechanism. SAE Tech Pap. 2016;2016-April(April). doi: 10.4271/2016-01-1538
278. Clough EC, Plaisted TA, Eckel ZC, Cante K, Hundley JM, Schaedler TA. Elastomeric Microlattice Impact Attenuators. Matter. 2019 Nov;1(6):1519–31
279. Joodaki H, Bailey A, Lessley D, Funk J, Sherwood C, Crandall J. Relative Motion between the Helmet and the Head in Football Impact Test. J Biomech Eng. 2019;141(8). doi: 10.1115/1.4043038
280. Giudice JS, Caudillo A, Mukherjee S, Kong K, Park G, Kent R, et al. Finite Element Model of a Deformable American Football Helmet Under Impact. Ann Biomed Eng. 2020;48(5):1524–39. doi: 10.1007/s10439-020-02472-6
281. Nagy A, ko WL, Lindholm US. Mechanical Behavior of Foamed Materials Under Dynamic Compression. J Cell Plast. 1974;10(3):127–34. doi: 10.1177/0021955X7401000306
282. Sarva SS, Deschanel S, Boyce MC, Chen W. Stress-strain behavior of a polyurea and a polyurethane from low to high strain rates. Polymer (Guildf). 2007;48(8):2208–13. doi: 10.1016/j.polymer.2007.02.058
283. Roland CM, Twigg JN, Vu Y, Mott PH. High strain rate mechanical behavior of polyurea. Polymer (Guildf). 2007;48(2):574–8. doi: 10.1016/j.polymer.2006.11.051
284. Yi J, Boyce MC, Lee GF, Balizer E. Large deformation rate-dependent stress-strain behavior of polyurea and polyurethanes. Polymer (Guildf). 2006;47(1):319–29. doi: 10.1016/j.polymer.2005.10.107
285. Ouellet S, Cronin D, Worswick M. Compressive response of polymeric foams under quasi-static, medium and high strain rate conditions. Polym Test. 2006;25(6):731–43. doi: 10.1016/j.polymertesting.2006.05.005

286. Yee AF, Lin Z, Wong A, Kikuchi N, Li VC, Nusholtz GS. Constitutive modeling and material characterization of polymeric foams. J Eng Mater Technol Trans ASME. 1997 Jul 1;119(3):284–91. doi: 10.1115/1.2812258
287. Ramirez BJ, Gupta V. Evaluation of novel temperature-stable viscoelastic polyurea foams as helmet liner materials. Mater Des. 2018;137:298–304. doi:10.1016/j.matdes.2017.10.037
288. Calladine CR, English RW. Strain-rate and inertia effects in the collapse of two types of energy-absorbing structure. Int J Mech Sci. 1984;26(11–12):689–701. doi: 10.1016/0020-7403(84)90021-3
289. Goldsmith W, Sackman JL. An experimental study of energy absorption in impact on sandwich plates. Int J Impact Eng. 1992 Jan 1;12(2):241–62. doi: 10.1016/0734-743X(92)90447-2
290. Wu E, Jiang WS. Axial crush of metallic honeycombs. Int J Impact Eng. 1997;19(5–6):439–56. doi: 10.1016/s0734-743x(97)00004-3
291. Zhao H, Gary G. Crushing behaviour of aluminium honeycombs under impact loading. Int J Impact Eng. 1998 Nov 1;21(10):827–36. doi: 10.1016/s0734-743x(98)00034-7
292. Ramirez BJ, Gupta V. Energy Absorption and Low Velocity Impact Response of Open-Cell Polyurea Foams. J Dyn Behav Mater. 2019;5(2):132–42. Available from: http://dx.doi.org/10.1007/s40870-019-00192-0
293. Bates SRG, Farrow IR, Trask RS. Compressive behaviour of 3D printed thermoplastic polyurethane honeycombs with graded densities. Mater Des. 2019;162:130–42. doi: 10.1016/j.matdes.2018.11.019
294. Wang W, Lu W, Goodwin A, Wang H, Yin P, Kang NG, et al. Recent advances in thermoplastic elastomers from living polymerizations: Macromolecular architectures and supramolecular chemistry. Prog Polym Sci. 2019;95:1–31. doi:10.1016/j.progpolymsci.2019.04.002
295. Lu G, Kalyon DM, Yilgör I, Yilgör E. Rheology and Extrusion of Medical-Grade Thermoplastic Polyurethane. Polym Eng Sci. 2003 Dec 1;43(12):1863–77. doi: http://doi.wiley.com/10.1002/pen.10158
296. Devine DM, editor. Polymer-Based Additive Manufacturing: Biomedical Applications. Springer Nature; 2019 Nov 15.
297. P. Zelinski, “Additive manufacturing and 3D printing are two different things,” AM Magazine, 2017. [accessed: 2020-05-16] available from: https://www.additivemanufacturing.media/blog/post/additive-manufacturing-and-3d-printing-are-two-different-things
298. ISO/ASTM 52900:2015. BSI Standards Publication Additive manufacturing — General principles — Terminology. 2017.
299. 3D Hubs. 3 Additive Manufacturing technologies to watch out for in 2017. Extreme Engineering. [accessed:2020 – 06-01] available from: https://medium.com/extreme-engineering/3-additive-manufacturing-technologies-to-watch-out-for-in-2017-7226d310ca56
300. Gaytan SM, Cadena MA, Karim H, Delfin D, Lin Y, Espalin D, et al. Fabrication of barium titanate by binder jetting additive manufacturing technology. Ceram Int. 2015;41(5):6610–9. doi: 10.1016/j.ceramint.2015.01.108
301. Bai Y, Williams CB. An exploration of binder jetting of copper. Rapid Prototyp J. 2015;21(2):177–85. doi: 10.1108/RPJ-12-2014-0180
302. Gibson I, Rosen D, Stucker B. Directed Energy Deposition Processes. In: Additive Manufacturing Technologies: 3D Printing, Rapid Prototyping, and Direct Digital Manufacturing. New York, NY: Springer New York; 2015. p. 245–68.
303. Torrado AR, Shemelya CM, English JD, Lin Y, Wicker RB, Roberson DA. Characterizing the effect of additives to ABS on the mechanical property anisotropy of specimens fabricated by material extrusion 3D printing. Addit Manuf. 2015;6:16–29.doi: http://dx.doi.org/10.1016/j.addma.2015.02.001
304. Park SI, Rosen DW, Choi S kyum, Duty CE. Effective mechanical properties of lattice material fabricated by material extrusion additive manufacturing. Addit Manuf. 2014;1:12–23. doi: http://dx.doi.org/10.1016/j.addma.2014.07.002
305. Yap HK, Ng HY, Yeow C-H. High-Force Soft Printable Pneumatics for Soft Robotic Applications. Soft Robot. 2016 Sep 1;3(3):144–58. doi: 10.1089/soro.2016.0030

306. Mansouri MR, Montazerian H, Schmauder S, Kadkhodapour J. 3D-printed multimaterial composites tailored for compliancy and strain recovery. Compos Struct. 2018 Jan 15;184:11–7
307. Yang C, Vora HD, Chang Y. Behavior of auxetic structures under compression and impact forces. Smart Mater Struct. 2018
308. Mohamed OA, Masood SH, Bhowmik JL. Optimization of fused deposition modeling process parameters: a review of current research and future prospects. Adv Manuf. 2015;3(1):42–53. doi: 10.1007/s40436-014-0097-7
309. Yap YL, Wang C, Sing SL, Dikshit V, Yeong WY, Wei J. Material jetting additive manufacturing: An experimental study using designed metrological benchmarks. Precis Eng. 2017;50:275–85. doi: 10.1016/j.precisioneng.2017.05.015
310. Gong H, Rafi K, Gu H, Starr T, Stucker B. Analysis of defect generation in Ti-6Al-4V parts made using powder bed fusion additive manufacturing processes. Addit Manuf. 2014;1:87–98doi: 10.1016/j.addma.2014.08.002
311. Yuan S, Shen F, Bai J, Chua CK, Wei J, Zhou K. 3D soft auxetic lattice structures fabricated by selective laser sintering: TPU powder evaluation and process optimization. Mater Des. 2017;120:317–27. doi: 10.1016/j.matdes.2017.01.098
312. Walker DA, Hedrick JL, Mirkin CA. Rapid, large-volume, thermally controlled 3D printing using a mobile liquid interface. Science (80-). 2019;366(6463):360–4. doi: 10.1126/science.aax1562
313. Lee JY, An J, Chua CK. Fundamentals and applications of 3D printing for novel materials. Vol. 7, Applied Materials Today. Elsevier; 2017. p. 120–33.
314. Janusziewicz R, Tumbleston JR, Quintanilla AL, Mecham SJ, DeSimone JM. Layerless fabrication with continuous liquid interface production. Proc Natl Acad Sci U S A. 2016;113(42):11703–8. doi: 10.1073/pnas.1605271113
315. Rafiee M, Farahani RD, Therriault D. Multi-Material 3D and 4D Printing: A Survey. Vol. 7, Adv Sci. 2020:7 doi: 10.1002/advs.201902307
316. Wu H, Fahy WP, Kim S, Kim H, Zhao N, Pilato L, et al. Recent developments in polymers/polymer nanocomposites for additive manufacturing. Progress in Materials Science. 2020: 111 doi: 10.1016/j.pmatsci.2020.100638
317. Varotsis A. B. Introduction to material jetting 3D printing. Amsterdam, 3D Hubs. [2020-05-23] Available from : https://www.3dhubs.com/knowledge-base/introduction-material-jetting-3d-printing/#materials
318. Lumpe TS, Mueller J, Shea K. Tensile properties of multi-material interfaces in 3D printed parts. Mater Des. 2019 Jan 15;162:1–9. doi: 10.1016/j.matdes.2018.11.024
319. Moore JP, Williams CB. Fatigue properties of parts printed by PolyJet material jetting. Rapid Prototyp J. 2015;21(6):675–85.
320. Tumbleston JR, Shirvanyants D, Ermoshkin N, Janusziewicz R, Johnson AR, Kelly D, et al. Continuous liquid interface production of 3D objects. Science (80-). 2015 Mar 20;347(6228):1349–52. doi: 10.1126/science.aaa2397
321. Janusziewicz, R., Mecham, S. J., Olson, K. R., Benhabbour, S. R., Design and Characterization of a Novel Series of Geometrically Complex Intravaginal Rings with Digital Light Synthesis. *Adv. Mater. Technol.* 2020, 5, 2000261. https://doi.org/10.1002/admt.202000261
322. Alharbi N, Osman R, Wismeijer D. Effects of build direction on the mechanical properties of 3D-printed complete coverage interim dental restorations. J Prosthet Dent. 2016;115(6):760–7. doi:10.1016/j.prosdent.2015.12.002
323. Das S, Beaman JJ, Bourell MWDL. Direct laser freeform fabrication of high performance metal components. Rapid Prototyp J. 1998;4(3):112–7. doi: 10.1108/13552549810222939
324. Zhu W, Yan C, Shi Y, Wen S, Liu J, Shi Y. Investigation into mechanical and microstructural properties of polypropylene manufactured by selective laser sintering in comparison with injection molding counterparts. Mater Des. 2015;82:37–45. doi:10.1016/j.matdes.2015.05.043
325. Soe SP. Quantitative analysis on SLS part curling using EOS P700 machine. J Mater Process Technol. 2012;212(11):2433–42. Available from: http://dx.doi.org/10.1016/j.jmatprotec.2012.06.012
326. Soe SP, Martindale N, Constantinou C, Robinson M. Mechanical characterisation of Duraform® Flex for FEA hyperelastic material modelling. Polym Test. 2014;34:103–12. Available from: http://dx.doi.org/10.1016/j.polymertesting.2014.01.004

327. Smith R. Laser Sintering vs Laser Melting. Modena, ADDITIVA, 2017-03-03. [2020-04-09] Available from: http://www.additivalab.com/en/blog/laser-sintering-vs-laser-melting/
328. Gringer. SLS System schematic. Wikipedia. 2018. [2020-04-09] Available from: https://commons.wikimedia.org/wiki/File:SLS_schematic.svg
329. Jiang D, Smith DE. Mechanical Behavior of Carbon Fiber Composites Produced with Fused Filament Fabrication. 27th Annu Int Solid Free Fabr Symp. 2016;884–98.
330. Burkhardt C, Freigassner P, Weber O, Imgrund P, Hampel S. Fused filament fabrication (FFF) of 316L green parts for the MIM process. World PM 2016 Congr Exhib. 2016;1.
331. Robinson M, Soe S, Johnston R, Adams R, Hanna B, Burek R, et al. Mechanical characterisation of additively manufactured elastomeric structures for variable strain rate applications. Addit Manuf. 2019 May 1;27:398–407. doi: 10.1016/j.addma.2019.03.022
332. Wang CC, Lin T, Hu S. Optimizing the rapid prototyping process by integrating the Taguchi method with the Gray relational analysis. Rapid Prototyp J. 2007;13(5):304–15. doi:10.1108/13552540710824814
333. Sood AK, Ohdar RK, Mahapatra SS. Improving dimensional accuracy of Fused Deposition Modelling processed part using grey Taguchi method. Mater Des. 2009 Dec 1;30(10):4243–52.
334. Nancharaiah T, Raju DR, Raju VR, Ranga Raju D, Ramachandra Raju V, Raju DR, et al. An experimental investigation on surface quality and dimensional accuracy of FDM components. Int J Emerg Technol. 2010;1(2):106–11.
335. Sahu RK, Mahapatra SS, Sood AK. A study on dimensional accuracy of fused deposition modeling (FDM) processed parts using fuzzy logic. Journal for Manufacturing Science and Production. 2013 Oct 25;13(3):183-97.
336. Herrero M, Peng F, Núñez Carrero KC, Merino JC, Vogt BD. Renewable Nanocomposites for Additive Manufacturing Using Fused Filament Fabrication. ACS Sustain Chem Eng. 2018;6(9):12393–402. doi: 10.1021/acssuschemeng.8b02919
337. Ang KC, Leong KF, Chua CK, Chandrasekaran M. Investigation of the mechanical properties and porosity relationships in fused deposition modelling-fabricated porous structures. Rapid Prototyp J. 2006 Mar 13;12(2):100–5. doi: 10.1108/13552540610652447
338. Sood AK, Ohdar RK, Mahapatra SS. Parametric appraisal of mechanical property of fused deposition modelling processed parts. Mater Des. 2010 Jan 1;31(1):287–95.
339. Rayegani F, Onwubolu GC. Fused deposition modelling (fdm) process parameter prediction and optimization using group method for data handling (gmdh) and differential evolution (de). Int J Adv Manuf Technol. 2014 Jul 25;73(1–4):509–19.
340. Hohimer CJ, Christ JF, Aliheidari N, Ameli A. 3D Printed Thermoplastic Polyurethane with Isotropic Material Properties. doi:10.1117/12.2259820
341. Xiao J, Gao Y. The manufacture of 3D printing of medical-grade TPU. Prog Addit Manuf. 2017 Sep 8;2(3):117–23. doi:10.1007/s40964-017-0023-1
342. Kotlinski J. Mechanical properties of commercial rapid prototyping materials. Rapid Prototyp J. 2014;20(6):499–510. doi: 10.1108/RPJ-06-2012-0052
343. Zhang Y, Chou K. A parametric study of part distortions in fused deposition modelling using three-dimensional finite element analysis. Proceedings of the Institution of Mechanical Engineers, Part B: Journal of Engineering Manufacture. 2008 Aug 1;222(8):959-68.
344. Ninjatek. 2016. Technical Specifications Cheetah 3D Printing Filament. Available at: https://ninjatek.fppsites.com/wp-content/uploads/2018/10/Cheetah-TDS.pdf [Accessed 28 November 2018]
345. Li Y, Linke BS, Voet H, Falk B, Schmitt R, Lam M. Cost, sustainability and surface roughness quality – A comprehensive analysis of products made with personal 3D printers. CIRP J Manuf Sci Technol. 2017 Jan 1;16:1–11. doi: 10.1016/j.cirpj.2016.10.001
346. Garcia J, Yang ZL, Mongrain R, Leask RL, Lachapelle K. 3D printing materials and their use in medical education: A review of current technology and trends for the future. BMJ Simul Technol Enhanc Learn. 2018;4(1):27–40. doi: 10.1136/bmjstel-2017-000234
347. Rengier F, Mehndiratta A, Von Tengg-Kobligk H, Zechmann CM, Unterhinninghofen R, Kauczor HU, et al. 3D printing based on imaging data: Review of medical applications. Int J Comput Assist Radiol Surg. 2010;5(4):335–41. doi: 10.1007/s11548-010-0476-x
348. Hopkinson N, Erasenthiran P. High Speed Sintering - Early Research into a New Rapid Manufacturing Process. 2003;(1):6–8.

349. Shah P, Racasan R, Bills P. Comparison of different additive manufacturing methods using computed tomography. Case Stud Nondestruct Test Eval. 2016 Nov 1;6:69–78. doi: 10.1016/j.csndt.2016.05.008
350. Ho ST, Hutmacher DW. A comparison of micro CT with other techniques used in the characterization of scaffolds. Vol. 27, Biomaterials. Elsevier; 2006. p. 1362–76.
351. Tellis BC, Szivek JA, Bliss CL, Margolis DS, Vaidyanathan RK, Calvert P. Trabecular scaffolds created using micro CT guided fused deposition modeling. Mater Sci Eng C. 2008;28(1):171–8. doi: 10.1016/j.msec.2006.11.010
352. Morris DE, Mather ML, Simon CG, Crowe JA. Time-optimized X-ray micro-CT imaging of polymer based scaffolds. J Biomed Mater Res - Part B Appl Biomater. 2012;100 B(2):360–7. doi: 10.1002/jbm.b.31957
353. Ahn SH, Montero M, Odell D, Roundy S, Wright PK. Anisotropic material properties of fused deposition modeling ABS. Rapid Prototyp J. 2002;8(4):248–57. doi: 10.1108/13552540210441166
354. British Standards Institution. 2017. BS ISO 37:2017 Rubber, vulcanized or thermoplastic. Determination of tensile stress-strain properties. London: BSI.
355. Ranjit R. A Primer on the Taguchi Method. New York: Van Nostrand Reinhold; 1990.
356. Deng X, Potula S, Grewal H, Solanki KN, Tschopp MA, Horstemeyer MF. Finite element analysis of occupant head injuries: Parametric effects of the side curtain airbag deployment interaction with a dummy head in a side impact crash. Accid Anal Prev. 2013;55:232–41. doi: 10.1016/j.aap.2013.03.016
357. Srivastava M, Rathee S. Optimisation of FDM process parameters by Taguchi method for imparting customised properties to components. Virtual Phys Prototyp. 2018 Jul 3;13(3):203–10. doi: 10.1080/17452759.2018.1440722
358. Forero Rueda MA, Cui L, Gilchrist MD. Optimisation of energy absorbing liner for equestrian helmets. Part I: Layered foam liner. Mater Des. 2009;30(9):3405–13. doi: 10.1016/j.matdes.2009.03.037
359. Cui L, Forero Rueda MA, Gilchrist MD. Optimisation of energy absorbing liner for equestrian helmets. Part II: Functionally graded foam liner. Mater Des. 2009;30(9):3414–9. doi: 10.1016/j.matdes.2009.03.044
360. NFL & NFLPA, Helmet Laboratory Testing Performance Results, Available at: https://www.playsmartplaysafe.com/resource/helmet-laboratory-testing-performance-results/ [Accssed 02/04/2020]
361. National Operating Committee on Standards for Athletic Equipment. (ND)001-17m20. Standard Test Method and Equipment Used in Evaluating the Performance Characteristics of Headgear/Equipment. NOCSAE:2020
362. Lisiecki J, Błazejewicz T, Kłysz S, Gmurczyk G, Reymer P, Mikułowski G. Tests of polyurethane foams with negative Poisson's ratio. Phys Status Solidi Basic Res. 2013;250(10):1988–95. doi: 10.1002/pssb.201384232
363. Lv C, Krishnaraju D, Konjevod G, Yu H, Jiang H. Origami based mechanical metamaterials. Sci Rep. 2014;4(1):5979.
364. Biocore. Finite Element Models. Charlottesville USA, Biocore, 2018. [2019-06-09] Available from: https://biocorellc.com/finite-element-models/
365. Zhang J, Wei H, Wang Z, Zhao L. Dynamic crushing of uniform and density graded cellular structures based on the circle arc model. Lat Am J Solids Struct. 2014;12(6):1102–25. doi: 10.1590/1679-78251630.
366. Avalle M, Belingardi G, Montanini R. Characterization of polymeric structural foams under compressive impact loading by means of energy-absorption diagram. Int J Impact Eng. 2001;25(5):455–72.
367. Kaya AC, Zaslansky P, Ipekoglu M, Fleck C. Strain hardening reduces energy absorption efficiency of austenitic stainless steel foams while porosity does not. Mater Des. 2018 Apr 5;143:297–308. doi: 10.1016/j.matdes.2018.02.009.
368. Mihai CD, Alexandru AD. Onset of densification and energy absorption efficiency of polyurethane foams. Technical Sciences. 2019;4(2):131-44.
369. Breedlove KM, Breedlove EL, Bowman TG, Arruda EM, Nauman EA. The effect of football helmet facemasks on impact behavior during linear drop tests. Journal of biomechanics. 2018;79:227-31.
370. Rush GA, Rush GA, Sbravati N, Prabhu R, Williams LN, DuBien JL, Horstemeyer MF. Comparison of shell-facemask responses in American football helmets during NOCSAE drop tests. Sports Engineering. 2017;20(3):199-211.

371. National Operating Committee on Standards for Athletic Equipment. (ND)081-18am19a. Standard Test Method and Equipment Used in Evaluating the Performance Characteristics of Headgear/Equipment. NOCSAE:2019
372. Zhang, J., Lu, G., & You, Z. (2020). Large deformation and energy absorption of additively manufactured auxetic materials and structures: A review. Composites Part B: Engineering, 108340. doi:10.1016/j.compositesb.2020.108340
373. Shepherd T, Winwood K, Venkatraman P, Alderson A, Allen T. Validation of a finite element modeling process for auxetic structures under impact. physica status solidi (b). 2020 Oct;257(10):1900197.
374. Qiao J, Chen CQ. Analyses on the in-plane impact resistance of auxetic double arrowhead honeycombs. Journal of Applied Mechanics. 2015 May 1;82(5)
375. Campbell KR, Marshall SW, Luck JF, Pinton GF, Stitzel JD, Boone JS, Guskiewicz KM, Mihalik JP. Head Impact Telemetry System's Video-based Impact Detection and Location Accuracy. Med Sci Sports Exerc. 52(10):2198-2206
376. Camarillo DB, Shull PB, Mattson J, Shultz R, Garza D. An instrumented mouthguard for measuring linear and angular head impact kinematics in American football. Annals of biomedical engineering. 2013 Sep 1;41(9):1939-49.
377. Mueller F, Cantu R. Annual Survey of Catastrophic Football Injuries: 1977–2011. 2012. doi: 10.1520/stp12800s
378. Casson IR, Viano DC. Long-term neurological consequences related to boxing and American football: A review of the literature. Vol. 69, Journal of Alzheimer's Disease. 2019. p. 935–52. doi: 10.3233/JAD-190115
379. Halldin P, Aare M, Kleiven S, von Holst H. Reduced risk for DAI by use of a new safety helmet. InInt. Conf. on Closed Head Trauma, US Army Medical Research and Material Command, and US Department of Transportation 2003.
380. Bliven E, Rouhier A, Tsai S, Willinger R, Bourdet N, Deck C, Madey SM, Bottlang M. Evaluation of a novel bicycle helmet concept in oblique impact testing. Accident Analysis & Prevention. 2019 Mar 1;124:58-65.

Chapter 10: Appendices

10.1. Additional Data.

10.1.1. Chapter 5.

10.1.1.1. L27 Array.

Table 10-1: L27 Array with all Parameter and Interaction values

	Geometrical Parameters				Interaction					
Sample	α	γ	β	t	α – γ	α – β	α – t	γ – β	γ – t	β – t
1_C	1	80	33	0.6	1	1	1	1	1	1
2_C	1	80	38	0.9	1	2	2	2	2	2
3_C	1	80	43	1.2	1	3	3	3	3	3
4_C	1	110	33	0.9	2	1	2	3	3	3
5_C	1	110	38	1.2	2	2	3	1	1	1
6_C	1	110	43	0.6	2	3	1	2	2	2
7_C	1	140	33	1.2	3	1	3	2	2	2
8_C	1	140	38	0.6	3	2	1	3	3	3
9_C	1	140	43	0.9	3	3	2	1	1	1
10_C	5	80	33	0.9	2	3	1	1	2	3
11_C	5	80	38	1.2	2	1	2	2	3	1
12_C	5	80	43	0.6	2	2	3	3	1	2
13_C	5	110	33	1.2	3	3	2	3	1	2
14_C	5	110	38	0.6	3	1	3	1	2	3
15_C	5	110	43	0.9	3	2	1	2	3	1
16_C	5	140	33	0.6	1	3	3	2	3	1
17_C	5	140	38	0.9	1	1	1	3	1	2
18_C	5	140	43	1.2	1	2	2	1	2	3
19_C	9	80	33	1.2	3	2	1	1	3	2
20_C	9	80	38	0.6	3	3	2	2	1	3
21_C	9	80	43	0.9	3	1	3	3	2	1
22_C	9	110	33	0.6	1	2	2	3	2	1
23_C	9	110	38	0.9	1	3	3	1	3	2
24_C	9	110	43	1.2	1	1	1	2	1	3
25_C	9	140	33	0.9	2	2	3	2	1	3
26_C	9	140	38	1.2	2	3	1	3	2	1
27_C	9	140	43	0.6	2	1	2	1	3	2

10.1.1.2. Quasi-Static Data

Table 10-2: Calculated onset and densification strains, transition strain length, stress at onset and densification strains and minimum IPR of all L27 samples with the Cheetah 2_N for comparison.

Sample	Strain (m/m)			Stress (MPa) at			
	ε_O	ε_l	ε_η	ε_O	ε_l	ε_η	ε_O
2_N	0.232	0.349	0.428	0.051	0.077	0.056	-0.13
1_C	0.328	0.407	0.341	0.100	0.130	0.183	-1.11
2_C	0.354	0.395	0.352	0.066	0.094	0.069	-0.25
3_C	0.314	0.406	0.375	0.189	0.226	0.188	-0.10
4_C	0.309	0.374	0.375	0.041	0.062	0.039	-0.24
5_C	0.269	0.479	0.424	0.114	0.140	0.141	-0.10
6_C	0.435	0.460	0.404	0.014	0.029	0.022	-0.68
7_C	0.253	0.553	0.498	0.093	0.103	0.082	-0.10
8_C	0.368	0.536	0.374	0.010	0.026	0.017	-0.65
9_C	0.280	0.326	0.349	0.067	0.135	0.069	-0.27
10_C	0.292	0.334	0.331	0.040	0.046	0.050	-0.36
11_C	0.253	0.374	0.392	0.105	0.121	0.119	-0.12
12_C	0.289	0.371	0.325	0.021	0.026	0.027	-0.41
13_C	0.230	0.393	0.401	0.070	0.096	0.078	-0.12
14_C	0.284	0.364	0.360	0.011	0.015	0.012	-0.76
15_C	0.173	0.509	0.541	0.046	0.061	0.060	-0.36
16_C	0.331	0.556	0.418	0.005	0.009	0.012	-0.35
17_C	0.368	0.536	0.371	0.025	0.099	0.035	-0.34
18_C	0.311	0.374	0.322	0.068	0.138	0.069	-0.27
19_C	0.265	0.398	0.368	0.088	0.120	0.092	-0.08
20_C	0.321	0.410	0.344	0.013	0.018	0.016	-0.58
21_C	0.269	0.459	0.413	0.070	0.103	0.075	-0.13
22_C	0.314	0.405	0.356	0.008	0.017	0.013	-0.84
23_C	0.366	0.416	0.351	0.042	0.067	0.050	-0.26
24_C	0.359	0.464	0.411	0.116	0.149	0.109	-0.07
25_C	0.300	0.334	0.370	0.033	0.059	0.043	-0.16
26_C	0.265	0.554	0.477	0.072	0.078	0.088	-0.03
27_C	0.232	0.349	0.428	0.010	0.032	0.018	-0.64

Table 10-3: Volumetric and normalised energy absorption for of all L27 samples with the Cheetah 2_N for comparison

	Volumetric Energy Absorption (kJm^{-3})			Normalised Energy absorption ($kJkg^{-1}$)		
Sample	ε_O	ε_l	ε_η	ε_O	ε_l	ε_η
2_N	137.55	198.39	155.21	0.378	0.546	0.427
1_C	31.33	44.17	56.29	0.145	0.205	0.261
2_C	188.95	250.98	197.77	0.503	0.668	0.527
3_C	528.76	613.23	525.00	0.897	1.040	0.891
4_C	130.67	176.58	158.80	0.530	0.717	0.645
5_C	309.34	390.78	392.19	0.857	1.083	1.087
6_C	45.28	85.09	71.29	0.227	0.427	0.358
7_C	293.41	317.95	266.21	1.040	1.127	0.944
8_C	33.24	74.12	62.53	0.220	0.491	0.414
9_C	204.74	365.19	208.81	0.845	1.506	0.861
10_C	112.29	131.68	142.66	0.347	0.406	0.440
11_C	262.98	310.14	306.54	0.524	0.618	0.610
12_C	55.42	82.47	87.22	0.188	0.279	0.295
13_C	176.77	243.15	203.28	0.537	0.738	0.617
14_C	35.69	45.89	39.76	0.197	0.254	0.220
15_C	134.83	176.19	173.77	0.450	0.589	0.580
16_C	14.50	29.42	32.69	0.103	0.208	0.231
17_C	89.28	196.21	114.39	0.394	0.865	0.504
18_C	206.94	369.82	209.00	0.639	1.141	0.645
19_C	208.29	272.85	218.23	0.479	0.627	0.502
20_C	35.30	55.19	49.97	0.140	0.218	0.198
21_C	183.95	258.35	200.59	0.412	0.579	0.449
22_C	26.01	46.58	39.82	0.157	0.281	0.240
23_C	124.58	171.96	143.69	0.456	0.630	0.526
24_C	296.53	362.06	279.72	0.738	0.902	0.697
25_C	113.36	159.61	132.85	0.531	0.748	0.622
26_C	182.06	207.48	237.17	0.598	0.682	0.779
27_C	35.59	80.46	61.96	0.218	0.494	0.380

10.1.1.3. Impact Data

Table 10-4: Relative maximum strain and impact duration for L27 samples.

Sample	Relative Maximum Strain			Duration (s)		
	3.30ms^{-1}	4.44ms^{-1}	5.58ms^{-1}	3.30ms^{-1}	4.44ms^{-1}	5.58ms^{-1}
1_C	1.05	1.71	2.37	0.0148	0.0118	0.0089
2_C	0.56	1.02	1.45	0.0071	0.0109	0.0109
3_C	0.39	0.60	0.85	0.0041	0.0047	0.0055
4_C	0.67	1.15	1.65	0.0096	0.0126	0.0122
5_C	0.47	0.76	1.12	0.0046	0.0070	0.0072
6_C	0.76	1.24	1.75	0.0164	0.0124	0.0098
7_C	0.46	0.80	1.19	0.0058	0.0094	0.0101
8_C	0.69	1.12	1.61	0.0159	0.0118	0.0092
9_C	0.42	0.77	1.10	0.0069	0.0108	0.0109
10_C	0.85	1.44	2.08	0.0098	0.0123	0.0095
11_C	0.55	0.87	1.34	0.0048	0.0070	0.0078
12_C	0.92	1.51	2.14	0.0168	0.0158	0.0135
13_C	0.60	1.03	1.49	0.0067	0.0095	0.0098
14_C	1.00	1.60	2.25	0.0148	0.0117	0.0094
15_C	0.68	1.20	1.74	0.0080	0.0117	0.0114
16_C	0.77	1.24	1.79	0.0139	0.0089	0.0083
17_C	0.53	0.91	1.33	0.0117	0.0150	0.0134
18_C	0.43	0.58	0.91	0.0070	0.0078	0.0085
19_C	0.62	0.96	1.44	0.0070	0.0086	0.0092
20_C	0.97	1.52	2.13	0.0145	0.0115	0.0095
21_C	0.62	0.96	1.46	0.0080	0.0097	0.0105
22_C	0.87	1.37	1.91	0.0133	0.0111	0.0084
23_C	0.72	1.15	1.68	0.0106	0.0119	0.0114
24_C	0.51	0.77	1.18	0.0058	0.0078	0.0084
25_C	0.68	1.10	1.58	0.0140	0.0136	0.0128
26_C	0.67	1.05	1.58	0.0067	0.0081	0.0091
27_C	0.70	1.10	1.59	0.0151	0.0120	0.0089

Table 10-5: Per impact velocity average and 3VS values for PLA and GSI for all L27 samples at all Impact velocities

Sample	PLA (g)				GSI			
	3.30ms^{-1}	4.44ms^{-1}	5.58ms^{-1}	3VS	3.30ms^{-1}	4.44ms^{-1}	5.58ms^{-1}	3VS
1C	58.12	170.55	230.90	23.59	132	744	1411	116.65
2C	140.80	129.14	128.90	21.88	578	665	827	111.68
3C	264.20	282.53	287.77	45.23	1799	2541	2811	380.02
4C	110.49	100.12	138.86	19.17	363	478	722	83.68
5C	222.05	216.54	204.29	35.10	1282	1493	1527	231.64
6C	49.05	147.96	221.01	21.50	109	582	1276	101.08
7C	157.54	150.31	141.58	24.58	663	745	791	118.76
8C	55.00	180.43	243.71	24.49	101	794	1482	120.55
9C	137.26	125.37	123.21	21.18	538	595	746	101.65
10C	103.07	104.36	149.15	19.41	310	504	774	84.02
11C	140.80	200.68	185.74	27.96	1011	1318	1325	195.14
12C	140.80	117.56	178.20	24.08	137	437	902	76.47
13C	142.96	138.40	139.43	22.99	562	709	863	114.33
14C	60.31	164.46	232.39	23.56	120	683	1404	112.95
15C	122.33	115.13	130.47	20.14	412	517	711	88.02
16C	100.87	229.67	294.58	32.40	220	1250	2207	187.00
17C	89.90	90.18	136.73	17.26	218	354	614	62.85
18C	181.34	185.85	166.35	29.01	860	1090	1046	160.31
19C	134.63	150.76	145.37	23.26	515	832	929	119.96
20C	73.64	175.51	238.79	25.27	152	762	1479	122.46
21C	117.99	134.47	124.28	20.32	419	681	743	97.03
22C	97.97	213.13	267.73	30.05	228	1094	1847	161.51
23C	91.06	102.39	149.39	18.53	243	470	760	77.31
24C	156.69	172.18	160.15	26.45	674	1001	1052	144.33
25C	76.14	99.82	154.46	17.70	153	385	722	65.64
26C	140.99	155.56	143.31	23.78	564	822	878	119.99
27C	72.01	178.92	248.28	25.82	139	789	1560	127.12

10.1.1.4. Initial ANOVA tables.

Table 10-6: Initial AVONA results for 3.30ms^{-1} impacts PLA S/N values.

Factor	f_g	S_g	V_g	P_g(%)	F_g	Confidence Level
α	2	5.27	2.63	1.50 %	0.4	-
γ	2	7.45	3.73	2.12 %	0.57	-
β	2	16.02	8.01	4.56 %	1.21	-
t	2	221.59	110.80	63.08 %	16.8	99%
α - γ Interaction	2	6.93	3.47	1.97 %	0.53	-
α - β Interaction	2	11.53	5.77	3.28 %	0.87	-
t - α Interaction	2	29.74	14.87	8.47 %	2.26	-
γ - β Interaction	2	5.81	2.90	1.65 %	0.44	-
t - γ Interaction	2	0.50	0.25	0.14 %	0.04	-
t - β Interaction	2	6.86	3.43	1.95 %	0.52	-
Error	6	39.56	6.59	11.26 %	-	-
Total	26	351.27	-	100.00 %	-	-

Table 10-7: Initial AVONA results for 4.44ms^{-1} impacts PLA values.

Factor	f_g	S_g	V_g	P_g(%)	F_g	Confidence Level
α	2	4.30	2.15	2.62	1.04	-
γ	2	1.34	0.67	0.82	0.33	-
β	2	2.06	1.03	1.25	0.5	-
t	2	99.17	49.58	60.46	24.06	99%
α - γ Interaction	2	8.96	4.48	5.46	2.17	-
α - β Interaction	2	0.78	0.39	0.48	0.19	-
t - α Interaction	2	5.97	2.99	3.64	1.45	-
γ - β Interaction	2	0.44	0.22	0.27	0.11	-
t - γ Interaction	2	7.03	3.51	4.28	1.7	-
t - β Interaction	2	21.61	10.80	13.18	5.24	95%
Error	6	12.36	2.06	7.54	-	-
Total	26	164.01	-	100.00	-	-

Table 10-8: Initial AVONA results for 5.58ms^{-1} impacts PLA values.

Factor	f_g	S_g	V_g	P_g(%)	F_g	Confidence Level
α	2	1.16	0.58	0.75	0.24	-
γ	2	0.09	0.05	0.06	0.02	-
β	2	0.28	0.14	0.18	0.06	-
t	2	104.75	52.37	67.87	22.08	99%
α - γ Interaction	2	10.16	5.08	6.58	2.14	-
α - β Interaction	2	1.79	0.89	1.16	0.38	-
α - t Interaction	2	4.10	2.05	2.65	0.86	-
γ - β Interaction	2	0.08	0.04	0.05	0.02	-
γ - t Interaction	2	7.95	3.98	5.15	1.68	-
β - t Interaction	2	9.75	4.88	6.32	2.06	-
Error	6	14.23	2.37	9.22	-	-
Total	26	154.34	-	100.00	-	-

Table 10-9: Initial AVONA results for 3.30ms^{-1} impacts GSI values

Factor	f_g	S_g	V_g	P_g(%)	F_g	Confidence Level
α	2	34.59	17.29	2.69	2.29	-
γ	2	22.94	11.47	1.78	1.52	-
β	2	20.86	10.43	1.62	1.38	-
t	2	1016.7	508.35	79.01	67.46	99%
α - γ Interaction	2	21.46	10.73	1.67	1.42	-
α - β Interaction	2	3.62	1.81	0.28	0.24	-
α - t Interaction	2	54.05	27.03	4.20	3.59	90%
γ - β Interaction	2	0.19	0.10	0.01	0.01	-
γ - t Interaction	2	10.08	5.04	0.78	0.67	-
β - t Interaction	2	57.09	28.54	4.44	3.79	90%
Error	6	45.21	7.54	3.51		
Total	26	1286.79		100.00		

Table 10-10: Initial AVONA results for 4.44ms^{-1} impacts GSI values

Factor	f_g	S_g	V_g	P_g(%)	F_g	Confidence Level
α	2	12.37	6.19	3.21	1.08	
γ	2	8.16	4.08	2.12	0.71	-
β	2	4.52	2.26	1.17	0.39	-
t	2	195.48	97.74	50.75	17.08	99%
α - γ Interaction	2	27.77	13.89	7.21	2.43	-
α - β Interaction	2	3.68	1.84	0.96	0.32	-
α - t Interaction	2	17.56	8.78	4.56	1.53	-
γ - β Interaction	2	0.13	0.06	0.03	0.01	-
γ - t Interaction	2	25.81	12.90	6.70	2.25	-
β - t Interaction	2	55.34	27.67	14.37	4.83	90%
Error	6	34.34	5.72	8.92	-	-
Total	26	385.15	-	100.00	-	-

Table 10-11: Initial AVONA results for 5.58ms^{-1} impacts GSI values

Factor	f_g	S_g	V_g	P_g(%)	F_g	Confidence Level
α	2	7.55	3.78	2.49	0.65	-
γ	2	3.61	1.81	1.19	0.31	-
β	2	0.81	0.40	0.26	0.07	-
t	2	168.70	84.35	55.51	14.53	99%
α γ Interaction	2	21.98	10.99	7.23	1.89	-
α β Interaction	2	6.95	3.48	2.29	0.6	-
α t Interation	2	11.16	5.58	3.67	0.96	-
γ β Interaction	2	0.11	0.05	0.03	0.01	-
γ t Interaction	2	21.28	10.64	7.00	1.83	-
β t Interaction	2	26.91	13.45	8.85	2.32	-
Error	6	34.83	5.80	11.46	-	-
Total	26	303.88	-	100.00	-	-

Table 10-12: Initial AVONA results for PLA based 3VS

Factor	f_g	S_g	V_g	P_g(%)	F_g	Confidence Level
α	2	40.04	20.02	4.30%	1.05	-
γ	2	14.93	7.47	1.60%	0.39	-
β	2	25.86	12.93	2.77%	0.68	-
t	2	394.82	197.41	42.37%	10.31	99%
α γ Interaction	2	91.13	45.57	9.78%	2.38	-
α β Interaction	2	28.75	14.38	3.09%	0.75	-
α t Interation	2	96.82	48.41	10.39%	2.53	-
γ β Interaction	2	5.75	2.87	0.62%	0.15	-
γ t Interaction	2	39.71	19.86	4.26%	1.04	-
β t Interaction	2	79.23	39.61	8.50%	2.07	-
Error	6	114.83	19.14	12.32%	-	-
Total	26	931.86	-	100.00%	-	-

Table 10-13: Initial AVONA results for PLA based 3VS

Factor	f_g	S_g	V_g	P_g(%)	F_g	Confidence Level
α	2	7120	3559.9	6.65%	1.34	-
γ	2	3539	1769.4	3.31%	0.66	-
β	2	2806	1402.9	2.62%	0.53	-
t	2	36889	18444.6	34.48%	6.92	95%
α γ Interaction	2	10116	5058.1	9.45%	1.9	-
α β Interaction	2	3026	1513.1	2.83%	0.57	-
α t Interation	2	8472	4236.2	7.92%	1.59	-
γ β Interaction	2	518	258.8	0.48%	0.1	-
γ t Interaction	2	7980	3989.9	7.46%	1.5	-
β t Interaction	2	10547	5273.3	9.86%	1.98	-
Error	6	15983	2663.8	14.94%	-	-
Total	26	106995	-	100.00%	-	-

10.1.1.5. Optimal Geometry results

Table 10-14: Recorded PLA values for all tested optimal geometries at all test conditions.

Metric	Optimal	3.30ms^{-1}	4.44ms^{-1}	5.58ms^{-1}	3VS
PLA	3.30ms^{-1}	54.62	180.17	242.15	24.37
	4.44 ms^{-1}	81.07	98.14	178.01	19.24
	5.58 ms^{-1}	137.23	125.36	120.31	21.02
	3VS	66.02	99.72	154.43	17.01
GSI	3.30 ms^{-1}	54.62	180.17	242.15	24.37
	4.44 ms^{-1}	76.14	99.72	154.43	17.69
	5.58 ms^{-1}	89.89	88.98	136.52	17.19
	3VS	78.79	111.08	203.52	21.01

Table 10-15: Recorded PLA values for all tested optimal geometries at all test conditions.

Metric	Optimal	3.30ms^{-1}	4.44ms^{-1}	5.58ms^{-1}	3VS
PLA	3.30ms^{-1}	101	792	1474	120
	4.44 ms^{-1}	191	382	987	82
	5.58 ms^{-1}	537	594	744	101
	3VS	153	384	719	65
GSI	3.30 ms^{-1}	101	792	1474	120
	4.44 ms^{-1}	153	384	719	65
	5.58 ms^{-1}	217	353	611	63
	3VS	170	415	1172	93

10.1.2. Chapter 6.

Table 10-16: Calculated values for strain of maximum efficiency (ε_η) normalised stress ($\tilde{\sigma}$) and normalised energy absorption ($\widetilde{W}$) values for each scale variant of the developed optimals.

		ε_η		$\tilde{\sigma}$		$\widetilde{W}$	
Optimum	Scale	(m/m)	Normalised		Normalsied	kJm^{-3}	Normalised
3.30ms-1	100%	0.497	1.00	0.050	1.000	0.383	1.000
	50%	0.466	0.94	0.045	0.890	0.314	0.820
	33%	0.508	1.02	0.063	1.256	0.494	1.291
4.44 ms-1 PLA	100%	0.380	1.00	0.082	1.000	0.524	1.000
	50%	0.459	1.21	0.111	1.351	0.690	1.317
	33%	0.555	1.46	0.196	2.376	1.244	2.375
4.44 ms-1 GSI	100%	0.414	1.00	0.081	1.000	0.537	1.000
	50%	0.408	0.99	0.078	0.965	0.479	0.893
	33%	0.600	1.45	0.135	1.656	1.024	1.908
5.58 ms-1 PLA	100%	0.370	1.00	0.133	1.000	0.859	1.000
	50%	0.486	1.31	0.124	0.932	1.022	1.190
	33%	0.480	1.30	0.132	0.994	1.052	1.224
5.58 ms-1 GSI	100%	0.415	1.00	0.067	1.000	0.463	1.000
	50%	0.415	1.00	0.067	1.000	0.463	1.000
	33%	0.600	1.45	0.290	4.339	1.969	4.250
3VS PLA	100%	0.414	1.00	0.081	1.000	0.538	1.000
	50%	0.408	0.99	0.078	0.962	0.479	0.890
	33%	0.600	1.45	0.135	1.651	1.024	1.902
3VS GSI	100%	0.393	1.00	0.050	1.000	0.313	1.000
	50%	0.390	0.99	0.066	1.320	0.395	1.263
	33%	0.427	1.09	0.108	2.154	0.657	2.100

Table 10-17: PLA and calculated GSI values for all test samples and geometries, with Rawlings and Riddell foams for comparison.

		3.30ms^{-1}		4.44ms^{-1}		5.58ms^{-1}	
Optimum	Scale	PLA (g)	GSI	PLA (g)	GSI	PLA (g)	GSI
Riddell Foam	-	62.57	148	108.06	403	165.32	841
Rawlings Foam	-	52.76	105	136.66	506	218.26	1180
3.30ms^{-1}	100%	54.62	101	180.17	792	242.15	1474
	50%	50.21	97	143.53	541	244.5	1271
	33%	48.9	103	102.48	343	176.98	880
4.44 ms^{-1} PLA	100%	81.07	153	98.14	384	178.01	719
	50%	66.02	185	100.6	394	166.85	876
	33%	62.47	185	95.71	380	133.44	685
4.44 ms^{-1} GSI	100%	81.07	191	98.14	382	178.01	987
	50%	73.16	216	103.24	430	162.27	904
	33%	90.64	298	110.32	513	142.61	858
5.58 ms^{-1} GSI	100%	89.89	217	88.98	353	136.52	611
	50%	55.88	113	95.55	389	135.92	705
	33%	80.36	243	102.47	476	135.54	761
5.58 ms^{-1} PLA	100%	137.23	537	125.36	594	120.31	744
	50%	110.72	345	104.96	509	119.45	742
	33%	110.51	367	109.86	508	114.3	713
3VS GSI	100%	78.79	170	111.08	415	203.52	1172
	50%	55.88	194	106.97	422	184.62	1035
	33%	88.79	299	104.58	497	146.75	844
3VS PLA	100%	66.02	153	99.72	384	154.43	719
	50%	66.02	185	100.6	394	166.85	876
	33%	62.47	185	95.71	380	133.44	685

Table 10-18: Normalised PLA and GSI for all tested MOM samples.

		3.30ms^{-1}		4.44ms^{-1}		5.58ms^{-1}	
Optimum	Scale	PLA (g)	GSI	PLA (g)	GSI	PLA (g)	GSI
3.30ms^{-1}	100%	1.000	1.000	1.000	1.000	1.000	1.000
	50%	0.919	0.960	0.797	0.683	1.010	0.862
	33%	0.895	1.020	0.569	0.433	0.731	0.597
4.44 ms^{-1} PLA	100%	1.000	1.000	1.000	1.000	1.000	1.000
	50%	0.867	1.209	1.009	1.026	1.080	1.218
	33%	0.820	1.209	0.960	0.990	0.864	0.953
4.44 ms^{-1} GSI	100%	1.000	1.000	1.000	1.000	1.000	1.000
	50%	0.902	1.131	1.052	1.126	0.912	0.916
	33%	1.118	1.560	1.124	1.343	0.801	0.869
5.58 ms^{-1} GSI	100%	1.000	1.000	1.000	1.000	1.000	1.000
	50%	0.622	0.521	1.074	1.102	0.996	1.154
	33%	0.894	1.120	1.152	1.348	0.993	1.245
5.58 ms^{-1} PLA	100%	1.000	1.000	1.000	1.000	1.000	1.000
	50%	0.807	0.642	0.837	0.857	0.993	0.997
	33%	0.805	0.683	0.876	0.855	0.950	0.958
3VS GSI	100%	1.000	1.000	1.000	1.000	1.000	1.000
	50%	0.709	1.141	0.963	1.017	0.907	0.883
	33%	1.127	1.759	0.941	1.198	0.721	0.720
3VS PLA	100%	1.000	1.000	1.000	1.000	1.000	1.000
	50%	1.000	1.209	1.009	1.026	1.080	1.218
	33%	0.946	1.209	0.960	0.990	0.864	0.953

Table 10-19: Calculated and normalised 3VS values for both GSI and PLA values for each scale variant of the develop optimals.

		GSI 3VS		PLA 3VS	
Optimum	Scale	(GSI)	Normalised	(g)	Normalised
Riddell Foam	-	72.52	-	17.72	-
Rawlings Foam	-	92.34	-	21.13	-
3.30ms-1	100%	119.96	1.000	24.37	1.000
	50%	98.29	0.819	22.67	0.930
	33%	69.16	0.577	17.20	0.706
4.44 ms-1 PLA	100%	82.45	1.000	19.24	1.000
	50%	81.69	1.170	18.06	0.94
	33%	88.12	1.002	18.46	0.96
4.44 ms-1 GSI	100%	65.45	1.000	19.24	1.000
	50%	76.55	0.991	18.06	0.939
	33%	65.56	1.069	18.46	0.960
5.58 ms-1 GSI	100%	62.58	1.000	17.19	1.000
	50%	62.19	0.994	15.14	0.881
	33%	77.64	1.241	17.06	0.992
5.58 ms-1 PLA	100%	101.40	1.000	21.02	1.000
	50%	84.83	0.837	18.33	0.872
	33%	84.66	0.835	18.24	0.868
3VS GSI	100%	92.54	1.000	21.01	1.000
	50%	86.94	0.940	18.27	0.869
	33%	86.80	0.938	18.33	0.872
3VS PLA	100%	65.45	1.000	17.01	1.000
	50%	76.55	1.170	17.72	1.042
	33%	65.56	1.002	15.46	0.909